A STUDY OF LUBRICATING FILMS GENERATED BY ORGANO-PHOSPHORUS ANTI-WEAR ADDITIVES

- by -

Gary James Johnston

A Thesis Submitted for the Degree of
DOCTOR OF PHILOSOPHY
of the University of London
and also for the
DIPLOMA OF IMPERIAL COLLEGE

January 1990

Tribology Section
Department of Mechanical Engineering
Imperial College of Science, Technology and Medicine
London SW 7

ABSTRACT

This thesis examines the reactions of organo-phosphorus ester anti-wear (AW) lubricant additives.

The role of additives in enhancing lubricant base oil performance is examined with particular reference to phosphorus AW additives. The major synthetic routes to these compounds are reviewed. The preparation, purification and characterisation of a range of esters of phosphoric and phosphonic acids, and their amine salts, are described.

The design, calibration and commissioning of a number of test rigs used to simulate different lubrication regimes is described. The role of different classes of phosphorus-based esters has been examined in two ways, firstly by direct study within the operating test rigs ("in lubro" approach) and secondly, by preparation of model polymeric compounds in static, solution tests by reacting additives with soluble Fe (III) salts ("in vitro approach"). The physical and chemical properties of the material formed in the two environments has been examined and compared.

The build-up of thick, protective polymeric layers has been demonstrated with long chain length mono and di-alkyl / aryl phosphonates at elevated temperature, in both boundary and full fluid film lubrication. No thick film build-up has been observed with short chain length versions, tri-alkyl phosphites and a range of di-alkyl acid phosphates.

A novel interferometric technique has been developed for measuring very thin lubricant films. This incorporates a thin silica spacer layer and spectroscopic analysis of fringe colours. Films of 1 ± 1 nanometer have been measured at the limits of the technique, with routine measurements down to 5 nanometers. The behaviour of lubricants and boundary / oiliness additives has been examined. This technique holds promise in the study of very thin anti-wear separating films.

ACKNOWLEDGEMENTS

The author would like to express his thanks to the following : -

Dr. Hugh Spikes for his consistently enthusiastic supervision.

The staff and students of the Tribology Section, past and present, for invaluable help and advice during the completion of this work. The names are too numerous to list individually. However, J.M.H, J.C.H, D.M.N and a supporting cast deserve mention for ensuring the work could reach completion. Thanks to C.V for photo-copying.

Thanks are due to the staff of the following organisations - the micro-analytical laboratory, Imperial College; the University of London NMR service, based at Kings College and Neal Components, Coventry for building the optical EHD rig.

The author is indebted to the Ministry of Defence for funding the project.

Finally, and most notably, I would like to thank K.E.M.S for her love, patience and not inconsiderable efforts in typing this work.

TABLE OF CONTENTS

		Page
ABSTRACT		i
ACKNOWLEDGEMENTS		ii
TABLE OF CONTENTS		iii
LIST OF FIGURES		xi
LIST OF TABLES		xv
LIST OF PLATES		xvii
NOMENCLATURE		xviii
Chapter 1	**General Introduction**	
1.1	Introduction	1
1.2	The dry contact of solid bodies - the importance of surface roughness	2
1.3	The lubricated contact of solid bodies - regimes of lubrication	4
1.4	Elastohydrodynamic (EHD) lubrication	9
1.5	Viscosity - the influence of temperature and pressure	13
1.6	Boundary lubrication	15
1.6.1	Interposed films	16
1.6.2	Interaction films	18
1.6.3	Asperity junction-growth inhibition	18
1.7	Additives included in formulated oils	19
1.8	Anti-wear (AW) and extreme pressure (EP) additives	21
1.9	Background to the current work - Organophosphorus esters, the 'thick film' effect	22
1.10	Proposed aims of the current work	24
1.11	Experimental approach employed in current work	25

Chapter 2 **Phosphorus Based Lubricant Additives - An Overview**

2.1	Introduction	27
2.2	Physical properties of phosphorus-based lubricant additives	28
2.3	Comparative performance studies in modal test-rigs	32
2.3.1	The influence of base oil type on additive performance	40
2.3.2	The influence of steel type on additive performance	43
2.3.3	The influence of oxygen on additive performance	44
2.3.4	The influence of water on additive performance	46
2.3.5	The influence of temperature on additive performance	48
2.4	The physical and chemical nature of the material formed by the reaction of steel / iron and additive	50
2.4.1	Studies into the mechanism of lubrication of tri-cresyl phosphate (TCP)	53
2.4.2	The thick film effect	60
2.5	Summary	63

Chapter 3 **Organophosphorus Compounds in Tribology. Nomenclature, Structure, Preparation and Characterisation**

3.1	Introduction	66
3.2	Nomenclature	67
3.3	Structure	69
3.3.1	Tautomerism	69
3.3.2	Structure and bonding	70
3.4	Preparation	71
3.4.1	General preparative methods - Esters of phosphonic and phosphoric acids	71
3.4.2	General preparative methods - Esters of phosphonic acid	72
3.4.3	General preparative methods - Esters of phosphoric acid	74
3.5	Synthesis of phosphoric acid esters	75

3.5.1	Synthesis of tri-alkyl and aryl phosphates	75
3.5.1.1	Esterification of phosphorus oxychlorides	75
3.5.1.2	Miscellaneous preparation of tri-aryl phosphates	76
3.5.1.3	Miscellaneous preparation of tri-alkyl phosphates	77
3.5.2	Synthesis of mono and di-alkyl and aryl phosphoric acid esters	78
3.5.2.1	Mono-alkyl and aryl acid phosphates	78
3.5.2.2	Di-alkyl and aryl acid phosphates	79
3.6	Synthesis of phosphonic acid esters	80
3.6.1	Synthesis of tri-alkyl and aryl phosphites	80
3.6.1.1	Alcoholysis of PCl_3	80
3.6.1.2	Miscellaneous preparation of tri-alkyl and aryl phosphites	81
3.6.2	Synthesis of di-alkyl and aryl phosphonates	81
3.6.2.1	Alcoholysis / hydrolysis of PCl_3	81
3.6.2.2	Miscellaneous preparation of di-alkyl and aryl phosphonates	82
3.6.3	Synthesis of mono alkyl and aryl phosphonates	84
3.6.3.1	Alcoholysis of PCl_3	84
3.6.3.2	Miscellaneous preparation of mono-alkyl and aryl phosphonates	84
3.7	Amine salts of acid esters of phosphoric and phosphonic acid	85
3.7.1	Amine salts of acid phosphates	86
3.7.2	Amine salts of mono-alkyl phosphonates	86
3.8	Characterisation of additives and surface films in tribology	87
3.8.1	Analytical techniques in the characterisation of synthetic additives	88
3.8.1.1	Phosphorus nuclear magnetic resonance ($^{31}P_{NMR}$)	88
3.8.1.2	Vibrational spectroscopy - Infra-red (IR) and Raman spectroscopy	89
3.8.1.3	Miscellaneous analytical techniques	90
3.8.2	Surface analytical techniques	91

Chapter 4 Preparation, Purification and Characterisation of Organophosphorus Esters and Ester Derivatives

4.1	Introduction	93
4.2	Preparation and purification of phosphoric acid esters and ester derivatives	94
4.2.1	Preparation of di-alkyl acid phosphates - $(RO)_2(HO)P(O)$	95
4.2.1.1	Di-methyl and di-butyl acid phosphates	96
4.2.1.2	Di-octyl and di-2-ethyl-hexyl acid phosphates	99
4.2.2	Amine salts of di-alkyl acid phosphates - $(C_6H_5.CH_2NH_3O)(RO)_2P(O)$	100
4.3	Preparation and purification of phosphonic acid esters and ester derivatives	101
4.3.1	Di-substituted phosphonates - $(RO)_2P(O)H$	101
4.3.1.1	Di-octyl and di-dodecyl phosphonate	102
4.3.1.2	Di-alkyl and di-aryl phosphonates from other sources	103
4.3.2	Mono-substituted phosphonates - $(RO)(HO)P(O)H$	109
4.3.2.1	Mono-alkyl phosphonates	109
4.3.2.2	Mono-aryl phosphonates	111
4.3.3	Amine salts of mono-alkyl phosphonates - $[CH_3(CH_2)_{17}NH_3O](RO)P(O)H$	113
4.4	Techniques for characterising organophosphorus esters and ester derivatives	114
4.4.1	Vibrational spectroscopy - Infra-red (IR) absorption spectra	114
4.4.1.1	Vibrational spectroscopy - theory	114
4.4.1.2	IR group frequency correlations	115
4.4.1.3	Recording IR spectra - practical details	118
4.4.2	Phosphorus nuclear magnetic resonance spectroscopy $^{31}P_{NMR}$	118
4.4.2.1	Measurement of $^{31}P_{NMR}$ spectra	120
4.4.3	Elemental analysis	121
4.4.3.1	Technique	121
4.4.4	Single parameter measurements	121
4.5	Characterisation of organophosphorus esters	122

and ester derivatives

4.5.1 Di-alkyl acid phosphates - $(RO)_2(HO)P(O)$ 122

4.5.2 Benzyl amine salts of di-alkyl acid phosphates - $(C_6H_5.CH_2NH_3O)(RO)_2P(O)$ 130

4.5.3 Di-alkyl phosphonates - $(RO)_2P(O)H$ 133

4.5.4 Mono-alkyl phosphonates - $(RO)(HO)P(O)H$ 134

4.5.5 Octadecylamine salts of mono-alkyl phosphonates - $[CH_3(CH_2)_{17}NH_3O](RO)P(O)H]$ 137

Chapter 5 Experimental details of test rigs used in current study. Design, calibration and commisioning tests.

5.1 Introduction 146

5.2 Elevated temperature optical interferometric test rigs 148

5.2.1 Optical interferometry 148

5.2.1.1 The monochromatic system - basic interferometry 149

5.2.1.2 Requirements for good fringe visibility 150

5.2.1.3 Calibration of monochromatic fringes and phase change on reflection 153

5.2.1.4 Duochromatic interferometry - calibration of fringes 161

5.2.1.5 White light (chromatic) interferometry - calibration of fringes 163

5.2.1.6 Refractive index of the separating medium 166

5.2.1.7 The interferometric systems - advantages and disadvantages 167

5.2.2 Elevated temperature optical EHD rig used in early testwork 169

5.2.3 Elevated temperature optical EHD rig designed and commissioned for use in current work 171

5.2.3.1 Temperature control and measurement 174

5.2.3.2 Ball loading systems - calibration of track radius 175

5.2.3.3 Motors - speed control and measurement 181

5.2.3.4 Optical system 183

5.2.3.5 Lubricant preparation viscosity / shear rate measurement 185

5.2.4 General experimental procedure - commissioning tests for EHD rig 186

5.2.4.1 Effective pressure viscosity coefficient 187

	(α value) as a function of temperature	
5.2.4.2	Separation as a function of slide-roll ratio (SRR)	192
5.2.4.3	General test procedure for monitoring thick film formation	198
5.3	High frequency reciprocating (HFR) test device	200
5.3.1	Calibration of HFR rig	202
5.3.2	Sample preparation and test procedure	204
5.4	Mini-disc machine	205

Chapter 6 Performance testing of organophosphorus esters

6.1	Introduction	207
6.2	Esters of phosphonic acid $(HO)_2P(O)H$	207
6.2.1	Di-alkyl / aryl phosphonates $(RO)_2P(O)H$	207
6.2.1.1	Maximum film thickness / depletion of additive (BOPP)	208
6.2.1.2	Rate of film build-up with other additives present	212
6.2.1.3	Performance in high sliding, boundary lubricated contact - HFR testing of BOPP	214
6.2.1.4	Physical nature of the film material - high viscosity liquid or solid ?	217
6.2.1.5	Behaviour of chemical film material in a rolling contact and in a stationary contact - high speed photography	224
6.2.1.6.	Miscellaneous esters - short chain di-alkyl phosphonates	227
6.2.2	Mono-alkyl phosphonates (RO)(HO)P(O)H and their amine salts	228
6.2.2.1	Mini-disc machine testing - mono-dodecyl phosphonate	228
6.2.2.2	Mono alkyl phosphonates - testing in EHD rig	231
6.2.2.3	Discussion - film build-up with mono-alkyl phosphonates / amine salts	233
6.3	Esters of phosphoric acid - $(HO)_3P(O)$	235
6.3.1	Tri-cresyl phosphate (TCP)	235
6.3.1.1	HFR testing of TCP	235
6.3.1.2	Static (in vitro) pretreatment with TCP	238
6.3.1.3	Dynamic pretreatment with TCP (in EHD rig)	241
6.3.2	Phosphoric acid esters and their amine salts	242

Chapter 7 Physical and chemical nature of organo-phosphorus additive / iron reaction product

7.1	Introduction	244
7.2	Physical nature of the iron / additive reaction product	245
7.2.1	Reaction films generated on steel surfaces	245
7.2.1.1	Chemical polishing vs. thick film formation Talysurf relocation - out of contact	246
7.2.1.2	Talysurf relocation - within the wear scar	251
7.2.2	Physical nature of film material generated in an EHD rig	252
7.2.2.1	Physical nature of material generated in pure sliding	252
7.2.2.2	SEM / EDAX analysis of material generated in pure sliding	257
7.2.2.3	Physical nature of material generated in a rolling EHD contact	259
7.2.2.4	Hardness of material generated in a rolling EHD contact	263
7.2.3	Physical nature of material generated 'in vitro'	267
7.2.3.1	Rheopecticity / refractive index of polymeric material	267
7.2.3.2	Importance of surface pretreatment	269
7.2.3.3	Life cycle / history of thick film material Dissolved iron content - Atomic Absorption Spectroscopy	271
7.3	Chemical nature of iron / additive reaction product	275
7.3.1	Chemical nature of reaction product formed 'in vitro'	275
7.3.1.1	Introduction - experimental procedure / additives tested	275
7.3.1.2	Experimental observations	276
7.3.1.3	Mechanism of polymer formation	279
7.3.1.4	Discussion	288
7.3.2	Chemical nature of reaction product formed on surfaces	288

Chapter 8 Development of optical interferometric method. The measurement and study of very thin lubricant films in concentrated contacts.

8.1	Introduction	291
8.1.1	Previous studies	291

8.2	Development of optical interferometry - experimental method	294
8.2.1	Spectral analysis of central film thickness	294
8.2.1.1	Calibration of the spectrometer	295
8.2.1.2	Spectral measurement of film thickness - conventional disc	298
8.2.2	Spacer layer method	299
8.2.2.1	Evaluation of silica film thickness as a function of disc radius	299
8.2.2.2	Evaluation of refractive index of silica film	301
8.2.2.3	Spectral measurement of film thickness (sputtered disc)	302
8.2.3	Experimental conditions and lubricants tested	303
8.3	Results	304
8.3.1	Validation of experimental technique	304
8.3.1.1	Spectral measurement of the film thickness - conventional disc	304
8.3.1.2	Spacer layer method	305
8.3.2	Results with different base stocks	306
8.3.2.1	Discussion - calculation of α values	308
8.3.2.2	Hexadecane ± stearic acid	310

Chapter 9 Conclusions and suggestions for further work

9.1	Conclusions	312
9.2	Suggestions for further work	317

Appendix

A1	Temperature-viscosity data for lubricants used in current study	319
A2	Alpha value as a function of temperature (SHC 234)	319

References 320 - 341

Authors Publications 342

LIST OF FIGURES

		Page
Figure 1.1	The statistical measurement of surface profile heights	4
Figure 1.2	Stribeck curve - coefficient of friction (μ) vs. operating conditions	5
Figure 1.3	Variation of coefficient of friction (μ) with specific film thickness (Λ)	7
Figure 1.4	Variation of the fraction of time metal-metal contact occurs and the life adjustment factor in rolling contact fatigue, with specific film thickness	8
Figure 1.5	Contour map of EHD point contact	10
Figure 1.6	Validity of EHD equation - g_V vs. g_E	12
Figure 1.7	Structure of polymer material	23
Figure 2.1	Wear scar diameter vs. pK_a	31
Figure 3.1	Nomenclature of main groups of phosphorus compounds	67
Figure 3.2	Nomenclature of main phosphorus acids	68
Figure 3.3	General preparative scheme - esters of phosphonic and phosphoric acids	72
Figure 4.1	Five port flat flange reaction vessel	97
Figure 4.2	Infra-red spectra of di-hexyl phosphonate as 'received' and 'distillate' fractions	105
Figure 4.3	Infra-red spectra of di-hexyl phosphonate 'remaining' fraction and mono-hexyl phosphonate	106
Figure 4.4	Apparatus for producing mono-alkyl phosphonates	110
Figure 4.5	$^{31}P_{NMR}$ spectrum of di-(2-ethyl-hexyl) acid phosphate	123
Figure 4.6 to 4.10	Infra-red spectra of di-alkyl acid phosphates - $(RO)_2(HO)P(O)$ (R = Me, But, 2-Et-hex, Oct and Dodec) and amine salts	125 to 129
Figure 4.11	$^{31}P_{NMR}$ spectrum of benzyl amine salt of di-(2-ethyl-hexyl) phosphate	131
Figure 4.12	Infra-red spectra of benzyl amine and octadecyl amine	132
Figure 4.13	$^{31}P_{NMR}$ spectrum of mono-(2-ethyl-hexyl) phosphonate	136

Figure 4.14 $^{31}P_{NMR}$ spectrum of octadecyl ammonium salt of mono (2-ethyl-hexyl) phosphonate 139
Figure 4.15 to 4.19 Infra-red spectra of mono alkyl phosphonates - (RO)(HO)P(O)H and their amine salts 141 to 145

Figure 5.1 Basic interferometric system (two beam) 149
Figure 5.2 Ball on plate contact used for fringe calibration 155
Figure 5.3 Spectral characteristics of monochromatic and duochromatic filters 156
Figure 5.4 Fringe radius calibration graph 157
Figure 5.5 Fringe radius (r_f) as a function of load (green light source) 158
Figure 5.6 Fringe radius (r_f) as a function of load (red light source) 159
Figure 5.7 Fringe thickness vs. order - phase change (ϕ) on reflection 161
Figure 5.8 Fringe radius (r_f) as a function of load (duochromatic light source) 162
Figure 5.9 Fringe radius (r_f) as a function of load (white light source) 165
Figure 5.10 Sectional view of EHD rig used in early test work 170
Figure 5.11 Schematic diagram of EHD test rig 172
Figure 5.12 Pneumatic ball and cage loading assembly ('cotton-reel' type) 176
Figure 5.13 Filar eyepiece calibration / measured fringe diameter (function of load) 177
Figure 5.14 Calibration graph for pneumatic loading system 178
Figure 5.15 3-Disc mount assembly showing set-up for track radius calibration 179
Figure 5.16 Schematic representation of jig for mounting ball on quill-drive 181
Figure 5.17 Log (h) vs. log (U), as a function of temperature (OEP 215 and Ref. oil) 189
Figure 5.18 Log (h) vs. log ($U\eta_0$), as a function of temperature (as Fig. 5.17) 190
Figure 5.19 Alpha value as a function of temperature (OEP 215) 191
Figure 5.20 Oil A - speed ratio ($R_{U\,(B/D)}$) vs. log speed 195
Figure 5.21 Log (separation vs. speed) as a function of slide-roll ratio 196
Figure 5.22 Oil A - log separation vs. log average speed 198
Figure 5.23 Schematic diagram of high frequency reciprocating (HFR) test rig 201
Figure 5.24 Schematic representation of set-up used to calibrate ECR in HFR rig 202
Figure 5.25 HFR rig - calibration of stroke length 203
Figure 5.26 Schematic diagram showing mini-disc machine and capacitance bridge set-up 205

Figure 6.1 Maximum film thickness (BOPP) - separation vs. time 209
Figure 6.2 Film build-up with time - 3 % BOPP in SHC 234 211
Figure 6.3 Film build-up with time - 3 % BOPP ± full additive package 213
Figure 6.4 Electrical contact resistance vs. temperature 215
- hexadecane ± 3 % BOPP
Figure 6.5 Coefficient of friction (μ) vs. temperature 216
- hexadecane ± 3 % BOPP
Figure 6.6 Maximum scar depth vs. temperature 217
- hexadecane ± 3 % BOPP
Figure 6.7 Film thickness predicted in a 'constant U' test 221
as a function of rolling speed ratio
Figure 6.8 Observed and predicted film thickness increase in a 'constant U' 222
test - 3 % BOPP in SHC 234
Figure 6.9 Observed and predicted film thickness increase in a 'constant U' 223
test - 3 % DDDP in SHC 234
Figure 6.10 Intensity / time profile for short duration Xe flash unit 224
Figure 6.11 Disc machine experimental vs. theoretical film thickness (± additive) 230
Figure 6.12 Chemical film build-up - mono and di-dodecyl phosphonate 233
Figure 6.13 HFR rig - coefficient of friction (μ) vs. time (SHC 234 ± 7% TCP) 236
Figure 6.14 HFR rig - electrical contact resistance vs. time (SHC 234 ± 7% TCP) 237
Figure 6.15 HFR rig - wear scar profilometry (SHC 234 ± 7% TCP) 238
Figure 6.16 Log h vs. log U - static pretreatment SHC 234 ± 3% TCP 239
Figure 6.17 Separation vs. disc speed - static pretreatment SHC 234 ± 3% TCP 240
Figure 6.18 Separation vs. disc speed 242
- dynamic pretreatment SHC 234 ± 5% TCP

Figure 7.1 Schematic diagram of test-piece relocation device 247
Figure 7.2 Relocation of surface profiles - untreated test piece (A) 248
Figure 7.3 Relocation of surface profiles - BOPP / hexadecane test piece (B) 250
Figure 7.4 Relocated wear scar surface profile after HFR testing in 251
BOPP / hexadecane - pre and post DMSO treatment
Figure 7.5 Schematic diagram of ball surface profile relocation device 255
Figure 7.6 Surface profile of ball after testing with BOPP - in pure sliding (XIV) 256

and in nominally pure rolling (XV)
Figure 7.7 EDAX emission spectrum 260
- ball run in pure sliding with BOPP / SHC 234
Figure 7.8 Surface profiles (along rolling track) for a ball tested with BOPP 266
in nominally pure rolling - effect of scribing film material
Figure 7.9 Polymer viscosity as a function of time / shear rate - pure DHP 268
Figure 7.10 Polymer viscosity as a function of time / shear rate 269
- 3% DHP / liquid paraffin
Figure 7.11 AAS calibration curve - spectrometer readout vs. iron concentration 273
Figure 7.12 Atomic absorption spectrophotometry (% iron content vs. time) 274
Figure 7.13 Infra-red spectra of dodecyl esters 280
Figure 7.14 Infra-red spectra of polymers formed with dodecyl esters and iron 281
Figure 7.15 Infra-red spectra of stearic acid and two stearate esters 284
Figure 7.16 Infra-red spectra of phenyl phosphinic acid 285
and polymer formed with iron
Figure 7.17 Infra-red spectra of TCP and polymer formed with iron 287
Figure 7.18 Phosphoryl bond vibration 289

Figure 8.1 Schematic representation of spacer layer method 293
Figure 8.2 Schematic representation of spectrometer set-up 295
Figure 8.3 (a) Schematic map of EHD point contact 296
(b) Schematic representation of screen display showing
Figure 8.4 Spectrometer calibration - wavelength against micrometer reading 297
Figure 8.5 Spectrometer calibration - micrometer reading vs screen dot position 298
Figure 8.6 Measured film thickness - thin spacer layer 299
Figure 8.7 Measured film thickness - thick spacer layer 301
Figure 8.8 Log separation vs. speed measured conventionally 305
and using spectrometer (uncoated disc)
Figure 8.9 Log separation vs. speed measured using spectrometer measured 306
on an uncoated disc and a disc coated with a spacer layer
Figure 8.10 Log separation vs. speed - liquid crystal and squalane 307
Figure 8.11 Log separation vs. speed - *tri*-tolyl phosphate and poly -α-olefin 307
Figure 8.12 Log separation vs. speed - siloxanes A and B, and polyol ester 308
Figure 8.13 Log separation vs. speed - purified hexadecane ± stearic acid 310

LIST OF TABLES

			Page
Table	1.1	Main features of lubrication regimes	6
Table	2.1	Thermal and hydrolytic stabilities of phosphate esters	30
Table	2.2	Elemental composition of 440 C and US 52100 steels	35
Table	3.1	Main features of surface analytical tools applied to tribological systems	92
Table	4.1	Refractive indices (η^{20}_D) of di-hexyl phosphonate and associated products	104
Table	4.2	Approximate group frequencies of di-hexyl phosphonate and associated products	107
Table	4.3	Literature values of main group frequency correlations - Organophosphorus esters	116
Table	4.4	R.I, $^{31}P_{NMR}$ and elemental analysis data for di-alkyl acid phosphates	124
Table	4.5	Main group frequency correlations for di-alkyl acid phosphates	124
Table	4.6	$^{31}P_{NMR}$ and elemental analysis data for benzyl amine salts of di-alkyl acid phosphates	130
Table	4.7	Main group frequency correlations for benzyl amine salts of di-alkyl acid phosphates	133
Table	4.8	R.I and elemental analysis data for mono-alkyl phosphonates	134
Table	4.9	$^{31}P_{NMR}$ data for mono-alkyl phosphonates	135
Table	4.10	Main group frequency correlations for mono-alkyl phosphonates	137
Table	4.11	$^{31}P_{NMR}$ and elemental analysis data for octadecylamine salts of mono-alkyl phosphonates	138
Table	4.12	Main group frequency correlations for octadecylamine salts of mono-alkyl phosphonates	138
Table	5.1	Phase changes on reflection for the contact of a flat and a sphere	154
Table	5.2	Values of parameters used in calculation of Hertzian radius (a)	158

Table	5.3	Comparison of fringe calibration with previous authors Duochromatic and white light sources	163
Table	5.4	Cone constants used in viscosity and shear rate calculations	186
Table	5.5	Refractive indices and viscosity data used in α value calculations	188
Table	5.6	α value calculation - data from figures 5.17 and appendix A1	189
Table	5.7	Evaluation of α values as a function of temperature (data from figure 5.18)	190
Table	5.8	Relationship between slide-roll ratio (SRR) and speed ratio $R_{U\,(B/D)}$	193
Table	5.9	Oil A - crude data for pure rolling and rolling / sliding studies	194
Table	5.10	Log U_D as a function of slide-roll ratio (data from figure 5.20)	196
Table	5.11	Calculation of average speed at which first red fringe was observed	197
Table	6.1	Fully formulated additive package	212
Table	6.2	Contact conditions for capacitance measurements in mini-disc machine	229
Table	6.3	Static pretreatment conditions (SHC ± 3% TCP)	238
Table	6.4	EHD rig - pretreatment conditions (SHC ± 3% TCP)	241
Table	7.1	Values for parameters used in EHD film thickness calculation	253
Table	7.2	Experimental conditions used for EDAX analysis	259
Table	7.3	Elemental composition of EN 31 and AISI 52100 steels	270
Table	7.4	Anti-wear additives reacted with Fe (III) stearate	277
Table	7.5	Presence of peaks and approximate group frequencies - dodecyl esters and polymers formed with iron stearate	282
Table	7.6	Presence of peaks and approximate group frequencies - phenyl phosphinic acid and polymer formed with iron stearate	286
Table	7.7	Approximate group frequencies - dodecyl esters and polymers formed with different iron sources	290
Table	8.1	Experimental conditions	303
Table	8.2	Measured viscosities and refractive indices for experimental lubricants	303
Table	8.3	Measured and literature α coefficients. Gradients for calculated values	309

LIST OF PLATES

		Page
Plate 5.1	Monochromatic fringes in oil (green source λ_{max} = 546 nm). Filters - Wratten 77A and 58. Stationary contact.	164
Plate 5.2	Duochromatic fringes in oil (green and red sources). Filters - Wratten 77A. Stationary contact.	164
Plate 5.3	Chromatic fringes in oil (white light source). Stationary contact.	164
Plate 5.4	Optical interferometric test rig (variable slide-roll ratio and temperature)	173
Plate 5.5	Monochromatic fringes in oil (green source λ_{max} = 546 nm). Filters - Wratten 77A and 58. Rolling contact.	184
Plate 5.6	Duochromatic fringes in oil (green and red sources). Filters - Wratten 77A. Rolling contact.	184
Plate 5.7	Chromatic fringes in oil (white light source). Rolling contact.	184
Plate 6.1	Short duration exposure of BOPP-generated film in rolling contact (U = 0.789 m/s)	225
Plate 6.2	BOPP film in loaded contact at end of test (temperature = 100° C)	226
Plate 7.1	Appearance of film material around contact after pure sliding test with BOPP	258
Plate 7.2	Scribed film material generated in central rolling track with BOPP	262
Plate 7.3	Surface distribution of thick film material	263

NOMENCLATURE

All of the symbols used in the text are included here for ease of reference.
Symbols not defined here are defined in the text, and are denoted *.

§	-	Section of thesis
μ	-	Coefficient of friction, μ = frictional resistance / perpendicular force
ν	m^2 / s	Kinematic viscosity or frequency (see text)*
R_a	m	Centre line average (CLA) value *
R_q	m	Root-mean-square (RMS) value *
Λ	-	Specific film thickness or 'Lambda' value *
λ	m	Wavelength
σ	cm^{-1}	Wavenumber
P	Pa	Pressure or Hertzian Pressure *
ρ	kg / m^3	Density
τ	N / m^2	Shear stress
IR	-	Infra red
NMR	-	Nuclear magnetic resonance
δ	ppm	Chemical shift
SRR	-	Slide-roll ratio*

Elastohydrodynamic (EHD) film thickness equation

Operating parameters

U	m / s	Mean surface speed, $U = (U_1 + U_2) / 2$
U_n	m / s	Surface speed of component n
W	N	Total normal load
h_c	m	Central film thickness *
h_o	m	Minimum film thickness *

Solid Parameters

E	N / m^2	Youngs modulus, E = stress / longitudinal strain

σ_n	-	Poisson's ratio, σ = lateral strain / longitudinal strain
E'	N/m^2	Reduced Young's modulus

$$\frac{1}{E} = \frac{1}{2}\left[\left(\frac{1-\sigma_1^2}{E_1}\right)+\left(\frac{1-\sigma_2^2}{E_2}\right)\right]$$

R_{11},R_{12}		Principal radii of contact
R_x'	m	Reduced radius perpendicular to the rolling direction
		$1/R_x' = 1/R_{11} + 1/R_{21}$
R_y'	m	Reduced radius parallel to the rolling direction
		$1/R_y' = 1/R_{12} + 1/R_{22}$

Lubricant Parameters

η_o	Pa.s	Effective dynamic viscosity at inlet (at appropriate shear rate) *
α	Pa^{-1}	Pressure viscosity coefficient *

Dimensionless Parameters

$\overline{U}$	-	Speed parameter *
$\overline{G}$	-	Materials parameter *
$\overline{W}$	-	Load parameter *

SUBSCRIPTS

B - Ball	D - Disc
1 - Component 1	2 - Component 2
c - Central	o - minimum

ABBREVIATIONS

da	10	deca	k	10^3	kilo	M	10^6	mega
d	10^{-1}	deci	c	10^{-2}	centi	m	10^{-3}	milli
μ	10^{-6}	micro	n	10^{-9}	nano	Å	-	10^{-10} m

CHAPTER 1 - GENERAL INTRODUCTION

1.1 Introduction

This thesis describes a study of the mechanism of action of phosphorus-based anti-wear additives. These additives are added to many conventional lubricating oils such as crankcase engine oils and gas turbine oils, to reduce the wear of rubbing metal parts immersed in the oil. Prior to a detailed description of these additives it is necessary to acquaint the reader with some general information on lubrication and lubricant additives included in formulated oils.

This chapter therefore provides a general introduction to the role of specialist additives included in formulated oils, to combat deficiencies observed when using the base stock alone. The reasons for including the additives are discussed in terms of their intended function. This necessitates a brief consideration of the lubricated contact of solid bodies. A number of distinct regimes of lubrication are identified in which the operating fluid - a formulated oil - carries different proportions of the total load. As such, the demands made on the oil are highly dependent on the regime of operation. The types of additives used to formulate an oil to operate in a specific environment, reflect this.

The discussion focuses on the role of phosphorus-based anti-wear and extreme-pressure additives, which are the subject of the current work. A number of theories conventionally used to describe the mechanistic role of organo-phosphorus additives are examined.

In recent years advances in the techniques available for investigating the protective layers formed, have shown that at least one family of additives operate by a radically different mechanism. The evidence for this new interpretation is briefly reviewed; a full critical survey of the literature is given in chapter 2. The new concept of anti-wear action raises a number of questions as to the extent of its applicability to other groups of anti-wear additives, and so on. These questions are discussed in the context of the aims and objectives of the current work. Finally, the experimental approach employed to achieve these objectives is discussed.

1.2 The dry contact of solid bodies - the importance of surface roughness

The dry, sliding contact of solid bodies is characterised by retarding forces emanating from the common boundary. A relationship between the resistive force - *friction* - and the load applied between the bodies was first observed by da Vinci in the fifteenth century. The first known systematic study of the phenomenon was published by Amonton (1699) who formulated the following laws:-

(i) Friction force is directly proportional to the load applied.
(ii) For a given load, friction force is independent of the apparent area of contact between the sliding surfaces.

The magnitude of the frictional force depends critically upon the nature of the contacting surfaces. This is usually described by a *coefficient of friction* (μ), where μ = frictional resistance divided by perpendicular force. A distinction should be drawn between the *static* friction (μ_S) i.e. the force required to start sliding and the *kinetic* friction (μ_K), the force required to maintain sliding (Coulomb 1781). This can result in a variable coefficient of friction, particularly at slow sliding speeds, and this phenomenon is often referred to as *stick-slip*.The variable coefficient of friction arises from two distinct contributions to the dry friction. These are *adhesion* of contacting asperities and *interlocking* or *ploughing* of opposing asperities during sliding. Nominally 'clean' surfaces are invariably poisoned by atmospheric contaminants that produce oxide coatings or chemical films which result in a reduction in the coefficient of friction. Atomically clean surfaces will weld instantly. Buckley [1] for example, has obtained values of μ up to 40 for annealed copper in a rigorously clean, high-vacuum environment.

The second of Amonton's laws results from the 'rough' nature of real surfaces, which are neither smooth on a geometrical nor on a molecular scale. Mechanical cleavage of ionic crystals having a layer-lattice structure can produce fairly large areas, of the order of mm^2, that are atomically smooth and lie at levels separated by steps of a few atoms height. Such surfaces have been characterised by field ion microscopy [2]. Highly reflective ground surfaces can possess structural irregularities up to approximately 130 nm. Lapping a mirror-finished specimen on a metallographic wheel will produce long waviness of the order of 25 nm. However, typical engineering finishing processes such as grinding, result

in surface features with peak to valley heights of 1 - 2 μm. Since molecular attraction occurs over a range of a few Angstroms, the 'real' area of intimate contact will therefore be restricted to the very small areas where the surface asperities are within range of this molecular attraction. In all but a few exceptional cases, for example when thin metallic films are present, the real area of contact increases proportionally with load. For this reason the coefficient of friction remains independent of load. This was demonstrated by Bowden and Tabor [3], who measured $\mu = 1.17 \pm 0.10$ for steel sliding on electrolytically polished aluminium, over the million-fold load range from 10 μg to 10 kg. Stylus probe instruments are often used to produce two dimensional surface profiles, usually chosen to run perpendicular to the orientation of any remaining grinding marks. Two statistical treatments of surface profiles are commonly used to describe the distribution of asperity heights. These are (I) the *centre line average* value R_a (CLA) and (II) the *root-mean square* value R_q (RMS). For a surface profile of length L, the CLA peak height is given by

$$R_a = \frac{1}{L} \int_0^L | Z | \, dx \qquad \text{(I)}$$

which is simply the average deviation of peak heights from the *centre line*, over the length L. The centre line is defined in figure 1.1. The root-mean-square peak height is given by

$$R_q = \sqrt{\frac{1}{L} \int_0^L Z^2 \, dx} \qquad \text{(II)}$$

which represents the standard deviation of the peak heights from the reference line, over the distance L.

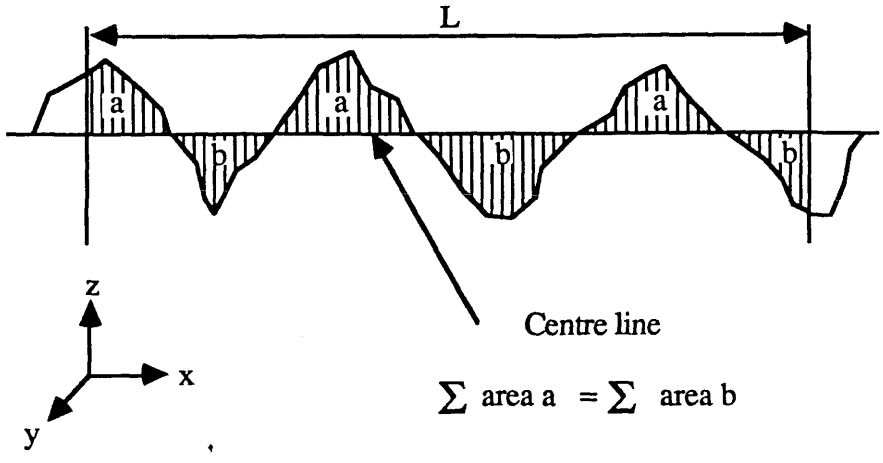


Figure 1.1 The statistical measurement of surface profile heights

A second parameter is necessary to describe the spatial distribution of the asperities in the plane of the surface. The measured value of CLA or RMS depends upon the sampling length L because, in increasing scale or wavelength, roughness is superimposed upon waviness which exists on any geometric error of form. In profilometry a maximum measured wavelength is determined by selecting a *cut-off length* or filter, the minimum wavelength is determined by the stylus tip radius, typically 2 or 10 μm. A full description of the measurement and statistical treatment of rough surfaces is beyond the scope of the current work and a full discussion can be found, for example, in [4].

1.3 The lubricated contact of solid bodies - regimes of lubrication

In many practical systems an oil is introduced to cut-down frictional power losses and with the aid of careful design, the fraction of the load carried by the oil is maximised. Secondary functions of the oil include debris removal and cooling, the latter occurs both by reducing local frictional heating and by bulk convection to a distant heat-exchanger. Lubricated contacts generally form a convergent wedge with the surfaces in relative motion, into which oil is dragged. Upon entering the contact, the nearly incompressible oil generates a load-bearing pressure, and shear resistance within the fluid transmits a frictional force - *traction* - between the contacting surfaces. The extent to which the total load carried is shared between the fluid and the larger surface asperities depends upon the relative height of the

asperities and the oil film thickness. This can be demonstrated by consideration of the well known 'Stribeck' curve shown schematically in figure 1.2 (this is sometimes referred to as the 'Petroff' curve, after Petroff who produced a theoretical relationship to predict the friction). The curve relates the coefficient of friction to the dimensionless parameter ($\eta U/P$) for a hydrodynamically lubricated journal bearing (where η is the viscosity of the lubricant, U is the speed and P is the nominal load). In the "boundary zone" the bearing is almost completely carried by asperity contact and the friction is largely independent of ($\eta U/P$) i.e. the the ability of the lubricant to form a separating oil film. In the "hydrodynamic" zone the surfaces are fully separated and the seemingly anomalous increase in friction with falling load results from an increased film thickness, which implies more lubricant being sheared viscously. In the transition between the regimes, the 'mixed' zone, the friction is highly sensitive to changes in ($\eta U/P$).

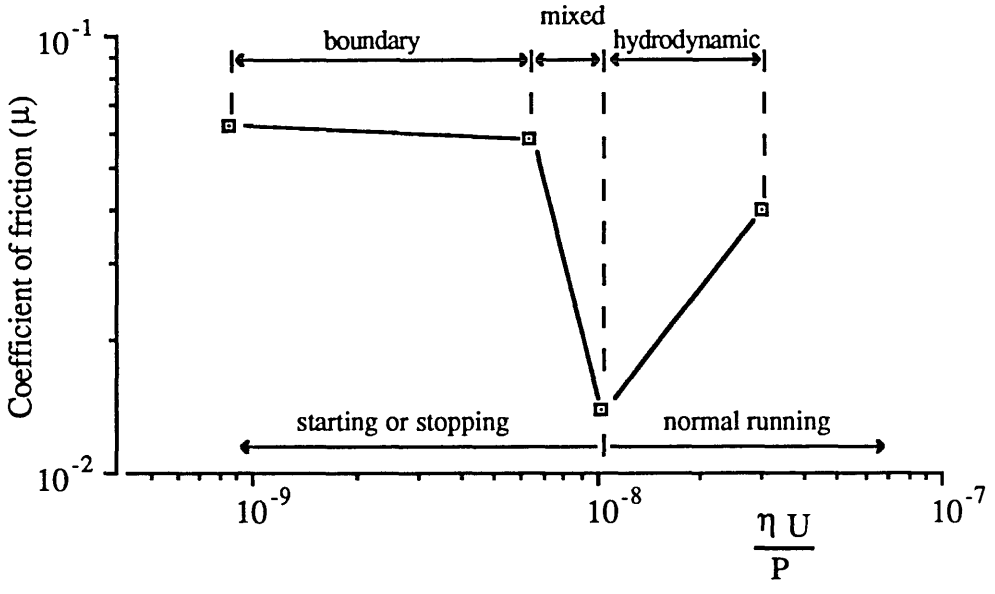


Figure 1.2 Stribeck curve - coefficient of friction (μ) vs. operating conditions

The relationship between asperity height and the oil film thickness is often described in terms of the *specific film thickness* or 'lambda value' (Λ). This relates the *minimum oil film thickness* in the contact (h_0) to the *composite surface roughness* (R_{qc}), defined as in (III). R_{qc} is a composite of R_{q1} and R_{q2}, the RMS roughnesses of the two contacting surfaces (IV).

$$\Lambda = \frac{h_o}{R_{qc}} \qquad \text{(III)}$$

where

$$R_{qc} = \sqrt{R_{q_1}^2 + R_{q_2}^2} \qquad \text{(IV)}$$

A number of distinct lubrication regimes can be identified depending upon how the load is carried. The main features of each lubrication regime are summarised in table 1.1.

REGIME	h /μm	Typical μ	Important Lubricant Parameters	Contacting Surfaces Geometry	Speed
Hydrodynamic	1 - 100	.007 - 0.03	$h \alpha (U\eta)$	conformal	moderate / high
Hydrostatic	1 - 100	~ 0 - 0.03	applied pressure, geometry	conformal	independent
EHD	0.1 - 1	~ 0 - 0.1	$h \alpha (U\eta)^{0.67}$ $\alpha (\alpha)^{\sim 0.5}$	counterformal	moderate / high
Boundary	10^{-3} - 0.05	0.08 - 0.3	anti-wear, extreme pressure formulation	variable	high
Dry	10^{-3} - 10^{-2} oxide	0.4 - 0.8	-	-	-

Table 1.1 Main features of lubrication regimes

The abbreviations used in table 1.1 are defined and discussed in sections 1.4 to 1.6. These sections consider the two regimes of interest in the current work - elastohydrodynamic (EHD) and boundary, and the moderate speed 'mixed' condition in which load-carrying is shared between the two regimes. Throughout this work the symbol (§) is used to denote other sections of the thesis.

Figure 1.3 gives typical lambda values within which each regime operates, together with typical values for the coefficient of friction. Both the elastohydrodynamic and the hydrodynamic regimes are preceded by a low speed / low viscosity 'mixed' regime. Figure 1.3 is not intended to imply that elastohydrodynamic and hydrodynamic regimes operate concurrently.

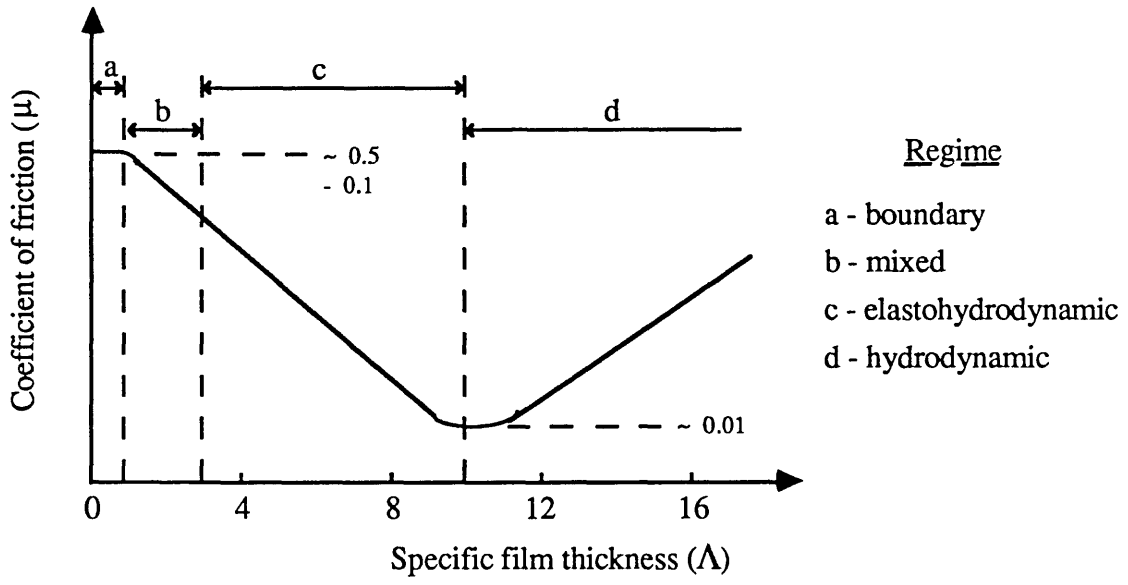


Figure 1.3 Variation of coefficient of friction with specific film thickness (Λ)

The lambda value is a critical operating parameter and it has been found to correlate with wear [5], scuffing and rolling contact fatigue [6]. Figure 1.4 demonstrates firstly the fraction of time that metal to metal contact occurs at various lamba values [7] and secondly, the resulting change in fatigue life of rolling element bearings at varying lambda [6]. The *life adjustment factor* (F), is the ratio of the actual life of a rough bearing to the predicted / book value, as defined by the American Society of Mechanical Engineers (ASME). Surface initiation of fatigue cracks is assumed to result from metal to metal contact.

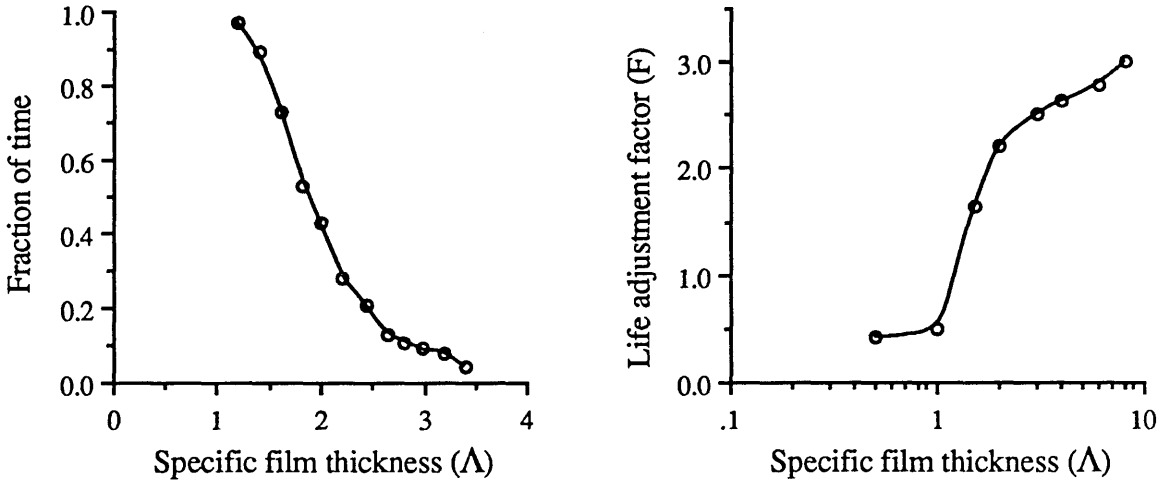


Figure 1.4 Variation of the fraction of time metal-metal contact occurs [7] and the life adjustment factor in rolling contact fatigue [6], with specific film thickness

1.4 Elastohydrodynamic (EHD) lubrication

Table 1.1 described the hydrodynamic regime as occurring in conformal contacts such as journal bearings, i.e. those in which the surfaces mate closely over a considerable distance. The load carried is therefore spread over a comparatively large area resulting in relatively low contact pressures, generally less than 0.1 GPa. A pressure of this magnitude will have a negligible effect on the oil viscosity and this regime is accurately described by the isoviscous Reynolds equation [8].

However, in many lubricated contacts, for example rolling element bearings, gear teeth and cam and tappet assemblies, the geometry is counterformal. The load is spread over a very small contact area, resulting in typical contact pressures of 1 - 5 GPa. Under these conditions the Reynold's equation predicts film thicknesses of molecular dimensions. The successful operation of these contacts observed in practice, results from two advantageous effects. Firstly, the area over which the load is carried increases as a result of the elastic deformation of the mating surfaces, and secondly the oil viscosity increases by several orders of magnitude, as a result of the very high local pressures.

The elastic deformation of concentrated contacts was first described by Hertz (1886), and for this reason the term 'Hertzian Contact' is often used. In the current work the most commonly considered example is the EHD 'point contact' of a ball on a flat. In this contact the oil inlet becomes a central plateau of nearly constant separation (h_c), bounded by a 'horseshoe-shaped' constriction around the sides and towards the outlet (h_o). The constriction in the exit occurs as a result of the rapid pressure drop and the accompanying exponential viscosity drop, that occurs at the outlet. The reversed pressure gradient and the resulting viscosity drop increases the lubricant loss-rate. The separation drops to maintain the continuity of flow. This is shown schematically as a 'contour map' of the contact in figure 1.5.

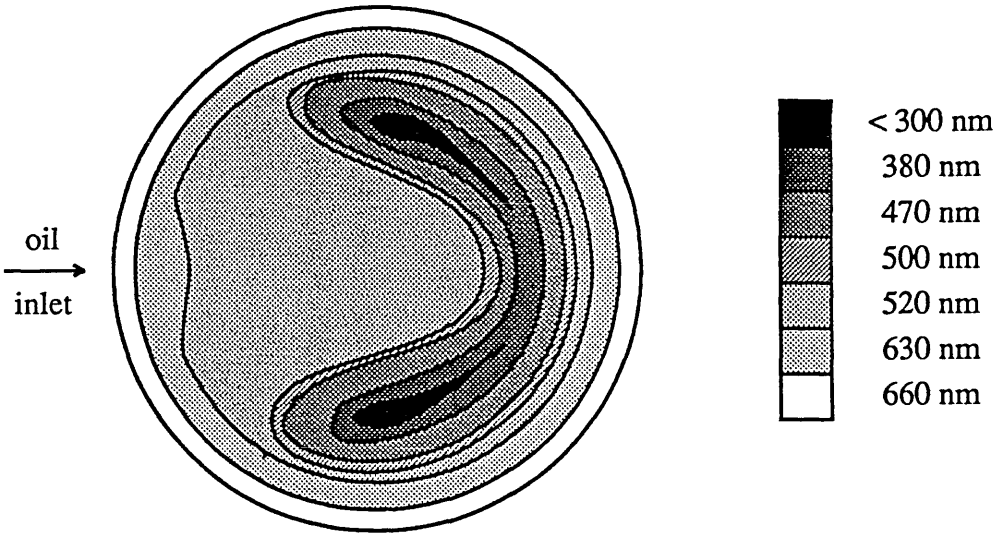


Figure 1.5 Contour map of EHD point contact

Dowson and Hamrock [9] have derived numerically based equations to predict the EHD film thickness under fully flooded, isothermal conditions for any contact geometry. The predicted central film thickness (h_c) and minimum film thickness (h_o) are given in (V) and (VI) respectively. The former is important in traction analysis and the latter is important in predicting fatigue life (§ 1.3). h_o is approximately 75 % of h_c. The constituent parameters are defined in the section 'Nomenclature' which preceded this chapter.

$$\frac{h_c}{R'_x} = 2.69 \left(\frac{U\eta_o}{E'R'_x}\right)^{0.67} (\alpha E')^{0.53} \left(\frac{W}{E'R'^2_x}\right)^{-0.067} (1 - 0.61\, e^{-0.73k}) \qquad \text{(V)}$$

$$\frac{h_o}{R'_x} = 3.63 \underbrace{\left(\frac{U\eta_o}{E'R'_x}\right)}_{\overline{U}}^{0.68} \underbrace{(\alpha E')}_{\overline{G}}^{0.49} \underbrace{\left(\frac{W}{E'R'^2_x}\right)}_{\overline{W}}^{-0.073} (1 - e^{-0.68k}) \qquad \text{(VI)}$$

$$\text{Where} \quad k = 1.03 \left(\frac{R'_y}{R'_x}\right)^{0.64} \qquad \text{(VII)}$$

k is the ellipticity parameter, which has the value 1.03 for a point contact and ∞ for a line contact. Koye and Winer [10] have experimentally demonstrated the accuracy of these equations with k in the range 0.1 - ∞. Film thicknesses below those predicted by (V) and (VI) can result from heating and starvation. References [11] and [12] contain respectively, thermal and starvation correction factors.

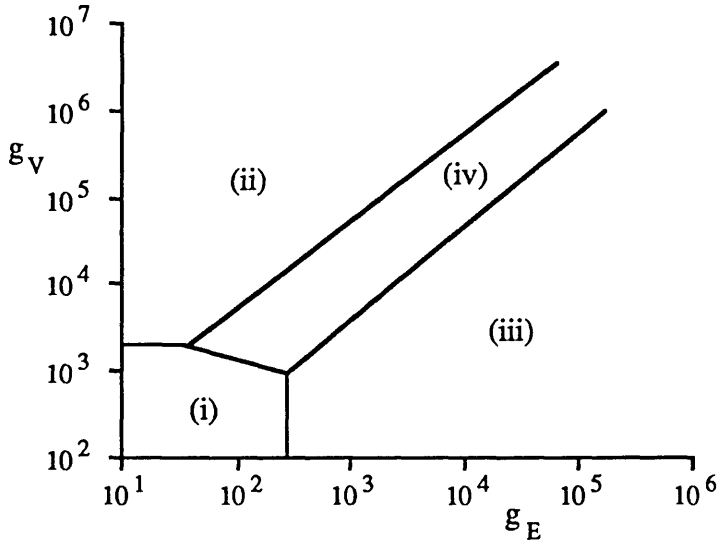
It is apparent from equations (V) and (VI) and the summary given table 1.1, that the EHD film thickness depends critically on the prevailing inlet conditions. For a given geometry, the film formed depends on the surface velocities and the oil's viscosity and pressure-viscosity coefficient. For this reason a brief description of viscosity and its dependence on pressure and temperature, is included in section 1.5.

The film thickness is usually defined in terms of three dimensionless groups, although just two can be used. These are the speed parameter ($\overline{U}$), the materials parameter ($\overline{G}$) and the load parameter ($\overline{W}$), as defined in equation (VI). The variables that constitute these equations are defined in the Nomenclature, that precedes chapter 1.The relative importance ascribed to each of these parameters depends on the nature of the particular EHD contact under consideration. A number of categories of concentrated contact have been identified and the exponents to which the dimensionless parameters are raised, are adjusted by computer regression to best describe the prevailing conditions. Equations (V) and (VI) provide the best general description, but it is important to understand the limit of their applicability. In general the equation is insensitive to load, as additional loading is countered by greater elastic deformation and load sharing, resulting in an almost unchanged Hertzian pressure. For a point contact, the type of concentrated contact present can be defined in terms of just two variables g_V and g_E . g_V and g_E are defined in terms of the three dimensionless parameters in the EHD equation as in (VIII) and (IX).

$$g_V = \frac{\overline{G}\,\overline{W}^3}{\overline{U}^2} \qquad \text{(VIII)}$$

$$g_E = \frac{\overline{W}^{8/3}}{\overline{U}^2} \qquad \text{(IX)}$$

Figure 1.6 shows a plot of g_V vs. g_E , in which four distinct regions can be identified, depending on the response of the contacting surfaces and the lubricant. It is found that the dimensionless parameters only combine to elastically deform the contact and pressure-thicken the oil in region (iv), and use of the EHD equations should be confined to contacts operating in this region. From the table included in Figure 1.5, it is apparent that region (i) is best described by the classical hydrodynamic equations. Highly pressure-thickening oils will operate in region (ii) at low loads, and isoviscous oils will operate in region (iii) with easily deformed materials such as rubber. A full discussion of this treatment can be found in [12].



Region	Solid	Oil η
(i)	rigid	constant
(ii)	rigid	P ↑
(iii)	elastic	constant
(iv)	elastic	P ↑

Figure 1.6 Validity of EHD equations - g_V vs. g_E

Before considering the important mixed / EHD regime a brief discussion of viscosity, and its dependence on pressure and temperature is included, as this is critical to EHD film formation.

1.5 Viscosity - the influence of temperature and pressure

The relationship between the force required to shear a fluid film, and the geometry and type of lubricant present, was first observed by Newton. He stated that the force (F) was proportional to two characteristics imposed by the geometry of the system - the *area* being sheared (A) and the *velocity gradient* (U / h), and to one property of the fluid - the *dynamic viscosity* (η) - which may be thought of as an 'internal friction'. This is probably better expressed by an analogy to Hooke's Law, in which a *shear stress* (τ) is applied to the top of a unit cube producing a velocity gradient or shear rate normal to (τ). (η) may now be thought of as the *modulus* of dynamic viscosity, and fluids that obey this linear relationship between stress and shear rate i.e. those in which the viscosity is independent of shear rate, are described as Newtonian . These relationships are summarised in equation (X). Many viscometers measure viscosity by the action of gravity acting on the mass of the fluid. The period required to flow a given distance under the propelling force of gravity is proportional to the *kinematic viscosity* (ν). $\nu = (\eta / \rho)$, where (ρ) is the density (kg / m^3).

$$F = \eta \,.\, A \,.\, \frac{U}{h}$$

$$\eta = \frac{F}{A} \cdot \frac{h}{U} = \frac{\tau}{(U/h)} \qquad \text{(Pa.s)} \qquad \text{(X)}$$

Fluid viscosity is highly dependent on temperature (T) and pressure (P). This is particularly true of high viscosity fluids; low viscosity fluids are far less sensitive to changes in temperature and pressure. Partington [13] lists 75 different, in the main empirical, expressions for the effect of temperature on viscosity. Two of the most accurate empirical relationships are the *Vogel* equation for dynamic viscosity (XI), and the *Walther* equation for kinematic viscosity (XII). In the following equations a,b,c and d are constants.

$$\eta = a\, e^{b/(T-c)} \qquad \text{(XI)}$$

$$\nu = a + b d^{1/T^{c}} \qquad \text{(XII)}$$

The latter expression is used in the ASTM (American Society for Testing Materials) method, which employs equation (XIII). ASTM paper is plotted so that two values of (ν,T) define all others.

$$\log \log (\nu + a) = a' - c' \log T \qquad \text{(XIII)}$$

The rapid increase in lubricant viscosity observed with increasing pressure, has been identified as being of vital importance to the lubrication of concentrated contacts. This is usually expressed in terms of a *pressure-viscosity coefficient* (α), defined as in (XIV).

$$\alpha = \frac{1}{\eta}\left(\frac{\partial \eta}{\partial P}\right)_T \qquad \text{(XIV)}$$

The Barus equation [14] is often used in EHD calculations, as the inlet pressures are low enough for this empirical relationship to be applied. The single value of (α) does not hold at all pressures, but for $P < 0.14$ GPa [15] the relationship can be applied with some confidence. The subscripts o and p in the defining equation (XV), refer to ambient pressure (usually atmospheric) and any pressure P.

$$\eta_P = \eta_O \, e^{\alpha P} \qquad \text{(XV)}$$

Klaus et al [16] have produced a single correlation equation which is claimed to predict the pressure-viscosity coefficient to good accuracy, for a wide range of base oils of different viscosity and chemical composition. The empirical correlation is given in (XVI), in which (m_0) is the *viscosity-temperature parameter*, ν_0 is the 'ambient' kinematic viscosity and the units of (α) are (kPa x 10^{-5}).

$$\alpha = 1.216 + 4.143\,(\log \nu_o)^{3.0627} + 2.848 \times 10^{-4} m_o^{5.1903} (\log \nu_o)^{1.5976} - 3.999\,(\log \nu_o)^{3.0975} \rho^{0.1162} \qquad \text{(XVI)}$$

1.6 Boundary lubrication

In hydrodynamic or EHD lubrication the extent of surface separation is largely dictated by the oil viscosity and the surface speeds. Whenever contacting surfaces have some relative motion a degree of hydrodynamic or EHD separation is ensured, but under conditions of low speeds and low viscosities this separation is reduced to molecular dimensions. Under these conditions the contact friction is determined by the nature of the surfaces, the chemical constitution of the lubricant and the properties of any chemical films formed. The separation is almost independent of lubricant viscosity. This regime is referred to as boundary lubrication. The simple friction model developed earlier in this chapter suggests successful boundary lubrication depends upon minimising asperity adhesion and interlocking (ploughing), that results in severe stick-slip. This implies an optimum surface roughness neither too rough nor too smooth. Surfaces in which $R_q < 0.02$ μm may immediately seize, and rough surfaces should be carefully run-in to avoid severe wear and seizure. Hirst and Hollander [17] rubbed stainless steel specimens of variable roughness, and found a correlation between R_q and the *correlation length* ($\log \Lambda_{1/e}$). Severe stick-slip was avoided when $R_q > 0.02$ μm and gross plastic yield of the asperities was avoided (i.e. when the plasticity index was not exceeded).

If an appreciable part of the load is carried by an elastohydrodynamic or hydrodynamic mechanism, the regime is described as 'mixed'. The following section develops a discussion of the mechanisms that operate in boundary lubrication, such as adsorption, chemisorption and chemical reaction. A number of factors complicate the investigation of these processes. The various mechanisms may operate separately, sequentially (there is strong evidence of a limited temperature range within which each mechanism can operate) or in conjunction.

In the past a great deal of research effort has been expended in rating the relative performance of additives, with a view to correlating this to important molecular parameters such as acidity, as a guide to additive functionality. Analyses of the surface films formed by additives or their decomposition products was limited, previously, by available technology. Even the highly complicated and expensive surface analytical tools available currently have a limited mechanistic value, as they require surfaces to be solvent-cleaned

and they operate in high vacuum. The following section deals with the mechanisms operating in boundary lubrication, broadly following the classification suggested by Dorinson and Ludema [2]. These authors sub-divide additive action into three categories - *interposed* films in which additive-adsorption prevents surface contact, *interaction* films in which the additives molecular structure is altered by reaction with the surface to produce additive-metal moieties and *asperity junction-growth inhibition* in which the additive interrupts the growth of asperity 'welds' preventing gross scuffing or seizure.

This classification is useful in understanding the physical processes at work on surfaces, though in practice none of these processes can be considered to operate in isolation. Subsequent sections consider the role of specialist additives included in formulated oils to improve this behaviour.

1.6.1 Interposed films

Interposed films are of three types - simple adsorbed films, chemisorbed films and chemically deposited films.

An *adsorbed* film may be characterised as consisting of adsorbed species that are not permanently altered by residence on a surface and can be desorped unchanged i.e. the process is reversible. The species generally consists of a surfactant molecule in which the polar head group is powerfully adsorped by electrostatic '*Van der Waals*' forces. The *lipophilic* hydrocarbon 'tails' are orientated out into the oil solution. A monolayer of surfactant with a straight-chain $C_{18}H_{37}$ hydrocarbon tail will form a 'hydrocarbon surface' [8] approximately 2.5 nm thick. A degree of coherence or '*adlineation*' will result from lateral attractions within the hydrocarbon chains. For example, Bigelow, Pickett and Zisman [18] demonstrated the spontaneous formation of a close-packed monolayer when clean platinum foil was dipped into solutions of eicosan-*1*-ol, *n*-octadecylamine or *n*-nonadecanoic acid in *n*-hexadecane (0.1 % w/w). Adlineation of the methylene chain binds the film laterally to such an extent that the *n*-hexadecane solvent cannot penetrate the oleophobic terminal methyl groups, preventing 'wetting' of the surface. This may also be due to repulsive forces between the polar head groups. Since the process is reversible it can be characterised by an equilibrium constant between the adsorbed and dissolved solute (high concentrations will favour the former). A full thermodynamic treatment [19] identifies

a characteristic temperature at which a critical degree of desorption occurs, accompanied by a sudden increase in the coefficient of friction. The term *physisorption* is often used when several layers of atoms or molecules are present.

Chemisorbed films may be considered to differ from adsorbed films by not being reversibly desorped at high temperature. This results from a chemically binding reaction with the surface. A number of factors are critical to this reaction - the reactivity of the surface (this is a function of the metallurgy) and the degree of surface coverage by adsorbed material. As the temperature is increased the reactivity towards chemisorption increases exponentially (according to the Arrhenius equation) and adsorbed material is thermodynamically desorped. This critical change-over has been called the 'temperature distress gap' [8]. The activity of an added surfactant is a compromise as it must compete for the surface, but should not become too corrosive at higher temperatures. Smith and co-workers [20],[21] investigated the reaction of C^{14} tagged nonadecanoic acid, with metal surfaces that were machined and stored in cyclohexane to prevent oxide formation. Reactive metals such as Cu and Mg adsorped a complete monolayer, inert metals such as Au and Pt adsorped a partial monolayer. Complete desorption of fatty acid occurred with the latter group at elevated temperature, though the reactive metals tenaciously retained the acid. The existence of a chemisorbed soap on the reactive metals was demonstrated by using a more aggressive solvent which desorped a monolayer-equivalent of metal soap i.e. the amount of metal going into solution corresponded to the amount of acid adsorped initially.

Chemically deposited films result from the reaction of precursors present in the oil that form substances which deposit onto rubbing surfaces. These reactions may occur in the bulk solution or as a result of catalysis at the surface. The deposited film is usually produced by a polymerisation or condensation reaction to give a product of higher molecular weight than the precursor. Typical examples are friction polymers or surface resins. Furey [22] studied the condensation of a C_{16} glycol and the C_{36} dibasic dimer of linoleic acid, to form a polyester film. A 1 % equimolar mixture reduced the wear rate to one tenth of the additive-free level; a similar reduction occurred with 1 % ZDDP. Direct addition of condensed ester fractions identified the relatively insoluble 'monoester' with greatest wear reduction.

1.6.2 Interaction films

The structure of a chemisorbed film is easily related to the additive from which it is derived, for example, the bulk structure may only be altered by a covalent bond to the metal surface. *Interaction* films result from extensive reaction of the rubbing surface and the additive or its decomposition products. The local high loads and rubbing speeds are often referred to as 'extreme-pressure' conditions and the rubbing energy expended will give very high local temperatures causing high additive reactivity. The films formed may contain both the metallic substrate and the additive in chemically altered states, and can be expected to show physical and chemical properties that vary as a function of proximity to the rubbing surface. For this reason precise definition of the composition and structure of these films, and consequently the mechanism by which they lubricate surfaces, has proven difficult. No example is included here as this is reviewed at length in chapter 2.

1.6.3 Asperity junction-growth inhibition

In situations such as metal cutting there is a single pass of the wearing surfaces, which would seem to negate the existence of an interaction film and little evidence for such a film has been found. It seems that under these extreme conditions the additives present can reduce interlocking by producing a weakened surface layer to a depth of the order of the surface asperities. The mechanism is not well understood, but it seems to involve dynamic competition between adhesion and adhesion-quenching by additives. A mathematical model based on this competition process has been developed by Dorinson [23]. This process, often referred to as the 'Rehbinder' effect, is not considered further as it is of limited importance in the current work.

1.7 Additives included in formulated oils

The previous section outlined the fundamental physical processes responsible for the formation of reaction-films in rubbing contacts. Most base stocks contain compounds such as fatty acids, phenols and sulphur containing impurities that exhibit some film-forming activity, but modern formulated oils contain a wide range of additives selected to extend the operating capability of the oil into more extreme environments. The classes of additives used are usually named in terms of their intended function, as described below. The type of base stock, its viscosity and the additive package it is 'fitted' with is highly dependent upon the intended regime of operation. If the environment can run with a full fluid-film then viscosity selection is critical, but in mixed or boundary lubrication a more aggressive surface active package is necessary. This section considers the type and functionality of additives commonly added to all oils. Friction modifying additives used are of three types - oiliness (or lubricity), anti-wear (AW) and extreme-pressure (EP). The latter two are of particular interest in the current study and these are the focus of section 1.8.

Oxidation inhibitors are used in almost all oils, as oxidation is accompanied by a viscosity increase (sludging) and the formation of corrosive by-products that invariably determine the useful life of a lubricant. Oxidation is a free radical process and the inhibitors operate by the deactivation of metal ions (that catalyse radical formation) or the direct removal of the chain-propagating species (free radicals and peroxides). Many additives included for AW / EP properties, such as zinc dialkyldithiophosphates (ZDDP's) and aromatic phosphorus esters, also act as anti-oxidants.

Viscosity index improvers are often included, in particular in multigrade oils. These consist of long polymeric molecules that uncoil at higher temperatures to improve the 'apparent' viscosity. However, they suffer from a 'temporary viscosity loss' at high shear rates, and extended running at high shear rates results in a 'permanent viscosity loss', as the polymer is broken-down. These compounds are also used as *pour point depressants* i.e. they prevent wax crystals forming in mineral oils, at low temperature. An empirical relationship developed to describe the rate of viscosity loss with temperature, is that of the *viscosity index*. The kinematic viscosity of the test oil (ν_U) at 40° C, is compared to those of two standard oils, one of V.I = 0 (ν_L) and one of V.I = 100 (ν_H), at 40° C. The standard

oils are chosen to have the same kinematic viscosity at 100° C. The V.I of the test oil ($V.I_U$) is defined in equation (XVII). This method was devised before the advent of synthetic and multigrade oils, which frequently have V.I's exceeding 100.

$$V.I_U = 100\left(\frac{\nu_L - \nu_U}{\nu_L - \nu_H}\right) \qquad \text{(XVII)}$$

A number of additives are included to deactivate surfaces against unwanted attack. These include *corrosion inhibitors* to protect non-ferrous metals such as Cu or Ag, and *rust inhibitors* which reduce the mobility of water adsorbed on ferrous metals, preventing the initiation of electrolytic cells. The former group includes benzotriazole and substituted azoles, and the latter uses surfactants such as metal sulphonates. The metal sulphonates should be used with caution as they are large molecules that are not easily desorped and they will compete to restrict AW / EP activity in the 'temperature gap' discussed previously. This process has been termed 'additive interference' [8].

Two groups of additives are used in crankcase oils to break-up coagulated deposits formed during combustion in IC engines. The compounds are often found to behave synergistically. *Detergents* are basic compounds such as metal salts of sulphuric acid that prevent the build-up of varnish and lacquer on pistons, and neutralise acidic impurities resulting, for example, from burning sulphur present in the fuel. *Dispersants* such as substituted succinimide are added to prevent low temperature coagulation of carbon which can block oil filters and lead to oil starvation.

Oiliness or *lubricity* additives are rarely included in commercial formulations as most base stocks have a degree of natural activity (silicone oils are a notable exception) and AW / EP additives provide more aggressive protection when required. These additives operate by adsorption with some chemisorption and this is reflected by the requirements of successful oiliness additives - strongly polar head group for powerful adsorption, chain lengths exceeding 12 carbon atoms to promote separation and straight chains to aid delineation and 'close-packing' on the surface. Long chain carboxylic acids and alcohols are used to fulfill these requirements. The critical temperature at which desorption occurs, which was described previously, can be maximised by matching the additive chain length to the average chain length of the base stock.

1.8 Anti-wear (AW) and extreme pressure (EP) additives

Anti-wear (AW) and *extreme pressure* (EP) additives are widely included in commercial formulations and although their value has been demonstrated in a range of performance tests, no unambiguous mechanism has emerged. AW additives are usually sulphur or phosphorus containing organic compounds included to control wear under conditions of moderate temperature and pressure. Examples include ZDDP and a range of phosphorus oxy-acid esters (see chapters 2 and 3). AW additives react chemically and irreversibly with the surface, and at higher temperatures their reactivity increases, unlike the reversible desorption observed with oiliness additives. The mechanism by which AW additives operate is generally believed to involve the formation of a thin metal-additive layer, though there is considerable disagreement as to the chemical nature of the layer. The protective film formed is believed to have a low shear strength and therefore abrasion is confined to the layer resulting in a gradual '*chemical polishing*' of the surface and load-sharing.

In contrast, EP additives are included as a 'last line of defence' and they should not be active under normal running conditions, as this will lead to gross corrosion at higher temperatures. Typical EP additives are sulphur, chlorine and to a lesser extent phosphorus containing compounds i.e. reactive non-metals incorporated in an inert 'carrier'. This is often achieved in gear oil additives by 'sulphurising' naturally occurring organic materials such as 'terpene' or *iso*-butenes and then post-treating to remove the most corrosive components such as polysulphides and free sulphur. EP additives are designed, as the name suggests, to be activated at higher temperatures such as those occurring as a result of high frictional heating at the onset of scuffing. During running-in EP additives form thick, inorganic and weakly-held films of the order of 50 monolayers thickness, that limit adhesion and encourage the formation of a mixed regime by a degree of polishing.

1.9 Background to the current work - Organophosphorus esters, the 'thick film' effect

Organophosphorus esters, the main subject of the current work, have long been added to oils as AW additives and to a lesser extent for their EP activity. Mechanistic studies began in 1940 with the work of Beeck et al [24], who studied tri-cresyl phosphate (TCP). These workers suggested a low-melting iron-phosphide eutectic was formed, and that the beneficial action resulted from chemical polishing and consequent load-sharing. This work was later refuted by Godfrey [61] who suggested the protective layer consisted of an inorganic metal phosphate. However, the implicit assumption in these two important papers, and in much of the later work, is that organophosphorus esters operate by the formation of a thin (0.1 - 2 nm) film of metal salt. These layers are assumed to be of low shear strength and to shear preferentially, thus reducing the severity of asperity contact events. Over the last twenty years a good deal of evidence has been published that suggests at least some of these compounds act by a radically different mechanism. In the 1970's NASA circulated a synthetic paraffinic hydrocarbon (XRM 177 F) containing a single *bis*-(alkyl substituted aryl) phosphonate to a number of test laboratories. At elevated temperatures, the lubricant gave good AW results, remarkable increases in fatigue life and film thicknesses much higher than those predicted by the (η) and (α) values alone. A number of workers, most notably Parker et al [25] and Fowles et al [26], observed the gradual build-up of an additional separation of the order of several hundred to one thousand nanometers thickness. A careful re-examination of the literature showed that similar reacted layers had been observed previously, by other workers. Rounds [27] used X-ray fluorescence (XRF) to show the formation of thick phosphorus-containing material on surfaces reacted with di-dodecyl phosphonate. Indeed Beeck [24], in the pioneering work on TCP, reports " *a smooth uniform film showing bright interference colours... incapable of resisting any shearing stress. Their presence is merely incidental and without influence on the mechanism of wear prevention.*" Modern EHD theory suggests this viscous, weakly-held material will contribute towards surface separation.

Recent work in the author's laboratory [28], [29] has extended these studies to show that a number of phosphonates [$(RO)_2P(O)H$, where R = hexyl, octyl, dodecyl, phenyl and octyl-phenyl] could form films of the order of 100 - 300 nm, at elevated temperatures of the order of 100^{o} C, in elastohydrodynamic contacts. The build-up of these films was

followed optically, using chromatic interferometry. They were found to augment normal EHD films, withstand up to 10 % sliding and continue to separate surfaces after rolling had ceased i.e. when the EHD component of the total separation fell to zero. Chemical analyses showed the protective films to be polymeric and to consist of, in the main, iron (III) mono alkyl / aryl phosphate oligimer (as shown in figure 1.7).

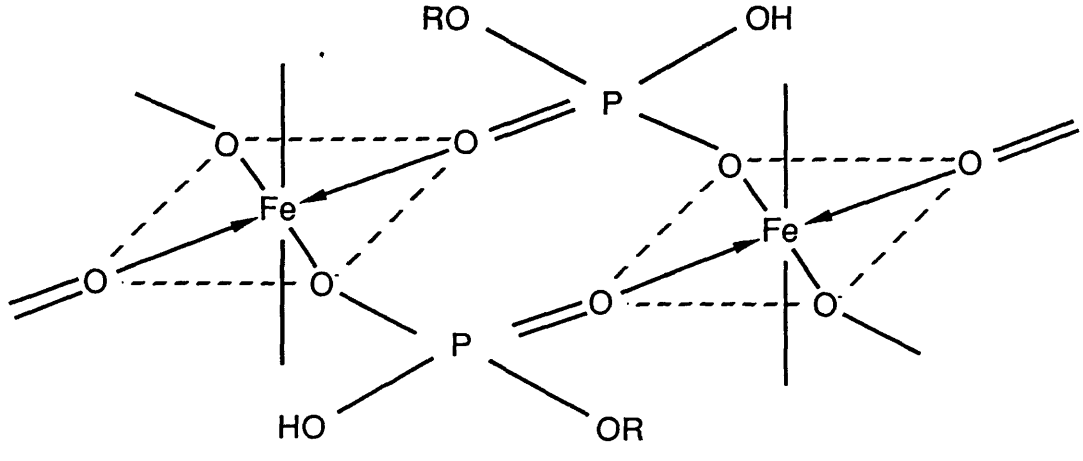


Figure 1.7 Structure of polymer material

Trachman and Cheng [30] studied the traction behaviour of XRM 177 F and in the authors' closure they state the following "*the mechanism by which the additive changes the film building capability of the lubricant is an interesting and important area for future research.*"

This section has briefly summarised the evidence for a new mechanism of anti-wear behaviour. This is considered at some length in chapter two. The following section discusses the aims and objectives of the current work.

1.10 Proposed aims of the current work

Clearly the realisation that phosphorus anti-wear additives can grow films on rubbing metal surfaces is of practical importance to both lubricant designers and users. Most simply, the appreciation of the mechanism of action of anti-wear additives may enable us to understand the variations between currently available lubricants and to explain observed deficiencies in performance under some conditions. Also the onset temperature and rate of film growth potentially provides a means of catagorising and quantifying anti-wear additive response and thus improving effective oil formulation. The build-up of protective chemical films at high temperatures may also provide a means of mitigating the decline in hydrodynamic oil film thickness which occurs at elevated temperature, due to reduced viscosity. Thus, it might permit the successful lubrication of transmission and other systems at higher temperatures than currently possible.

In view of the practical significance of the phenomenon of thick film growth, further work was proposed in the following areas, to help clarify some details of film formation and its effects.

(i) The conditions of formation of thick films. What are the effects of higher temperatures and loads, and can films could form at lower film thicknesses i.e. in mixed or boundary lubrication. These are important considerations for applying thick film concepts in practical formulations.

(ii) The effect of sliding on thick films. Are thick films relevant to high sliding conditions found for example, in many geared systems.

(iii) The life history / cycle of film formation. Are protective films lost into the surrounding lubricant with time, thereby requiring re-formation on start-up ?

(iv) Performance of various phosphonates. Thick film formation has been observed for longer chain phosphonates, but does it occur for shorter and branched chain versions that are currently included in many oil formulations ?

(v) Effect of other additives. Is thick film behaviour affected by other additives generally found in formulated oils e.g. anti-oxidants, corrosion / rust inhibitors ?

(vi) Other classes of phosphorus additives - do other additives operate by a thick film mechanism at elevated temperatures ?

(vii) Physical and chemical properties of thick films. The physical properties can be tested by applying shear and increasing traction forces in an EHD contact (also, the reported rheopecticity [76] of the polymer produced in static tests is to be investigated).

(viii) Effect of roughness of contacting surfaces on film formation.

(ix) Effectiveness of thick films in controlling friction and damage.

1.11 Experimental approach employed in current work

The following section briefly discusses the experimental approach employed in the current study to investigate the areas of interest identified in the previous section.

Previous work in the author's laboratory [28],[29],[76] and work described elsewhere in the literature (see § 1.9) has afforded a considerable mechanistic and structural insight into the compounds expected to function by a thick-film mechanism. The molecular component associated with polymer formation by the additive or its decomposition products, appears to be PO_2^-. A wide range of compounds expected to result in this active component were therefore tested for thick-film forming behaviour. Where possible, the compounds were obtained commercially, but a number of unavailable groups of compounds were synthesised by the author. Compounds containing labile acid groups were prepared as neutral amine salts. This serves the dual purpose of increasing the additive's oil solubility and decreasing the excessively corrosive behaviour associated with free acid groups.

A high temperature, ball on disc EHD test-rig was designed and commissioned for use in the current work. This permits film build-up to be followed using optical interferometry. The rig circulates a small volume of test-lubricant (~ 100 cm^3) which is heated to give accurately variable inlet temperatures up to 200 ± 1° C. Traction forces in the contact can be measured as a function of the slide-roll ratio (SRR). The SRR is accurately controlled by driving both the ball and the disc (speed holding has been shown to be better than 0.1 % for 100 % load change, to very slow speeds). This rig has been used to demonstrate the build-up of thick film material with a wide range of additives in situ, and the effects of other additives commonly included in formulated oils has been investigated. The rig has also been used to demonstrate the existence of films on balls pretreated in additive-containing solutions.

The optical EHD rig can be used indirectly to monitor film build-up under initial conditions of low specific film thickness, but it is of limited use in this respect. For this reason a conventional mini-disc machine and a high frequency reciprocating (HFR) test-device were used to investigate additive response in boundary lubrication. The mini-disc machine measures film-thickness using a capacitance technique and the HFR device provides friction and wear data as well as electrical contact resistance measurements (which provide a qualitative measure of thick-film build-up).

'Model compounds' have been prepared by reacting additives directly with iron powders or oil-soluble iron salts, in particular ferric stearate. The physical and chemical properties of the polymeric materials formed have been investigated and compared to the properties of films generated directly in rubbing contacts. The evidence from 'solution chemistry' has provided an insight into the mechanism by which additive break-down occurs and has highlighted the importance of surface metallurgy and pretreatment.

An improved interferometric technique has been developed which permits the measurement of film thicknesses two orders of magnitude thinner than previously possible. This technique has been used to investigate the behaviour of EHD films at thicknesses of a few nanometers and to investigate the behaviour of boundary additives directly, within an operating contact.

CHAPTER 2 - PHOSPHORUS BASED LUBRICANT ADDITIVES AN OVERVIEW

2.1 Introduction

The previous chapter identified the role of protective chemical layers in the successful operation of lubricated contacts. Phosphorus-containing compounds have long been added to lubricating oils to produce such layers, and therefore to control wear and seizure. This chapter critically reviews past work done with one such group of organo-phosphorus compounds - the esters of phosphorus oxy-acids - and considers attempts at elucidating the mechanism by which they function.

As the previous chapter explained, the pioneering research in this field was carried out by Beeck et al in the 1940's [24] and although the mode of action of phosphorus-based AW additives has been the subject of considerable research effort ever since, no unequivocal mechanism has emerged. A number of complimentary approaches have been employed and these are reflected in the structure of the current chapter.

Historically, additive evaluation was limited to comparative performance data obtained from test-rigs built to model a particular regime of lubrication. Under fixed conditions a comparison would be made, for example, between two different groups of compounds - such as phosphonates and phosphates (see chapter 3) - or between a homologous series of a single class. The aim was then to correlate the observed AW / EP behaviour to a relevant molecular parameter such as the hydrolytic or pyrolytic stability, the acid strength (pK_a) or the presence of catalytic trace impurities. Observed correlations then provided insights into the mechanism by which the additives operate, permitting the synthesis of improved additives. In this chapter section 2.2 describes the relevant physical properties of the additives considered; these may then be compared with the trends observed in the results from comparative performance studies in model test rigs, which are described in § 2.3. The latter section is sub-divided to reflect the relevance of important operating parameters such as temperature and the presence of dissolved oxygen or water.

A second approach to understanding the role of phosphorus lubricant additives has been to examine the direct reaction of metals with additives in solution. The solutions consist of pure additive or additive in oil, and the metal used is often in the form of a ground or milled 'powder.' The 'model-compounds' that are formed are used for physical and chemical analyses and, as previously, the aim is to correlate the observed structure with the relevant operating parameters, to gain some mechanistic insight. These studies are described as they arise in § 2.2 and 2.3.

The third important approach is based on chemical analysis of the reacted material. In the 1940's, when the study of anti-wear behaviour began, there were few analytical, and no surface analytical, techniques available. Since then many tools have become available and these have have been used to analyse the nature of the material formed both within a contact and *in vitro*. The physical and chemical nature of the film formed in these two environments, is considered in section 2.4. This section includes a summary of mechanistic studies into the action of TCP (§ 2.4.1) and a discussion of the importance of thick, reacted layers in lubrication (§ 2.4.2).

Section 2.5 consists of an overall discussion and some concluding remarks.

2.2 Physical properties of phosphorus-based lubricant additives

Barcroft and Daniel [31] attempted to correlate the observed EP activity of a series of phosphates in a cam and tappet test, with various physical and chemical characteristics of the esters. Adsorption onto iron powder was monitored using radio-tagged additives. Very similar rates were observed for tri-phenyl, tri-tolyl and tri-xylyl phosphate - respectively (TϕP), (TTP) and (TXP) - at room temperature and at 60° C. However, a comparison of the respective di-aryl acid phosphates - (DϕAP), (DTAP) and (DXAP) - resulted in irreversible 'adsorption' in the order DϕAP >> DTAP ~ DXAP; the former gave a multiple layer. At 60° C the 'adsorption' increased, with all of the additives exceeding a mono-layer. This, coupled with the irreversibility, suggests the 'adsorption' may be better thought of as salt formation.

Goldblatt and Appeldoorn [32] showed that neutral tri-cresyl phosphate (TCP) is not

adsorbed onto iron powder from a low concentration base stock solution (15 - 30 ppm i.e. sufficient to produce two mono-layers). By comparison, an acid phosphate adsorbed strongly and the phosphorus content of the oil was found to drop by two thirds during the test. This suggests the metal surface may have been contaminated, as Morecroft [66] as shown that even non-polar alkanes adsorb on clean metal surfaces.

Barcroft and Daniel [31] compared the 'thermal stability' (this might more accurately be described as an oxidative stability, as the experiment was done in air) and the hydrolytic stability of aryl phosphates when refluxed with acid or alkali. The ease of hydrolysis was as in (I); the ease of 'thermolysis' was the reverse of this.

$$T\phi P > TTP > TXP \qquad (I)$$

A good correlation was observed between scuffing resistance and the ease of hydrolysis of the phosphates. This led the authors to compare a number of alkyl / aryl di-phenyl phosphates (RDϕP) - where R = benzyl (B), allyl (Al), ethyl (E), octyl (O) and 2-ethyl-hexyl (2-EH) - of widely differing hydrolytic stabilities. The relative ease of hydrolysis is given in (II).

$$BD\phi P > AlD\phi P > ED\phi P > OD\phi P > T\phi P > TTP > 2\text{-}EHD\phi P \qquad (II)$$

In a discussion of the work [31] Gallopoulos presents results comparing the oxidative and thermal (deaerated solution, N_2 atmosphere) stabilities, and the hydrolytic stability determined in water and in acid. The results as given in table 2.1, indicate the importance of the hydrolytic environment. 1 indicates the most stable phosphate. This casts doubt on Barcroft and Daniel's assumption that the rate of hydrolysis in an acidic or alkaline solution in the absence of metal, will be the same as that at the metal surface in an oil solution. In favour of hydrolysis, the authors quote Zisman's observation [33] that "*no matter what extremes of purification were used*" tri-*o*-tolyl phosphate immediately hydrolysed on contacting hydrophilic surfaces such as synthetic sapphire (α-Al_2O_3). This process would occur more readily, they suggest, under the conditions prevalent in their cam and tappet tester.

Further details of the acid and alkaline hydrolysis of phosphonates in 'model' aqueous

systems can be found in [34].

PHOSPHATE	Oxidative Stability	Thermal Stability	Acid Hydrolysis	Water Hydrolysis
TTP	-	-	2	3
TOP	1	1	-	-
ODϕP	-	-	1	1
2EHDϕP	3	3	3	2
2EHDTP	2	2	-	-

Table 2.1 Thermal and hydrolytic stabilities of phosphate esters, data from [31]

Forbes and Battersby [35] monitored the rate of adsorption of a range of di-alkyl phosphonates [$(RO)_2P(O)H$] from liquid paraffin solution, onto ground iron powder, at 130° C. The rate of adsorption / reaction fell with increasing chain length (R), according to (III).

$$Et > Bu > 2\text{-Et-Hex} > Cyclo\text{-}Hex > Dodec > Octadec \qquad (III)$$

Soluble iron was detected in solutions containing additives with a chain length $\geq C_8$; added water was found to increase the reaction rate.

Di-alkyl phosphinic derivatives [$R_2P(O)X$, where X = H, alkoxy, amine, hydroxyl or hydroxyl-amine] are characterised by sole scission of the P—X bond and very stable C—P bonds. Forbes and Silver [36] attributed the poor AW activity of these compounds to the weak acidity of the parent acids ($pK_a \sim 3.4$) into which they degrade during testing i.e. the poor AW activity results from the poor availability of the active anion involved in formation of a protective film. They further tested this 'acid hypothesis' by comparing the wear scar diameter (WSD) from a four-ball test, with the strength of the parent acid for the rather limited series of phosphinic, phosphonic and phosphoric acid derivatives shown in figure 2.1. Direct comparison of the free acids was limited by the insolubility of the intermediate strength phosphonic acids, although the strong (di-alkyl phosphate) acids proved better AW additives than the weak (di-alkyl phosphinic) acids.

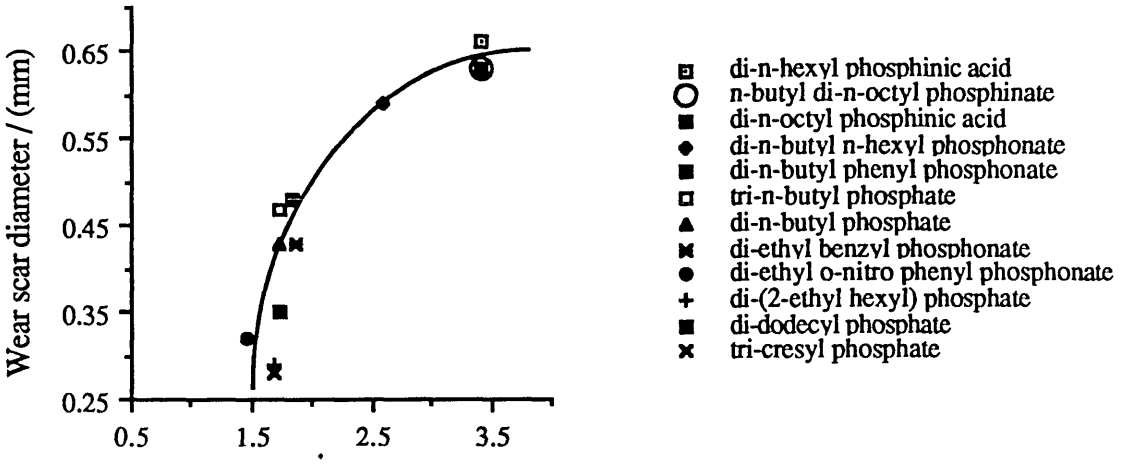


Figure 2.1 Wear scar diameter vs. pK_a , data from [35] and [36]

In a later series of tests with the amine salts of acid phosphates, Forbes et al [43] were forced to reject the theory that the strength of the parent acid was the only factor affecting anti-wear activity. A wide range of compounds with parent acids of similar strength showed a considerable variation in AW activity with chain length (see § 2.3).

Lacey et al [29], [76] investigated the reaction of a range of di-alkyl / aryl phosphonates and phosphonate / hexadecane solutions with iron powder and foil (purity 99.9 %+). The dissolved iron content was monitored as a function of time by atomic absorption spectroscopy (AAS); a nitrogen agitant and a test temperature of 157° C were employed. The order of reactivity was found to be as in (IV).

phenyl > hexyl > octyl > dodecyl (IV)

The reaction rate was found to increase with time (suggesting an 'autocatalytic' process) and with temperature. The rate of reaction increased in direct proportion to the surface area of the iron foil used. With solutions of phosphonate in hexadecane, a drop in iron content was observed after approximately 2 hours. The authors ascribed this to depletion of phosphonate and the relative insolubility of iron-containing product in pure hexadecane. The dependence of reaction rate on dissolved water, oxygen etc is discussed in § 2.3.

A number of workers have used the 'hot-wire corrosion' method of Barcroft [37], to study the high temperature reaction of iron in oils containing phosphorus-based compounds. Notable amongst these are Wiegard and Broszeit [38] and Sakurai and Sato [39], both of whom reported the presence of inorganic iron phosphates. The latter group compared the thickness of iron corroded at 500° C - as measured by resistance changes in the wire - for di-dodecyl phosphonate (DDP), tri-dodecyl phosphite (TDPi), mixed mono / di-dodecyl acid phosphate (M/DDPa) and tri-dodecyl phosphate (TDPa) in a refined bright stock (BS).

$$DDP >> M/DDPa > TDPa \sim BS > TDPi \qquad (V)$$

DDP produced a surface layer ~ 1800 nm thick in 15 minutes. The unformulated base stock alone produced a 500 nm thick film under the extreme test conditions employed. This test may therefore be measuring the ability of the additive to function as an anti-oxidant.

2.3 Comparative performance studies in model test-rigs

In their pioneering work, Beeck and co-workers [24] observed a wear minimum at a critical TCP concentration of ~ 1.5 %. The authors attributed this to the formation of a low-melting ternary eutectic consisting of iron, phosphorus, carbon and iron phosphide (Fe_3P) with a melting point of 952° C, compared to 1535° C for pure iron. The low shear-strength material would promote 'chemical polishing'. The polishing action was believed to improve load distribution, thereby reducing local temperatures and pressures. Beeck supports the iron-phosphide theory by demonstrating a further improved wear reduction with tri-phenyl phosphine i.e. a compound containing phosphorus in a 'pre-reduced' form. Iron phosphide was also produced by refluxing iron powder in TCP. The compound was as identified as iron-phosphide, as it rapidly decomposed in dilute acid to give phosphine. A synergistic wear reduction was observed in the presence of long-chain polar compounds such as fatty acids or ketones.

Davey [40] compared tri-alkyl / aryl phosphates and phosphites in mineral oil blends, in a four-ball machine. The phosphites were shown to be superior to the phosphates. The longer chain aliphatic esters generally out-performed aryl esters. The findings of Beeck [24] with regard to synergism, critical additive concentration and the nature and mode of

action of the film, were confirmed by Davey. Improved EP activity was observed with chlorinated phosphorus esters, and with thiophosphates and thiophosphites.

Thorpe and Larsen [41] reported the formation of a thin, solid, non-conducting film with 1 % TCP in white oil, in a four-ball rig. The film was believed to prevent seizure by shearing preferentially, thus preventing metal / metal contact. The synergistic improvement observed with long chain polar compounds was attributed to adsorption onto the thin, chemical film and not to the formation of a metal soap. Any metal soap formed would be unlikely to survive such rigorous conditions.

A wide range of phosphorus-containing compounds were synthesised and tested as a part of the German war effort. A summary of the results was published by Tingle in 1948 [42]. The studies identified the following as being necessary for good EP activity (i) a phosphorus atom; (ii) an active group for attachment to the surface, such as OH or Cl; (iii) an alkyl / aryl group (free acids were rejected). Di-phenyl phenyl phosphonate was found to possess the best EP activity. Attempts to correlate the observed activity to physical properties such as the acidity failed. This work was the first to involve interferometry in mechanistic studies.

Barcroft and Daniel [31] compared the EP activity of a number of tri-aryl phosphates and alkyl / aryl di-phenyl phosphates in a cam and tappet scuffing test. The compounds tested were detailed in § 2.2. The latter group were tested as they exhibit widely different stabilities, but they result in the same compound on hydrolysis). The effectiveness in preventing scuffing directly correlated with the ease of hydrolysis, as summarised in (I) and (II) above. Some further tests with alkyl and chlorinated-aryl esters suggested that the ease of hydrolysis was more important than the nature of the hydrolysis product.

A number of different groups of compounds were systematically compared in a four-ball rig, by Forbes and co-workers, in a series of papers [35], [36] and [43]. AW activity was determined from the mean wear scar diameter (WSD) after fixed periods of running at a constant low load (15 kg), and at a constant temperature (50° C) and speed (1500 rpm). EP activity was expressed as an initial seizure load (ISL) measured at ambient temperature, by incrementally increasing the load every 60 seconds. In [36] the authors tested a range of mono and di-*N*-substituted di-*n*-butyl phosphoramidates [$(ButO)_2P(O)NRR'$]. These

compounds demonstrated a similar improvement in the low load AW region, but the mono-substituted versions were generally found to be superior at higher loads. The related di-hexyl and di-octyl phosphinic acids (and their amide and alkyl ester derivatives) demonstrated poor AW / EP activity. The authors attributed this to the weak acidity of the parent acids, as discussed previously. However, the best load carrying activity was shown by a series of amine di-*n*-butyl phosphates. The observed effectiveness was shown to be independent of the degree of substitution on the nitrogen atom.

These findings prompted the investigation of a wider range of di-alkyl phosphates and their amine salts, by Forbes et al [43]. All of the di-alkyl phosphates tested were effective under AW conditions (particularly with an alkyl chain > C_4), but under EP conditions the general improvement observed was found to increase with alkyl chains length ≤ C_4. In general, the amine salts of short chain di-alkyl acid phosphates showed good AW / EP behaviour irrespective of the amine used. The longer chain length phosphates demonstrated poor load-carrying as salts of long-chain amines, but good AW / EP activity with short-chain, bulky amines. Benzyl amine demonstrated particularly good AW / EP activity.

The same test methods were applied to a range of di-alkyl phosphonates, by Forbes and Battersby [35]. The relative EP activity of the phosphonates at 4 mmol / 100 g oil is shown in (VI) below. Poor results were invariably obtained at a 0.1 mmol level, and random activity was observed with 1 mmol.

$$\text{Et} > \text{Bu} \geq \text{Dodec} \geq \text{Octadec, 2-Et Hex} > \text{Cyclohex} \qquad \text{(VI)}$$

Under AW conditions the following performance trend was observed at 4 mmol / 100 g oil (VII), although at lower concentrations di-ethyl and di-butyl phosphonate demonstrated the best, though moderate, behaviour.

$$\text{Octadec, Cyclohex, Dodec} \geq \text{2-Et Hex} >> \text{Bu} \geq \text{Et} \qquad \text{(VII)}$$

The authors explained the trends observed as follows. Under EP conditions abrasive wear would constantly expose fresh metal. The best anti-scuff behaviour would be expected from the fastest reacting species i.e. the least stable with respect to hydrolysis (that is di-ethyl phosphonate). The load carrying is largely attributed to iron inorgano-

phosphonate, i.e. an iron salt of phosphonic acid. The argument for complete hydrolysis is supported by the presence of levels of alcohols exceeding 90 % (based on both alkyl groups) after 24 hours in the adsorption tests. Under AW conditions the slowest reacting, longest chain length additives are argued to give thicker films of greater stability. The films were believed to consist of highly adlineated iron organo-phosphonate films, resulting from partial hydrolysis.

A comparison of the 4-ball test results obtained for phosphonates with those obtained for the corresponding di-alkyl acid phosphates under identical conditions, show the phosphates to be much better AW additives. Although the difference observed decreases as the AW activity improves (with increasing alkyl chain length). With an alkyl chain length of C_{12} the order is reversed. The EP activity of the phosphonates greatly exceeds that of the corresponding phosphate. A general improvement was observed with shorter chain length esters.

Hall [44] used a 4-ball rig to investigate the low load AW activity of a number of tri and di-substituted phosphates, tri-phosphites, di-phosphonates and phosphoric acid. A neopentyl ester base stock and a relatively passive, high-chromium stainless steel (440 C) were used. The composition of 440 C is compared with AISI 52100, which is a typical bearing steel, in table 2.2.

STEEL	Rockwell Hardness	ELEMENTAL COMPOSITION									
		C	Mn	Si	Ni	Cr	Mo	V	S	P	Fe
440 C	61 - 62	1.01	0.45	0.39	0.3	16.9	0.49	0.03	0.01	0.01	80.4
52100	63.5	1.14	0.35	0.29	0.1	1.43	0.005	0.01	-	-	96.7

Table 2.2 Elemental composition of 440 C and US 52100 steels

In general, di-alkyl acid phosphates and phosphoric acid gave the lowest wear rates; only these compounds were found to give consistently low, smooth wear scars. The author concludes that with unreactive 440 C steel only these compounds are "*apparently capable of forming and maintaining a beneficial film that prevented the usual irregular wear mode of 440 C steel.*" The author observed the relative wear rates summarised in (VIII).

tri-*p*-tolyl phosphite < tri-*p*-tolyl phosphate

(VIII)

di-octyl phosphonate < di-ethyl phosphonate < tri-ethyl phosphite

Hall [44] also compared a series of tri-alkyl phosphites and di-alkyl phosphonates before and after percolation to remove acid impurities. No change in AW performance was observed at low loads, but percolated samples exhibited a much reduced AW capability at higher loads. A similar load dependence was observed when di-alkyl acid phosphates were compared with their neutral amine salts. This led Hall to conclude that at higher loads acid impurities were vital for good AW activity. He also concluded that the films formed with longer alkyl chain length esters gave smaller wear scars. However, a comparison of the following relative wear rates with the acid number (these are included in brackets, a high number indicates high acidity) shows that both chain length and acidity are important, but that the relationship is a complex one (IX).

di-octyl phosphonate (21) ~ di-octyl acid phosphate (149) $\leq H_3PO_4$

(IX)

< di-butyl acid phosphate (518)

In a discussion of Hall's work [44] Rounds cites results that support the observed superiority of di-alkyl phosphonates over tri-alkyl phosphites; and he further suggests that for di-alkyl phosphonates branched chain versions are far less effective than straight chains. In static immersion tests with di-dodecyl phosphonate and 52100 balls, Rounds monitored the decomposition of additive (and the formation of di-dodecyl acid phosphate). In addition the surface phosphorus content was monitored as a function of time in both atmospheric and very low oxygen environments. The rapid additive decomposition and the rapid surface film build-up observed at atmospheric levels of oxygen caused Rounds to conclude that oxidation to the acid phosphate is necessary for surface coating formation. However, Round's implicit assumption that the acid phosphate oxidation product is the same as the acid impurities observed by Hall, is open to question.

Yamamoto and Hirano [45], [46] compared the behaviour of a tri-alkyl (octyl) phosphate (TOP) and a tri-aryl (cresyl) phosphate (TCP), under various conditions. In a 4 ball rig [45] at low temperatures and loads, the more reactive TOP gave lower friction, but the anti-

scuff protection failed under more severe contact conditions. With TCP the initially high friction observed fell after a period of running-in, and the film formed continued to lubricate at higher temperatures and loads. The authors used micro X-ray analysis to demonstrate the presence of $FePO_4$, FeO and Fe_3O_4 (and the absence of Fe_3P). The behaviour observed with TOP was attributed to the rapid formation of a film of low mechanical and thermal strength that failed under severe conditions. TCP was believed to produce a film that was more stable under severe conditions. The consequent drop in friction was found to correlate with increased levels of phosphorus in the wear scar. In addition, the surface levels of phosphorus and oxygen were compared for static 'corrosion' tests and 4-ball tests. TOP showed a rapid film build-up in static testing, and a consistent P : O ratio under both static and dynamic test conditions (suggesting a similar type of film throughout). TCP produced a smaller quantity of film with a high P : O ratio in static tests (up to the maximum test-temperature of 200° C). However in the 4-ball test the ratio was close to that observed for TOP, although the absolute concentration was much increased. This suggested the formation of a more stable film of similar structure to the TOP-based film, but at higher levels. In a later paper [46] the esters were compared in a Timkin test-rig, with a number of base stocks of different viscosity. With pure base stocks the scuffing resistance was found to increase with viscosity. In the absence of oil TOP and TCP both improved the scuffing load, although the better performance observed with TCP may have been due to its higher viscosity. In solution TOP was shown to be superior to TCP, but only at concentrations ≥ 2 % and only in base stocks with a viscosity exceeding that of the ester. The authors suggested that the TOP generated film could only function in the presence of a partial oil film. TCP improved the scuffing resistance at low concentrations and low loads, although higher friction was observed than for the base stock alone. The authors attributed this to the strong adsorption of TCP, which would prevent the formation of a stable low-friction oxide film. ESCA analyses (see chapter 3) demonstrated the presence of $FePO_4$ as previously.

Barber [47], [48] produced a range of amine salts of mono-alkyl hydrogen phosphonates and esters of phosphonic and phosphinic acids, and tested them in a 4-ball rig. The amine salts gave exceptionally high initial seizure loads (ISL). The best results were obtained by combining a primary, branched chain C_{12} - C_{14} amine with an ester bearing a methyl group (this also resulted in a much improved weld point). Forbes et al [36], [43] had previously

shown high additive activity with the structurally related amine salts of di-alkyl acid phosphates. In tests on phosphonates of the form $[(RO)_2P(O)R']$, Barber found that for a given ester substituent (R) variation of the phosphonate group (R') had little or no effect on the ISL. However, for a series of compounds in which R' was fixed, the ISL was found to vary as in (X). When R' consisted of an aryl substituent bearing electron withdrawing groups e.g. nitro or carbomethoxy, the ISL reverted to that of the base oil, presumably as a result of strengthening the C—O bond.

$$Me > i\text{-}Pr > Bu \qquad (X)$$

With di-octyl alkyl phosphinates $[(Oct)_2P(O)OR']$, the variation in ISL with ester substituent was also found to follow the order given in (X).

Lacey et al [28], [76] used optical interferometry at elevated temperature to follow the build-up of thick, protective layers in an EHD point contact, from a synthetic hydrocarbon containing a range of di-alkyl / aryl phosphonates. All of the phosphonates tested 'grew' films in nominally pure rolling and mixed rolling-sliding up to a thickness of approximately 300 nm, although this 'maximum' value was later shown to be depletion controlled. The observed rate of film build-up is given in (XI), but close observation of the film-growth curves shows the rate of film build-up to be approximately constant, after a variable 'initiation' period. No increase in film thickness was observed with tri-hexyl phosphite (or with the base stock alone). The full structure of the aryl phosphonate - termed *bis*-*t*-octyl-phenyl phosphonate and denoted (*t*-Oct ϕ) below - is given in § 4.3.1.2.

$$Dodec \geq t\text{-}Oct\ \phi >> Hex > Oct \qquad (XI)$$

The film formed was shown to withstand up to 10 % sliding - the maximum tested - and to grow at a faster rate when sliding was present. The authors showed that small quantities of thick film material remaining from previous tests catalysed film growth in subsequent tests (although not as a result of direct transfer). They attributed this to a polymerisation process. The film build-up was shown to be unaffected by the presence of a corrosion inhibitor. The thick film material continued to contribute towards separating the surfaces in the absence of an EHD film i.e. in the stationary contact after testing.

Rounds [49 - 50], [52 - 53] systematically investigated the importance of a wide range of relevant operating parameters to the friction and wear performance of a group of commonly employed additives. In the first of these studies [49] the author used electron microscopy and X-ray fluorescence to observe the surface topography and to semi-quantitatively measure the film composition of specimens run in a boundary lubricated thrust bearing rig, designed to measure friction. The following commercial grade additives germane to the current study were included - a mixed di-alkyl phosphate [C_{12} av. (A)], di-dodecyl phosphonate (B), TCP (C) and *bis*-β-chloromethyl vinyl phosphonate (D). X-ray fluorescence examination of the raceways after testing suggested that long-chain oiliness additives gave films of the order of 10 mono layers thickness. The phosphorus based additives gave (A) ~ 150, (B) ~ 300, (C) ~ 650 and (D) ~ 10 monolayers respectively. In the light of the oiliness additive data the suggestion of Larson et al, made in the discussion accompanying [49], that the values should be reduced by between $1/7^{th}$ and $1/15^{th}$, seem reasonable.

Rounds demonstrated a maximum reduction in friction with (A) and (B) at a 1 % level of additive. Although the reduction in μ_K (see § 1.2) exceeded that observed with longer chain oiliness additives, the author concluded that the phosphorus-based additives operate by a similar mechanism and not by the phosphide polishing mechanism of Beeck [24]. The friction reduction was quoted by Rounds as the ratio of the kinetic friction (μ_K) - or the static friction (μ_S) - observed with the additive in solution and the pure base stock alone i.e. $\mu_{K \text{ or } S\ R} = \mu_{K \text{ or } S \text{ Additive}} / \mu_{K \text{ or } S \text{ Base oil}}$. Therefore a low value implies an active additive. The friction reduction observed for additive (B) was highly temperature dependent. At 100° F kinetic friction values close to the base oil were observed, at 200° F a reasonable reduction occurred and at 300° F the value was greatly reduced. Evidence that (B) was producing a thick reacted layer comes from the observation of a "*pale blue colour*" in the track at 200° F (suggesting at least the minimum film thickness observable by interferometry i.e. a layer of the order of 150 nm thickness). Secondly, the small reduction in the kinetic friction ratio $\mu_{K\ R} = 0.8$, but the large reduction in static friction $\mu_{S\ R} = 0.4$, suggested the presence of a reacted layer contributing towards separation of the stationary surfaces. In addition, unexplained phosphorus was found to be present on bearings testing with P-free oils, suggesting some thick film material that resisted solvent-cleaning may have remained in the rig between tests. This paper by Rounds [49] is important as it was

the first work to stress the importance of the alkyl-chain portion of the molecule in the film building process. In most previous work the simple presence of a reactive element such as phosphorus was taken to imply AW / EP activity, by the formation of a phosphide film.

In contrast to a number of the studies above, Goldblatt and Appeldoorn [32] found that a range of phosphates and phosphites gave a similar increase in wear and scuff-load in wet-air (a reduced scuff-load was observed in dry argon). From this the authors concluded that "*phosphates and phosphites are generally similar in their behaviour and mode of action, and that they respond in the same way to changes in oxygen and humidity.*"

2.3.1 The influence of base oil type on additive performance

Goldblatt and Appeldoorn [32] investigated the importance of different hydrocarbon base stocks and different atmospheres to the friction and wear behaviour of TCP (this work is summarised in § 2.4.1). This paper also contains a summary of the importance of these variables in the absence of of additives [32 [7,8,9]]. The major findings were (i) under mild conditions oxygen and water promoted firstly corrosive and then abrasive wear, but under more severe conditions both contaminants reduced the tendency to scuff; (ii) aliphatic base stocks gave high corrosive wear with oxygen present; (iii) condensed ring aromatics scuffed in inert (argon) atmospheres and (iv) mixed base stocks combined synergistically to give a low wear / low scuffing condition. TCP was found to be effective in improving the scuffing resistance of aliphatic oils, but it did little to improve the naturally good behaviour observed with base stocks containing aromatic species.

Comparisons of additive effectiveness in widely differing base stocks are complicated by the frequent inability to find base oils in which the viscosity and pressure-viscosity characteristics are matched over the desired temperature range. This ensures operation at the same specific film thickness. Therefore any differences in additive response should be attributable to the base oil alone. In practice this is rarely achieved, as the following discussion demonstrates. The work of Cann and Spikes [51] has shown that the temperature rise in a contact (and therefore the reactivity of an AW / EP film-forming additive present) is highly dependent on the base oil structure for contacts operating at similar Lambda values. This is briefly discussed below.

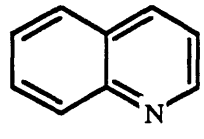
Rounds contributed a series of papers [50], [52] and [53] comparing the frictional behaviour of di-dodecyl phosphonate (B) and TCP (C) in a range of base stocks, in the rig described in the previous section. In [50] additive (B) gave values of $\mu_{K\,R}$ and $\mu_{S\,R}$ close to unity i.e. no improvement over the base stock with an 'as distilled' naphthenic oil. A large reduction in $\mu_{S\,R}$ and a slight reduction in $\mu_{K\,R}$ was observed in a highly refined naphthenic base stock. The treated naphthenic underwent a heavy SO_2 extraction, fuming H_2SO_4 treatment and benonite clay treatment, which greatly reduced the aromatic, asphaltic and polar impurity content. The surface phosphorus levels fell slightly with increasing base stock treatment. With a hindered phenol anti-oxidant i.e. a free radical inhibitor (*2,6*-di-*t*-butyl-*4*-methyl phenol) present, a marked reduction in $\mu_{S\,R}$ and $\mu_{K\,R}$ was observed with the unrefined naphthenic base stock, but very little change was observed with the equivalent refined oil. Generally, in the absence of an anti-oxidant, increased refining of a single crude resulted in a greater reduction in $\mu_{S/K\,R}$ i.e. the inherent AW / EP activity of the base stock fell with increased refining.

A factor not considered by Rounds which may be important is the shear-induced temperature rise in the contact. Cann and Spikes [51] used an IR emission technique to measure the surface temperature rise in a sliding EHD contact, for various base stocks. The observed temperature rises are compared with the surface phosphorus levels observed by Rounds [50] (in brackets), for the 'nearest equivalent' base stock in (XII) below.

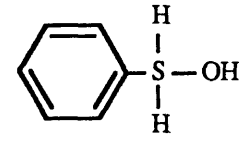
T rise [51]	mineral	>	polyglycol	>	synthetic hydrocarbon	(XII)
P level [50]	'as distilled' naphthenic (37)		polyglycol (46)		highly refined naphthenic (12)	

The very rough 'correlation' may point to higher phosphorus levels being the result of increased additive reactivity in 'hotter' contacts. In general, the friction data for a wide range of synthetic oils fell within the values observed for the variously refined mineral oils [50]. Rounds attributed the greater friction reduction with refined mineral oils or un-refined / anti-oxidant combinations, to competition for surface sites between oxidation products / polar impurities and the AW / EP additive.

In two later papers [52], [53] Rounds investigated the friction effects by selectively re-adding trace components - hydrocarbons, oxidation products and nitrogen / sulphur compounds found in unrefined base stocks - to a highly refined mixed naphthenic / paraffinic base stock. Di-dodecyl phosphonate was unaffected by the addition of hydrocarbon impurities, but levels of ~ 0.07 % of the compounds shown in (XIII) increased the μ_S and μ_K to the values observed with base oil alone, and doubled the surface phosphorus levels observed. Other compounds, in particular unsatured basic nitrogen heterocyclics, produced a similar effect at higher concentrations. The increased phosphorus levels observed led the author to drop the surface-site competition mechanism, in favour of an altered film structure. This was speculative as the X-ray fluorescence technique used gave a semi-quantitative measure of the elements present, but no information about the compounds present i.e. the bond types.



Quinoline



Benzenethiol

(XIII)

A number of authors have compared base stocks in less wide-ranging studies. Forbes and Silver [36] compared a range of amine salts of di-butyl acid phosphate in a liquid paraffin and in di-*iso*-octyl sebacate (a polar synthetic ester) of similar viscosity. Variable AW activity was observed, but the ester gave superior EP activity and its additional polarity permitted solution of a tetra-alkyl ammonium derivative. This compound gave the best EP / AW results observed during testing.

Forbes et al [54] compared TCP in 4-ball tests and adsorption tests in the following solvents - a liquid paraffin, a paraffinic mineral oil, α-methyl naphthalene and a 50 : 50 mixture of the first and the third. TCP demonstrated good AW behaviour in all but the latter at high concentration. TCP was found to be less effective as the aromatic / naphthenic content increased, at low concentrations. Phosphorus uptake from solution similarly fell with increasingly aromatic solvents.

Fowles, Jackson and Murphy [26] observed the build-up of a thick reacted layer from a mineral oil and an ester oil containing a *bis*-(nonyl phenyl) phosphonate, at elevated temperature. Tests with the mineral oil at ± 0.3 % w/w additive with SAE 52100 specimens ($\Lambda = 1.3$) gave a slightly improved fatigue life with additive present, but a remarkable improvement was observed with additive after pretreating the rollers in additive solution. With the ester base stock ± 0.1 % additive ($\Lambda = 0.4$) pretreatment did not improve the fatigue life, although a significant increase in fatigue life occurred with additive present. Pre-formed film-material was shown to transfer to the test specimen, due to greater asperity interaction, but this material did not improve the fatigue life. The authors suggested this implied a slower film formation at higher Λ values, presumably as a result of less frictional heating and lower contact temperatures. Observation of the wear track after testing with additive showed the presence of a bluish film (with yellow streaks) in the track and a pewter-coloured film around the track. Calculations based upon the geometry of a microhardness diamond indenter used to scratch the film, suggested film thicknesses of 70 nm inside the track and 1600 nm outside the track.

Klaus et al [62], [63] compared wear scars for TCP in super-refined mineral oils and ester base stocks. A much higher concentration of TCP was required to achieve a given wear reduction in the more polar ester (di-*3*-methylbutyl adipate); concentration increases of several orders of magnitude were required as the base stock polarity was increased.

2.3.2 The influence of steel type on additive performance

Rounds [55] investigated the influence of steel composition on friction, wear, fatigue and surface coating formation, for two case hardened steels (1018 and 4118) and five through hardened alloys (51100, 52100, M-50, 440-C and stellite # 3). The rate of surface film formation with di-dodecyl phosphonate was found to be as in (XIV) below. A decrease in surface phosphorus levels occurred as the amount of alloying elements present increased (the values in brackets are % Cr, the major alloying element present).

$$1018\ (-) > 4118\ (0.49) > 52100\ (1.43) > \text{M-50}\ (4.18) > 440\text{-C}\ (16.9) > \text{stellite}\ (30.5) \qquad \text{(XIV)}$$

In 4-ball tests [55] the phosphonate reduced wear in all cases, although less reduction was observed with high alloy and deep case hardened steels. No obvious relationship was found between steel type and fatigue life. The additive gave lower values for μ_S and μ_K, and increased phosphorus levels with 1018 (low Cr, shallow case) compared to 52100 (higher Cr, through hardened). Test balls heated in static immersion tests showed a rapid increase in surface phosphorus at temperatures exceeding 400° F with all but the stellite. IR analyses suggested oxidation to di-dodecyl acid phosphate preceded surface reaction. This was confirmed by a slower reaction rate and reduced levels of phosphorus when the atmospheric oxygen level was reduced by ~ 100 times. 52100 test balls heated to 400° F for 2 hours to increase the oxide coating, demonstrated a rapid increase in phosphorus levels across the whole temperature range tested. Rounds therefore concluded that reaction was between the acid phosphate (resulting from oxidation) and a surface iron-oxide. Higher Cr content steels were believed to be relatively unreactive as a result of passive chromic oxide at the surface. The corrosion studies of Mortimer and Sharp [56] show that if the Cr content of a steel exceeds 8 %, the surface oxides change from iron oxides to predominantly chromic oxide.

Much of the work of Hall with 52100 and 440-C steels [44] was detailed in § 2.3. This work confirmed the passive nature of the high Cr steel when reacted with a range of P-based additives. In an earlier paper [57], Hall compared the lubrication of three steels with TCP in a neopentyl ester base stock. The order of effective lubrication, summarised in (XV), was as observed by Rounds [55].

$$52100 > \text{M-50} > \text{440-C} \qquad \text{(XV)}$$

The work of Fowles et al [26] with SAE 52100 in an ester base stock, was detailed in the previous section. The authors also tested M-50 steel. A similar life-enhancement was observed, although to a slightly higher degree with the M-50 steel.

2.3.3 The influence of oxygen on additive performance

Lacey et al [29], [76] used atomic absorption spectroscopy (AAS) to monitor the appearance of iron in solution, when solutions of di-alkyl / aryl phosphonates were reacted with iron powder. A much increased dissolved iron content was observed with an oxygen

'agitant' (compared to nitrogen) with both di-hexyl and di-phenyl phosphonate. A comparison of the relative reaction rates for iron samples reduced in hydrogen or oxidised in air with those for 'as received' iron powder, gave the order summarised in (XVI).

$$\text{Oxidised Fe} > Fe_2O_3 > \text{untreated Fe} > \text{reduced Fe} \qquad \text{(XVI)}$$

No iron was found in solution when a chromium powder was used. A similar dependence of reaction rate on O_2 / N_2 was found for a solution of di-hexyl phosphonate in hexadecane.

This work agrees with the observations of Rounds [55], [77] who studied TCP and di-dodecyl phosphonate, but disagrees with the findings of Forbes and Battersby [35]. In AW and static tests Rounds found reduced surface levels of phosphorus at reduced oxygen levels. The author attributed this to decomposition of additive in the bulk oil (via oxidation to the acid phosphate in the case of the phosphonate). Rounds [55] also reported higher phosphorus levels when the surface oxide was increased by heating in air, prior to testing. In contrast, Forbes and Battersby [35] compared the oxygen uptake of *n*-tetradecane at 130° C ± iron and di-butyl phosphonate. The base stock alone oxidised under these conditions. The rate of oxidation increased appreciably with iron powder present, but only a slight additional increase was observed with phosphonate present. A calculation of the volume of oxygen required for complete oxidation to acid phosphate demonstrated little or no oxidation of the phosphonate. Indeed, di-alkyl phosphonates are known to demonstrate good anti-oxidant behaviour by decomposing peroxide intermediates [78]. When combined with hindered alkyl-phenols a marked synergistic effect is observed as an anti-oxidant package [78].

Many authors have investigated the role of oxygen in the film forming behaviour of TCP (this work is detailed in § 2.4.1). Godfrey [61] observed much higher rates of wear in a nitrogen atmosphere. However he was unable to conclusively link this to the presence of oxygen, as changes in moisture levels occurred simultaneously. Lindinger [79] observed a wear reducing layer with TCP in an oxygen or mixed oxygen / nitrogen atmosphere. No film formation was observed with nitrogen alone. Goldblatt and Appeldoorn [32] compared the scuff-load for TCP and a range of tri-phosphites in wet-air and dry-argon. In all cases a reduced scuff-load was observed under dry argon. Contact resistance measurements were

used to demonstrate an increased film build-up rate, with oxygen present. Faut and Wheeler [72], [73] demonstrated poor AW / EP behaviour with TCP in the absence of adsorbed surface oxygen (see 2.4.1). The authors showed that oxygen was essential for TCP reaction, and that its role was in determining the effectiveness of the film formed, rather than its rate of formation.

Llopis et al [71] investigated the reaction of iron with hexadecane containing TCP (see § 2.4.1) and tri-butyl phosphite. With aerated solutions film build-up occurred rapidly, after an induction period that fell with increasing temperature. Very little film build-up was observed in (i) aerated solutions below 210° C and (ii) in de-aerated (nitrogen-purged) solutions at temperatures up to 248° C. The authors ignored the probable changes in dissolved water content that their aeration / de-aeration procedure would have produced. High levels of thick, dull-grey deposits were observed after testing.

The synthetic hydrocarbon / phosphonate package (XRM 177 F) developed by NASA, is dealt with in § 2.4.2. The high test temperatures employed necessitated the use of low oxygen levels, but in the main the exceptional AW properties observed appear to be unaffected by the levels of oxygen present.

2.3.4 The influence of water on additive performance

Lacey et al [29],[76] compared the rate of reaction of pure di-hexyl and di-phenyl phosphonate with iron powder, in the presence of added water and under 'dry' conditions. A faster reaction rate was observed with both compounds as the water content was increased. A further increase in the respective reaction rates was observed using oxygen as the agitant gas. A solution of di-hexyl phosphonate in hexadecane gave a lower reaction rate. The authors ascribed this to inhibition of the iron surface by adsorption of water.

Forbes and Battersby [35] monitored the percentage of phosphorus remaining in di-alkyl phosphonate / liquid paraffin solution heated to 130° C, with iron powder. The hydrolytic break-down proposed by the authors was supported by the increased reaction rates observed with added water. The authors calculated that sufficient moisture was present in the standard comparison tests for complete hydrolysis to have occurred.

Barcroft and Daniel [31] concluded that hydrolysis was the important break-down mode, after finding a correlation between the hydrolytic stability and the observed activity for a range of tri-aryl / alkyl phosphates.

A detailed discussion of the role of water in TCP lubrication is given in § 2.4.1. Ravner and co-workers investigated the corrosion of lead [64] and steel [65] with solutions of TCP in neopentyl polyol ester base stocks. Corrosion was believed to occur as a result of acidic impurities / hydrolysis products initially present in TCP, or resulting from the hydrolysis of TCP (§ 2.4.1). Godfrey [61] also identified the important role of phosphoric acid impurities. He suggested that oxygen or atmospheric moisture was necessary either for additive decomposition or for film build-up.

Klaus and co-workers [62], [63] used P^{32} radio-tagged TCP (see § 2.4.1) to demonstrate the importance of acid phosphate impurities to the AW behaviour of TCP. The bulk TCP was believed to act as a reservoir for the formation of acid phosphate. The authors did not discuss the mode of TCP breakdown.

In direct contrast to the work reported above, Goldblatt and Appeldoorn [32] found that in aromatic-containing base stocks water had an adverse affect on the stability of films formed with TCP. The authors used contact resistance measurements to show that the films formed in the presence of moisture - by the TCP hydrolysis products - had limited adherence, thus preventing any beneficial film build-up. As received and purified TCP (in which the acidic impurity content was much reduced) were found to be equally effective. Thus the authors concluded that TCP, and not its hydrolysis products, that was the active component.

Forbes et al [54] investigated the affect of water on the performance of TCP in 4-ball and adsorption tests. The results, which are discussed in detail in § 2.4.1, showed that water had a detrimental affect on the AW behaviour of TCP. This was believed to result from the formation of corrosive acids, by hydrolysis of TCP.

Faut and Wheeler [72],[73] similarly showed that water had an adverse affect on TCP lubrication.

2.3.5 The influence of temperature on additive performance

Temperature is a critical parameter in the successful operation of tribological systems. Chapter 1 identified the importance of the highly temperature sensitive pressure-viscosity and viscosity parameters in fluid film lubrication. The successful operation of an anti-wear package is similarly affected by temperature. The polar phosphorus oxy-esters discussed to date would be expected to produce an adsorbed mono-layer at low temperature. In addition, ample evidence has been presented in the current chapter for the formation of reacted layers at elevated temperatures (see § 2.4.2 also). However, accurate measurement of the temperature at which this film-formation occurs in lubricated contacts is complicated by additional heating effects. In static tests the additive reactivity is dictated by the bulk temperature, but in rolling / sliding contacts additional temperature rises result from (i) frictional heating due to asperity interaction ($\Lambda < 3$) and (ii) shear and compression heating in fully separated contacts ($\Lambda > 3$). In the latter case, the work of Spikes and Cann [51], for example, has demonstrated surface temperature rises of up to 100° C with traction fluids, in a sliding contact. The following section reviews the evidence for particular groups of additives having a distinct 'activation temperature' at which chemical film formation is initiated.

Di-alkyl / aryl phosphonates appear to require temperatures of approximately 100° C. Lacey et al [28],[76] observed the build-up of thick films in a rolling / sliding EHD contact with a range of phosphonates at 100° C. A much reduced rate was observed at 75° C. In static tests with di-hexyl phosphonate, iron was slowly taken into solution at 117° C; a very much faster uptake was observed at 180° C.

Rounds [49], [77] investigated the temperature response of di-dodecyl phosphonate. A small reduction in kinetic friction, with respect to the base oil, was observed at 100° F. A further slight reduction was observed at 200° F and a much reduced value was found at 300° F [49]. This correlates well with the increased surface phosphorus levels at calculated surface temperatures in excess of 250° F in dynamic tests, and 350° F in static tests [77].

A number of workers have reported a similar temperature dependence with *bis*-(nonyl-phenyl) phosphonate, the AW additive included in the NASA experimental lubricant XRM

177 F. Parker and Kannel [25] found additional film thicknesses of 500 to 1000 nm in the temperature range 65 - 315° C. Fowles et al [26] used optical interferometry to demonstrate the growth of a film 150 nm thick at 99° C; almost no film formation was observed at 66° C. The authors observed build-up rates of the order of 0.3 to 0.1 nm / min at 99° C. Two quite different types of EHD contact were present in the authors' optical rig. The observed central rolling track and the 'cotton-reel' support rollers. Considerably more micro-slip would have occurred in the latter contact as a result of spin and the support roller was rough in comparison to the glass plate. Electron probe analysis (EPA) demonstrated the presence of phosphorus in the observed rolling track. In the case of the support roller, the phosphorus-containing material was deposited on either side of the track. The authors suggested that the material formed in the rough, spinning contact was worn off and deposited outside the track. The absence of film material where the ball was not in contact, was attributed to the deposition kinetics being dependent on pressure or shear-rate. In static immersion tests Raich [83] reported the presence of adherent blue films with SAE 52100 and M-50 tool steels, at temperatures between 150 and 250° F.

Gentle and Day [80] found no increase in film thickness with XRM 177 F in an optical rig at room temperature. The authors also used a 'mercury squeeze' technique to demonstrate the presence of residual films formed in static immersion tests. After a 30 minute immersion at test temperatures of 27, 93 and 149° C, the bearing was lowered into mercury to 'squeeze' off excess lubricant. The thickness of the stable residual film was monitored by capacitance. Film thicknesses of 43 nm at 93° C and 300 nm at 149° C were found when additive was present. The absence of an appreciably thick film at room temperature was confirmed by Chiu, Hahn and Rosenberg [81]. These authors used optical interferometry to demonstrate additional film thicknesses of between 12 and 45 nm.

A review of the literature has identified many studies that suggest TCP has an 'activation temperature' of approximately 220° C. Rounds [77] found some increase in surface phosphorus levels at temperatures up to 450° F in dynamic tests, but no decrease in friction was observed, suggesting the absence of a reacted layer. In static tests no film growth was observed up to the maximum test temperature of 450° F. Yamamoto and Hirano [46] similarly observed little film formation statically up to the maximum test temperature of 200° C. However the authors observed high levels of phosphorus in 4-ball tests at elevated temperatures. Godfrey [61] observed much reduced wear rates at temperatures exceeding

200° C, with TCP present.

Eberhardt [67], [68] found that a steel plate maintained in TCP at 180° C for 100 hours did not give rise to a reaction film, but surface film formation was observed at 240° C. The results of Llopis et al [71] correlate well with those of Eberhardt. The authors observed no reaction between iron and TCP below 210° C in aerated solutions; no reaction occurred in de-aerated solutions up to 248° C. Some adsorption has been observed at lower temperatures after much longer periods, for example by Forbes et al [54], and Shafrin and Murday [69], [70]. This work is described in detail in § 2.4.1.

Faut and Wheeler [72], [73] monitored the coefficient of friction in a pin on disc tribometer, as a function of temperature. The authors noted a 'basis temperature' of 218° C, around which the TCP reaction revolves (see § 2.4.1).

2.4 The physical and chemical nature of the material formed by the reaction of steel / iron and additive

The following section considers the physical and chemical nature of the material formed during the reaction between iron / steel and phosphonates, phosphites etc. TCP is not included here, as it is dealt with in detail in § 2.4.1 (below). The widely held belief that AW / EP additives function by forming a thin film of low shear strength, has meant that comparatively little work has been done on the physical nature of the film material. The chemical nature of the material has been the subject of much more interest. However, early workers were denied the use of modern analytical machinery that can provide bonding information (see § 3.8.2). As such until recently many workers were limited to simply demonstrating the presence of key elements such as phosphorus, at the surface.

The iron-iron phosphide eutectic proposed by Beeck et al [24] was influential in many early studies. Davey [40] reacted a series of tri-alkyl / aryl phosphates and phosphites with iron powder. Benzene was used to remove excess additive; the residue liberated phosphine when treated with dilute hydrochloric acid. This was taken as evidence of the existence of iron phosphide. The iron phosphide mechanism is no longer believed to play an important role. No examples of the presence of iron phosphide have been found in rolling / sliding

contacts using modern analytical techniques. The only later report of iron phosphide occurs in the 'hot-wire corrosion' test of Barcroft [37] at temperatures of 400 - 600° C. The iron phosphide observed may result from reaction with active reducing agents. Albertson [61] suggested that reducing agents are produced by pyrolysis of the organic components of the AW molecule at temperatures exceeding 250° C.

Rounds [49] studied the film build-up with di-dodecyl phosphonate and a mixed di-alkyl acid phosphate (C_{12} average). The author combined electron microscopy (to observe the surface topography) and X-ray fluorescence (to get a semi-quantitative measurement of the film composition). The phosphonate in particular, gave rise to thick-lumps of material that survived solvent-cleaning. The material was found to be concentrated around the contact. The XRF data demonstrated the importance of the hydrocarbon portion of the molecule in the film material. In later papers [55], [77] Rounds concluded that the oxidation of phosphonate to acid phosphate preceded film formation. Film formation was believed to occur as a result of reaction with iron-oxide present at the surface.

Barcroft and Daniel [4] compared a range of tri-aryl phosphates in static tests and in a cam and tappet test-rig. The material formed was chemically separated and analysed by radio-labelling. Mechanistic studies suggested hydrolysis to the respective di-aryl phosphate preceded surface reaction. The separative techniques demonstrated the presence of organic iron phosphate (benzene soluble) and inorganic iron phosphates (acid soluble). The authors suggest the organic phosphate provides primary protection, but that the organic part of the molecule is lost under more severe conditions.

Inorganic phosphates were also found in hot-wire tests by Wiegard and Broszeit [38] and Sakurai and Sato [39]. Similar inorganic products were obtained after reaction with phosphites, phosphonates and phosphates. This suggests that the extreme test temperatures of 400-500° C used, may have resulted in the decomposition of any organic species present.

Forbes and Battersby [35] carried out a study designed to determine the mechanism by which di-alkyl phosphonates function. IR and micro-analysis data suggested the following structure for the static phosphonate / iron product - $[(RO)(H)P(O)_2]_3Fe$ (where R = ethyl). The authors carried out a mechanistic study based on the three possible break-down modes

- oxidative, thermal and hydrolytic. These routes and the products that result are summarised in scheme (VI) chapter 4. The authors identified hydrolysis as the important break-down mode. Under AW conditions partial hydrolysis was believed to occur to yield iron organo-phosphonate. Under more severe anti-scuff conditions further hydrolysis was thought to occur, yielding mainly iron inorgano-phosphonate. This explains the relative AW / EP results obtained by the authors, and also the greater levels of phosphorus observed in wear scars generated with phosphonates. Much lower phosphorus levels were obtained with phosphates.

In static tests, Barber [47] showed that alkyl phosphonates can react with iron powder with the retention of the P—R bond.

Yamamoto and Hirano used X-ray analysis [46] and ESCA [47] to investigate the films formed with tri-octyl and tri-cresyl phosphate. Inorganic phosphate ($FePO_4$) was found, as was FeO and Fe_3O_4. No phosphide was found.

Probably the most comprehensive investigation into the chemical nature of the surface material formed by the reaction of di-alkyl / aryl phosphonates and iron was that carried out by Lacey et al [29], [76]. The authors found that the thick film material generated in a rolling / sliding EHD contact could also be produced in shear-free, static-immersion tests. The material formed in each environment was shown to be very similar and to consist of, in the main, iron (III) phosphate monoester polymer (see figure 1.7). Most of the analyses were conducted on material produced in static tests. For hexyl and octyl phosphonate, breakdown was believed to occur as a result of oxidation. However, the increased reaction rate observed with added water and the presence of parent alcohols in the condensed vapour suggests some hydrolysis may also have taken place. The enhanced reaction rates observed with oxidised iron and in an oxygen environment suggest surface oxidation is also important. The structure represented in figure 1.7 shows an acid group on the bridging phosphate; the hydrogen atom might well be replaced by an alkyl group or a ligand to another iron atom. Some of the species co-ordinating to the central Fe (III) were not defined. These may consist of phosphonates or phosphates in variable states of bridging or substitution. With di-dodecyl phosphonate there little evidence of oxidation to phosphate, although this may have simply resulted from a reduced reaction rate.

The material generated in a rolling contact was subjected to a range of analyses after severe solvent cleaning. Only the most strongly held material would be expected to survive such a treatment. The IR spectrum showed a much reduced C—H peak, suggesting a largely hydrolysed, inorganic phosphate polymer. Some evidence of chelation i.e. double co-ordination on the same iron atom was found in the mass spectrum.

A search of the literature uncovered ample evidence of this type of bridging. Hardy and Fletcher [95] report the formation of similar polymer species from the reaction of acid phosphates and high concentrations of uranium, vanadium and iron salts. The work of Lacey et al [29], [76] suggested that some of the bridging groups may consist of acid phosphonates. Phosphonate bridges in which the phosphorus atom has an alkyl substituent, rather than a hydrogen atom, have been reported previously by Mikulski et al [96]. Block [97] has shown that an ester in which the phosphorus atom is bonded directly to two alkyl groups i.e. a phosphinate, will also form a bridged polymer. These phosphinate polymers have been used as lubricating greases [97].

2.4.1 Studies into the mechanism of lubrication of tri-cresyl phosphate (TCP)

TCP is probably the additive most frequently included in formulated oils and although it has been the subject of much research, its mechanistic role is still not clearly resolved. The pioneering work of Beeck [24] used TCP and, perhaps as a consequence, it has been included in many of the comparative studies described in this chapter to date. In addition, many studies have been largely or wholly dedicated to understanding the mode of action of TCP. This work is summarised in the following section.

The iron - iron phosphide eutectic proposed by Beeck [24] and confirmed by Davey [40], has been proven to be incorrect in a large number of subsequent studies. Iron phosphide was shown to be formed by Barcroft [37] under the extreme conditions prevalent in his 'hot-wire corrosion' test, but no examples of its existence have been found in an operating contact. Furey [58] compared the friction and the degree of metal to metal contact as a function of surface roughness, in a pure sliding mixed hydrodynamic / boundary lubricated contact. Very rough and very smooth surfaces were shown to give less metallic contact; the latter also resulted in lower friction. With TCP present the metallic contact and friction were

both reduced, although the surface roughness was largely unchanged. Thus Furey showed that TCP actually retarded the 'running-in' process and prevented load sharing. This disagreed with the 'chemical polishing' mechanism of Beeck [24].

Larson and Perry [59] and Bita and Dinka [60] suggested that TCP forms a film of iron phosphate on ferrous surfaces in air, as a result of the surface reacting with phosphoric acid initially present or formed within the TCP. Godfrey [61] confirmed this finding by identifying $FePO_4$ and its di-hydrate $FePO_4 . 2 H_2O$, after pin on disc and static corrosion tests. No phosphide was detected. The author also compared friction data obtained with a commercial TCP solution, an iron phosphate paste ($FePO_4 . 2 H_2O$) and an iron phosphide paste (Fe_2P). A similar beneficial effect was demonstrated for the first two, but poor results were obtained with the phosphide. No other phosphides, for example FeP, FeP_2 or Fe_3P, were tested. Wear rates for the base stock ± TCP showed a much greater reduction with TCP present at temperatures exceeding 200° C. The importance of impurities and the operating environment were investigated by comparing solutions containing commercial TCP and a 'purified' TCP (tri-*p*-tolyl phosphate or TTP), both in air and in a nitrogen atmosphere. TTP gave friction values that were intermediate between those of the TCP solution and the base stock. In addition TCP gave much higher wear rates in a N_2 atmosphere (suggesting the importance of oxygen or atmospheric moisture in the decomposition or film formation reaction). Godfrey [61] refuted the phosphide-film theory of Thorpe and Larson [41], after obtaining the electrical resistance measurements summarised in (XVII).

$$FePO_4 . 2 H_2O >> \text{Fe powder} > Fe_2P \qquad \text{(XVII)}$$

Godfrey [61] concluded that inorganic iron phosphate was formed by reaction with phosphoric acid impurities and that the consequent wear reduction resulted from one or all of the following (i) physical separation by the inorganic salt, (ii) oil absorbtion / retention by the film and / or (iii) plateau formation encouraging hydrodynamic lubrication. In a discussion of the paper [61] Albertson suggested the organic constituents of TCP pyrolyse at temperatures exceeding 250° C to become active reducing agents. Rubbing tests were not believed to generate high enough temperatures. The phosphides observed by Barcroft at 400 - 600° C [37] would seem to support this view.

The results of Barcroft and Daniel [31] largely concurred with those of Godfrey [61], although they suggested that adsorption of the neutral ester precedes hydrolysis at the surface to give the acid phosphate. Wear reduction was believed to result both from these organic phosphates and the inorganic phosphates into which they decompose under more severe conditions.

Klaus and Bieber [62] used P^{32} radio-tagged TCP (TCP-32) to investigate the importance of (i) P-containing impurities present in the TCP-32 and (ii) added polar impurities. Iron powder chromatography and thin-layer chromatography were used to remove polar impurities and to identify and semi-quantitatively measure the impurities present. The best commercially available grades of TCP-32 were found to contain between 11 and 4 % of polar impurities (mainly mono and di-acid phosphates). These values were artificially increased, as required, by neutron activation. A comparison of the wear scars obtained with TCP and with acid phosphates (di-dodecyl acid phosphate or hydrolysed TCP) in mineral and ester base stocks, showed a similar wear reduction occurred at lower additive concentration with the acidic species. The amount of P^{32} in the scar fell as increasingly refined blends were employed. Most or all of the phosphorus present in the scar was identified as coming from polar impurities. The addition of un-tagged phosphonates and phosphites to TCP-32 blends increased the total concentration of phosphorus in the scar, but reduced the P^{32} concentration. The phosphorus content of the scar dropped to zero in the presence of a barium sulphonate rust inhibitor. Static immersion tests conducted with glass and 52100 steel balls, demonstrated a directly proportional correlation between the surface phosphorus levels and the percentage of P^{32} impurities present. The phosphorus levels were found to be independent of the TCP-32 concentration.

In a later paper Klaus et al [63] modified the techniques described above to isolate and tentatively identify the impurities present in TCP. Two major impurities were identified. These were shown to be acid phosphates and chlorophosphates (the latter resulted from the synthetic procedures used, as described in chapter 3). The improvement in wear behaviour was found to be directly related to the levels of acid phosphate present. The authors concluded that TCP is important only as a reservoir for the formation of acid phosphates during the life of the lubricant.

Ravner and co-workers [64], [65] have investigated the thermal stability of neopentyl polyol ester base stocks (these are often used in high temperature environments e.g. gas turbines), in the presence of TCP and various metals. With lead the authors [64] showed that (i) corrosion resulted from acid half-esters (produced by hydrolysis of the di-esters); (ii) rapid hydrolysis only occurred with TCP present and it was initiated by the hydrolysis products / acid impurities present in the TCP; (iii) dissolved water was necessary and (iv) an aliphatic amine (*2,6*-di-*t*-butyl-α-di-methylamino-*p*-cresol) reduced hydrolysis by stabilising the acidic impurities present in the TCP. The authors reported very similar results [65] using a range of steels and pure iron in static tests at 500° F. With ferrous metals TCP was shown to 'passivate' the surface by the formation of an inert spinel oxide corresponding to Fe_3O_4.

Goldblatt and Appeldoorn [32] compared the performance of TCP in different atmospheres (O_2 / N_2) and in different hydrocarbon base stocks. A high and a low viscosity sample of each of the following base stocks was used - an aliphatic (mixed paraffinic / naphthenic), an aromatic (*1*-methyl naphthalene) and a mixed aliphatic / aromatic. TCP showed typical anti-scuff, anti-wear and anti-friction behaviour in both the high and the low viscosity aliphatic oil in wet-air. Very little improvement was observed with the naturally scuff-resistant aromatic base stock. TCP was found to be detrimental to the performance of the synergistic mixed oil (see § 2.3.1). A similar pattern was observed in dry argon, with a slightly improved and slightly reduced scuff-protection in the aliphatic and the mixed base stock, respectively. The film build-up was also monitored by using contact resistance to derive the '% metallic contact'. Oxygen was shown to aid film build-up and moisture to hinder it. No film formation occurred in dry argon. The thicker films observed with higher levels of TCP gave reduced wear in an aliphatic base stock, but increased wear was observed in the aromatic oil. This suggested poor adherence. The authors investigated the affect of acidic impurities by comparing commercial TCP with a 'purified' sample (in which the acid number was reduced from 56 to 3.4 µg KOH / g). A dry argon atmosphere was used. The additives were found to be equally effective. This led the authors to conclude that direct reaction of TCP (and not its hydrolysis products), was responsible for its observed AW / EP behaviour. The authors also concluded that the poor scuffing resistance observed by Godfrey [61] in the absence of H_2O / O_2 was therefore due not to alteration of the additive, but to alteration of the surface.

Eberhardt [67], [68] showed TCP to be stable to 300° C, but to decompose at 180° C in the presence of water. No reaction was observed with a steel plate immersed in TCP for 100 hours at 180° C, but surface films were formed at 240° C. IR analyses failed to find any mono or di-cresyl acid phosphate salts, which suggested the material was mostly inorganic iron phosphate. The workers [68] also used the semi-quantitative technique of electron probe micro-analysis (EPMA) to compare the levels of various elements in the wear scar, after testing in base stock ± TCP. Increased levels of phosphorus and oxygen were found with TCP present, but similar levels of carbon were reported in both cases. This was concluded to support the presence of an inorganic phosphate film.

Forbes et al [54] compared the performance of TCP in 4-ball and adsorption tests, in the base stocks listed in § 2.3.1. Three additives were used (A) commercial TCP (acid number < 0.01 μg KOH / g), (B) hydrolysed TCP (18.6 μg KOH / g) and (C) a mixture of acids isolated from (B). These were believed to consist of mono and di-acid cresyl phosphates. The following results were obtained from the 4-ball tests (i) at low concentrations TCP was less effective in polar base stocks, (ii) water was shown to be detrimental to the AW behaviour of all the additives and (iii) at low concentration additives (B) and (C) were much more effective than (A), a similar effectiveness was observed at higher concentration. In the adsorption studies, no adsorption was found to occur at 50° C, but a multilayer formed after 24 and 3 hours at 130° C and 170° C, respectively. In the latter case, levels of cresols were found that suggested the loss of one and occasionally two aromatic rings per molecule. With (A) the addition of water increased both the rate of phosphorus up-take and the final levels of phosphorus and cresol present. With (B) the reaction was faster, but the final concentrations were unchanged and with (C) 100 % phosphorus up-take was found to occur after only 3 hours at 170° C. No iron salts were found in solution, although this may simply reflect their low solubility. The authors attributed the poor AW behaviour observed in a mixed solvent to competitive adsorption. The increased wear observed with water present was attributed to the formation of corrosive acids resulting from the hydrolysis of TCP. This was supported by the invariant wear levels observed with and with out added H_2O when stearic acid - a non-hydrolysible AW additive - was substituted for TCP. The authors believed the improved AW performance of (B) and (C) at low concentrations proved TCP impurities / break-down products to be the active species in film-formation. The levels of cresols observed caused the authors to conclude that metal organic phosphate

films were responsible for load-carrying, although inorganic phosphates were not ruled out under more severe conditions.

Shafrin and Murday [69], [70] used Auger electron spectroscopy (AES) and argon-ion sputter depth profiling, to study the surface composition of 52100 and 440 C steels reacted with TCP. AES was shown to be able to distinguish between iron phosphate and iron phosphide, but it was unable to distinguish separate phosphorus oxy-anions such as PO_4^{3-}, PO_3^- and P_2O_5. The steel samples used were either solvent cleaned (SC) or glow discharge cleaned (GDC) and then kept at 110° C in TCP. The high chromium 440 C steel formed no appreciable surface film. After 15 days the 52100 (SC) produced an "*observable*" layer; this period was found to correlate with the minimum period of pretreatment required to optimise friction and wear performance [70]. The surface material formed contained approximately 5 atomic % of phosphorus and it had an Auger spectrum very similar to that of pure iron phosphate (no iron phosphide was found). However, the authors found the ratio of Fe / P was ~ 8 - 10, compared to ~ 1.5 for $FePO_4$. As a result they concluded that a P-containing compound was filling the lattice vacancies of some iron-oxygen containing moiety. The authors further suggested that the reaction was rate limited by the diffusion of iron to the external surface. This was supported by the slower reaction rates observed with the 52100 (GDC) steel. The GDC procedure was shown to give a much thicker oxide layer.

Llopis et al [71] investigated the reaction of iron with solutions of TCP and tri-butyl phosphite in hexadecane. At temperatures exceeding 220° C the TCP solution formed small random crystals on the surface. The film formation was found to increase with temperature and to occur very much faster in aerated solutions, compared to nitrogen-purged, de-aerated solutions. In the presence of oxygen the authors found that the crystalline material "*by further growth covered the whole surface as a thick film.*"

Faut and Wheeler have investigated the lubrication mechanism [72] and adsorption characteristics [73] of TCP. In the first of these papers [72] the authors monitored the coefficient of friction in a pin on disc tribometer as a function of temperature. TCP was used as bulk lubricant and as a 'limited' lubricant i.e. a single liquid layer applied to the disc. In the latter case the following operating conditions were used with CVM M-50 steel specimens (i) dry air (< 200 ppm H_2O); (ii) dry nitrogen (< 20 ppm H_2O); (iii) a dry

nitrogen atmosphere after pre-heating the disc to 700° C to remove adsorbed oxygen and (iv) moist nitrogen (with a similarly pretreated disc). Condition (iii) gave a sharp failure at 218° C, which caused the authors to conclude that oxygen is necessary for TCP reaction. With condition (iv) failure occurred at T < 218° C, suggesting that water has an adverse affect on TCP lubrication. This is in direct disagreement with the work of Klaus et al [62], [63] which identifies the acid phosphate hydrolysis product as being necessary for good AW / EP behaviour. Under conditions in which the specimens retained an oxide coating, the authors [72] identified a characteristic temperature - denoted T_r - at which a reduction in friction occurred. T_r varied as follows with the operating environment - 265° C bulk, 225° C (i) and 215° C (ii). This caused the authors to identify 218° C as a "*basis temperature*" around which the TCP reaction revolves. The hypothesis that TCP reacts at a critical temperature to form a load carrying film was further investigated [72] using pure iron specimens (for which T_r = 313° C). X-ray photoelectron spectroscopy (XPS) and sputter-profiling were used to investigate the nature and distribution of the surface material at $T < T_r$ (245° C), $T > T_r$ (345° C) and at failure (390° C). At $T < T_r$ a small phosphate signal was detected (which fell on sputtering); at $T > T_r$ a "*thick phosphate layer*" was observed (the phosphate signal increased with sputter depth). At the failure temperature a high phosphate level was observed, with a maximum at a sputter depth of 50 nm. No iron phosphide was detected.

In a later paper [73] Faut and Wheeler used XPS to monitor the levels of a number of atoms present in TCP. By monitoring the shielding of various signals, the authors demonstrated the close proximity of both the phosphoryl group and the tolyl oxygen to the surface. Thus TCP was suggested to be adsorbed onto iron in a 'tilted' configuration. At temperature of ~ 200 - 220° C, the surface level of carbon dropped by approximately one third, while the levels of phosphorus and oxygen both approximately doubled. The authors believed this resulted from the formation of a mixed iron inorganic / organic phosphate film, at a temperature that correlates well with that observed in the friction tests [72]. Very similar reaction products and kinetics were observed with iron oxide (Fe_2O_3) substrate. This suggests that oxygen is important in determining the effectiveness of the reaction layer, rather than its rate of formation.

Georges et al [74] monitored the rate of wear and the rate of film build-up (from electrical contact resistance measurements) for AISI 52100 lubricated with hexadecane ± TCP. Two

distinct phases of wear and film formation were identified. In the early stages of a test rapid wear occurred. This was accompanied by the formation of a poorly insulating 'brown' film. Later in the test a thicker, insulating 'blue' film was observed. The authors used XPS and AES to show that the different coloured films consisted of $Fe_3(PO_4)_2$ and an organic polyphosphate $[(PO_4C_xH_y)_n]$ respectively. The former was believed to result from corrosive wear and the latter from the polymerisation of organic phosphoric acids formed by the decomposition of TCP, in the absence of further iron. The presence of ferrous phosphate in the brown film was demonstrated by its instant solubility in KCN (aq); ferric phosphate is insoluble [75]. A surface profile run at the edge of an area cleaned with potassium cyanide shows a smooth, flat valley approximately 100 nm below an irregular, rough 'shoulder'. The authors [74] suggest this explains the conflicting views of Beeck [24] (chemical polishing) and Furey [58] (roughness increase).

2.4.2 The thick film effect

Section 1.9 explained the basis for the widely-held belief that AW additives operate by reacting to form a thin (0.1 - 2 nm) film of low shear strength. A careful review of the literature, however, has uncovered numerous examples of the presence of relatively thick AW films. The widespread acceptance of the latter mechanism has been slowed by the comparatively recent availability of surface analytical techniques and by the special operating requirements of the techniques. Heavy solvent cleaning is necessary before subjecting specimens to the high vacuum environment required by most analytical techniques; this treatment results in the removal of any loosely held viscous material that would contribute towards surface separation in an EHD contact. Rounds [49] observed the presence of thick phosphorus-containing layers on surfaces reacted with di-dodecyl phosphonate; a film having a "*pale blue color*" was reported. Many authors have obtained similar results with TCP. For example, Beeck [24] reported a "*smooth uniform film showing bright interference colours;*" Barcroft and Daniel [31] calculated iron phosphate film thicknesses of 7 - 28 nm using radio tagged TCP; Shafrin and Murday [70] reported an "*observable*" layer ; Faut and Wheeler [72] reported a "*thick phosphate layer;*" Georges et al [74] reported the presence of both "*blue*" and "*brown*" AW films. Similarly, in static immersion tests, Llopis et al [71] reported the presence of a crystalline material that "*covered the whole surface as a thick film.*"

In the 1970's NASA circulated a synthetic paraffinic hydrocarbon (XRM 177 F) for evaluation as a high temperature lubricant. A single *bis*-(alkyl-substituted aryl) phosphonate AW additive was included. A series of patents obtained by the Mobil Oil Corp. [82] - [84] suggests the additive used was *bis*-(*4-n*-nonylphenyl) phosphonate. Bearings immersed in lubricant / additive solutions (0.1 % w/w) for 16 hours, at temperatures in the range 150 - 250° F, were found to possess surface coatings "*indicated by the appearance of bluish colors and / or dull surface films. These adherent films could not be removed by scratching*" [83]. The additive is claimed to provide both antioxidant and EP protection [82].

Much of the dynamic testing carried out with XRM 177 F has already been described in this chapter and in § 1.9. For this reason, the major findings are only briefly re-stated. In 1971 Parker and Kannel [25] used an X-ray technique to monitor the EHD film thickness for XRM 177 F with and without additive present, in the temperature range 65 - 315° C. A nitrogen atmosphere was used to prevent gross oxidation of the base stock. The authors observed an additional separation of 500 - 1000 nm; the additional separation was found to increase with increasing temperature. A log-log plot of film thickness vs. the EHD speed parameter ($\overline{U}$), see § 1.4, gave a slope close to that predicted theoretically, in the absence of additive. The reduced slope observed with additive present is consistent with the addition of a constant film thickness to the EHD-generated film since the added value dominates at low film thicknesses. After tests in which the additive was present the authors described "... *a very obvious surface film on the discs. The film exhibited very pronounced dielectric properties when the discs were loaded together statically.*" The findings of this paper provide a mechanistic explanation for a series of anomalous results obtained by NASA with the additive [86] - [91]. These results are summarised in chronological order below.

Zaretsky et al [85] compared the 10 % fatigue life levels obtained with a synthetic hydrocarbon ± additive, with those observed for a fluorocarbon and a polyphenyl ether of similar viscosity, at the a temperature of 600° F. The latter two base oils were additive-free. The synthetic hydrocarbon / additive combination (NA-XL-24) was found to increase the fatigue life by 2 to 3 times. In a bearing torque tester all of the lubricants tested, with the exception of NA-XL-24, exhibited a pronounced torque increase at 700° F; this

temperature marks the beginning of a mixed boundary / EHD regime. No such friction increase was observed with NA-XL-24. In a second paper, Zaretsky and his co-workers [86] observed many early smearing and fatigue related failures with a synthetic hydrocarbon, in the temperature range 260 - 315° C. With the organic phosphonate AW additive present, no signs of surface distress or wear were observed on dismantling the test-bearings, after they had been running for twice the predicted / catalogue life. The findings of these two papers were subsequently published as reference [87].

The same group of workers continued these studies in a second series of papers [88] - [90]. In [88] the authors compared the fatigue lives obtained using a synthetic hydrocarbon containing the AW additive and an unformulated fluorocarbon. The base oils had very similar temperature / viscosity relationships; low oxygen levels were maintained throughout. The test lubricants exceeded their predicted catalogue lives by 14 and 3 times respectively (the latter specimens demonstrated surface distress and superficial pitting). The formulated synthetic hydrocarbon gave similar life increases [89] when tested at the following temperatures (the values in brackets are the prevailing Λ values) - 400° F (3.6), 500° F (2.5) and 600° F (1.8). This suggests the importance of an additional chemical film, as considerable asperity contact would be expected at 600° F (Λ = 1.8).

Chiu et al [81] used optical interferometry at room temperature, to measure the film thicknesses observed with XRM 177 and XRM 109 (i.e. synthetic hydrocarbon with and without additive). The former gave additional film thicknesses of between 12 and 45 nm.

Trachman and Cheng [30] investigated the traction response of XRM 109 F4 and XRM 177 F4 in an EHD line contact. In both cases increasing sliding speed caused the traction coefficient to increase to a maximum, after which it gradually fell. The coefficient was also found to increase with increasing load and to fall with an increase in both speed and temperature. In general however, a lower traction coefficient was observed for a given operating condition, with the formulated oil. The peak value was reduced by approximately 25 %. The authors speculated that the 'antifatigue' additive increased the film thickness. The reduction in traction at low sliding speeds was attributed to the increased film thickness, which reduces the shear rate. At higher sliding speeds the increased film thickness results in a higher film temperature and a lower limiting shear modulus.

Jones et al [93], [94] used a high-pressure capillary viscometer to measure the viscosity of XRM 177 and XRM 109 as a function of pressure, temperature and shear stress. The bulk properties of the two fluids were shown to be essentially the same. Thus the apparently anomalous results obtained in the NASA-sponsored studies were not due to changes in the bulk rheological properties of the lubricant. The improved performance has been shown to result from the 'growth' of a thick protective layer in the contact. This build-up was clearly demonstrated by the X-ray studies of Parker and Kannel [25], the capacitance studies of Gentle and Day [80] and the optical interferometric work of Fowles, Jackson and Murphy [26]. The work of Lacey et al [28], [76] has extended these studies to show that the build-up of thick polymeric films at elevated temperature is a general properties of longer-chain di-alkyl / aryl phosphonates. These studies were detailed earlier in the current chapter.

2.5 Summary

This chapter has reviewed the considerable research efforts of the last forty years aimed at elucidating the mechanism by which phosphorus in based AW additives function. The fact that no unequivocal mechanism has emerged demonstrates the complexity of the problem. The continued absence of a unifying mechanism results mainly from two considerations.

Firstly, much of the work has been conducted by commercial organisations. These studies are often limited to comparative performance testing of commercially available additives. These additives are often poorly characterised in terms of purity. The results of any mechanistic studies that accompany performance tests represent a competitive advantage and these are often kept 'in house.' The second reason why no single mechanism has emerged results from the complexity of comparative systems. The apparently contradictory relative performance data observed for different classes of additive by different workers, can be traced to variations in the systems compared. The relative performance of two classes of additive will depend critically on the operating regime i.e. the specific film thickness, the temperature, atmospheric moisture and oxygen levels, and competitive reactions with polar impurities / other additives in the base stock. Perhaps the most important factor dictating relative performance is the nature and level of impurities present in AW additives. Thus the relative performance of two classes of additive may be dictated by the levels of a given impurity rather than by the bulk components present.

The arguments presented above are helpful in explaining the anomalous comparative performance data obtained by different workers which was detailed in § 2.2 and 2.3.

Davey [40] and Hall [44] both found that tri-aryl phosphites were superior to tri-aryl phosphates. However, acidic di-alkyl phosphates were found to be superior to tri-alkyl phosphites. Di-aryl phosphates are known to adsorb irreversibly i.e. to form salts; no similar adsorption was observed with tri-aryl phosphate [32].

There is much evidence that phosphates and phosphonates form different films and that the mechanism is chain length dependent within each class. The role of water and oxygen is important. Oxygen can function by oxidising the surface or the additive (phosphonates and phosphites only). Water can function by passivating the surface or hydrolysing the additives. The AW / EP properties of phosphates correlate well with their ease of hydrolysis [31]. However, the more easily hydrolysed aryl phosphates form less stable films [31], [35]. The ease of decomposition to the active thick film forming species is therefore not the only important consideration. On balance, the work reviewed in § 2.4.1 suggests that TCP reacts predominately through its hydrolysis products. Oxidation of the surface is necessary, but water can hinder reaction by passivating the surface.

Forbes et al [43], [35] compared the AW and EP properties of di-alkyl phosphates and di-alkyl phosphonates. With phosphonates good EP behaviour was observed with the most easily hydrolysed species i.e. the shortest chain lengths; AW performance increased with chain length (soluble iron was found for C_{8+}). With phosphates, short chain lengths gave better EP performance; little variation in AW performance was found with chain length. EP activity was attributed to iron salts of the parent acids; AW activity with phosphonates was believed to result from the formation of iron organo-phosphonate by partial hydrolysis. Phosphonates generally demonstrated improved performance, compared to phosphates, both in EP activity and AW activity (with longer chain lengths). This appears to rule out the oxidation of phosphonate to phosphate, prior to reaction, which is the mechanism favoured by Rounds [49-50], [52-53] and Lacey [76]. However, the results of these authors all provide evidence that longer chain length phosphonates function by a different mechanism. This is confirmed by the evidence presented in § 2.4.2.

There is some evidence that additives such as TCP can also function in this way, although they have higher activation temperatures (§ 2.4.2 and 2.4.1).

The physical and chemical nature of the anti-wear film material was detailed in § 2.4. The iron-iron phosphide eutectic proposed by Beeck [24] has been disproved. The single observation of iron phosphide formation since the work of Beeck comes from very high temperature 'hot-wire' testing [37], probably as a result of formation of active reducing agents [61]. These extreme test conditions produced similar inorganic phosphates from phosphites, phosphonates and phosphates [38], [39] suggesting decomposition of organic species present. More recent studies have demonstrated the importance of the organic part of the molecule [49], [35] and [76]. The work described in § 2.4.2 describes film material with physical and chemical properties that suggest a polymeric compound. There is considerable evidence for phosphate or phosphonate-bridged species in the literature [95] - [97]. These species were observed by Lacey et al in rolling / sliding contacts [76].

The following general conclusions about the mechanism by which phosphorus-based anti-wear additives operate can be drawn from the literature reviewed in this chapter.

Organophosphates, phosphonates and phosphites - or their active thick film forming impurities - are adsorbed at the surface. Further reaction can take place, generally as a result of partial hydrolysis of the additive, at a well defined 'activation temperature' (§ 2.3.5) which is characteristic of the class of additive used. Water is important in additive break-down, but it may also passivate the surface (§ 2.3.4). Surface oxidation of iron is necessary for the second stage of additive reaction (§ 2.3.3). Polar impurities in the base stock or other components in the additive package may compete with AW additives for surface sites (§ 2.3.1). The steel surface reactivity drops with increases in the quantity of alloying elements present and in particular chromium (§ 2.3.2). Under very severe conditions further hydrolysis can occur to give inorganic iron phosphates (§ 2.4). Under less severe conditions longer chain di-substituted phosphonates can produce bridged oligomers and eventually thick polymeric layers (§ 2.4.2). There is evidence that other additives such as TCP can function similarly (§ 2.4.1 and 2.4.2).

CHAPTER 3 - ORGANOPHOSPHORUS COMPOUNDS IN TRIBOLOGY. NOMENCLATURE, STRUCTURE, PREPARATION AND CHARACTERISATION

3.1 Introduction

The preceding two chapters demonstrate the importance of a wide range of phosphorus-based compounds in tribological systems. This chapter draws together the conflicting and often confusing rules for naming phosphorus compounds, and demonstrates their structural basis. The major synthetic routes for preparing phosphorus esters are discussed as are the methods of characterising the compounds produced. The latter section includes an overview of the analytical methods used both to characterise synthetic additives and to investigate the materials resulting from the reaction of additives in tribological systems.

3.2 Nomenclature

If the rules for naming phosphorus compounds are strictly enforced only those examples containing a P — C linkage should be referred to as 'organophosphorus compounds'. This was noted for example in [98] , where the term 'organic phosphorus compounds' is suggested for examples without a P — C linkage. However, common usage includes the latter group as 'organophosphorus compounds' and that is the convention followed in this work. Products containing a P — C linkage are generally more difficult to prepare than the ester derivatives of phosphorus oxy-acids described in this chapter [99] and are less widely used in lubricant formulations. Commercially available examples have been used elsewhere in this study however, in particular to produce model compounds by reaction with iron containing species.

Most phosphorus-based compounds can be named as derivatives of the groups summarised in figure 3.1 .

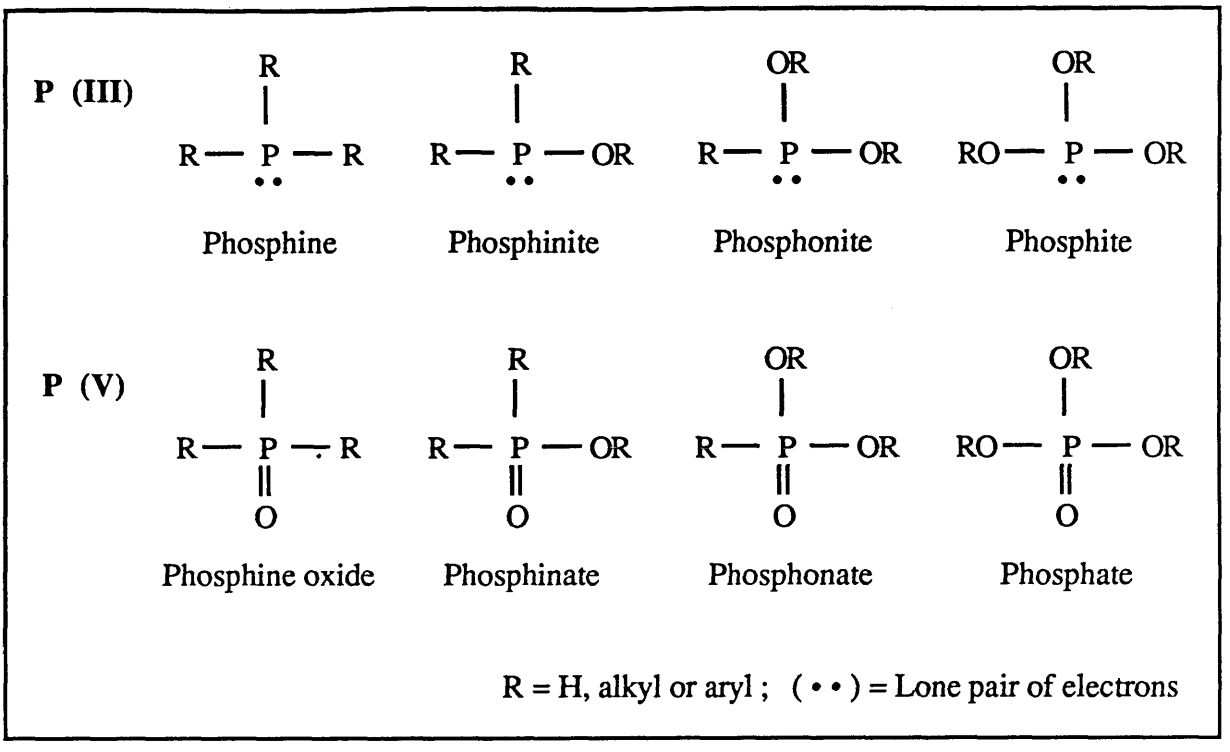


Figure 3.1 Nomenclature of main groups of phosphorus compounds

This study is particularly concerned with phosphorus compounds containing the phosphoryl bond (P = O). The high bond energy of the phosphoryl bond predicts that it will occur frequently [100] and this is found to be the case. It is important, for example, in determining the tautomeric equilibrium position between trivalent and tetracoordinate, pentavalent isomers. Examples of the equilibria appear for the phosphorus / phosphonic and phosphonous / phosphinic acids in figure 3.2 . Similar examples occur for esters. This is discussed in more detail in § 3.3 .

Phosphorus esters are named as ester derivatives of their respective parent phosphorus oxy-acid (these are listed in figure 3.2 with their pK_a values, taken from reference [101]). They are strong acids with first ionisation constants in the region of 1 - 2 and they broadly follow Pauling's general guide for the successive dissociation constants of oxy-acids [102], that is $1 : 10^{-5} : 10^{-10}$. The inductive effects of substituents on phosphorus alter the acid strengths / dissociation constants similarly to those observed with carboxylic acids. That is, from strongest to weakest acid, H > RO > HO > Aryl > Alkyl . Readers unfamiliar with the concept of pK_a will find it defined in any standard chemistry text book; reference

[103] contains a particularly good discussion of acid strength in terms of the entropy contribution to the Gibbs free energy.

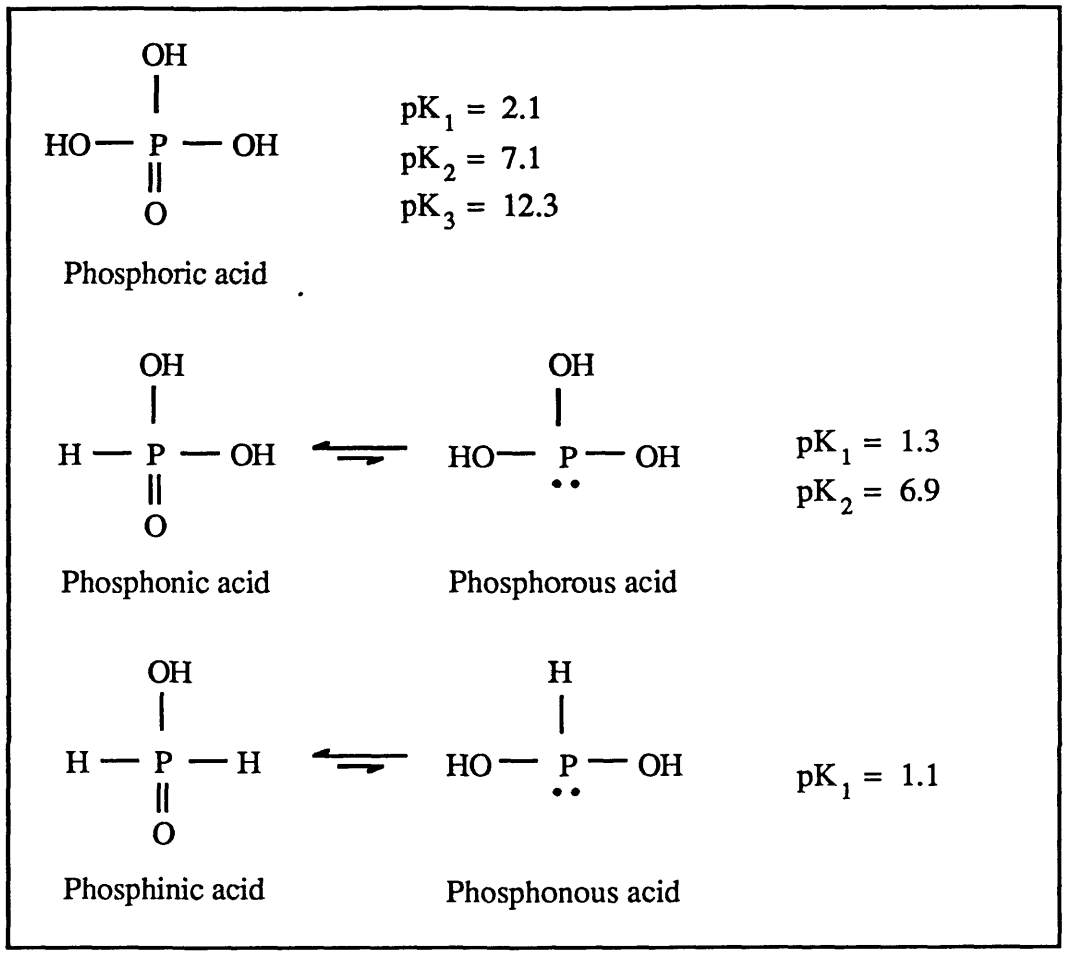


Figure 3.2 Nomenclature of main phosphorus acids

The nomenclature of phosphorus compounds is complicated and confusing. For example each of the phosphorus / phosphonic and phosphonous / phosphinic systems uses two names, one derived from organic and one from inorganic chemistry, to describe a single compound. Greater understanding of the equilibria involved, as described in the next section, has resulted in increasingly common usage of the name of the phosphoryl-containing isomer. In 1952 the British and American Chemical Societies jointly agreed on a scheme of nomenclature for naming compounds containing one P atom [104] ; this is the system summarised in figure 3.1 (and used throughout this work). The following rules from reference [105] should be noted. The names of acids containing a (P = O) end with

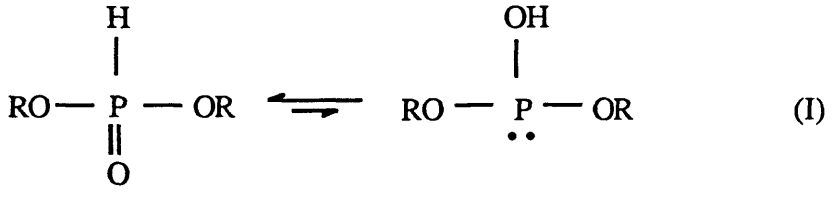
the suffix "ic," the trivalent acids end in "ous." The corresponding esters are "ates" and "ites" respectively. Compounds with three hydroxy or alkoxy substituents have the generic name "phosphor," compounds with two hydroxy / alkoxy groups and one hydrogen / alkyl / aryl are generically "phosphon" and finally, those with respectively one and two groups attached to phosphorus begin with "phospin." The examples in figures 3.1 and 3.2 should clarify these rules.

3.3 Structure

This section considers the dynamic equilibrium or tautomerism exhibited by many phosphoryl esters and seeks to find a bonding model that explains the observed structure.

3.3.1 Tautomerism

Figure 3.2 demonstrates the potential for the existence of two tautomeric forms of phosphorus-containing acids and their ester derivatives. In the parent acids these are suffixed "ic" for the phosphoryl containing acids and "ous" for the trivalent acids. The lower oxy-acids exist almost entirely in the phosphoryl form [101]. An example of the group most important in this work is given in (I).



(I)

Phosphonate (i)

Phosphite (ii)

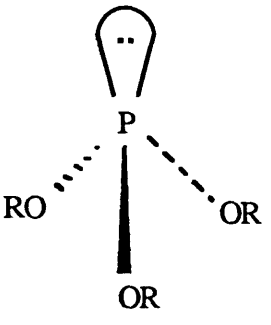
The the high bond energy of the phosphoryl bond (P = O) ensures the equilibrium favours the phosphonate form (i) to more than 95 % in most cases [106], for example if R = Butyl the phosphite form accounts for only $\sim 10^{-4}$ % of the total [101]. In the generalised case X_2POH (X = any group attached to P), the phosphoryl form is widely favoured [101]. For example, if X = alkyl it accounts for over 99 % of total [105] and if X = H K_a is

estimated to be ~ 10^{-12} [101]. The concentration of the phosphite form is so low as to have prevented detection in a wide range of spectroscopic studies [107].

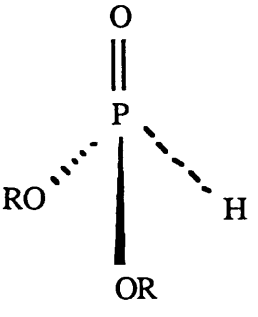
The phosphite form does exist for a small number of tri-substituted alkyl / aryl esters and in a few metal salts [108]. In theory the thermal isomerisation from phosphite to phosphonate can be carried out even with tri-substituted alkyl / aryl esters although the rates and conditions required vary greatly. For example if R = Me complete conversion takes 18 hours at 200° C, but with R = But no change occurs at 223° C. It has been suggested [108] that the isomerisation can only occur if traces of phosphonate are present initially.

3.3.2 Structure and bonding

Tri-coordinate phosphites and tetra-coordinate phosphonates have the structures shown in (II). These are respectively pyramidal (iii) and tetrahedral (iv).



(iii)



(iv)

(II)

How can these structures be explained from the electronic structure of phosphorus $1s^2\ 2s^2\ 2p^6\ 3s^2\ 3p^3\ 3d^0$? A molecular orbital (MO) treatment of the mutually orthogonal $3p_x$, $3p_y$ and $3p_z$ orbitals would be expected to show bond angles close to 90° in a purely σ-bonded compound of type PX_3 . This is not quite true although the observed angle of 93° in PH_3 (compared to 108° in NH_3) suggests less sp^3 hybridisation in the phosphorus compound [106] . This is perhaps better explained by the 'Valence-shell electron-pair repulsion' theory (VSEPR).

In the tetravalent case the VSEPR theory explains the shape, but affords little insight into the bonding; the MO modelling is the subject of some debate. The simple tetrahedral arrangement results from sp^3 hybridisation, but there is considerable disagreement over the nature of the phosphoryl bond and in particular the extent of $d_\pi - p_\pi$ involvement. Full descriptions of the VSEPR theory and the arguments for $d_\pi - p_\pi$ bonding in the phosphoryl bond are beyond the scope of this text, but full descriptions can be found in [109] and [110] respectively. Although no incontravertable evidence exists for d_π bonding in phosphorus compounds it is valuable in accounting for many of the observed properties and in particular for the important strength of the phosphoryl bond.

3.4 Preparation

The following section deals with the preparation of the ester derivatives of phosphonic and phosphoric acids. A number of these oxy-acid esters and their amine salts were synthesised for use in the current work (see chapter 4). Other organophosphorus derivatives used were obtained commercially and no synthetic details are given. These can be found in the two most comprehensive specialist texts dealing with preparative phosphorus chemistry [111], [112] . The section gives a general outline of preparative methods, before considering in detail the synthesis of specific types of ester.

3.4.1 General preparative methods - Esters of phosphonic and phosphoric acids

Preparation of esters of phosphonic and phosphoric acids usually involves nucleophilic substitution of halide in respectively, a phosphorus trihalide and a phosphorus oxy-halide (usually PCl_3 and $P(O)Cl_3$). The process involves a stepwise esterification with the appropriate alcohol or phenol followed, where necessary, by hydrolysis. As figure 3.3 demonstrates, careful control of the reactant stoichiometry yields the full range of phosphorus esters.

Phosphonic Acid Esters		ROH : H_2O		Phosphoric Acid Esters
$(RO)_3P$		3 : 0		$(RO)_3P(O)$
$(RO)_2P(O)H$	← PCl_3 +	2 : 1	+ $Cl_3P(O)$ →	$(RO)_2(HO)P(O)$
$(RO)(HO)P(O)H$		1 : 2		$(RO)(HO)_2P(O)$

Figure 3.3 General preparative scheme - esters of phosphonic and phosphoric acids

The remainder of § 3.4 considers the reaction scheme commonly employed and summarised in figure 3.3. Details of the application of this reaction and other reaction schemes to the preparation of specific phosphoric and phosphonic acid esters are given in sections 3.5 and 3.6 respectively. Synthesis of amine salts is considered in § 3.7.

3.4.2 General preparative methods - Esters of phosphonic acid

The differences in the preparative chemistry of phosphonic and phosphoric acid esters result from the following considerations [113]. Firstly, phosphorus trichloride is much more reactive towards nucleophilic attack by hydroxy compounds than phosphorus oxychloride and substitution of successive chlorine atoms does little to affect the subsequent reactivity. Secondly, phosphonic acid esters hydrolyse easily; this is especially true of the tri-aryl esters. The third consideration is the relative ease of cleavage of alkyl phosphonates and phosphites by hydrogen halide by-products. Finally, the lower valence state of phosphonic acid esters mean they are frequently subject to oxidation, disproportionation and isomerisation.

The interaction of phosphorus trichloride with the required alcohol or phenol results in the consecutive and concurrent reactions (III) - (V), forming successive alkyl / aryl phosphorochlorides.

$$PCl_3 + ROH \longrightarrow (RO)PCl_2 + HCl \qquad \text{(III)}$$

$$(RO)PCl_2 + ROH \longrightarrow (RO)_2PCl + HCl \qquad \text{(IV)}$$

$$(RO)_2PCl + ROH \longrightarrow (RO)_3P + HCl \qquad (V)$$

However, with most alcohols the major product is the di-alkyl / aryl phosphonate [114] due to the dealkylation reaction (VI).

$$(RO)_3P + HCl \longrightarrow (RO)_2P(O)H + RCl \qquad (VI)$$

Stepwise dealkylation can continue through to phosphonic acid in the presence of high concentrations of HCl [115] as shown in (VII - VIII).

$$(RO)_2P(O)H + HCl \longrightarrow (HO)(RO)P(O)H + RCl \qquad (VII)$$

$$(HO)(RO)P(O)H + HCl \longrightarrow (HO)_2P(O)H + RCl \qquad (VIII)$$

These competitive dealkylation reactions can be controlled by using a hydrogen chloride receptor to prevent reaction (VI). Typical receptors include tertiary amines [115], and pyridine [108]. Tri-alkyl / aryl phosphites can be prepared in good yield, the former require a receptor, but the latter approach tri-aryl phosphates in their insensitivity to hydrogen chloride [113]. This is due to electron displacement in the aryl-oxygen bond [116]. Use of a receptor can permit isolation of mono and di-alkyl phosphonates in good yield [108]. However, mixtures of tri-phosphites, mono and di-phosphonates and unreacted phosphorus trichloride invariably result [99].

Ester formation is highly exothermic and the reaction must be moderated. The PCl_3 is typically added in an inert solvent, with cooling [117]. The cooling, ideally to less than 10^{o} C, has been achieved by ice / water baths and by controlled evaporation of solvent [118]. In addition to moderating the reaction, the solvent dilutes the mixture permitting stirring of the hydrogen chloride / amine-receptor slurry.

3.4.3 General preparative methods - Esters of phosphoric acid

The synthetic chemistry of pentavalent phosphorus is simplified by a stable oxidation state, and the much improved thermal and hydrolytic stability exhibited by these compounds [113]. The classical method of preparation involves partial esterification of phosphorus oxychloride, followed by hydrolysis where necessary. As such, preparation of the important mono and di-substituted phosphoryl chlorides warrants some mention.

Alkyl phosphoryl chlorides are prepared by slow addition of primary alcohol at about 0° C, with removal of HCl by evacuation / or a stream of inert gas. Non-selective esterification and cleavage of the alkyl ester by HCl formed, results in mixtures [115] and secondary or higher alcohols do not give satisfactory products [119]. Stepwise addition can give the desired products in good yield according to (IX), R' can be secondary. The following considerations are important (i) the decreasing ease of replacement of successive chlorines atoms; (ii) addition of alcohol so as to maintain oxychloride in excess until completion; (iii) maintenance of low temperatures to control di-substitution, minimise dealkylation and loss of oxychloride with evolved HCl and (iv) application of high vacuum only after formation of high-boiling phosphoryl dichloride.

$$ROH + P(O)Cl_3 \longrightarrow HCl + (RO)P(O)Cl_2 \xrightarrow{R'OH} (RO)(R'O)P(O)Cl + HCl \qquad (IX)$$

Di-alkyl phosphoryl chlorides have been prepared by reacting di-alkyl phosphonates and chlorine [117]. Tri-alkyl versions can be prepared in good yield with primary alcohols [120].

Reaction of phenols with phosphorus oxychloride tends to produce mixtures heavily favouring mono and di-aryl phosphoryl chlorides, but with good total yield [121]. These can be separated by distillation under reduced pressure. High yields of mono or di-substituted versions, of high purity, are claimed in the presence of catalysts such as magnesium [122], iron [123] and aluminium trichloride [124]. Tri-aryl phosphate formation from unreactive di-aryl phosphoryl chloride requires high temperatures around 150 - 300° C [125], depending on catalyst [126] and an excess of phenol to favour

complete esterification. A moderate pressure is maintained to prevent heavy loss of oxychloride with evolved HCl [127].

3.5 Synthesis of phosphoric acid esters

The following section covers the preparation of alkyl and aryl esters of phosphoric acid. Synthetic procedures are discussed for the classic reaction described previously and for other, more modern reaction schemes.

3.5.1 Synthesis of tri-alkyl and aryl phosphates

3.5.1.1 Esterification of phosphorus oxychlorides

The classic condensation reaction (X) is used in all commercial manufacture of tri-aryl phosphates. Cleavage of the alkyl ester by liberated HCl can cause problems in the preparation of tri-alkyl phosphates.

$$P(O)Cl_3 + 3\,ROH \longrightarrow (RO)_3P(O) + 3\,HCl \qquad (X)$$

Formation of alkyl chloride can be largely prevented by adding a primary alcohol at 0 - 20° C, although this results in reaction times of approximately 24 hours [128]. Reducing pressure to remove HCl can permit reduced reaction times [127]. Final removal of HCl is discussed in [113] and methods employed have included neutralisation with ammonia, an aqueous alkaline wash, blowing with an inert gas and use of an ion exchange resin. As mentioned in § 3.4.3 tri-aryl phosphates require high temperatures, catalysts and long reaction times. Metal halides appear preferred catalysts although even these entail condensation times of 6 - 9 hours at approximately 200° C [126]. Purification is by distillation at reduced pressure, often after washing with dilute caustic to neutralise any HCl and to hydrolyse and extract traces of partial esterification products / unreacted phenols or cresols [129]. Although stable under normal conditions tri-esters will decompose after about 24 hours at 150° C. The thermal decomposition is acid catalysed for alkyl versions and occurs as in (XI). This indicates O — C to be the weakest bond at raised temperatures [130]. No similar process can occur for aryl versions and these decompose less readily.

$$(RCH_2CH_2O)P(O)(OPh)_2 \xrightarrow[24\ hrs.]{150^\circ C} R.CH=CH_2 + (HO)P(O)(OPh)_2 \qquad (XI)$$

Preparation of mixed alkyl / aryl phosphates is not covered here, a full discussion is given in [113].

3.5.1.2 Miscellaneous preparation of tri-aryl phosphates

Many preparations have been used to produce tri-aryl phosphates, of which the following are the most important :-

(i) Reaction of the phenolic compound with phosphorus pentachloride [131], (XII).

$$3\ C_6H_5OH + PCl_5 \longrightarrow (C_6H_5O)_3PCl_2 \xrightarrow{H_2O} (C_6H_5O)_3P(O) + 2\ HCl \qquad (XII)$$

(ii) Condensation of a sodium arylate with phosphorus oxychloride in an organic solvent [132] or an aqueous medium [133], as in (XIII).

$$3\ C_6H_5ONa + P(O)Cl_3 \longrightarrow (C_6H_5O)_3P(O) + 3\ NaCl \qquad (XIII)$$

(iii) Reaction of the phenolic compound with phosphorus pentachloride, then with phosphorus pentoxide [134], as in (XIV).

$$15\ C_6H_5OH + 3\ PCl_5 \longrightarrow [\ 3\ (C_6H_5O)_2PCl_3 + 9\ C_6H_5OH\ ] \xrightarrow{P_2O_5} 5\ (C_6H_5O)_3P(O) \qquad (XIV)$$

(iv) Oxidation of tri-aryl phosphites [135], as in (XV).

$$(C_6H_5O)_3P + SO_3 \longrightarrow (C_6H_5O)_3P(O) + SO_2 \qquad (XV)$$

3.5.1.3 Miscellaneous preparation of tri-alkyl phosphates

The following represent the most important sources of tri-alkyl phosphates:-

(i) Reaction of sodium [111] or aluminium [136] alkoxides and phosphorus oxychloride (XVI).

$$3\,RONa + P(O)Cl_3 \longrightarrow (RO)_3P(O) + 3\,NaCl \qquad (XVI)$$

(ii) Use of a tertiary amine in the traditional alcohol / oxychloride system [111], (XVII).

$$3\,ROH + P(O)Cl_3 + 3\,C_6H_5N(CH_3)_2 \longrightarrow (RO)_3P(O) + 3\,C_6H_5N(CH_3)_2.HCl \qquad (XVII)$$

(iii) Oxidation of tri-alkyl phosphite [135], (XVIII).

$$(RO)_3P: + SO_3 \longrightarrow (RO)_3P(O) + SO_2 \qquad (XVIII)$$

(iv) Pyrolysis of salts of mixed partial esters of phosphoric acid [137], (XIX).

$$\left.\begin{matrix}(RO)(HO)_2P(O)\\(RO)_2(HO)P(O)\end{matrix}\right] \xrightarrow{NaOH} \left[\begin{matrix}(RO)(NaO)_2P(O)\\(RO)_2(ONa)P(O)\\(RO)(HO)_2P(O)\\(RO)_2(HO)P(O)\end{matrix}\right] \xrightarrow{150\text{ - }300^\circ C} (RO)_3P(O) \qquad (XIX)$$

(v) Reaction of alcohols with phosphorus pentachloride [138], (XX).

$$PCl_5 + 4\,ROH \longrightarrow (RO)_3P(O) + 4\,HCl + RCl \qquad (XX)$$

3.5.2 Synthesis of mono and di-alkyl and aryl phosphoric acid esters

The classical method of producing mono and di-substituted phosphoric acid esters (or acid phosphates) from phosphorus oxychloride by partial esterification and hydrolysis, is of limited use as mixtures usually result. A few procedures designed to prepare single esters are included below, but in the main mixed esters are prepared and then techniques are employed to separate them [113].

Approximately equi-molar proportions of mono and di-alkyl phosphates result from reaction (XXI). Low contamination by condensed phosphates and phosphoric acid is reported, and both water in the alcohol / pentoxide and higher molecular weight alcohols favour the mono-alkyl ester [139]. Mixed aryl esters can be produced similarly by reacting phenols with pentoxide. In both cases pentoxide is added directly, in the absence of solvent, at a rate that ensures complete dissolution and maintains the temperature in the range 30 - 80° C.

$$P_2O_5 + 3\,ROH \longrightarrow (RO)_2(HO)P(O) + (RO)(HO)_2P(O) \qquad \text{(XXI)}$$

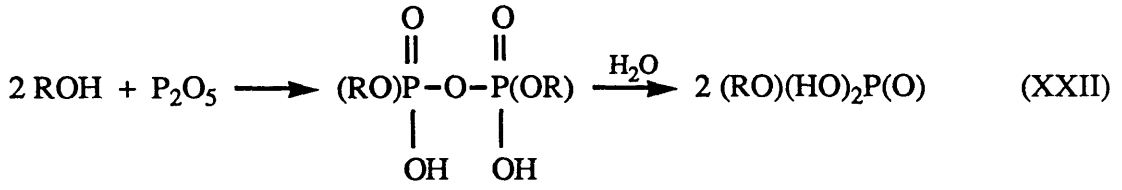
Separative techniques make use of the different solubilities of mono and di-esters, as disproportionation on heating prevents distillation [130]. With alkyl phosphates in the range C_1 - C_6 calcium or barium salts are prepared and the more water soluble di-alkyl salt is extracted. In the range C_7 - C_{12} the mono-alkyl alkali salt may be extracted into water [140] or the di-alkyl salt into non-polar pentane or benzene [141].

3.5.2.1 Mono-alkyl and aryl acid phosphates

In general, preparation of the mono ester from the oxychloride is not satisfactory [113]. However, mono-*p*-(*tert*-octylphenyl) acid phosphate has been prepared in good yield and high purity from the corresponding dichloride [142], by careful control of the reaction conditions.

Other methods have been used to give products rich in mono-alkyl acid phosphate. These include reacting alcohol with pentoxide and hydrolysing the resultant di-alkyl

pyrophosphate [143], as in (XXII).



(XXII)

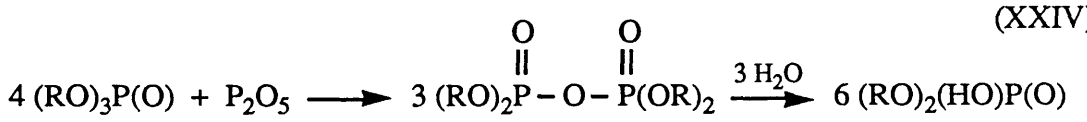
Similar products result from reacting tri-alkyl phosphate and pentoxide, and hydrating [143] the alkyl metaphosphate [144], as in (XXIII).



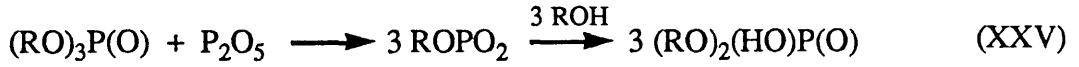
(XXIII)

3.5.2.2 Di-alkyl and aryl acid phosphates

A wide range of preparative routes have been used to produce di-substituted acid phosphates. These include alkaline hydrolysis of tri-alkyl phosphate [145], separation from mono / di-alkyl mixtures, and procedures similar to those described for mono-alkyl acid phosphates (XXIV),(XXV).



(XXIV)



(XXV)

A further important synthetic route involves oxidation of di-alkyl phosphonates with potassium permanganate, in aqueous sodium hydrogen carbonate (C_1-C_7) or pyridine (C_{8+}). Free acid phosphate is liberated on addition of HCl [146]. The scheme is shown in (XXVI).

$$3(RO)_2P(O)H + 2KMnO_4 + NaHCO_3 \xrightarrow[0-5\,^\circ C]{H_2O} 2(RO)_2P(O)OK + (RO)_2P(O)ONa + 2MnO_2 + CO_2 + 2H_2O \quad \text{(XXVI)}$$

$$\downarrow \text{HCl}$$

$$3(RO)_2P(O)OH + 2KCl + NaCl$$

3.6 Synthesis of phosphonic acid esters

Section 3.6 covers the preparation of alkyl and aryl esters of phosphonic acid. Brief consideration is given to the classical preparation discussed in § 3.4.2; other syntheses are then outlined.

3.6.1 Synthesis of tri-alkyl and aryl phosphites

3.6.1.1 Alcoholysis of PCl_3

The general method is shown in (XXVII).

$$PCl_3 + 3\,ROH + 3\,Base \longrightarrow (RO)_3P: + 3\,Base:HCl \quad \text{(XXVII)}$$

The base is present to prevent HCl causing dealkylation, although tri-aryl phosphites have been prepared in the absence of base [147]. Typically secondary or tertiary amines are used as bases for example aniline [148], pyridine [149], trialkylamines [150], [151] and ammonia gas [152].

PCl_3 is usually added to the amine / alcohol solution. The amine hydrohalide formed is removed by filtration, however this results in some loss of product. Improved techniques include aqueous extraction [152], and treatment with dilute alkali to liberate the tertiary amine and form the corresponding alkaline halide salt [151].

3.6.1.2 Miscellaneous preparation of tri-alkyl and aryl phosphites

(i) Transesterification of tri-arylphosphites (XXVIII) with alcohols has been used as a route to tri-alkylphosphites [153]. The absence of HCl prevents dealkylation (no similar breakdown occurs during tri-aryl phosphite synthesis). Yields of 70% have been achieved using elevated temperatures of approximately 50° C and catalysts [153].

$$(ArO)_3P \overset{ROH}{\rightleftharpoons} (ArO)_2(RO)P \overset{ROH}{\rightleftharpoons} (ArO)(RO)_2P \overset{ROH}{\rightleftharpoons} (RO)_3P \qquad \text{(XXVIII)}$$

(ii) Tri-phenyl phosphite has been prepared at room temperature by disproportionation of di-phenyl phosphonate with tertiary amine present. Reaction times of the order of days and very impure products result [154].

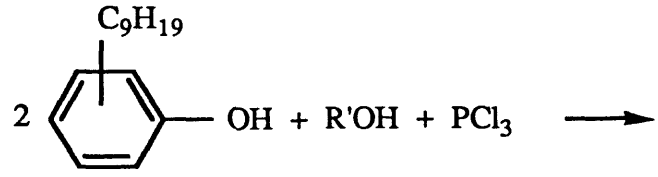
3.6.2 Synthesis of di-alkyl and aryl phosphonates

3.6.2.1 Alcoholysis / hydrolysis of PCl_3

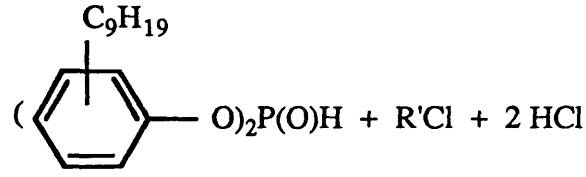
Di-alkyl and aryl phosphonates are usually prepared by reacting PCl_3 with the appropriate alcohol or phenol, and hydrolysing the resulting monochloride (XXIX).

$$2\,R'OH + PCl_3 + 2\,R_3N \longrightarrow (R'O)_2PCl + 2\,R_3N{:}HCl$$
$$(R'O)_2PCl + H_2O + R_3N \longrightarrow (R'O)_2P(O)H + R_3N{:}HCl \qquad \text{(XXIX)}$$

Di-substituted phosphonates are less susceptible to dealkylation and have been prepared in the absence of an HCl acceptor. An important improvement of the procedure for aryl esters is the one-step method of Myers [82], shown in reaction scheme (XXX).

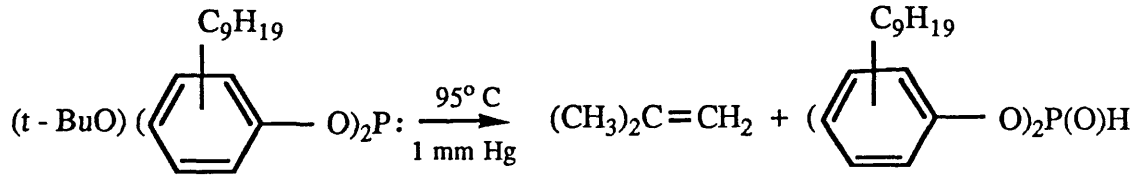


(XXX)



Stoichiometric quantities are preferred in which R'OH is an aliphatic alcohol (primary for an unsubstituted phenol and tertiary for an alkyl-substituted phenol), or water. Cooling is recommended to maintain temperatures in the range 40 - 70° C.

Schmitt [84] produced *bis*-(4-*n*-nonyl-phenyl)-*t*-butyl phosphite using first *t*-butanol and then two mole-equivalents of nonylphenol, with diethylaniline as base, according to (XXVII). Heating the product at low pressure (XXXI) gave *bis*-(4-*n*-nonylphenyl) phosphonate in 100% yield.



(XXXI)

3.6.2.2 Miscellaneous preparation of di-alkyl and aryl phosphonates.

A wide range of synthetic procedures have been used to produce di-substituted phosphonates:-

(i) Transesterification of di-ethyl phosphonate with the required alcohol or phenol has been achieved in the presence of a catalyst [155] as in (XXXII).

$$(C_2H_5O)_2P(O)H \xrightarrow{ROH} (C_2H_5O)(RO)P(O)H \xrightarrow{ROH} (RO)_2P(O)H \qquad \text{(XXXII)}$$

(ii) Disproportionation of $(RO)_3P$:

Refluxing a tri-substituted phosphite, where available, with phosphorus / phosphonic acid (XXXIII) results in a di-substituted phosphonate, by disproportionation [115], [156]. Good yields are reported.

$$2\,(RO)_3P: + (HO)_2P(O)H \longrightarrow 3\,(RO)_2P(O)H \qquad \text{(XXXIII)}$$

(iii) Esterification of $(HO)_2P(O)H$

Excess alcohol or phenol refluxed with $(HO)_2P(O)H$ produces an equilibrium mixture high in di-substituted ester [157], according to (XXXIV). Azeotropic removal of water encourages formation of the desired product by Le Chatelier's principle.

$$(HO)_2P(O)H + 2\,ROH \rightleftharpoons (HO)(RO)P(O)H + ROH + H_2O \qquad \text{(XXXIV)}$$

$$\rightleftharpoons (RO)_2P(O)H + 2\,H_2O$$

(iv) Dealkylation of tri-alkyl phosphites

The susceptibility of tri-alkyl phosphites to dealkylation discussed previously, has been used to advantage in the preparation of di-alkyl phosphonates [158]. As scheme (XXXV) shows preferential dealkylation occurs at the lower alkoxy group (ROH is a higher alcohol).

$$2\,ROH + CH_3OH + PCl_3 \longrightarrow (RO)_2(CH_3O)P: + 3\,HCl$$

$$(RO)_2(CH_3O)P + HCl \longrightarrow (RO)_2P(O)H + CH_3Cl \qquad \text{(XXXV)}$$

(v) Heating alkyl halide, phosphorus acid and a tertiary amine at 80 - 85° C in a solvent such as toluene, results in the desired product in good yield [159]. This is shown in (XXXVI).

$$2\,RX + (HO)_2P(O)H + 2\,R'_3N \longrightarrow (RO)_2P(O)H + 2\,R'_3N{:}HX \qquad \text{(XXXVI)}$$

3.6.3 Synthesis of mono-alkyl and aryl phosphonates

3.6.3.1 Alcoholysis of PCl_3

Stoichiometric quantities of PCl_3 and alcohol or phenol produce mono-alkyl dichlorophosphite to good purity [147], hydrolysis with water or methanol gives mono-alkyl phosphonate [160], as in (XXXVII).

$$PCl_3 + ROH \longrightarrow (RO)PCl_2 + HCl \qquad \text{(XXXVII)}$$

$$(RO)PCl_2 + 2\,CH_3OH \longrightarrow (RO)(CH_3O)_2P: + 2\,HCl \longrightarrow (RO)(HO)P(O)H + 2\,CH_3Cl$$

The absence of an HCl receptor aids dealkylation of the phosphite initially formed by methanol attack.

3.6.3.2 Miscellaneous preparation of mono-alkyl and aryl phosphonates

(i) Direct esterification of phosphorus / phosphonic acid with alcohol is reported to give near quantitative yields [48]. Reactants are refluxed in toluene in a vessel fitted with a condenser and a water separator. Reaction is according to scheme (XXXVIII).

$$ROH + (HO)_2P(O)H \xrightarrow[\text{Reflux}]{\text{Toluene}} (RO)(HO)P(O)H + H_2O \qquad \text{(XXXVIII)}$$

(ii) Mono-aryl phosphonates can be prepared according to the scheme below (XXXIX) according to [161]. The aryl-*di*-*t*-alkyl phosphite is produced by reversing the alcohol stoicheiometry described in § 3.6.2.1 [84]. The desired product results from first thermal cleavage and then acid catalysed elimination of *iso*-butylene. This is achieved in a single step by refluxing with an ion exchange resin.

$$[(CH_3)_3CO]_2(ArO)P \xrightarrow{heat} [(CH_3)_3CO](ArO)P(O)H + (CH_3)_2C{=}CH_2$$

$$[(CH_3)_3CO](ArO)P(O)H \xrightarrow[resin]{ion\ exchange} (ArO)(HO)P(O)H + (CH_3)_2C{=}CH_2 \qquad \text{(XXXIX)}$$

(iii) Mono-alkyl phosphonates have been prepared by disproportionation of phosphorus acid and tri-alkyl phosphite or di-alkyl phosphonate in the stoicheiometric ratios of 2 : 1 and 1 : 1 respectively [115].

(iv) Alkaline hydrolysis of di-alkyl or aryl phosphonates results in the mono-substituted sodium salt, as in (XL), according to [162].

$$(RO)_2P(O)H + NaOH \longrightarrow (RO)(NaO)P(O)H + ROH \qquad \text{(XL)}$$

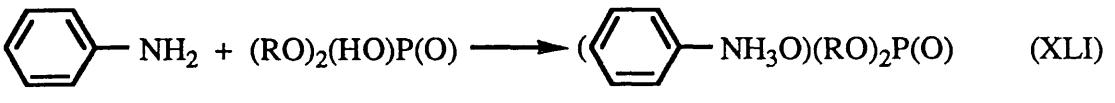
Vacuum distillation of the ethanol / water solvent, after several hours refluxing, gives the sodium salt which is converted to the required product by bubbling HCl through a suspension of the salt in toluene.

3.7 Amine salts of acid esters of phosphoric and phosphonic acid

Mono-alkyl / aryl phosphonates and both mono and di-alkyl / aryl phosphates possess strongly acidic hydroxyl groups. Cleavage of the labile O — H bond results in the species believed to be the active 'thick-film' forming agents, as explained later in this work. As such, these acid esters would be expected to be extremely active anti-wear additives. Their use in tribological systems in an unmodified form however is limited, as they give a much increased acid number and lead to wide-spread corrosion. For this reason neutral amine salts are prepared. These possess a number of advantages. A labile O — H bond is retained, the formation of less acidic alkyl / aryl ammonium ions occurs on decomposition and variation of the amine substituents permits control of the additive's oil solubility. The long chain ammonium ions may possess some value as lubricity or oiliness additives. This section briefly examines the preparative chemistry of these amine salts.

3.7.1 Amine salts of acid phosphates

Amine salts of di-alkyl acid phosphates have been prepared in a number of studies. The method of Zweierzak [146] has generally been adopted to produce the acid phosphates (XXVI). In [146] anilinium salts were found to give pure, stable and non hygroscopic crystalline derivatives as in (XLI). For di-alkyl acid phosphates in the range C_3 - C_{12} an equimolar quantity of aniline was added to a solution of phosphate in petroleum ether. For di-methyl and di-ethyl acid phosphates acetone and ether respectively, were used as solvents. Crystallisation occurred at room temperature.



(XLI)

Forbes et al [36], [43] produced a range of mono, di and tri-substituted amine di-alkyl phosphates as in (XLII). The method of Zweierzak [146] was used, for periods of 3 - 16 hours in *n*-pentane or diethyl ether, followed by evaporation of solvent at 10^{-1} mm Hg. Quantitative yields are reported. In equation (XLII) R ranges from butyl to stearyl, R^1, R^2 and R^3 are variously H, alkyl and aryl.

$$(RO)_2(HO)P(O) + R^1R^2R^3N: \longrightarrow (RO)_2P(O)(OH: NR^1R^2R^3) \qquad \text{(XLII)}$$

Di-alkyl ammonium phosphates have been prepared directly from the reaction of tri-alkyl phosphites with ammonium thiocyanate [163]. The reaction scheme is directly analogous to that of (XLIII) below.

3.7.2 Amine salts of mono-alkyl phosphonates

Ammonium salts of mono-alkyl phosphonates have been prepared directly by the method of Smith [164], from di-alkyl phosphonates reacted with ammonium thiocyanate as in (XLVIII).

$$(RO)_2P(O)H + NH_4.SCN \xrightarrow[4\ hrs]{125^\circ C} (RO)(NH_4O)P(O)H + RSCN \qquad (XLIII)$$

The products separate into two distinct phases. The lower yields mono-alkyl ammonium phosphonate on treatment with acetone, followed by filtration and recrystallisation. High yields of good purity result, particularly for short chain phosphonates.

Barber et al [48], [47] produced amine salts of mono-alkyl phosphonates in two ways. For phosphonates in the range C_1 - C_4 amines were used to displace ammonia from the ammonium salt prepared as in (XLIII) above. This shown in (XLIV).

$$(NH_4O)(HO)P(O)H + RNH_2 \longrightarrow (RNH_3O)(HO)P(O)H + NH_3 \qquad (XLIV)$$

For phosphonates in the range C_{4+} the mono-alkyl phosphonate (prepared as described in § 3.6.3.2) is refluxed in toluene with the required amine. The reaction scheme is directly analogous to that of (XLII).

In both cases long chain, branched primary amines in the range C_{18} - C_{22} gave the best results and acceptable oil solubility. Secondary and tertiary amines resulted in products of uncertain composition.

3.8 Characterisation of additives and surface films in tribology

The following section consists of a very brief overview of the use of analytical techniques in the characterisation both of synthetic additives and of the materials resulting from the reaction of additives in tribological systems. Throughout the emphasis is on the information available from the various techniques. Detailed discussion of the practice and theoretical principles are included later in the text, for the specific techniques used in the current study.

3.8.1 Analytical techniques in the characterisation of synthetic additives

The preparative chemist attempting to identify the products and purity of a reaction will usually involve a number of complimentary techniques. In preparative phosphorus chemistry nuclear magnetic resonance (NMR) and infra-red (IR) vibrational spectroscopy are particularly useful [165], [166], although complimentary information is available from a wide range of methods, as described below.

3.8.1.1 Phosphorus nuclear magnetic resonance ($^{31}P_{NMR}$)

All nuclei possessing a non-zero (ie. an integral or half-integral) spin quantum number (I) possess a magnetic moment. This is the prerequisite for the observation of a nuclear magnetic resonance spectrum. The ^{31}P nucleus has I = 1/2. The magnetic moment results from spinning of the charged nuclei. The resulting circulation of change generates a magnetic moment along the axis of spin, so that the nuclei behave as tiny bar magnets. If the nucleus is placed in an appropriate magnetic field and radiation of the correct energy is applied, the nucleus is 'flipped' from its stable ground state alignment with the field, to a less stable alignment against the field. The theory is considered in more detail in chapter 4.

Simply stated $^{31}P_{NMR}$ spectra can provide the following information:-

(i) The number of distinct peaks identifies how many different kinds of phosphorus atom 'environments' are present in a sample. This is particularly useful as a guide to purity for molecules containing a single phosphorus atom, as is the case in most preparative phosphorus chemistry. A pure product will contain a single $^{31}P_{NMR}$ signal.

(ii) Where more than one phosphorus environment and therefore signal is present, the $^{31}P_{NMR}$ peak areas are proportional to the relative amounts of the active nuclei causing the particular peaks. This permits an estimation of the quantities of any impurities present.

(iii) The peak position or chemical shift (δ) relative to a standard, is dictated by the electronic environment of a given atom. This is useful in identifying species present in a reaction mixture.

(iv) The splitting of a signal (due to coupling with other magnetically active nuclei) gives rise to characteristic coupling constants (J). These provide information about the environment of a phosphorus atom with respect to other active nuclei up to three bonds away [167].

(v) Finally the 'line shape' or peak width can be used to provide fundamental information about intra or intermolecular exchange processes, such as hybrid resonance. This has limited application in the current context.

As mentioned previously, details of practice and principles of $^{31}P_{NMR}$ are included elsewhere in this study. In-depth coverage can be found, for example, in [168].

3.8.1.2 Vibrational spectroscopy - Infra-red (IR) and Raman spectroscopy

Experimentally obtained spectra are of three types - emission, absorption and Raman. In the first two cases energy levels within molecules are investigated by respectively measuring (i) the frequency of light emitted during an intramolecular transition from higher to lower energy state and (ii) the frequencies of radiation absorped from incident radiation as it passes through the sample. The energy change (E) on absorption or emission is related to the frequency (ν) by $E = h\nu$, (h is Planck's constant). The method chosen is usually determined by practical considerations. The information available is detailed in the section on IR below.

In Raman spectroscopy molecular energy levels are examined by the scattering of high energy incident radiation. The scattered radiation and the exciting radiation differ in frequency by an amount equal to the vibrational frequencies of the molecule. Molecules in pre-excited states decay by passing energy to the scattered beam, and ground state molecules are excited by lowering the energy of the incident beam. This results in a series of bands symmetrically arranged to the high and low sides of the incident frequency. Small shifts occur and near monochromatic sources are required.

The ability of a molecular vibration to interact with radiation ie. to be IR or Raman active is dictated by a series of selection rules. These are discussed in Chapter 4.

Molecules are in a constant state of vibration, the bonds stretch and bend relative to each other as a result of absorbing infra-red radiation. The IR spectrum provides an insight into the nature and strength of bonding in a molecule as the vibration is basically a function of the masses of the bonding elements and the bond-type linking them. The following information is available from IR spectra.

(i) 'Group frequency *correlations*' are used to relate the presence of a band or set of bands in the spectrum to the presence of a particular group of atoms in a molecule. The vibrational frequencies of these groups are largely independent of other atoms or groups present within the molecule. Group frequency correlations for phosphorus compounds are given in [169] and [170], for example. The applications in preparative chemistry are evident.

(ii) 'Vibrational *assignment*' identifies a spectral band as arising in terms of a particular vibrational mode of the molecule. Absorptions may be identified as being due to a particular bond stretching, or deformation of a bond angle. This has a particular application in the coordination-type reactions observed between anti-wear additives and metal species, in tribological systems.

(iii) In a mixture, individual bands can usually be found for each component that are largely independent of interference from other components present. This permits semi quantitative data to be obtained from the qualitative spectrum of a multi-component sample.

A full theoretical treatment of applied IR spectroscopy can be found in [171].

3.8.1.3 Miscellaneous analytical techniques

Elemental micro-analysis (EMA) permits quantitative determination of the elements present in a very small quantity of product (0.05 - 0.5 g is typical). In a compound containing C, H, P and O the first three components are measured directly and the latter is determined by arithmetic difference between the combined total and 100%. A full description is given in [172].

Mass spectroscopy is a useful tool in structure determination, particularly if comparisons can be made to standards, as compounds possess unique mass spectra for a given set of conditions. The technique also provides a guide to how decomposition occurs within a molecule, which has an evident application in tribology. The mass spectroscopy of organophosphites and phosphorus and phosphonic acid esters, are covered in references [173] and [174] respectively.

In addition to the above, single-parameter measurement of melting point, density, refractive index, dipole moment and viscosity are used to characterise products and determine purity.

3.8.2 Surface analytical techniques

Many of the techniques discussed above can be applied in a modified way to the investigation of surface films. Reflection IR and Raman spectroscopy provide useful information about the nature of the bonding at the surface. A comparison of the bond types present in the additive and the resultant surface film, gives an indication of the mechanism of additive decomposition that occurs during reaction. In addition to the application of existing techniques to surface analysis, some techniques have been developed specifically to investigate surfaces. These are briefly reviewed in the following section.

The application of surface analytical techniques in tribology have been the subject of a number of reviews. Their use in studying microstructures [175] and wear [176] has been reviewed by Buckley at al. Godfrey and Ferrante considered their application in studying boundary lubrication [177] and tribological surfaces [178] respectively.

A complete description of these techniques is beyond the scope of the current work. Table 3.1 is based around a table from reference [178] and is included to provide a summary of the current state of development of the four surface analytical techniques widely agreed to be the most applicable to tribological systems. These are as follows, (the reference numbers refer to papers detailing the theory and application of the techniques). Auger electron spectroscopy / scanning Auger microscopy (AES / SAM) [179]. Electron spectroscopy for chemical analysis / X-ray photoelectron spectroscopy (ESCA / XPS) [180]; ion-scattering spectroscopy and secondary ion mass spectroscopy (ISS) and (SIMS) [181] respectively.

	Auger	ESCA	ISS	SIMS
Spatial resolution imaging	3μ m elemental maps	2 mm no scanning	100 μm scanning	100 μm ion microprobe 5 μm
Depth resolution profiling	2 nm continuous profiles	2 nm step profiles	1 atom layer continuous profiles	1 atom layer contiuous profiles
Chemical information	possible developmental stage	yes	no, poor discrimination at high mass	yes, unclear determination
Elemental data	yes, easy	yes,slow	yes,easy	some
Compound data	some	yes	no	some
Structural data	no	no	no	yes
Interpretation	involved	simple	simple	difficult
Atomic number	> 3	> 3	all	all, good higher
Quantitative	semi	semi	semi	unreliable
Sensitivity	0.1 % bulk 0.01 monolayer	as left 0.1 / 0.1	0.01 % monolayer	ppm
Sample perturbation	intense beam of electrons alters surface chemistry	X-rays little effect	less damage than Auger	damage has little effect on analysis

Table 3.1 Main features of surface analytical tools applied to tribological systems.

CHAPTER 4 - PREPARATION, PURIFICATION AND CHARACTERISATION OF ORGANOPHOSPHORUS ESTERS AND ESTER DERIVATIVES

4.1 Introduction

This chapter describes synthetic procedures used to prepare a range of organophosphorus esters for the current study. The subsequent purification and characterisation of the esters using a number of analytical techniques, is described. A number of phosphoric and phosphonic acid esters have been produced. Where the partial esters contain labile acid groups, amine salts have been prepared for the reasons described in § 3.7.

The compounds chosen for synthesis were those that might be expected to produce thick, polymeric anti-wear films in rolling or rolling / sliding metal contacts. The concept of anti-wear additives functioning by a thick-film mechanism was described in chapter 2. The decision of which additives to produce was made as a result both of previous work carried out in the author's laboratory and of work described elsewhere in the literature. These studies have afforded a considerable structural and mechanistic insight into the compounds expected to produce thick anti-wear films. Subsequent chapters will further develop the concept that thick-film formation depends on certain structural components within the additive molecule or its break-down products.

Polymer formation appears to involve the interaction of Fe (III) cations with the species $(X)_2P(O)O^-$, where X is any species bonded to P, for example a hydrogen, alkyl / aryl or alkoxy / aryloxy group. The molecular component associated with polymer formation by the additive or its decomposition products, appears to be PO_2^-. However, as discussed in later chapters, polymer formation only results in enhanced anti-wear behaviour if the polymeric material possesses physical properties that result in its contributing towards separation of load-bearing surfaces.

4.2 Preparation and purification of phosphoric acid esters and ester derivatives

As discussed in § 3.5, tri-substituted phosphoric acid esters can be prepared in high purity, though long reaction times and catalysts are required. Preparation of mono or di-substituted esters invariably results in mixtures and considerable purification is necessary to produce a single ester of high purity. These synthetic difficulties are reflected in the commercial availability of phosphoric acid esters. Many tri-alkyl / aryl esters are available 'off the shelf,' but very few mono or di-substituted versions can be obtained commercially. The thermolytic or hydrolytic break-down products of all of these esters contain the PO_2^- group identified previously as being important in thick film formation.

Many tri-substituted esters are used in commercial lubricant formulations. Probably the most common of these is tri-cresyl phosphate (TCP), which has the formula [$(CH_3.C_6H_4O)_3P(O)$]. It is probable that much of the anti-wear activity results from the controlled corrosion that will occur with the more active acid break-down product [$(CH_3.C_6H_4O)_2(HO)P(O)$]. This must result from hydrolysis of the tri-aryl phosphate, but can also result from thermolysis with tri-alkyl phosphates [130]. Mono and di-substituted phosphoric acid esters are commercially available as mixtures, but have received limited application as oil additives. This is for the reasons discussed in § 3.7, i.e. they lead to an increased acid number and corrosion.

In the current work the subjective observations discussed above were tested in two ways. A number of tri-substituted phosphates were tested directly for thick-film forming ability. As discussed above, these compounds possess high thermal and hydrolytic stability. As such, break-down to give the acid phosphate [$(RO)_2(HO)P(O)$], thought to be important in film formation, will be limited. A number of di-alkyl acid phosphates and their neutral amine salts were therefore prepared directly. These compounds have been investigated as anti-wear / extreme pressure additives [36], [43].

Chapter six contains details of experiments aimed at investigating the thick-film forming behaviour of tri-substituted phosphates, the amine salts of acid phosphates etc. An initial test with a commercially available amine phosphate - (Vanlube 672) - with which thick film formation was observed, is also described. The following two sections describe the

synthesis of a range of di-alkyl acid phosphates and their neutral amine salts, for use in the thick film studies described in chapters six and seven.

4.2.1 Preparation of di-alkyl acid phosphates - $(RO)_2(HO)P(O)$

Many procedures have been tried to produce di-substituted acid phosphates. As explained in § 3.5.2 these reaction schemes, including the classical partial esterification and hydrolysis of phosphorus oxychloride, are of limited use as mixtures invariably result. In the main, previous synthetic procedures have involved the exhaustive separation of mixtures in which the proportion of the required ester has been maximised.

In the current work the procedure adopted was the method of Zwierzak [146], who states that "*among the various methods described in chemical literature [146] [1] - [9] for the synthesis of dialkyl hydrogen phosphates there is, however, no simple and inexpensive procedure which could easily be adopted for large-scale preparation of these compounds. Oxidation of dialkyl phosphites, which are the most readily accessible starting materials in organophosphorus chemistry, seems to be the method of choice , but so far, the reaction was not studied extensively from the preparative point of view and no final conclusions could be drawn as to the wide applicability of the method for practical purposes.*" The scheme involves oxidation of di-alkyl phosphonates with potassium permanganate in aqueous base, as in (I).

$$3(RO)_2P(O)H + 2KMnO_4 + NaHCO_3 \xrightarrow[0-5\,^\circ C]{H_2O} 2(RO)_2P(O)OK + (RO)_2P(O)ONa + 2MnO_2 + CO_2 + 2H_2O \quad \text{(I)}$$

$$\xrightarrow{HCl} 3(RO)_2P(O)OH + 2KCl + NaCl$$

This scheme was used to prepare di-methyl and di-butyl acid phosphates. Di-octyl and di-(2-ethyl-hexyl) acid phosphates were prepared in a similar reaction using aqueous pyridine as base. The following two sections contain details of these preparations and subsequent purification. Di-dodecyl hydrogen phosphate was obtained commercially (Labimex Chemical Co. Amsterdam) and no purification was attempted.

4.2.1.1 Di-methyl and di-butyl acid phosphates

Much of the experimental work described in this chapter was carried out in round bottom flat flange reaction vessels, fitted with five port lids (as shown in figure 4.1). These vessels were used when the reaction mixture contained suspended solids, as they were easily dismantled for the removal of solid suspensions (by filtration). In figure 4.1 the vessel is fitted with a pressure equalising dropping funnel and a condenser. This set-up was used for producing di-alkyl phosphonates (see § 4.3.1). In the current reaction a plastic 'paddle' stirrer and a thermometer were fitted (the latter was arranged to monitor the bulk temperature of the reaction mixture). The stirrer was driven by a variable speed electric motor. A piece of pressure tubing acted as a flexible coupling. The stirrer guide used was made in two parts. The lower section consisted of a ground-glass cone above which a ground-glass guide and reservoir were concentrically arranged. This was greased and remained stationary in the central port of the head. A ground-glass guide attached to the stirrer-rod by a PTFE screw-joint, rotated around the inner tube when the stirrer was driven. A very light lubricant was placed in the reservoir to perfect a seal. However, 'capillary action' in the liquid results in its filling the narrow space between the ground glass tubes. When the mixture is stirred considerable shear takes place in the thin oil film and the resulting shear heating and thermal expansion can lead to seizure. Reactants were added through a funnel which occupied a third port, and the remaining ports were sealed with ground-glass stoppers lightly coated with silicone grease (LX-51, ICI Ltd.).

In the current procedure the reaction vessel was cooled in a polystyrene container filled with an ice and salt mixture. Di-methyl phosphonate (110 g, 1 mole) was added to a solution of sodium hydrogen carbonate (28 g, 0.33 mole) in water (660 ml). This mixture was cooled to ~ - 2^{o} C, by stirring at 200 r.p.m., for 30 minutes. A slight excess of finely powdered potassium permanganate (115.8 g, 0.733 mole) was added portion-wise, over a period of 3 1/2 hours. During this period rapid stirring was maintained and efficient cooling kept the temperature below 0^{o} C. The cooling bath was removed and the mixture was further stirred, at room temperature, for 1 hour.

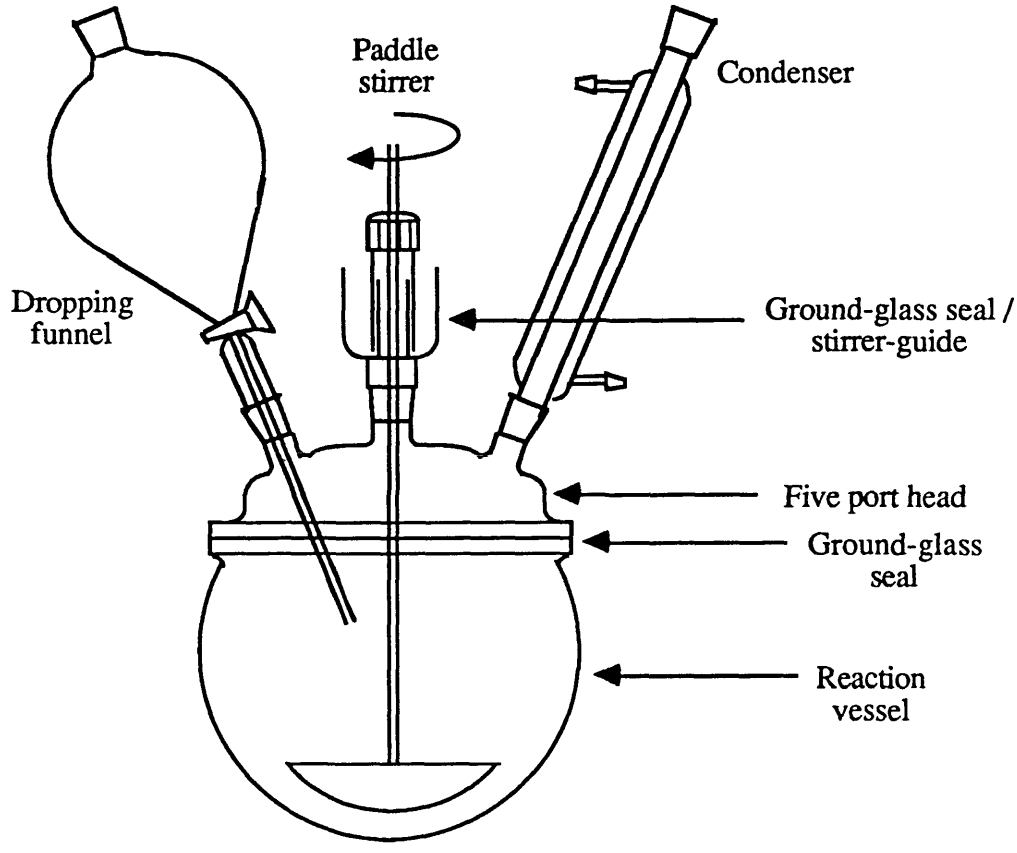


Figure 4.1 Five port flat flange reaction vessel

The reaction mixture was vacuum filtered through a Buchner funnel. The brown manganese dioxide solid removed was washed with water (2 x 120 ml). The pale brown filtrate and washings were decolourised by boiling with powdered charcoal (6 g), filtered to remove charcoal and neutralised with a few grams of sodium hydrogen carbonate (during which a large volume of carbon dioxide was evolved).

The sodium and potassium salts of di-methyl acid phosphate were concentrated by 'stripping-off' water in a rotary evaporator. This resulted in an oily 'syrup' in which crystalline salts of the acids could be seen. Concentrated hydrochloric acid (107 ml, specific gravity 1.18) was added to the syrup in a fume cupboard. Potassium and sodium chloride salts were filtered off and the filtrate was vacuum stripped of the water added with the acid. The precipitates were washed with chloroform (2 x 30 ml), which was combined with the concentrated filtrate and further diluted with chloroform (320 ml). The solution

was dried with anhydrous magnesium sulphate and removal of the chloroform *in vacuo* gave crude di-methyl acid phosphate as a colourless oil (77.5 g, 61% yield).

Crude di-butyl acid phosphate (126.2 g, 60% yield) was similarly prepared. This reaction was found to be even more vigorously exothermic than the first procedure. The rate of permanganate addition had to be further reduced, to prevent an observed spontaneous flame, as permanganate entered the reaction mixture. During addition of permanganate the temperature was maintained in the region of 0 - 5° C. The crude products were purified as described in § 4.3.

Zwierzak [146] concluded that distillation *in vacuo* was unsuitable as a method of purifying di-alkyl hydrogen phosphates and that it did not afford analytically pure products (although he used this method to purify methyl and ethyl versions). Chromatographic analysis was carried out on crude and vacuum distilled di-ethyl acid phosphates [146]. The latter consisted of 95.3% di-ethyl hydrogen phosphate (i), 1.7% ethyl di-hydrogen phosphate (ii) and 3.0% tri-ethyl phosphate (iii), whereas the crude acid was found to be free of these contaminants. This was attributed to an acid catalysed, partial thermal decomposition during distillation, as in (II).

$$\underset{\text{(i)}}{2\ (C_2H_5O)_2(HO)P(O)} \xrightarrow{H^+\ ?} \underset{\text{(ii)}}{(C_2H_5O)(HO)_2P(O)} + \underset{\text{(iii)}}{(C_2H_5O)_3P(O)} \qquad \text{(II)}$$

As a result of this, the purification techniques suggested in [146] were modified. Di-methyl acid phosphate was heated in an oil bath at 80° C / 0.02 mm Hg to remove volatile impurities. A liquid nitrogen trap prevented volatile impurities reaching the vacuum pump. The reaction vessel was evacuated through a 'quick-fit' boiling tube immersed in a Dewar flask containing liquid nitrogen, into which volatile impurities condensed. This was attached to the vacuum pump through a three-way valve. The vessel pressure was monitored using a 'Macleod' gauge attached to the third arm of the valve. Pure product was collected after 1 hour (76.0 g, 60% yield). No thermolytic break-down was expected as the product distilled over at 92-3° C / 0.01 mm Hg [146]. Di-butyl acid phosphate was purified by extracting polar impurities with water. A solution of the product in chloroform

was shaken in a separating funnel with water (3 x 100 ml), dried with anhydrous magnesium sulphate and filtered. Final purification was achieved by heating the product at 80° C / 0.03 mm Hg for 1 hour to give pure di-butyl phosphate (105.8 g, 50% yield). In both cases high purity resulted (see § 4.5).

4.2.1.2 Di-octyl and di-2-ethyl-hexyl acid phosphates

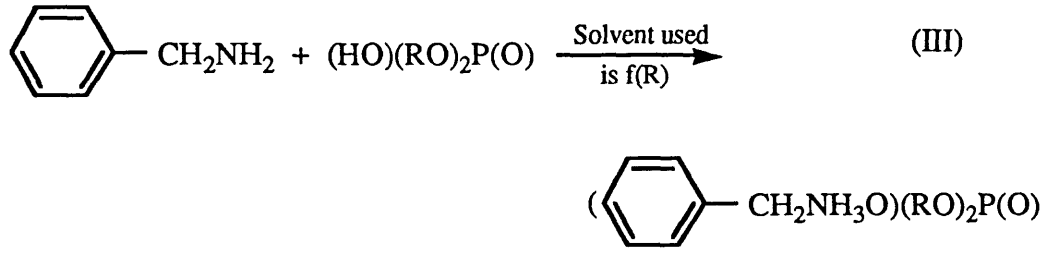
Di-octyl and di-(2-ethyl-hexyl) acid phosphate were synthesised by a method similar to that described in 4.2.1.1. Di-octyl phosphonate (45.9 g, 0.15 mole) and pyridine (66.75 g, 0.75 mole) were added to water (600 ml), in the reaction vessel described previously. Stirring and cooling reduced the temperature to ~ - 4° C, whereupon portion-wise addition of powdered potassium permanganate (18.75 g, 0.1185 mole) was started. The use of smaller quantities of reactants and a large volume of solvent moderated the reaction rate. The reduction of permanganate to manganese dioxide, observed as a purple to brown colour change, took several minutes.

When the oxidation was completed the stirring 'paddle' was replaced with a condenser, and the remaining ports were sealed. The ice / salt bath was replaced by a heating mantle, and the mixture was refluxed to coagulate the colloidal suspension of manganese dioxide. On cooling, the manganese dioxide was removed by vacuum filtration. The filtrate was decolourised by boiling with charcoal (3 g) and filtered again. Addition of concentrated hydrochloric acid (195 ml) to the aqueous mixture resulted in an opaque suspension of insoluble product, in the aqueous phase. The crude product was extracted into chloroform (3 x 75 ml) by vigorous shaking in a separating funnel. The lower chloroform / product fractions were dried with anhydrous magnesium sulphate, filtered and vacuum stripped to yield crude di-octyl acid phosphate as a clear, oily liquid (33.78 g, 70% yield). Crude di-(2-ethyl-hexyl) acid phosphate was similarly worked-up to give a clear, pale yellow liquid (35.26 g, 73% yield).

Both products were purified by heating at reduced pressures, using the set up described previously. Di-octyl acid phosphate was heated in an oil bath at 145° C / 0.1 mm Hg for three hours to yield pure product (32.05 g, 66% yield). Similar treatment of di-(2-ethyl-hexyl) acid phosphate at 140° C / 0.1 mm Hg for 2 1/2 hours gave pure product (34.30 g, 70% yield). In both cases high product purity resulted (see § 4.5).

4.2.2 Amine salts of di-alkyl acid phosphates - $(C_6H_5.CH_2NH_3O)(RO)_2P(O)$

The reasons for preparing amine salts of acid phosphates were discussed in § 3.7. Pure, stable, non-hygroscopic crystalline derivatives were reported to result from the reaction of di-alkyl acid phosphates with aniline ($C_6H_5.NH_2$) in [146]. Forbes and Silver [36], [43] prepared a range of mono, di and tri-substituted amine di-alkyl phosphates (see § 3.7.1). Bulky, short chain primary amines were shown to give the best anti-wear / extreme pressure results. Particularly good results were observed with benzyl amine ($C_6H_5.CH_2NH_2$). This was discussed in more detail in chapter 2. As a result of this, a range of benzyl amine salts of di-alkyl acid phosphates were prepared, for use in the current work. The reaction scheme is shown in (III).



Acid phosphate and benzyl amine were mixed together in stoichiometric proportions, in a low-boiling solvent. Example preparations are given below. This is best achieved by adding a carrier solution of the amine, pre-weighed into solvent, to an acid phosphate / solvent mixture, at room temperature. Addition of the amine direct was found to be unsatisfactory as the considerable 'heat of neutralisation' results in evaporation of solvent and a potential error in the weight of amine added.

The benzyl amine salt of di-methyl acid phosphate was prepared and purified, as follows. A solution of benzyl amine (10.72 g, 0.1 mole) in acetone (25 ml) was added portion-wise to di-methyl acid phosphate (12.6 g, 0.1 mole) in acetone (25 ml), in a 100 ml round bottom flask, with shaking. Crude product began crystallising out as 'white' crystals in a pale yellow solution, after about twenty minutes. The crude product was filtered, re-crystallised from acetone (~ 35 ml) and the solvent was stripped in a rotary evaporator. The reaction vessel was warmed to remove any remaining acetone and pure product was obtained as fine white crystals (25.5 g, 88% yield).

Benzyl amine salts of di-butyl, di-(2-ethyl-hexyl), di-octyl and di-dodecyl acid phosphates were similarly prepared, using 40 - 60 petroleum ether, as solvent. Near quantitative yields were obtained in all cases. Di-butyl and di-dodecyl acid phosphates gave solid, crystalline amine salts. Di-(2-ethyl-hexyl) and di-octyl acid phosphates resulted in pale yellow, 'near-solid' jelly-like amine salts. The purity of these compounds is discussed in § 4.5.

4.3 Preparation and purification of phosphonic acid esters and ester derivatives

A wide range of phosphonic acid esters and ester derivatives, have been tested for thick-film anti-wear activity (see chapter six). As discussed earlier in this chapter, tri-substituted esters of the phosphite type would not be expected to operate by a thick film mechanism. However, de-alkylation / arylation during testing, would result in formation of the phosphonate tautomer that might be expected to operate in this way. For this reason, a number of phosphites were tested as potential thick-film forming additives. The phosphites tested were commercially available, and no synthetic details are given here.

Di-substituted esters were extensively studied, in the current context, by Lacey [76]. A number of these compounds were prepared, by the author, for use in the current work. Synthetic details of the preparation and purification of di-substituted esters are given in § 4.3.1. Mono-substituted alkyl and aryl esters would be expected to operate similarly. A number of these acid esters and their neutral amine salts were therefore prepared for use in the current study. Synthetic details are given in § 4.3.2.

4.3.1 Di-substituted phosphonates - $(RO)_2P(O)H$

The classical partial alcoholysis and hydrolysis of phosphorus trichloride, was used by the author to prepare di-alkyl phosphonates (§ 4.3.1.1). This reaction scheme, summarised in (IV) below, had been successfully used previously to prepare di-alkyl / aryl phosphonates, in the author's laboratory (this is briefly considered in § 4.3.1.2).

$$PCl_3 + 2\,ROH + 2\,(C_2H_5)_3N \longrightarrow (RO)_2PCl + 2\,(C_2H_5)_3N : HCl$$

$$(RO)_2PCl + H_2O + (C_2H_5)_3N \longrightarrow (RO)_2P(O)H + (C_2H_5)_3N : HCl \qquad \text{(IV)}$$

4.3.1.1 Di-octyl and di-dodecyl phosphonate

The two-stage reaction scheme (IV) was used to produce di-octyl and di-dodecyl phosphonate. Di-alkyl chlorophosphite was produced by reacting phosphorus trichloride with two equivalents of alcohol, using triethylamine as a hydrogen chloride acceptor. Hydrolysis with one equivalent of water, again with a hydrogen chloride acceptor present, yielded di-alkyl phosphonate.

Di-octyl phosphonate was prepared using the apparatus shown earlier in figure 4.1. A two litre capacity reaction-vessel, was employed. A condenser prevented loss of solvent during the highly exothermic reaction and a nitrogen blanket was maintained throughout. A solution of phosphorus trichloride (116.5 ml, 183.1 g, 1 1/3 mole) in diethyl ether (250 ml), was slowly added, using a pressure-equalising funnel, to a solution of triethylamine (557 ml, 404.7 g, 4 mole) and octanol (422 ml, 347.3 g, 2 2/3 mole), in di-ethyl ether (1000 ml).

The amine and alcohol mixture was previously cooled in an ice / salt bath to ~ 3° C, with stirring. Addition of phosphorus trichloride was completed in ~ 5 1/2 hours, during which vigorous stirring maintained a temperature of ~ 5° C. Rapid stirring was also necessary to maintain mobility of the slurry formed by the large volume of triethylammonium chloride produced. The reaction was completed by stirring for a further three hours in the absence of cooling. The ice / salt bath was then replaced, and the mixture cooled to ~ 4° C prior to the very slow addition of distilled water (24 g, 1 1/3 mole). Addition of water was completed in 2 1/2 hours, after which the ice / salt bath was removed. The mixture was stirred overnight, vacuum filtered and the triethylammonium chloride 'cake' was washed with diethyl ether (2 x 75 ml). Rotary evaporation of solvent gave crude di-octyl phosphonate (249 g, 61% yield), as a clear, colourless liquid.

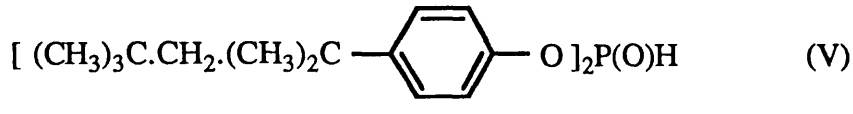
Di-dodecyl phosphonate was similarly prepared (the molar quantities were reduced by 1/4 throughout). Crude product (284.2 g, 68% yield), was obtained as a pale yellow solid.

Crude di-octyl phosphonate was purified by vacuum distillation. The apparatus was similar to that described in § 4.2.1.1, but the reaction vessel consisted of a 500 ml round bottom flask fitted with a 'Claisen' head and a thermometer. A partial vacuum was maintained by using a finely-drawn capillary bleed, attached to a balloon filled with dry nitrogen. Pure di-octyl phosphonate (232.5 g, 57% yield), distilled over at 140° C / 0.1 mm Hg. Pure di-dodecyl phosphonate (267 g, 64% yield) remained after heating the mixture at 185° C / 0.25 mm Hg for 3 hours. Lacey [76] claims pure product was collected at 165° C / 0.3 mm Hg, though Zwierzak [146] observed no distillation at 190° C / 0.1 mm Hg.

Infra-red absorption spectra were taken and compared to those given in [76] (which are for products with a purity exceeding 99% [28]). No differences were observed between the respective spectra. Because of this, no further analyses were carried out.

4.3.1.2 Di-alkyl and di-aryl phosphonates from other sources

As mentioned previously, Lacey [76] prepared a range of di-alkyl and di-aryl phosphonates. Two of these products were used in the current study. The purity of the products used was assessed by comparing the current absorption infra-red spectra, with those measured at the time of preparation / purification, given in [76]. *Bis*-(*t*-octyl-phenyl) phosphonate (BOPP), was found to be unchanged and was used without purification, in the current study. This abbreviated name is used throughout the current work, but as BOPP has the structure shown in (V), it should more correctly be termed *bis*-[*4* (*1,1,3,3* tetra-methyl butyl) phenyl] phosphonate.



(V)

(BOPP)

Di-hexyl phosphonate (DHP) prepared for use in [76], reportedly with an original purity exceeding 99% [28], was found to have degraded during storage. This conclusion was based on comparisons between the infra-red (IR) absorption spectra measured in this study and those found in the literature. The significance of infra-red absorption spectra and refractive indices in characterising products for purity was discussed briefly in § 3.8. This is dealt with in detail in § 4.4.

The 'received' di-hexyl phosphonate was vacuum distilled as described in the previous section, with the intention of collecting pure DHP. However, a low-boiling 'distillate' was collected in the temperature range 42 - 62° C / 1.5 mm Hg. No further distillation of the 'remainder' occurred. IR absorption spectra of the various components of the mixture and of mono-hexyl phosphonate (MHP) prepared as described in § 4.3.2, were measured. Figures 4.2 and 4.3 show the IR spectra of the 'received' and 'distillate' samples , and the 'remaining' and MHP samples, respectively. The refractive indices are given in table 4.1, where (R = $CH_3(CH_2)_5$).

'Received'	'Distillate'	'Remaining'
1.4272	1.4179	1.4350
$(RO)_2P(O)H$ [182]	ROH [183]	(RO)(HO)P(O)H
1.4325	1.4178	1.4340

Table 4.1 Refractive indices (η_D^{20}) of di-hexyl phosphonate and associated products

The IR and RI measurements indicated the 'distillate' to be pure hexanol. An IR spectrum run using a sample of commercially available hexanol was indistinguishable from that of the distillate. Table 4.2 lists the approximate group frequency correlations of groups present in DHP and related compounds (§ 4.4.1 contains details and references), as taken from figures 4.2 and 4.3.

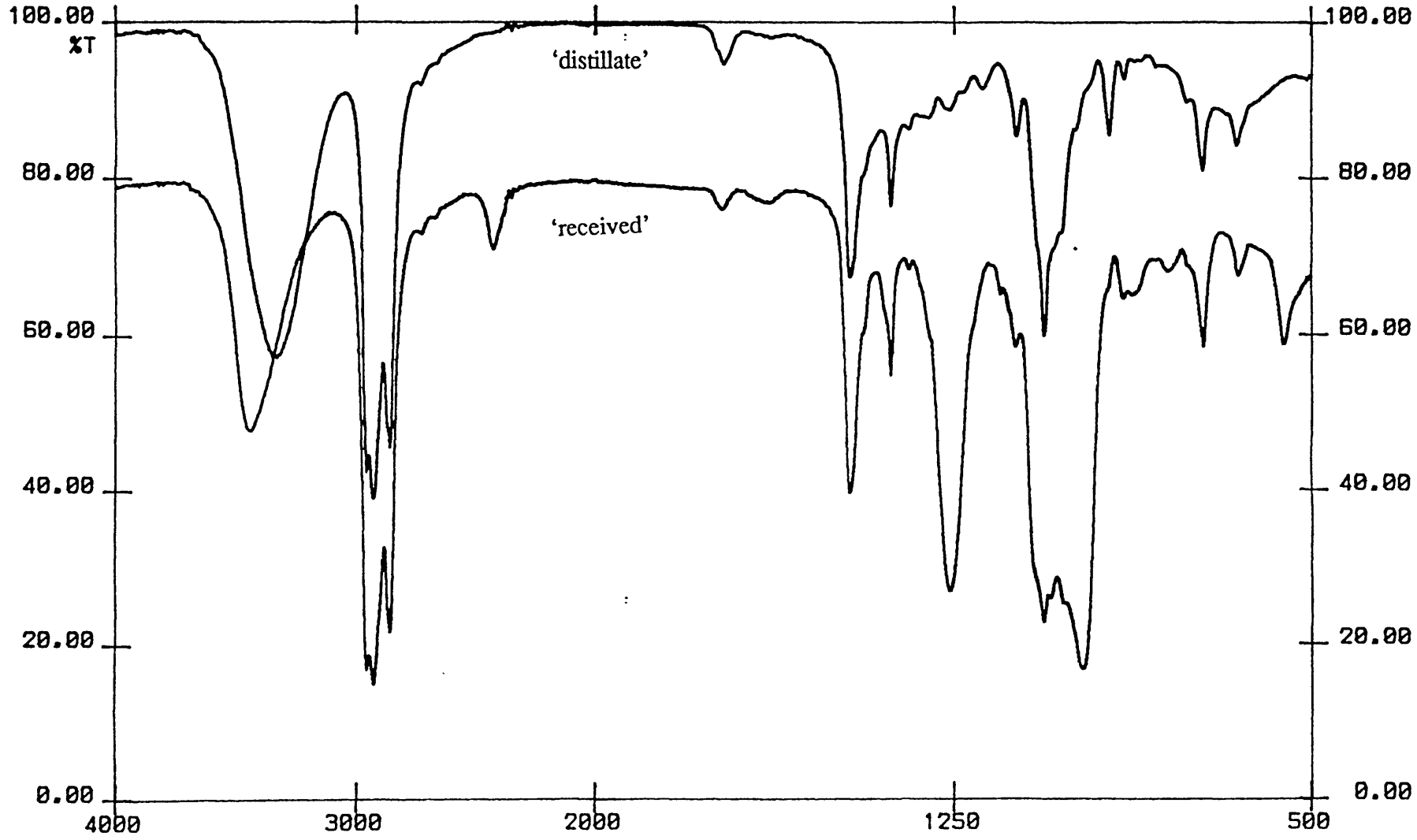


Figure 4.2 Infra-red spectra of di-hexyl phosphonate as 'received' and 'distillate' fractions

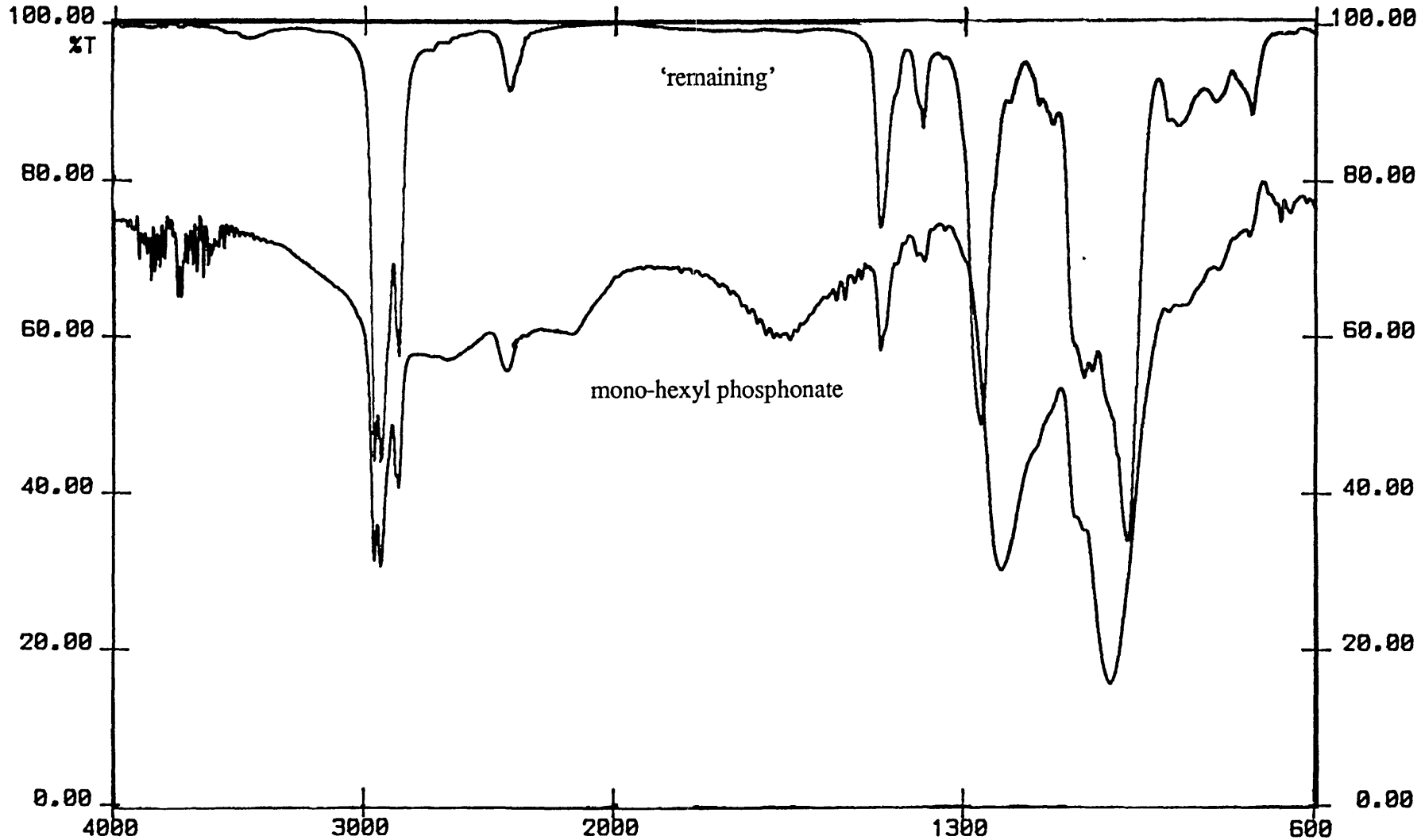


Figure 4.3 Infra-red spectra of di-hexyl phosphonate 'remaining' fraction and mono-hexyl phosphonate

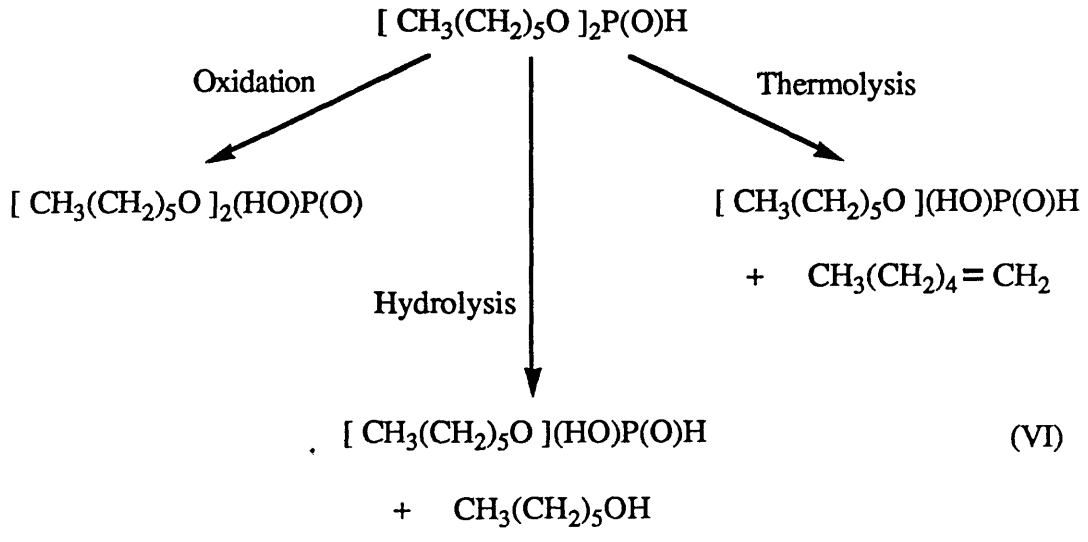
The 'received' DHP was heavily contaminated with parent hexanol, which was collected as 'distillate'. IR and RI measurements show the hexanol distillate (approximately 40% by volume), to be pure and the 'remaining' product to be free of contamination by alcohol i.e. to have lost the peak at ~ 3340 cm^{-1}. This contamination by parent alcohol is present in the 'pure DHP' spectrum of Lacey [76] who attributes it to hydrogen-bonding, quoting Thomas [184], in which no such conclusion was drawn.

	Approximate Group Frequencies / cm^{-1}					
	P(O)OH	P-O-H	P = O	P-H	P-O-C	ROH
SAMPLE	~ 2700	~ 1660	~ 1250	~ 2430	~ 975	~ 3340
'Received'	- / x	x	x	x	x	x
'Distillate'	-	-	-	-	-	x
'Remaining'	- / x	x	x	x	x	-
$(RO)_2P(O)H$	-	-	x	x	x	-
(RO)(HO)P(O)H	x	x	x	x	x	-
ROH	-	-	-	-	-	x

x band present ; - no band in spectrum

Table 4.2 Approximate group frequencies of di-hexyl phosphonates and associated products.

Parent alcohol present in the crude reaction mixture might have been collected with pure DHP during distillation. However, the IR spectrum, the large volume of hexanol collected and, in particular, the RI measurement, suggested that DHP underwent some decomposition resulting in its contamination and the formation of hexanol. Of the three likely reactions - oxidation, hydrolysis or thermolytic degradation - only hydrolysis would result in hexanol formation (VI). Evidence for the hydrolytic formation of MHP came from the measured RI and a small peak at ~ 1660 cm^{-1}, which was due to a P-O-H vibration [184]. This peak was also found to be present in MHP produced by the author (at ~ 1653 cm^{-1}).



(VI)

These analyses suggest that di-substituted phosphonates break-down by a hydrolytic mechanism under these experimental conditions. The alcohol produced would be unlikely to form films of more than a few monolayers thickness in boundary lubrication. The mono-substituted phosphonate formed would, however, be expected to be more reactive, and to operate by a thick-film mechanism (as discussed previously). For this reason a range of mono-alkyl phosphonates were synthesised for use in the current work (as described in the next section). The hydrolytic break-down observed under the experimental conditions described should not be assumed to operate in tribological systems, although water is known to enhance the rate of polymer formation with di-substituted phosphonates [76].

Di-substituted phosphonates are finding increasing industrial use, mostly as lubricant additives and in metal extraction. As a consequence, many of the di-phosphonates became commercially available during the course of the current work. Commercial additives were used where possible.

4.3.2 Mono-substituted phosphonates - (RO)(HO)P(O)H

Preparation of mono-substituted phosphonates has been achieved in the past using a number of synthetic procedures - see § 3.6.3 - although the degree of purity achieved is doubtful. For example, Lacey [76] used three separate, synthetic routes in an attempt to produce mono-phenyl phosphonate. In each case a very low yield of low purity product was reported.

In the current work, two different procedures were used to produce mono-alkyl and mono-aryl phosphonates respectively. The former method resulted in near quantitative yields, although product purity was limited. Some attempts were made at purification. The latter synthesis proved unsuccessful at the first attempt. The synthetic route to mono-aryl phosphonates is an improvement on those employed previously and would probably have proven successful if time were available for its further development.

4.3.2.1 Mono-alkyl phosphonates

Two synthetic routes to mono-alkyl phosphonates were employed, based on the method of Barber et al [47],[48]. As described previously, neutral amine salts are often prepared for use in tribological systems. Attempts were made to produce ammonium salts of mono-alkyl phosphonates in the range C_1 - C_3, directly (see § 4.3.3). Phosphonates with an alkyl chain length in the range C_{4+}, were prepared by the method of Barber [48], according to scheme (VII). This involves the direct esterification of phosphorus acid, with simultaneous removal of water, which prevents hydrolysis of product and pulls the reaction through to completion (by Le Chatelier's principle).

$$ROH + (HO)_2P(O)H \xrightarrow[\text{Reflux}]{\text{Toluene}} (RO)(HO)P(O)H + H_2O \qquad \text{(VII)}$$

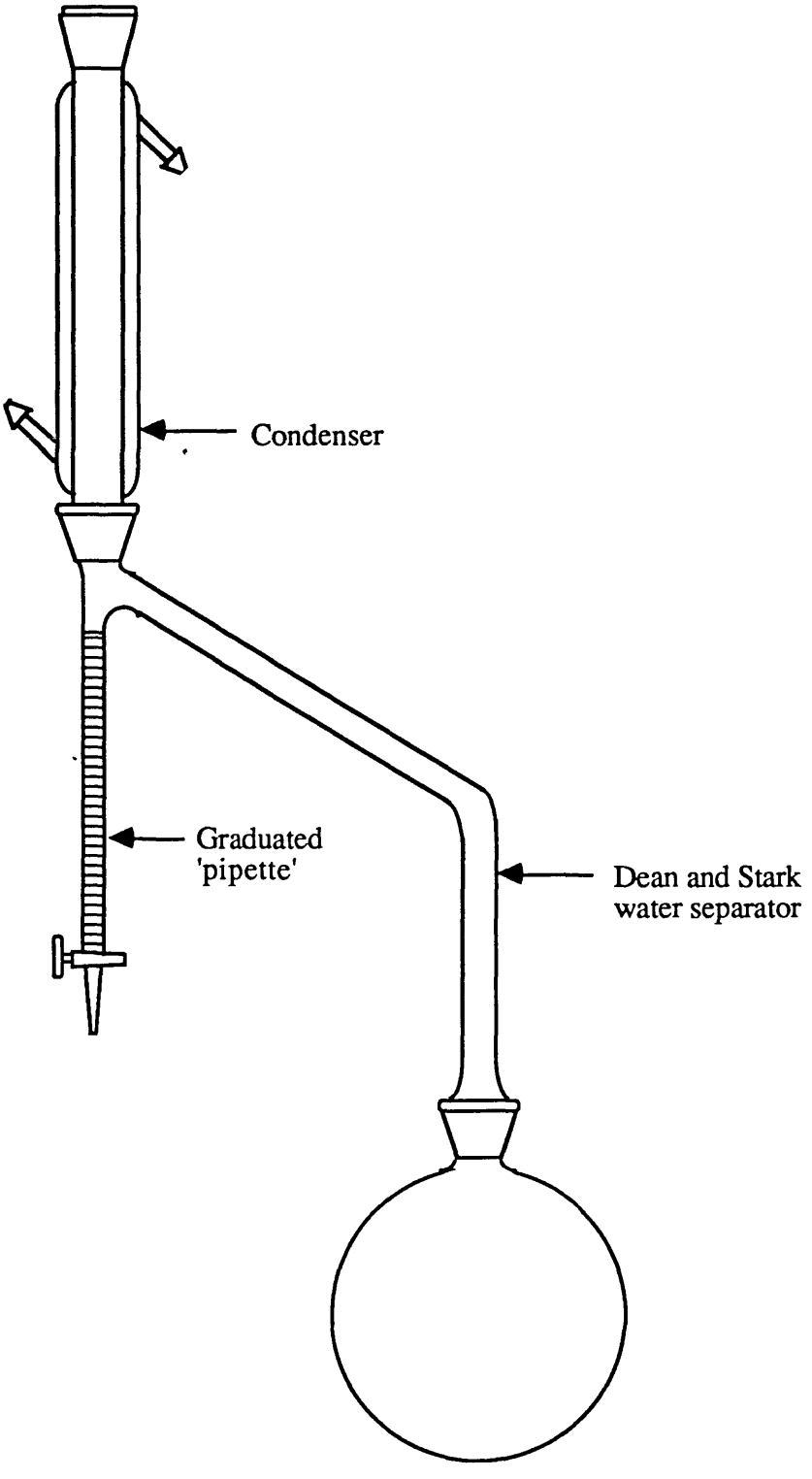


Figure 4.4 Apparatus for producing mono-alkyl phosphonates

Phosphorus acid (41 g, 0.5 mole) and *n*-butanol (40.7 g, 0.5 mole) were refluxed in toluene (200 ml) in the apparatus shown in figure 4.4. Care was taken to rapidly transfer phosphorus acid, because of its highly hygroscopic nature. A Dean and Stark water separator was used. The graduated pipette initially filled with toluene, but as the reaction progressed, higher density water displaced the toluene. This provided a means of following the reaction. The reaction was deemed to be complete when no more water was produced (9 ml, 0.5 mole having been collected), this typically took approximately 4 hours. Rotary evaporation of solvent gave mono-*n*-butyl phosphonate (62.5 g, ~ 100 % yield), as a clear, colourless liquid.

The following mono-alkyl phosphonates were similarly synthesised. R = hexyl, 2-(ethyl-hexyl), octyl, dodecyl and octadecyl. These were all prepared in near quantitative yields as mobile, colourless liquids (the exception being the octadecyl version which was a waxy, white solid).

No details of purity or attempts at purification were given in [48]. Two methods were attempted in the current work, although neither method proved very successful. Fractional distillation resulted in gross breakdown of the product; no attempts were made to analyse the resulting material. This decomposition was considered to be initiated by traces of phosphorus acid in the product since colourless crystals were occasionally observed when the product was dissolved in deuterated chloroform ($CDCl_3$), for $^{31}P_{NMR}$ analyses. As a result of this observation, fractional crystallisation was investigated as a means of purification of mono-alkyl phosphonates, both in the presence and absence of solvents. This too proved to be of little use. Subsequently, neutral amine salts were prepared directly (see § 4.3.3) to prevent further decomposition of the product.

4.3.2.2 Mono-aryl phosphonates

Two attempts were made to produce mono-aryl phosphonate, by the improved method of Bridger [161], shown in (VIII). This involves reacting an alkyl-substituted phenol with excess phosphorus trichloride, in the presence of *n,n*-diethyl aniline as a hydrogen chloride acceptor. The resulting alkyl-substituted phenyl phosphorochlorodite is reacted with two equivalents of *t*-butanol, again with base present. The mono-alkyl-substituted-

aryl phosphonate is produced on refluxing the alkyl-substituted-phenyl di-*t*-butyl phosphite with an ion exchange resin, with the elimination of two equivalents of butene.

(VIII)

$$R.ArOH + (C_6H_5)(C_2H_5)_2N + PCl_3 \longrightarrow (R.ArO)PCl_2 + (C_6H_5)(C_2H_5)_2N : HCl$$

$$(R.ArO)PCl_2 + 2\,(CH_3)_3COH + 2\,(C_6H_5)(C_2H_5)_2N \longrightarrow (R.ArO)[(CH_3)_3CO]_2P + 2\,(C_6H_5)(C_2H_5)_2N : HCl$$

$$[(CH_3)_3CO]_2(R.ArO)P \xrightarrow{heat} [(CH_3)_3CO](R.ArO)P(O)H + (CH_3)_2C{=}CH_2$$

$$[(CH_3)_3CO](R.ArO)P(O)H \xrightarrow[resin]{ion\ exchange} (R.ArO)(HO)P(O)H + (CH_3)_2C{=}CH_2$$

A solution of *4-t*-butyl-phenol (12.02 g, 0.08 mole) and *n,n*-diethylaniline (11.92 g, 0.08 mole) in hexane (200 ml) was added dropwise, to excess phosphorus trichloride (110 g, 0.8 mole), with stirring, over a two hour period. The 'milky' suspension cleared after a further 70 minutes of stirring and the white suspension of base:HCl adduct, was removed by filtration. The solvent and excess PCl_3 was removed using a rotary evaporator, yielding *4-t*-butyl-phenyl-phosphorochlorodite (24.8 g, ~ 100 %). A solution of *t*-butanol (11.85 g, 0.16 mole) and *n,n*-diethylaniline (23.87 g, 0.16 mole) in hexane (200 ml), was added dropwise to the phosphorochlorodite in hexane (100 ml), over a period of 2 hours. The resulting mixture was refluxed for 1 hour, the base:HCl adduct was removed by filtration and the solvent was vacuum stripped to give *4-t*-butyl-phenyl di-*t*-butyl phosphite (27 g, ~ 100 % yield). The phosphite was refluxed with Amberlyst ® 15 ion exchange resin (4 g), in hexane (100 ml). A white gas was given off and an orange precipitate appeared. An orange precipitate has been observed previously during the decomposition of phosphonates [76]. In a similar preparation, Bridger reported a colourless oil (after filtration of resin and vacuum removal of solvent). The white gas observed in the current procedure was probably hydrogen chloride, resulting from the reaction of traces of phosphorus trichloride remaining after vacuum stripping, with the ion exchange resin. Due to constraints of time the procedure was not further investigated, although it seems probable that a pure product could have been obtained.

4.3.3 Amine salts of mono-alkyl phosphonates - $[CH_3(CH_2)_{17}NH_3O](RO)P(O)H$

A range of amine salts of mono-alkyl phosphonates were prepared using the method of Barber et al [48], who had found that the best anti-wear / extreme pressure behaviour was obtained by using a branched primary amine, in the range C_{16} - C_{36}. A straight-chain C_{18} amine - $CH_3(CH_2)_{17}NH_2$ - was chosen from the amines that were commercially available.

Mono-alkyl phosphonates were produced as described in § 4.3.2.1, but using 0.2 moles of each reactant in toluene (100 ml). In the case of mono-butyl phosphonate, heating was stopped on collection of 3.6 ml of water. When the solution had cooled sufficiently, the Dean and Stark apparatus was removed and octadecyl amine (53.1 g, 0.2 mole), was added. The dried condenser was then replaced in the vessel and the mixture was refluxed for a further two hours. Removal of toluene *in vacuo* gave the octadecylamine salt of mono-butyl phosphonate (81g, ~ 100 % yield), as a waxy white solid. The procedure was repeated to produce octadecyl amine salts of the following mono-alkyl phosphonates - hexyl, 2-(ethyl-hexyl), octyl and dodecyl. Near quantitative yields of white, waxy solids were obtained throughout.

Amine salts of mono-alkyl phosphonates with chain lengths of less than 4 carbon atoms, can be prepared by combining the methods of Smith [163] and Barber et al [48]. This was discussed in more detail in § 3.7.2. Initial attempts at producing these products proved unsuccessful. No further attempts were made to produce these compounds, for two reasons. Firstly, as described in chapters six and seven, short chain di-alkyl phosphonates do not appear to operate by a thick film mechanism and secondly, the products have a low oil solubility even with the attachment of a long, branched-chain amine [47].

4.4 Techniques for characterising organophosphorus esters and ester derivatives

Section 3.8.1 briefly described the information available from a number of complementary techniques used to identify the products and purity of a reaction. The following section considers in more detail the physical and theoretical basis of these techniques and discusses their practical application. Section 4.5 contains the results obtained from the application of the various analyses to the products prepared for use in the current work. Some concluding remarks about product purity are included.

4.4.1 Vibrational spectroscopy - Infra-red (IR) absorption spectra

As discussed in § 3.8.1.2, experimentally obtained spectra are of three types - emission, absorption and Raman. The ability of a molecular vibration to interact with radiation i.e. to be IR or Raman active, is dictated by a series of selection rules. The compounds prepared in the current study possess a number of characteristic, well-documented IR absorption bands. For this reason characterisation of products by vibrational spectroscopy has been limited to the use of IR absorption spectra.

4.4.1.1 Vibrational spectroscopy - theory

The energy change on absorption or emission (ΔE) is related to the frequency (ν), by $\Delta E = h\nu$ (h is Planck's constant). Spectroscopists often express this relationship in terms of the wavelength $\lambda = c / \nu$ (typical units are microns, μm), or the *wavenumber* $\sigma = 1 / \lambda$ (for which the units are cm^{-1}). c is the speed of light. However many spectral bands, for which appropriately separated energy levels are present, are absent from the spectrum. The following *gross selection rules* dictate which vibrational modes will be IR or Raman active. Simply stated on electromagnetic wave of frequency (ν) is generated by an electric dipole oscillating at the frequency (ν). *Vibrational transitions* occur when bonds bend or stretch altering the dipole moment. The oscillating dipole encourages the electromagnetic field to oscillate, permitting the absorption or emission of radiation. The selection rule therefore, is that only vibrations accompanied by a changing dipole moment can generate, or absorb, electromagnetic radiation. For *rotational transitions* the selection rule states that only molecules possessing a permanent electric dipole moment can emit or absorb

radiation, by a transition between different states of rotation. This is best explained by imagining a molecule with a permanent dipole rotating in the plane of observation. The molecule appears to be a fluctuating dipole 'handle', that can 'stir' the electromagnetic field into oscillation (the reverse is true for absorption). Pure rotational spectra appear in the far infra-red and microwave regions of the spectrum. Any vibrational or rotational mode that leaves the dipole moment unchanged will be inactive spectroscopically.

The gross selection rules for Raman activity are as follows. For *rotational Raman* activity the molecule must possess an *anisotropic polarizability* and for *vibrational Raman* activity a change in *polarizability* must occur during the vibration. Any molecule placed in an electric field is distorted by the forces acting on its nuclei and electrons. Distortion of a non-polar molecule, in which the centres of positive and negative charge are initially coincident, may result in a dipole moment being induced in it. The extent of dipole inducing distortion is a measure of the molecule's polarizability. An atom's polarizability is determined by the degree of attraction between nucleus and electrons, and is independent of the direction of applied field i.e. it is isotropic. A diatomic molecule possesses a higher polarizability along the bond than perpendicular to it i.e. it has an anisotropic polarizability.

A simple rule exists for distinguishing the active and inactive vibrational modes in polyatomic species. The *exclusion rule* states that if a molecule has a centre of symmetry then modes that are infrared inactive are Raman active, and vice versa.

4.4.1.2 IR group frequency correlations

As mentioned previously, IR absorption spectroscopy is particularly useful in characterising synthetic products. Observed vibrations afford an insight into the nature and strength of bonding in a molecule, as they are basically a function of the masses of the bonding elements and the bond-type linking them. Of particular use are '*group frequency correlations*' which relate the presence of a band or set of bands in the spectrum, to a particular group of atoms in the molecule. The vibrational frequencies of these groups are largely independent of other atoms or groups present in the molecule. Table 4.3 lists the literature values for groups germane to the current study. The values quoted are in wavenumbers (cm^{-1}).

P = O	P - O - Ar	P - O - C	P - O - H
1350 - 1250 [186]	1240 - 1190 [186]	1150 [186]	2700 - 2560 [186]
1250 - 1175 [187]	995 - 850 [186]	1050 - 990 [186]	2700 - 2650 [170]
1097 - 1300 [188]	1250 - 1165 [187]	1110 - 1000 [187]	1050 - 850 [170]
1300 - 1250 [170]	1055 - 870 [187]	1000 - 870 [187]	$(RO)_2(HO)P(O)$ [185]
(RO)(HO)P(O)H	1240 - 1190 [170]	835 - 715 [187]	1031 - 1000 [185]
1261 - 1170 [166]	P - O - (Ar) [185]	1190 - 1150 [187]	(RO)(HO)P(O)H [185]
P (O) OH	996 - 905 [185]	1050 - 980 [170]	1040 - 1000 [185]
2727 - 2525 [184] [185]	Ar - O - (P) [185]	770 - 650 [170]	
2350 - 2150 [184] [185]	1242 - 1110 [185]	**P - O - (C)**	**P - H**
1700 - 1600 [184] [185]	**P (O) O$^-$**	1060 - 950 [185]	2457 - 2270 [186]
530 - 480 [184] [185]	P (O) O [170]	**P - O - (P)**	2440 [187]
1040 - 917 [185]	1300 - 1150 [170]	1200 - 1087 [185]	2440 - 2280 [170]

Table 4.3 Literature values for main group frequency correlations - Organophosphorus esters

A full vibrational assignment relating spectral bands to particular vibrational modes of the molecule, is beyond the scope of the current study. References [166] and [169] contain particularly good discussions of this matter. Some disagreement exists, for example, in assigning the two vibrations observed with P — O — C. Thomas [185] and Bellamy [186] attribute the higher frequency to the P — O — (C) vibration (i.e. vibration of the phosphorus-oxygen bond). The intense phosphoryl vibration $\nu_{P=O}$ around 1200 cm^{-1}, has been the subject of much study and the following factors have been found to affect $\nu_{P=O}$ [167].

(i) The electronegativity of the three ligands attached to phosphorus. Thomas [166] produced the following empirical relationship (where π is the *Phosphorus Inductive Constant*). The constant is closely related to the Pauling electronegativity, and is based upon data from over 1500 compounds, giving agreement to $\pm$ 12 cm^{-1} in almost all cases.

$$\nu_{P=O}/(cm^{-1}) = 930 + 40 \sum \pi \qquad (IX)$$

(ii) Conjugation or delocalisation involving other atoms attached to phosphorus, for example in $X_2P(O)_2^-$ (where X is any species attached to P).

(iii) The involvement of the oxygen atom in hydrogen bonding, for example in phosphorus acids. Table 4.3 showed a number of regions of IR activity associated with $P(O)_2H$ groups. Of particular importance is the vibration at 1030 - 820 cm^{-1}, usually attributed to P — O — (H) vibration. A similar, though less universally applicable correlation with the electronegativities of the other substituents, has also been observed for this vibration [169] as in (X).

$$\nu_{P-O-(H)}/(cm^{-1}) = 650 + 40 \sum \pi \qquad (X)$$

(iv) Complex formation can occur, with the oxygen atom acting as donor. Thomas [166] observed the existence of two separate P — O — M bond-types in the literature, often without distinction (M = metal). These are respectively metal complexes in which metal forms a coordinate bond with oxygen, and compounds in which a covalent bond links oxygen to the metal. This is important in the current work, as described in chapter seven. As thick-film polymeric material is formed, the lone pair on oxygen coordinates into the central Fe (III) species. This results in a loss of double bond character and a shift to lower wavenumber. Thus IR analysis gives evidence of polymer formation.

(v) Finally, solvent effects are known to affect the $\nu_{P=O}$ position, though this is of limited importance in the current work.

4.4.1.3 Recording IR spectra - practical details

Two infra-red spectrophotometers were used to record spectra. The majority of spectra were recorded using a Perkin-Elmer 1740 FT-IR spectrometer. A few spectra were also recorded using Perkin-Elmer 580 B double beam high energy ratio recording spectrophotometer. Both apparatus are microprocessor controlled via a P-E 3500 data handling station. This digitally stores upto three spectra for ordinate expansion, smoothed noise reduction, subtraction of spectra etc.

IR absorption spectra of synthetic products were recorded as thin liquid films, 'sandwiched' between IR transparent salt plates. A drop of the required liquid formed a capillary film of the order of ~ 0.01 mm thick, when a second plate was lowered onto the sample. Three types of plates were used, sodium chloride (NaCl), potassium bromide (KBr) and silver chloride (AgCl). Solid samples were analysed as a finely divided suspension in an inert carrier. A high molecular weight paraffin 'Nujol,' was used as a carrier fluid. This only shows IR absorption bands associated with C — H and C — C vibrations. A 'Nujol' mull of the sample was prepared by grinding a small quantity of the sample (~ 50 mg) with a few drops of 'Nujol', in an agate mortar. The resulting liquid was treated as described previously.

Details of the spectra obtained, including group frequency correlations, can be found in § 4.5.

4.4.2 Phosphorus nuclear magnetic resonance spectroscopy $^{31}P_{NMR}$

The nuclei of certain atoms *spin*, and the spinning of the charged nucleus generates a magnetic moment along the axis of spin. All nuclei possessing a non-zero (i.e. an integral or half-integral) *spin quantum number* (I) possess a magnetic moment, which is the prerequisite for the observation of a nuclear magnetic resonance spectrum. The ^{31}P nucleus has $I = 1/2$. If the nuclear 'bar magnet' is placed in an appropriate magnetic field and radiation of the correct energy is supplied the nucleus is 'flipped' from its stable ground state alignment with the field, to a less stable alignment against the field. The nucleus can align in $(2I + 1)$ directions relative to the field. The frequency (ν) and the magnetic field

strength (H_0) are related mathematically shown in equation (XI).

$$\nu = \frac{\gamma H_o}{2\pi} \qquad \text{(XI)}$$

Where (γ) is a constant known as the *magnetogyric ratio*. This is characteristic of the particular nucleus, and is defined in equation (XII).

$$\gamma = \frac{2\pi}{h} \cdot \frac{\mu}{I} \qquad \text{(XII)}$$

where (μ) is the magnetic moment and the other symbols are as defined previously. As such, a proton placed in a fixed field (H_0) of 2.35 tesla (T) will resonate at 100 MHz, and a ^{31}P nucleus would resonate at 40.48 MHz.

Each nucleus is partly shielded from the full applied field (H_0) by rapidly moving electrons or other nearby nuclei which generate small, local magnetic fields that partly cancel the applied field. All nuclei therefore absorb at the same *effective* field strength, but at a different *applied* field strength. Because the extent of the shielding cannot be measured directly, the resonance of the ^{31}P nucleus in an arbitrary standard (85 % H_3PO_4) is assigned the value of zero and the ^{31}P chemical shifts of other phosphorus compounds are reported relative to this reference compound, in terms of the parts per million (ppm) change in the magnetic field between the two resonances. This results in a non-dimensional parameter (δ), termed the *chemical shift*, defined as in (XIII). This permits direct comparison of data from different spectrometers.

$$\delta(\text{ppm}) = \frac{H_{\text{SAMPLE}} - H_{H_3PO_4}}{H_{H_3PO_4}} \times 10^6 \qquad \text{(XIII)}$$

$$= - \frac{\upsilon_{\text{SAMPLE}}\ (\text{Hz}) - \upsilon_{H_3PO_4}(\text{Hz})}{\text{Spectrometer Frequency (MHz)}}$$

The relationship between field and frequency given in (XIII) indicates that NMR spectra can be obtained either by varying the field strength at fixed frequency (*field sweep*) or by varying the frequency at fixed field (*frequency sweep*). The latter method is more commonly employed in practice. In $^{31}P_{NMR}$ signals appearing at higher field (field sweep) or lower frequency (frequency sweep) are given positive (δ) values (the reverse convention is used in $^{1}H_{NMR}$).

The ^{31}P nucleus is the only stable isotope of phosphorus (i.e. it occurs in 100% abundance) and although its magnetic moment is only 6.7 % that of ^{1}H, its suitability for NMR studies remains high. Peak overlap is rare because of the wide range over which ^{31}P (δ) values are observed (~ - 250 to + 500 ppm), with typical line widths of ~ 0.7 Hz [167]. The signal to noise ratio is further improved by spinning sample tubes (to increase field homogeneity), increasing the tube diameter to 13 mm and the use of spin-decoupling techniques, which collapse even highly coupled signals to a single sharp peak. The signal of a $^{31}P_{NMR}$ nucleus having *n* equivalent near-neighbours with I = 1/2, is split into a multiplet having *(n + 1)* peaks, (i.e. the *n* nuclei can couple in *n + 1* ways to alter the effective field). Spin decoupling collapses the multiplet by irradiating the *n* nuclei with a second, much stronger beam that results in their 'flipping' so rapidly as to appear to have a single average alignment.

All of the $^{31}P_{NMR}$ spectra in the current study were spin-decoupled for ^{13}C and ^{1}H nuclei.

4.4.2.1 Measurement of $^{31}P_{NMR}$ spectra

The $^{31}P_{NMR}$ spectra were recorded by the staff of the University of London NMR service, based at Kings College, to whom the author's thanks are due.

Two 'Bruker' NMR spectrometers were used. The machines used were of the frequency sweep type. In the early stages of the project, a fixed field of 90 MHz was used. For these measurements a comparatively large sample (~ 150 mg) was dissolved in deuterated chloroform ($CDCl_3$, 2 1/2 ml). Solubility problems occasionally arose and a few drops of deuterated di-methyl sulphoxide [$(D_3C)_2S = O$] were added to improve solubility. Later in the project a 250 MHz machine was used. This machine will record spectra from as little as

a few mgs in 2 1/2 ml of solvent.

The information available from $^{31}P_{NMR}$ was detailed in § 3.8.1.1. Examples of the spectra obtained are given in section 4.5. A more comprehensive discussion of the principles and practice of $^{31}P_{NMR}$, together with chemical shift (δ) data for a wide range of phosphorus compounds, can be found in [168].

4.4.3 Elemental analysis

Elemental analyses of products were carried out by the staff of the micro-analytical laboratory, Imperial Collage, to whom the author's thanks are due. Analysis for phosphorus could not be carried out, but the C, H and N analyses available provided an adequate guide to product purity.

4.4.3.1 Technique

Carbon, hydrogen and nitrogen were simultaneously analysed in a Carlo Erba automatic gas chromatographic microanalyser. This functions as follows. A pre-weighed quantity of product (typically 0.6 - 1 mg $\pm$ 0.1 μg) is sealed in a tin-foil carrier. Flash combustion (at 1050 $\pm$ 10^{o} C) is carried out in a stream of helium / oxygen, complete combustion is ensured by passing the gas over a layer of chromium oxide / cobaltic oxide-silver. This results in a mixture of water, carbon dioxide, nitrogen and nitrogen oxides. The gas mixture then passes through a 'reduction tube' containing metallic copper at 650^{o} C. This reduces nitrogen oxides to nitrogen and retains excess oxygen. The component gases are separated on the chromatographic column and detected using a hot-wire detector or *katharometer*. This estimates the quantity of a gas present from its thermal conductivity, by comparison with values obtained for a standard reference sample. The detector produces a signal in which the area is proportional to the quantity of product present (the signal is electronically integrated and the component percentages are printed out).

4.4.4 Single parameter measurements

Single parameter measurements can be useful in determining the nature and purity of reaction products. Of particular use are boiling point / pressure data and refractive indices

(RI), see § 4.3.1.2 for example.

The RI is defined as the ratio of the speed of light in free space to that in the medium. In this study RI's were determined using an 'Abbe 60' refractometer, at room temperature. The refractive index drops with increasing temperature, but standard samples measured at an ambient temperature of 22° C were indistinguishable from those in the literature. Literature values are usually denoted η^{20}_{D} as they are measured using a sodium 'd' line at 20° C. As well as being useful in determining purity, the measurement of RI is important in the interferometric determination of oil-film thickness (see chapter five).

4.5 Characterisation of organophosphorus esters and ester derivatives

The techniques discussed in the previous section were applied to the synthetic products. The following section details the various analyses for each group of products and briefly discusses the results in terms of product purity.

4.5.1 Di-alkyl acid phosphates - $(RO)_2(HO)P(O)$

Table 4.4 summarises the RI, $^{31}P_{NMR}$ peak position (ppm) and elemental analysis data obtained. Figure 4.5 shows a typical $^{31}P_{NMR}$ spectrum. In this case the product is $(2\text{-Et-HexO})_2(HO)P(O)$, run as described previously on a Bruker 250 MHz machine.

.52 21* SPEC. NO. 28463

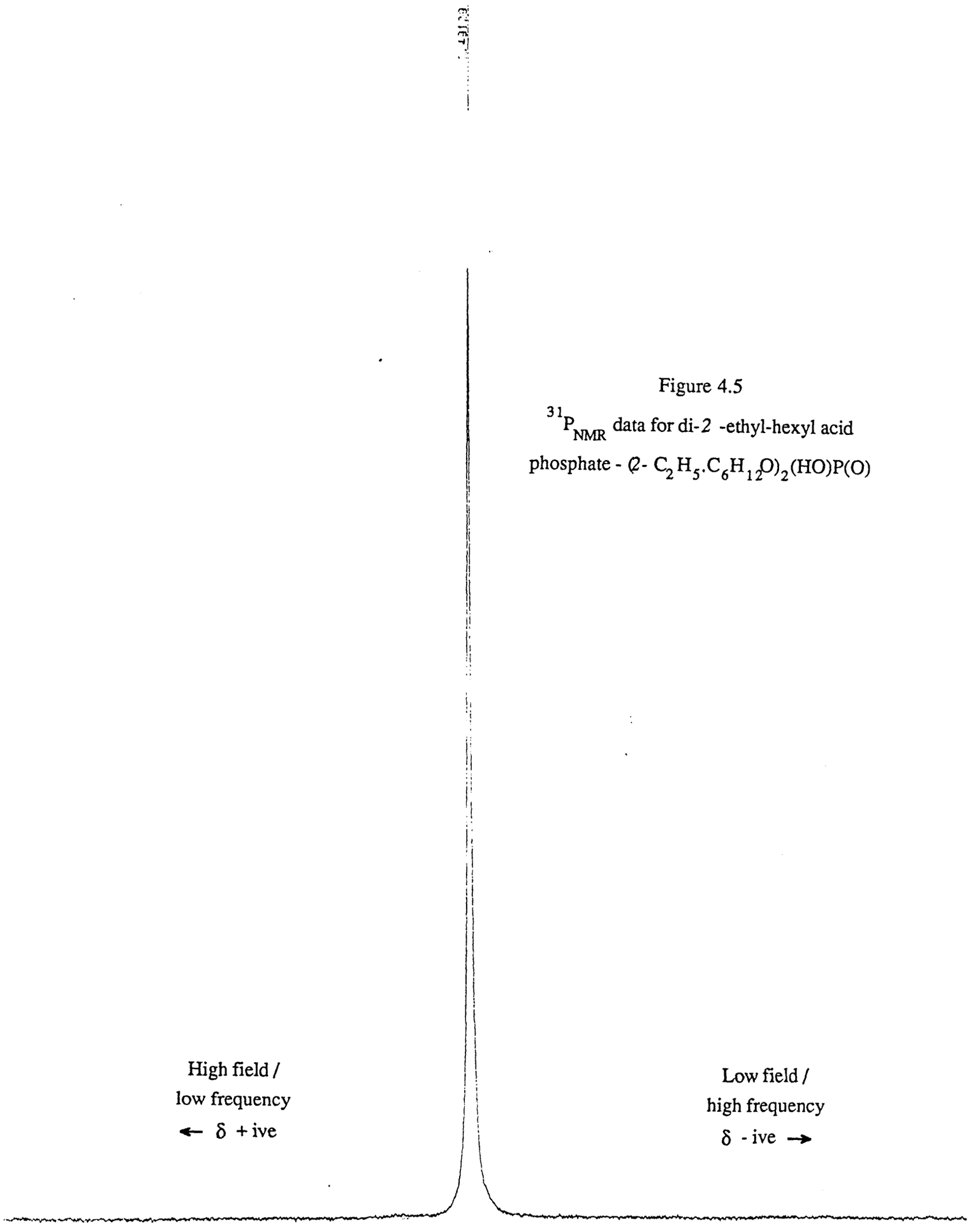


Figure 4.5

$^{31}P_{NMR}$ data for di-*2* -ethyl-hexyl acid phosphate - $(2\text{-}\ C_2H_5.C_6H_{12}O)_2(HO)P(O)$

			ELEMENTAL ANALYSIS			
$(RO)_2(HO)P(O)$	R.I	$^{31}P_{NMR}$	% C_P	% C_A	% H_P	% H_A
R = Methyl	1.4082	3.0834	19.04	20.15	5.55	5.73
Butyl	1.4258	1.8556	45.71	44.50	9.05	9.20
2-Et-Hexyl	1.4410	2.4912	59.62	59.88	10.87	11.07
Octyl	1.4405	2.4061	59.62	59.91	10.87	11.28
Dodecyl	-	2.1499	66.36	66.24	11.75	12.19

Subscripts : P - predicted, A - actual

Table 4.4 R.I, $^{31}P_{NMR}$ and elemental analysis data for di-alkyl acid phosphates

Infra red spectra of the various products are shown in figures 4.6 - 4.10. Table 4.5 summarises the group frequency correlations taken from the figures.

	Group frequency / cm^{-1}		
$(RO)_2(HO)P(O)$	P = O	P - O - C	P (O) H
R = Methyl	~ 1220	1046, -	1699
Butyl	1234	1032, ~1070	1684
2-Et-Hexyl	1228	1032, -	1698
Octyl	1230	1035, -	1699
Dodecyl	1215	1030, 1067	~ 1680

Table 4.5 Main group frequency correlations for di-alkyl acid phosphates - $(RO)_2(HO)P(O)$

The various analyses, in particular the single $^{31}P_{NMR}$ peak observed and the good correlation between predicted and determined carbon and hydrogen contents, suggest a high degree of purity for all di-alkyl acid phosphates.

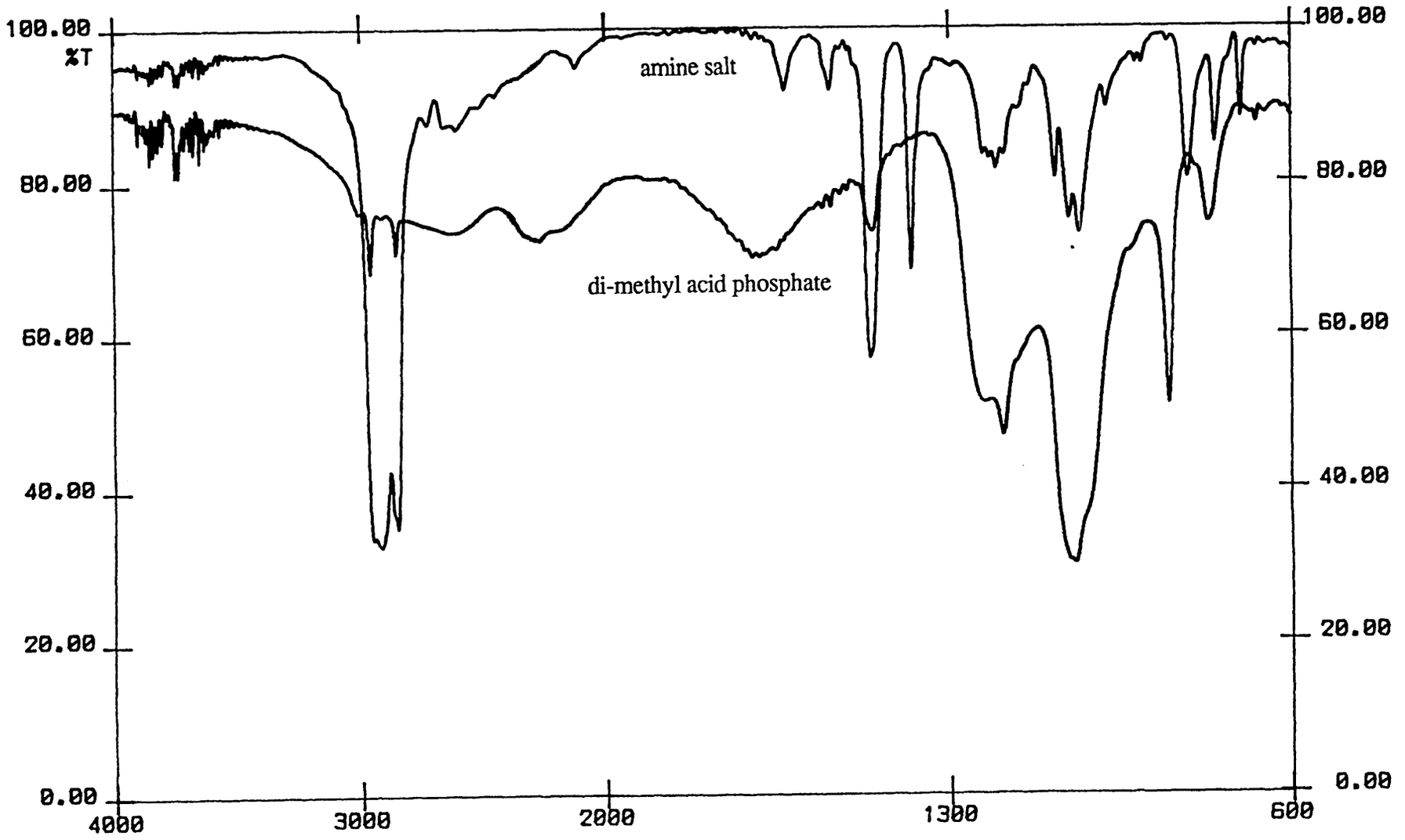


Figure 4.6 Infra-red spectra of di-methyl acid phosphate and benzyl amine salt

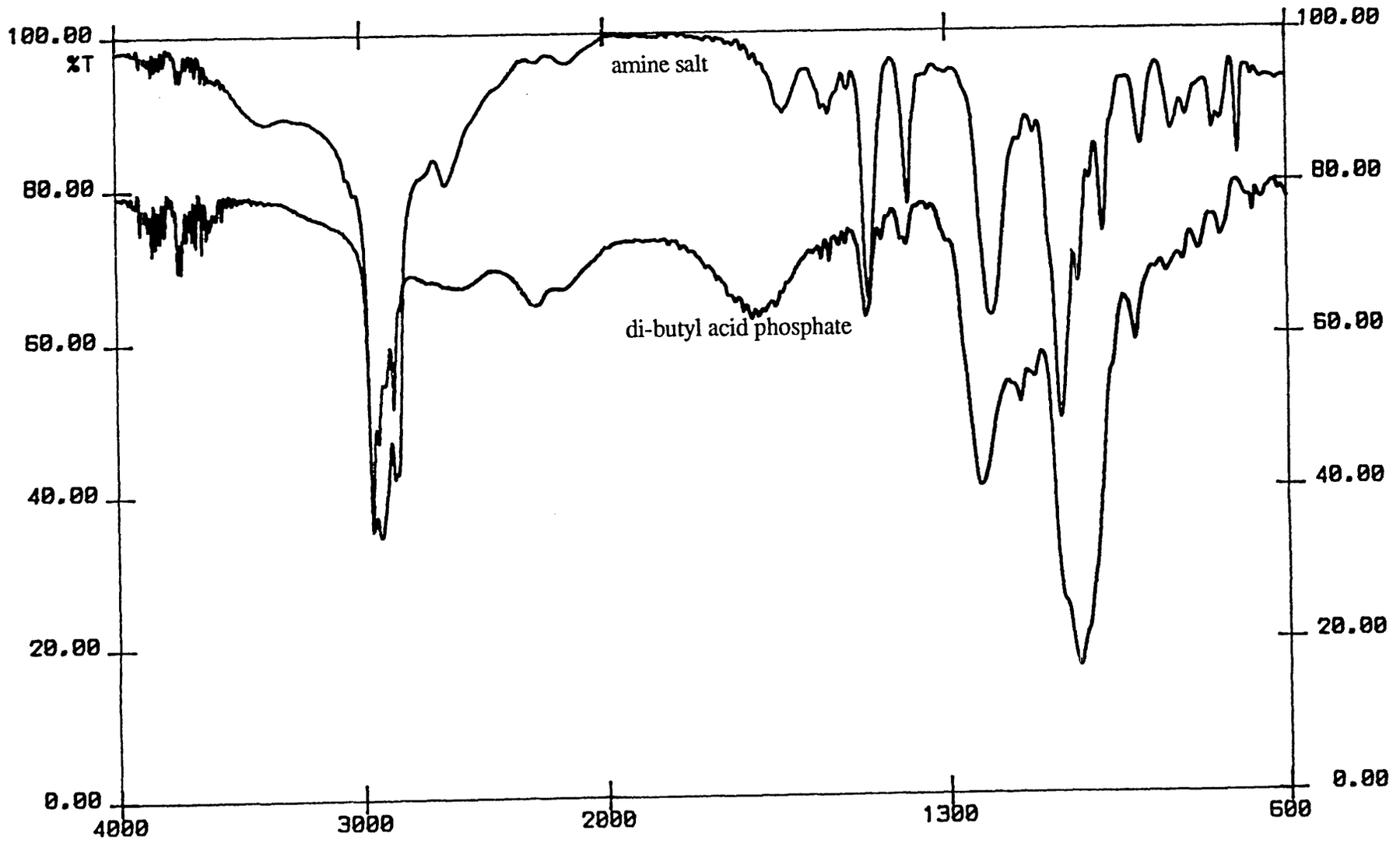


Figure 4.7 Infra-red spectra of di-butyl acid phosphate and benzyl amine salt

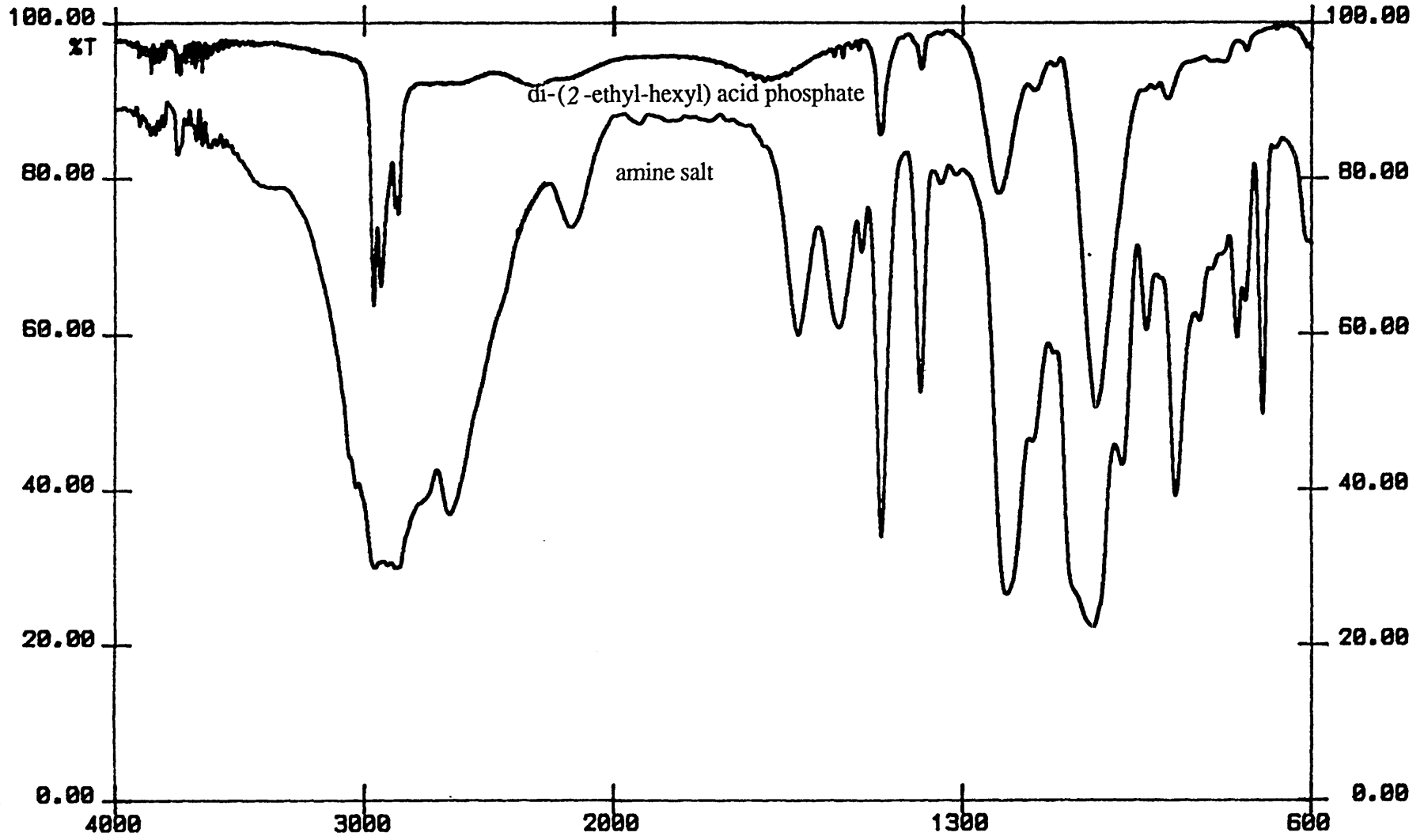


Figure 4.8 Infra-red spectra of di-(2 -ethyl-hexyl) acid phosphate and benzyl amine salt

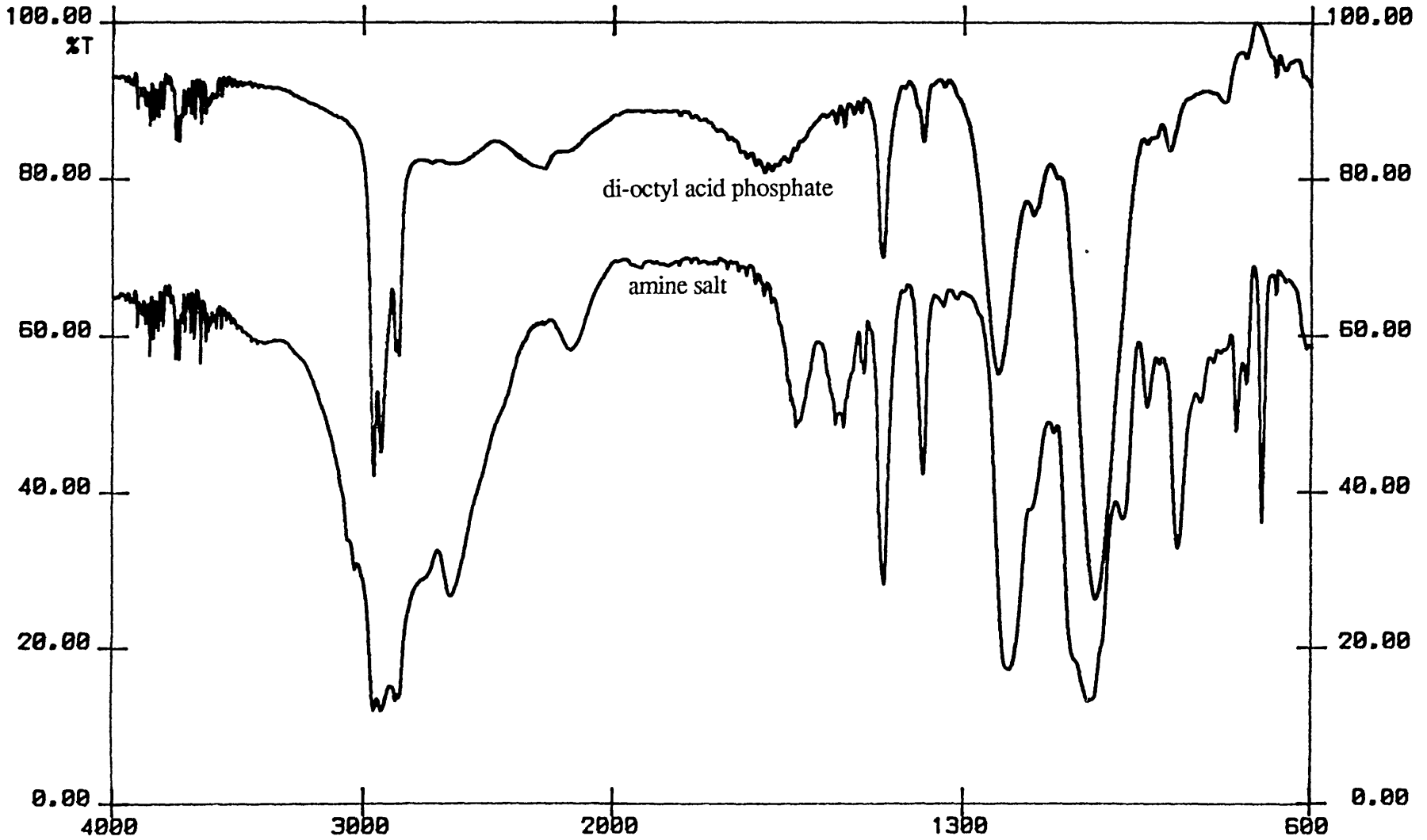


Figure 4.9 Infra-red spectra of di-octyl acid phosphate and benzyl amine salt

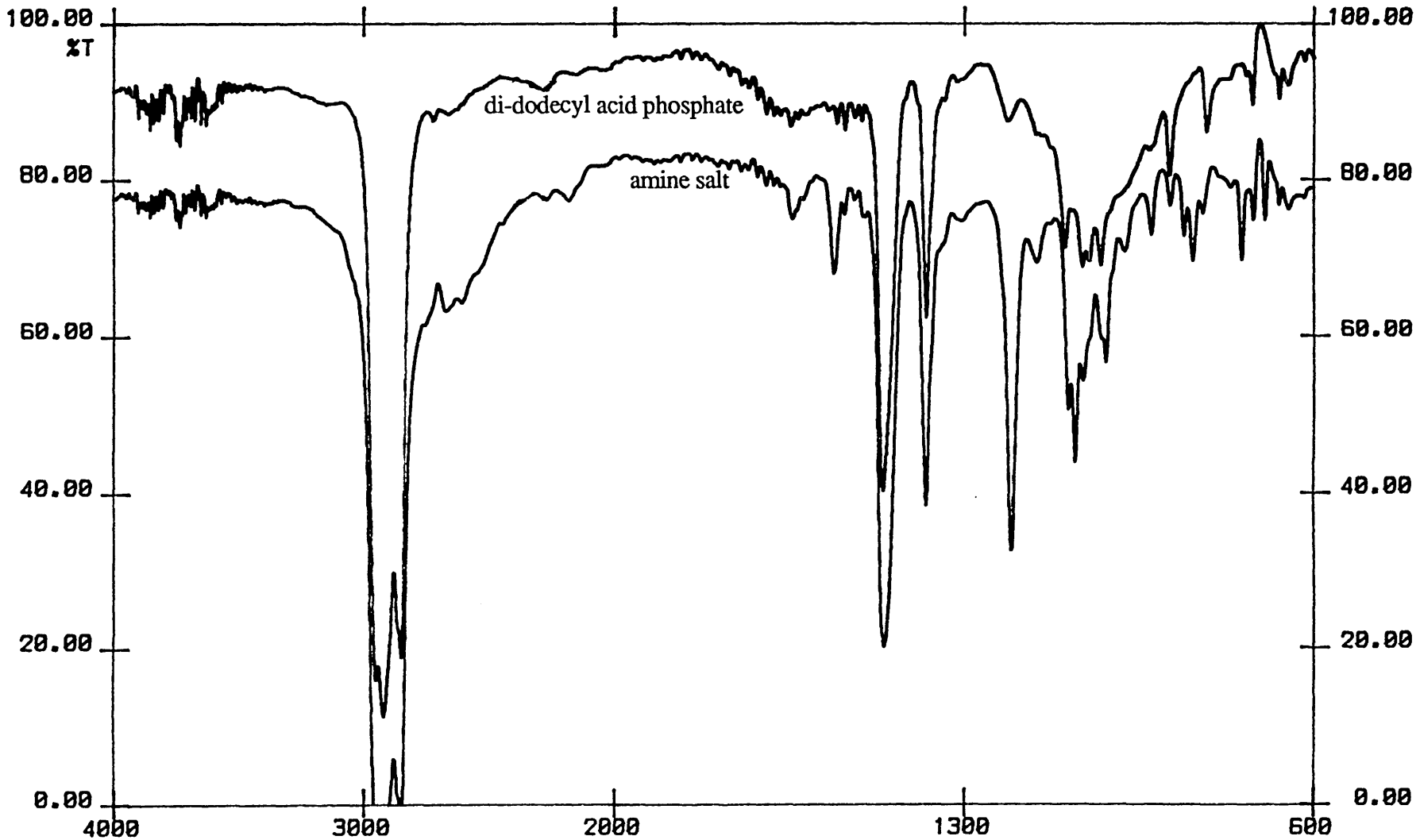


Figure 4.10 Infra-red spectra of di-dodecyl acid phosphate and benzyl amine salt

4.5.2 Benzyl amine salts of di-alkyl acid phosphates - $(C_6H_5.CH_2NH_3O)(RO)_2P(O)$

Table 4.6 summarises the $^{31}P_{NMR}$ peak positions (ppm) and elemental analyses data for this group of compounds. Figure 4.11 shows a typical $^{31}P_{NMR}$ spectrum, in this case for the benzyl amine salt of di-(2-ethyl-hexyl) acid phosphate.

		ELEMENTAL ANALYSIS					
		% C		% H		% N	
$(R'NH_3O)(RO)_2P(O)$	$^{31}P_{NMR}$	P	A	P	A	P	A
R = Methyl	2.8773	46.35	46.33	6.44	6.74	6.01	6.18
Butyl	0.9599	56.78	54.80	8.52	9.08	4.42	4.00
2-Et-Hexyl	1.3367	64.34	62.68	10.02	10.31	3.26	3.39
Octyl	1.4108	64.34	62.58	10.02	10.42	3.26	3.79
Dodecyl	0.9531	70.06	68.33	11.11	11.57	2.64	2.35

Subscripts : P - predicted, A- actual

R' - $C_6H_5.CH_2$

Table 4.6 $^{31}P_{NMR}$ and elemental analysis data for benzyl amine salts of di-alkyl acid phosphate

Table 4.7 lists the main group frequency correlations for these compounds, taken from IR spectra recorded for each compound (figures 4.6 - 4.10). IR spectra for pure benzyl amine and pure octadecylamine are shown in figure 4.12. The spectra of the pure amines are shown, so that comparisons can be made between the amine salt and the parent compounds.

No group frequency correlations are recorded for the pure amines as these can be found in any of the numerous texts on infra-red or general spectroscopy.

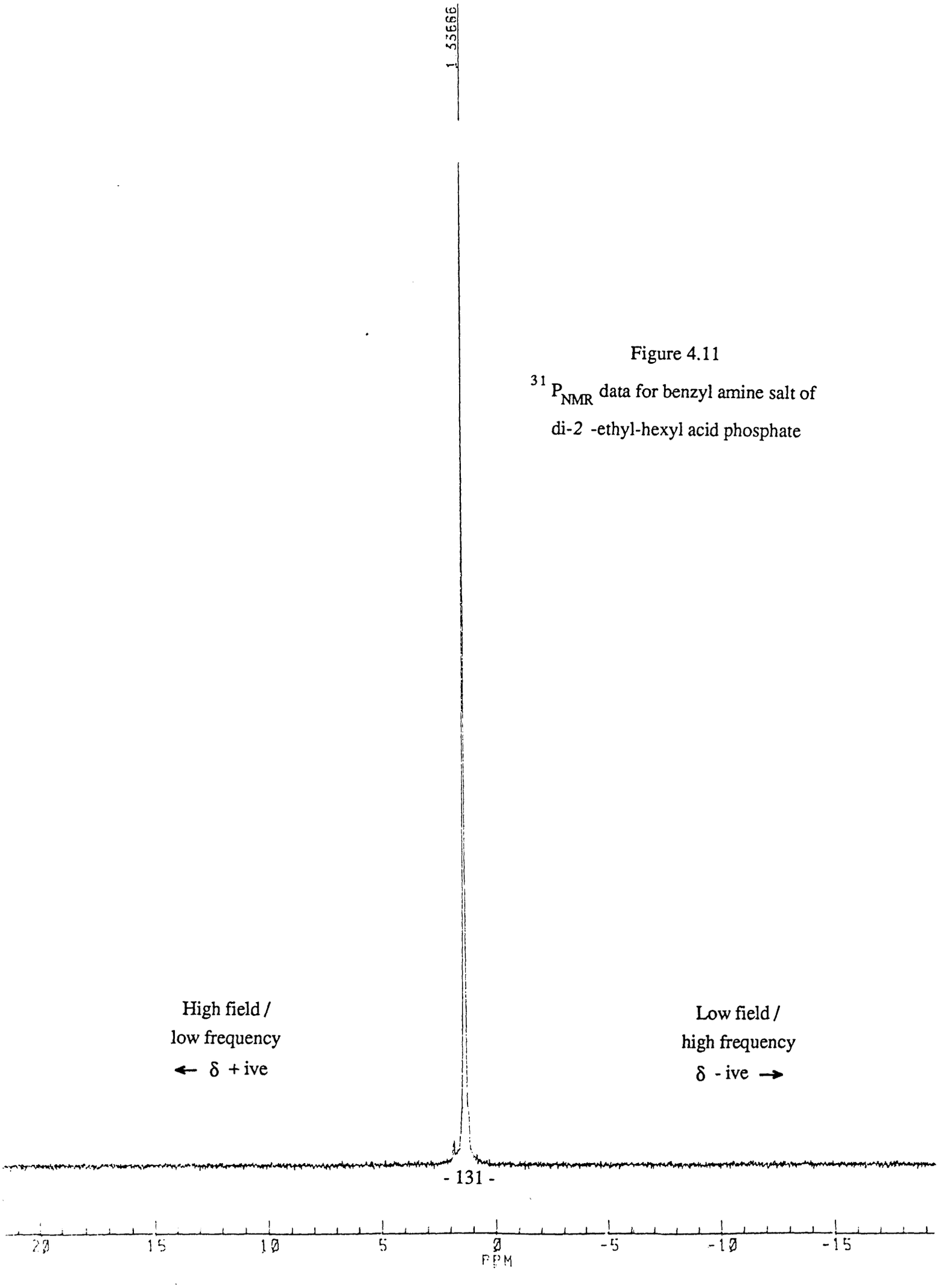


Figure 4.11

$^{31}P_{NMR}$ data for benzyl amine salt of di-2 -ethyl-hexyl acid phosphate

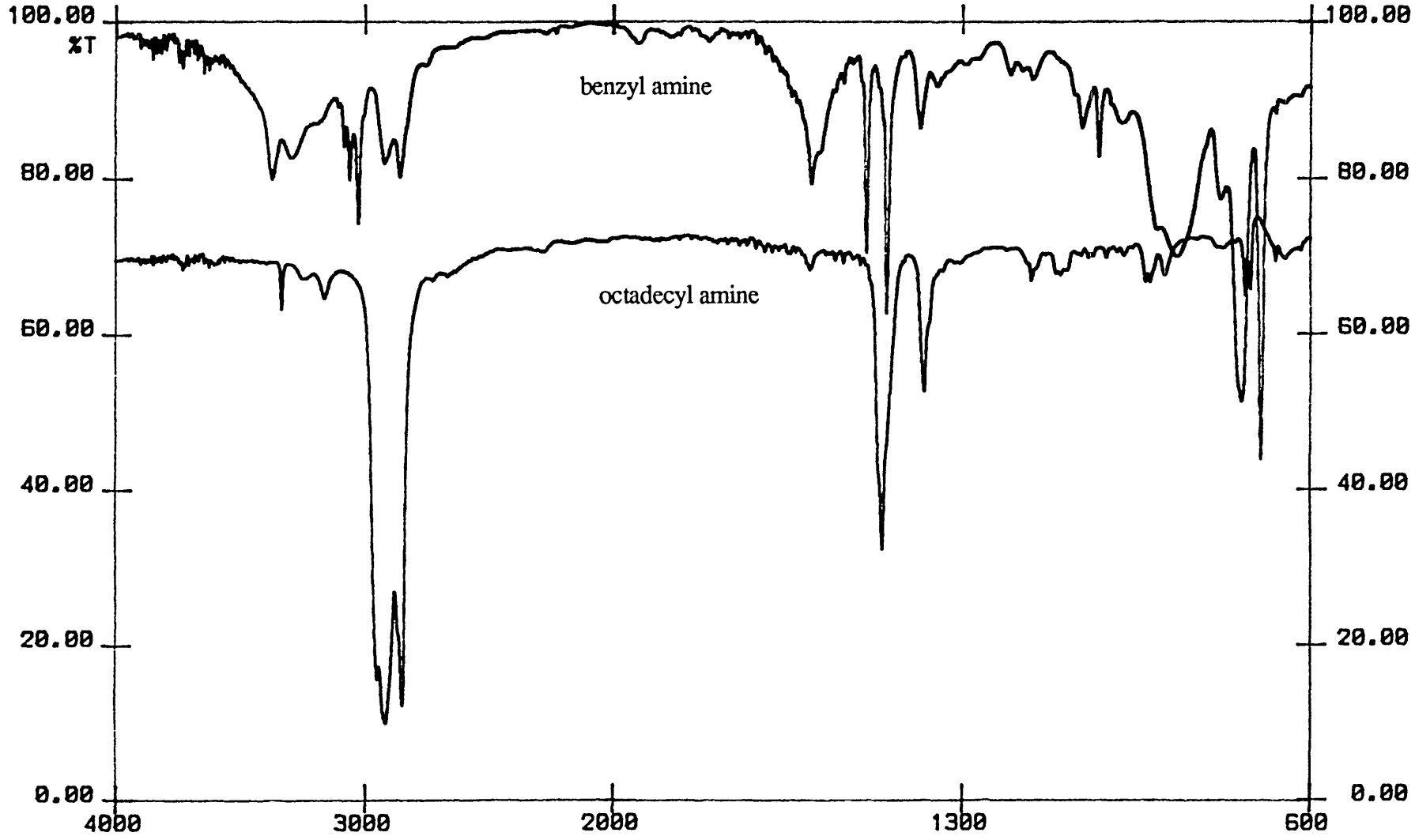


Figure 4.12 Infra-red spectra of benzyl amine and octadecyl amine

	Group frequency / cm^{-1}	
$(R'NH_3O)(RO)_2P(O)$	P = O	P - O - C
R = Methyl	~ 1204	1035, ~ 1084
Butyl	1208	~ 1005, ~1067
2-Et-Hexyl	1212	~ 1038, -
Octyl	1208	- , 1049
Dodecyl	1207	1013, 1065

R' - $C_6H_5.CH_2$

Table 4.7 Main group frequency correlations for benzyl amine salts of di-alkyl acid phosphates - $(C_6H_5.CH_2NH_3O)(RO)_2P(O)$

The conclusions with respect to purity, for these compounds, are very similar to those of the parent di-alkyl acid phosphates. A high degree of purity was observed throughout.

4.5.3 Di-alkyl phosphonates - $(RO)_2P(O)H$

As explained in § 4.3.1, a number of di-alkyl phosphonates were prepared or purified from existing products, during the course of this work. Comparisons of infra-red spectra recorded for synthesised products and those prepared for used in [76] - for which a purity exceeding 99% is reported - showed no observable differences. For this reason no further analyses were carried out.

As explained previously, a number of di-alkyl phosphonates became commercially available during the course of this work. The purification of existing di-hexyl phosphonate and the subsequent IR and RI analyses suggested that hydrolytic break-down occurred over time. For this reason the IR spectra of phosphonates obtained commercially were recorded prior to use. These were invariably alcohol-free, suggesting little hydrolytic break-down, but where alcohol was present in the IR spectrum the materials were purified or replaced with a new batch.

4.5.4 Mono-alkyl phosphonates - (RO)(HO)P(O)H

The refractive index and elemental analysis data for mono-alkyl phosphonates are given in table 4.8

		ELEMENTAL ANALYSIS			
(RO)(HO)P(O)H	R.I	% C_P	% C_A	% H_P	% H_A
R = Butyl	1.4265	34.78	36.43	7.79	8.42
Hexyl	1.4340	43.37	43.97	9.03	9.42
2-Et-Hexyl	1.4410	49.48	51.55	9.75	10.34
Octyl	1.4398	49.48	47.45	9.75	10.07
Dodecyl	1.4476	57.60	56.36	10.80	11.07
Octadecyl	-	64.67	64.68	11.68	12.15

Subscripts : P- predicted, A- actual

Table 4.8 R.I and elemental analysis data for mono-alkyl phosphonates

The elemental analyses suggested a limited product purity. This was confirmed by the $^{31}P_{NMR}$ data given in table 4.9.

The main IR group frequency correlations are given in table 4.10. As well as the peaks included in the table two further broad, ill-defined peaks can be seen at ~ 2600 and ~ 2340 cm^{-1}. These are due to P(O)OH.

(RO)(HO)P(O)H	1st peak (ppm)	Area	2nd peak (ppm)	Area	3rd peak (ppm)	Area	Relative Intensity
R = Butyl	9.093	22.01	8.476	9.00	-	-	2.5 : 1
Hexyl	9.235	22.00	8.710	3.00	8.489	6.01	7.3 : 1 : 2
2-Et-Hexyl	9.572	23.01	8.925	7.39	-	-	3.1 : 1
Octyl	9.203	22.05	8.703	3.19	8.476	5.56	6.9 : 1 : 1.7
Dodecyl	9.492	22.02	9.073	2.29	8.489	6.66	9.6 : 1 : 2.9
Octadecyl	9.604	22.02	9.376	3.23	8.507	0.632	34.8 : 5.1 : 1

Table 4.9 $^{31}P_{NMR}$ data for mono-alkyl phosphonates

Table 4.9 shows the existence of an additional one or two peaks per spectrum. Each peak represents a separate product and the relative peak-areas are proportional to the relative quantities of products present. The relative intensity of the major peak, which the elemental analyses suggest is mono-alkyl phosphonate, increases with alkyl chain length. In the butyl version the desired product accounts for approximately 2/5 of total, in the octadecyl version it accounts for approximately 5/6 of total. The $^{31}P_{NMR}$ spectra were re-recorded after approximately 1 year and the product ratios were almost unchanged. Brief attempts were made to identify the impurities. The synthetic procedure employed suggested unreacted phosphonic acid [$(HO)_2P(O)H$] or di-substituted phosphonates, as likely contaminants. A $^{31}P_{NMR}$ spectrum recorded for the largely insoluble phosphonic acid gave a single peak at (δ) = + 2.6614 ppm. A 50 : 50 mixture by weight of phosphonic acid and mono-(2-ethyl hexyl) phosphonate gave an additional peak and shifted the peaks already present. In pure form di-alkyl phosphonates have (δ) ~ 7.6 to 7.9 [76]. A 50 : 50 mixture by weight of mono and di-octyl phosphonate gave overlapping sharp peaks at (δ) = 6.2975 (broad) and ~ 0.0708 (sharp, close to that of H_3PO_4). No further attempts were made to identify the impurities present. Attempts to purify the products proved unsuccessful (§ 4.3.2). A representative $^{31}P_{NMR}$ spectrum is given in figure 4.13, this is for mono-(2-ethyl-hexyl) phosphonate. IR spectra for this group of compounds are included with those of the amine salts in figures 4.15 - 4.19. Group frequency correlations are given in table 4.10.

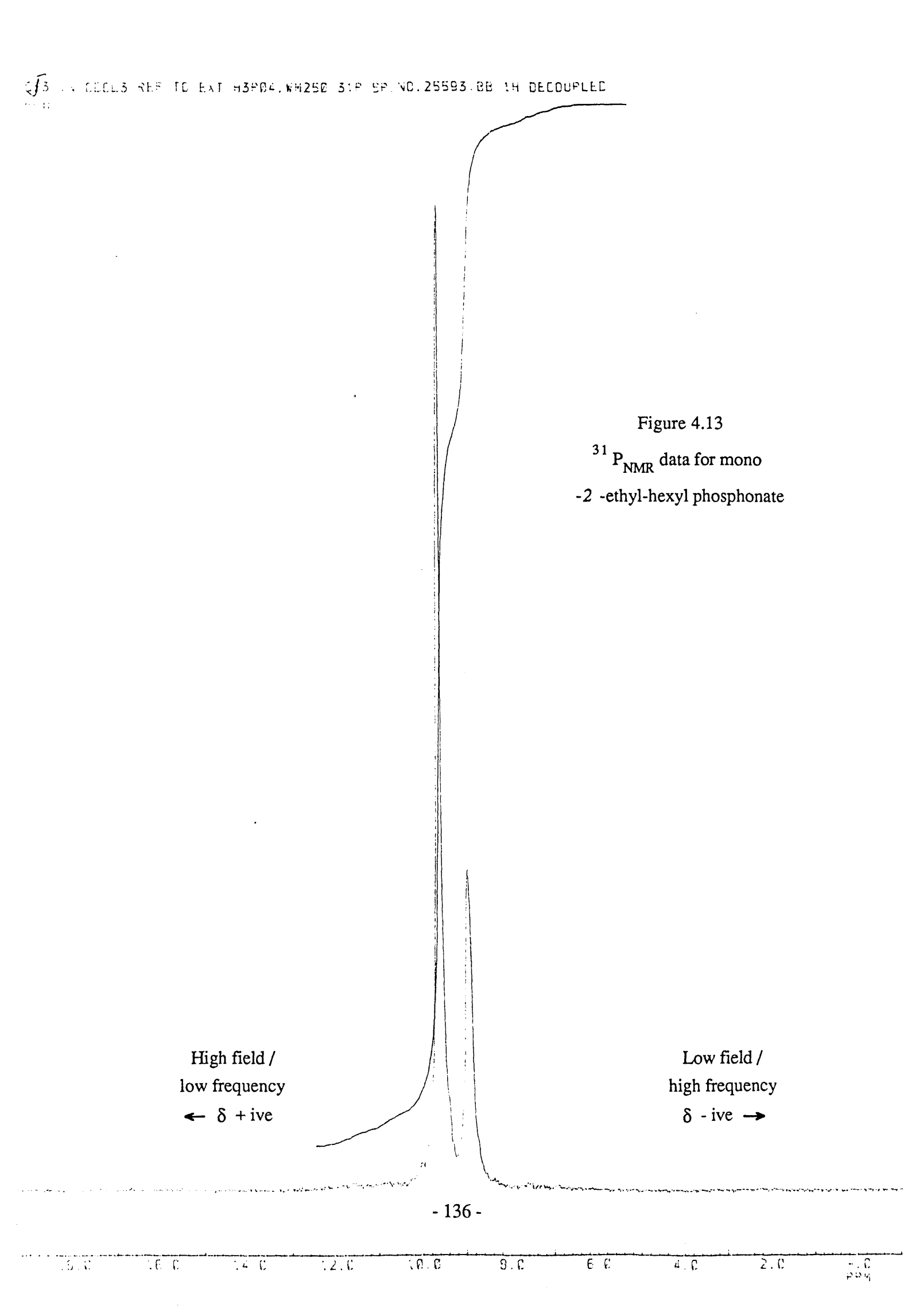


Figure 4.13

$^{31}P_{NMR}$ data for mono

-2 -ethyl-hexyl phosphonate

	Group frequency / cm^{-1}			
(RO)(HO)P(O)H	P = O	P - H	P - O - C	P (O) H
R = Butyl	1224	2432	1008, 1062	1654
Hexyl	1225	2433	1009, ~ 1065	1653
2-Et-Hexyl	1226	2433	1009, 1070	1651
Octyl	1224	2433	1006, ~ 1070	1651
Dodecyl	1227	2436	1006, 1081	1650

Table 4.10 Main group frequency correlations for mono-alkyl phosphonates - (RO)(HO)P(O)H

The synthetic procedure used to produce mono-alkyl phosphonates in the current work evidently suffers from the same problems as the other procedures reviewed in § 3.6.3, namely the preparation of mixed products. However, the total yield and the proportion of the desired product is high and as described in the next section, preparation of the amine salts can further improve this.

4.5.5 Octadecylamine salts of mono-alkyl phosphonates $[CH_3(CH_2)_{17}NH_3O](RO)P(O)H]$

The $^{31}P_{NMR}$ and elemental analysis data for this group of compounds is given in table 4.11. The $^{31}P_{NMR}$ spectra show a single additional peak for butyl, hexyl and (2-ethyl-hexyl) versions, and two extra peaks for octyl and dodecyl versions. No relative peak intensity data was available, but the relative intensity of the major product peak was much improved. This can be seen by comparing the $^{31}P_{NMR}$ spectra for octadecylammonium (2-ethyl-hexyl) phosphonate (figure 4.14), with that of the corresponding mono-phosphonate (figure 4.13). In table 4.11, only the chemical shift of the major product peak is included.

		ELEMENTAL ANALYSIS					
		% C		% H		% N	
$(R'NH_3O)(RO)P(O)H$	$^{31}P_{NMR}$	P	A	P	A	P	A
R = Butyl	5.0162	64.86	63.91	12.28	12.76	3.44	3.77
Hexyl	5.3527	66.21	64.56	12.41	12.74	3.22	2.99
2-Et-Hexyl	5.8718	67.39	66.85	12.53	13.00	3.02	3.97
Octyl	5.6537	67.39	61.45	12.53	11.91	3.02	2.48
Dodecyl	5.2016	69.36	63.48	12.72	12.40	2.70	2.29

Subscripts : P - predicted, A- actual

R' - $CH_3(CH_2)_{17}$

Table 4.11 $^{31}P_{NMR}$ and elemental analysis data for octadecylamine salts of mono-alkyl phosphonates

Figures 4.15 - 4.19 show the IR spectra of the mono-alkyl phosphonates, and their octadecylamine salts. The main group frequency correlations are given in table 4.12.

	Group frequency / cm^{-1}		
$(R'NH_3O)(RO)P(O)H$	P = O	P - H	P - O - C
R = Butyl	1210	-	999, -
Hexyl	1214	-	998, -
2-Et-Hexyl	1206	-	994, -
Octyl	1196	2359	998, -
Dodecyl	1196	-	999, -

R' - $CH_3(CH_2)_{17}$

Table 4.12 Main group frequency correlations for octadecylamine salts of mono-alkyl phosphonates - (RO)(HO)P(O)H

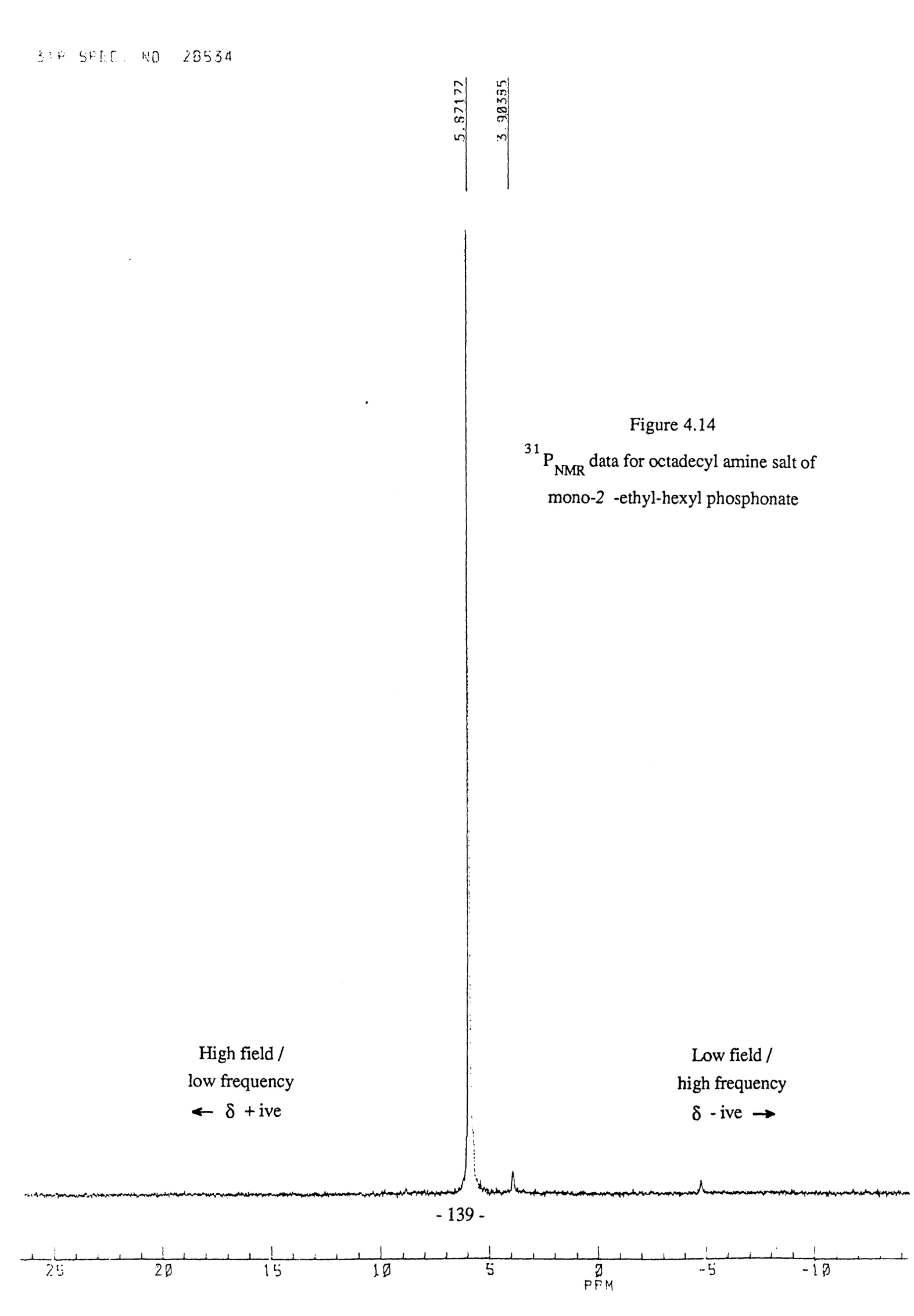


Figure 4.14

$^{31}P_{NMR}$ data for octadecyl amine salt of mono-2 -ethyl-hexyl phosphonate

The elemental analyses suggest a limited product purity as observed with the mono-alkyl phosphonates. However, the number of $^{31}P_{NMR}$ peaks observed and the improved ratio of the major to minor peak-areas suggest an improved purity. The elemental analyses data and the $^{31}P_{NMR}$ data both suggest this improvement deteriorates with increasing alkyl chain length.

In addition to this the infrared spectra of the amine salts continue to show some of the peaks associated with the free acid i.e. the P(O)OH group, which should be absent from the spectrum. The P—H peak ~ 2350 cm^{-1} is masked by the amine in many of the spectra.

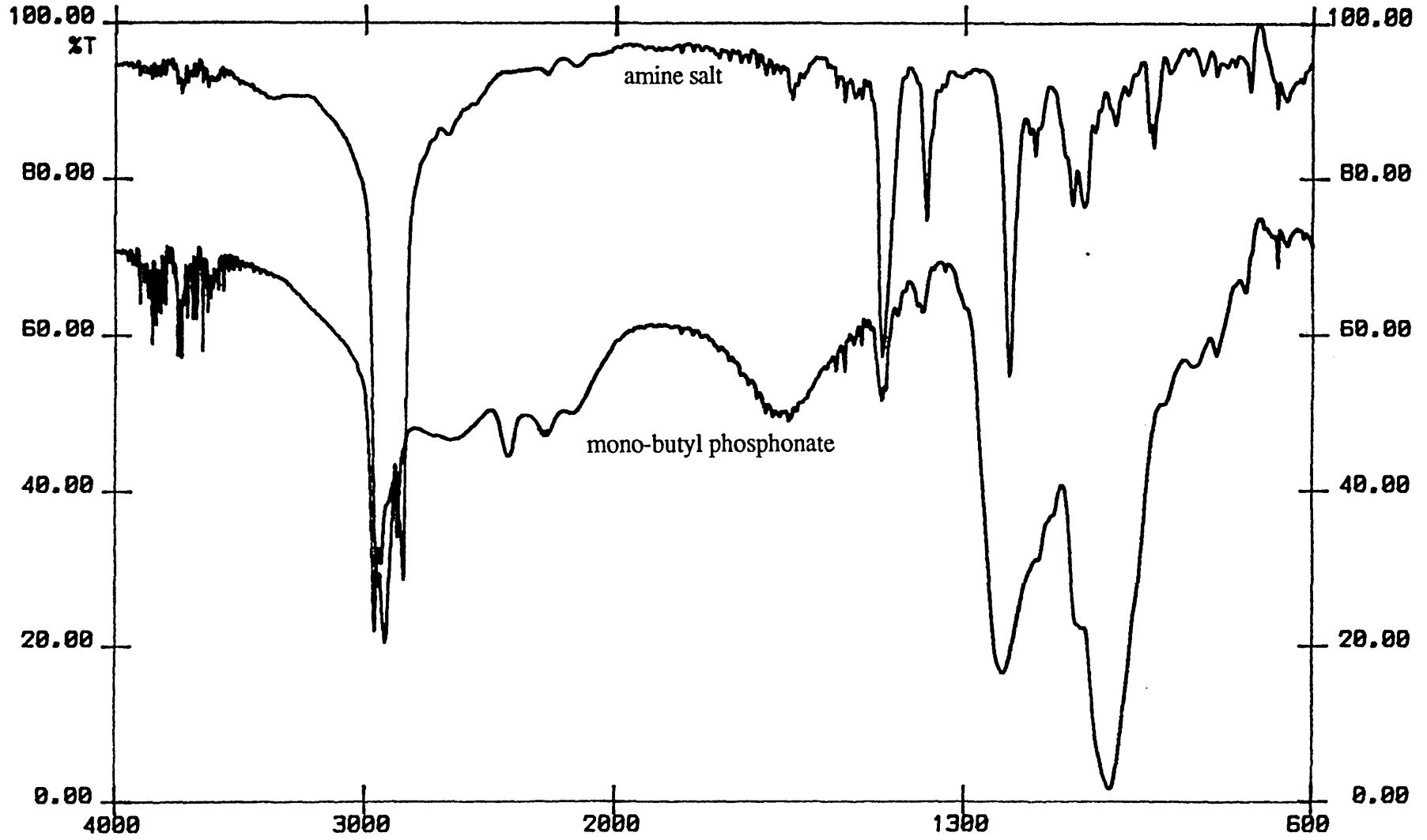


Figure 4.15 Infra-red spectra of mono-butyl phosphonate and octadecylamine salt

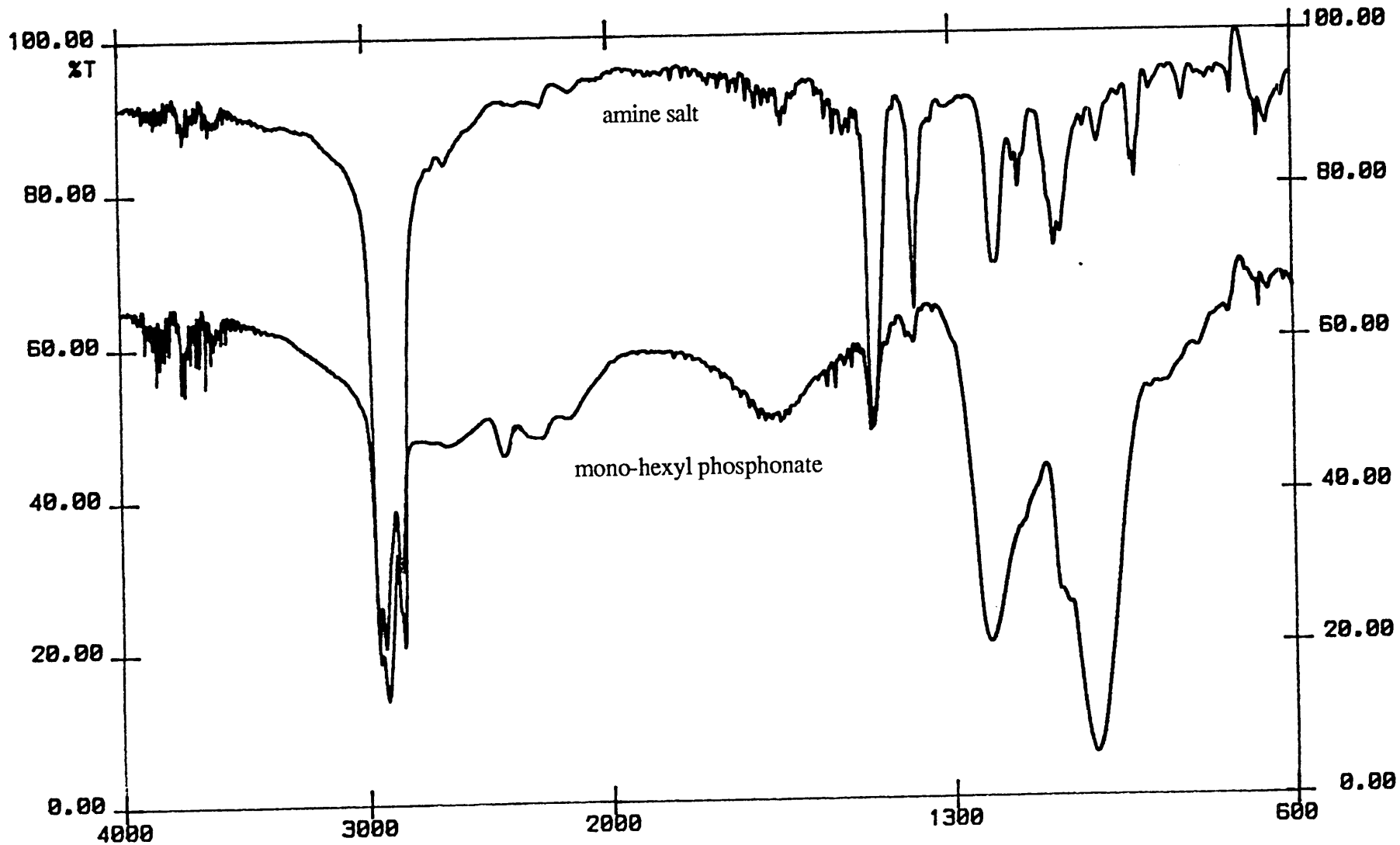


Figure 4.16 Infra-red spectra of mono-hexyl phosphonate and octadecylamine salt

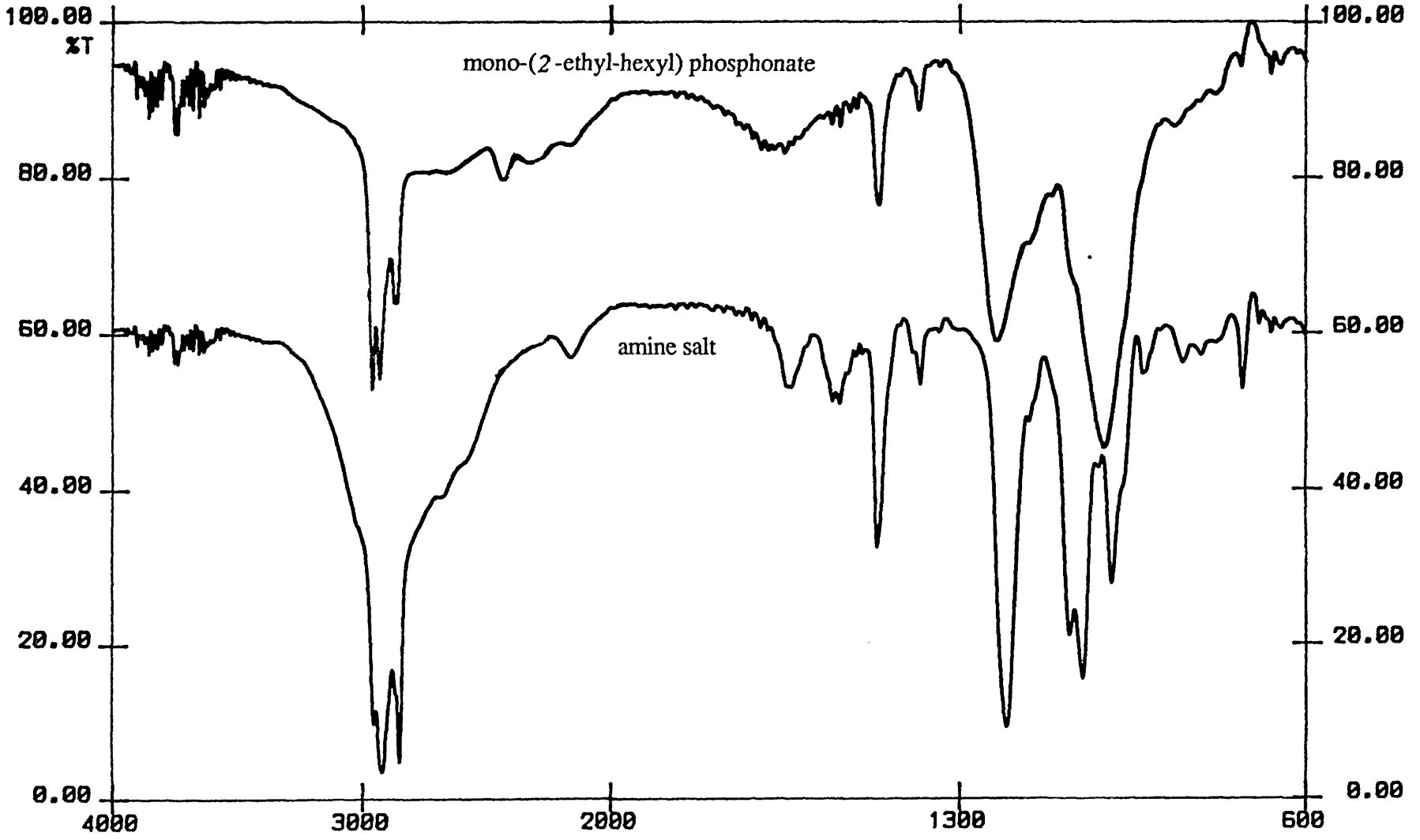


Figure 4.17 Infra-red spectra of mono-(2-ethyl-hexyl) phosphonate and octadecylamine salt

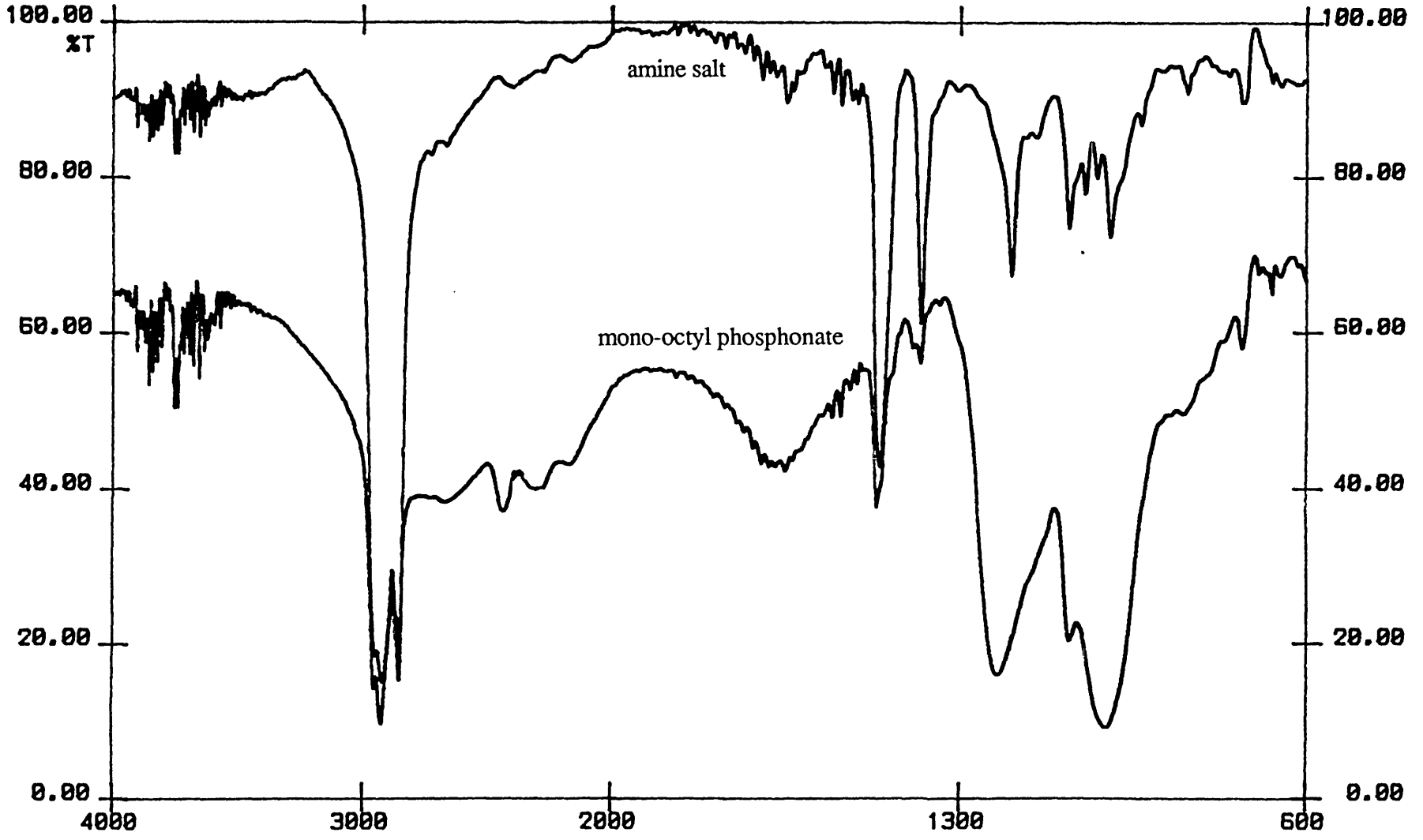


Figure 4.18 Infra-red spectra of mono-octyl phosphonate and octadecylamine salt

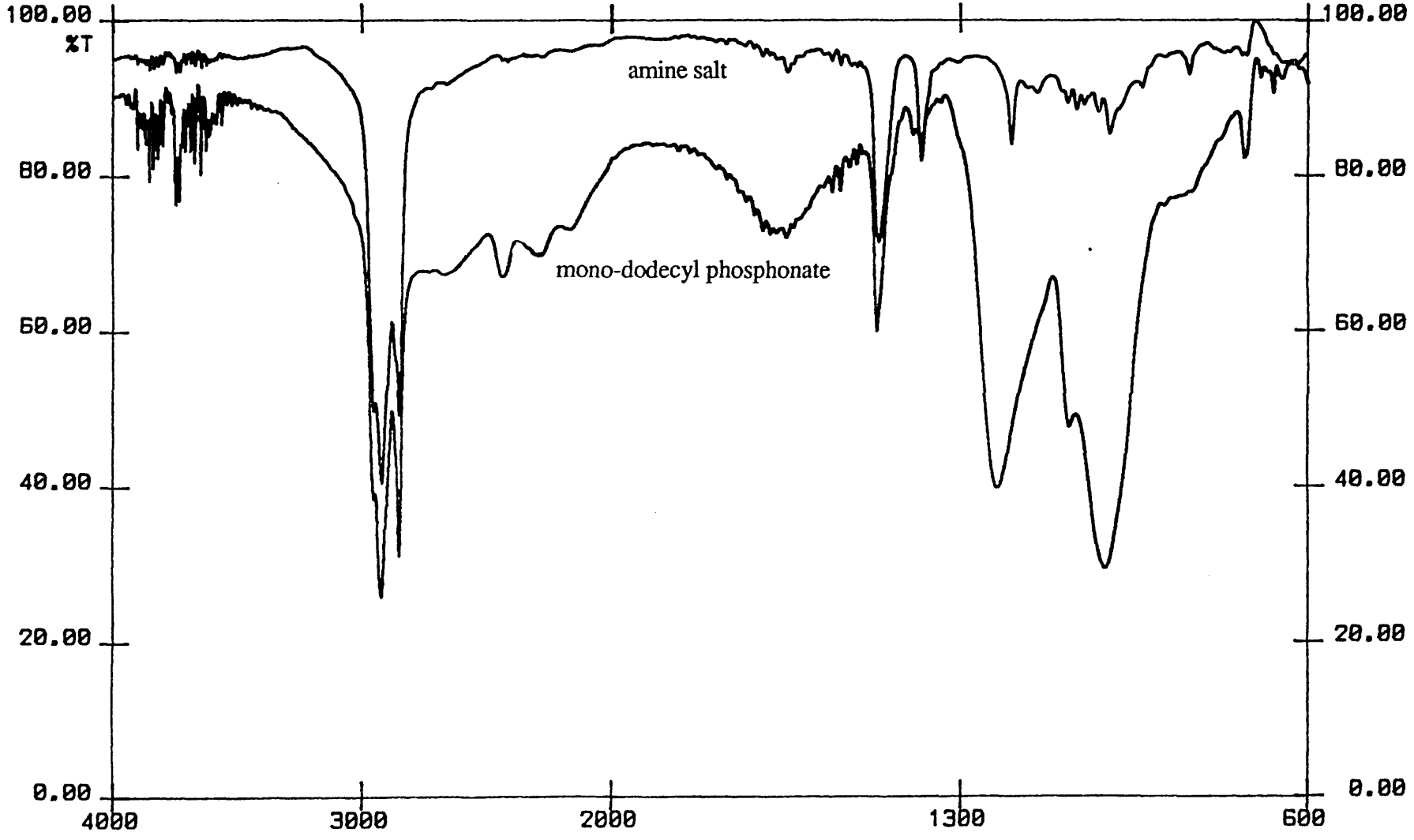


Figure 4.19 Infra-red spectra of mono-dodecyl phosphonate and octadecylamine salt

CHAPTER 5 - EXPERIMENTAL DETAILS OF TEST RIGS USED IN CURRENT STUDY. DESIGN, CALIBRATION AND COMMISIONING TESTS.

5.1 Introduction

The following chapter describes the test rigs that were used in the current study, to follow the build-up of reacted layers in operating contacts. It is apparent that the methods chosen to follow film build-up are largely dictated by the lubrication regime under consideration (i.e. the operating Λ value). The test rigs described in this chapter were used to monitor film-formation in a range of circumstances from fully separated EHD contacts - through a mixed regime - to boundary lubricated contacts. Wherever possible the film-formation was followed 'in lubro,' that is within the operating contact. Much of the work in the literature has relied upon the retrospective use of surface analytical techniques, to imply the presence of reacted layers during running. The heavy solvent cleaning required by most of these techniques [178] will lead to the corruption or removal of much of the material that contributes towards separation of the operating surfaces. The 'in lubro' approach is discussed in more detail in § 7.1.

In the past a number of complimentary techniques have been used to measure the thickness of oil films / reacted layers directly, within operating contacts. Thick hydrodynamic or elastohydrodynamic films are will suited to direct mechanical measurement, for example by using strain gauges [189] or spring dynamometers [190]. X-rays have also produced film thickness measurements that agree well with theory [191]. Two electrical techniques have proven useful - capacitance measurements [192] and electrical contact resistance measurements [193]. The latter has also been used as a qualitative measure of the build-up of reacted layers in boundary lubricated contacts. Some of the most elegant measurements of oil film thickness have been achieved by optical examination of the contact. Laser beam diffraction has been used to measure bulk film thickness [194]. Optical interferometry has been used to map the film thickness distribution in an EHD contact [195].

Much of the work described in the current study looks at film build-up under fully separated EHD conditions. The technique of optical interferometry - which was developed in the author's laboratory - was chosen, as the build-up of a reacted layer can be followed directly, in real time. This provides unequivocal evidence of the presence of thick reacted layers and measures their contribution towards the total film separation. However, the conventional interferometric technique is not well-suited to the investigation of thin reacted layers and therefore to the study of boundary lubrication. The wavelength of visible light imposes a minimum observable separation of the order of 130 nm. In addition, the technique requires one of the surfaces to be transparent. In the current study an optically flat glass disc was run against a rolling / sliding steel ball. The conventional interferometric technique was developed, in the course of the current work, in two ways (these are detailed in chapter 8). The developments permitted the measurement of very much thinner films and the continuous measurement of film thicknesses, above the reduced threshold. The conventional technique only permits the measurement of discrete film thicknesses, spaced at a series of predetermined, fixed intervals.

Although development of the interferometric technique reduced the minimum film thickness that could be measured, the technique was still not well-suited for boundary lubrication studies. The glass disc imposed an unrealistic surface roughness and metallurgy on the contact. Because of this, two other rigs were used to investigate the role of additives under conditions of low initial specific film thickness. A high frequency reciprocating (HFR) rig was used in a series of more conventional friction and wear studies. This rig permitted the simultaneous measurement of electrical contact resistance (ECR) which, as discussed above, gives a qualitative measure of reacted film build-up. A limited study of additive behaviour in a disc machine was also undertaken. A capacitance technique was used to monitor film thickness in the disc machine.

The following chapter details the calibration and experimental procedure employed for each of the rigs. Section 5.2 describes the technique of optical interferometry and its use in two elevated temperature EHD rigs. The first of these was 'inherited' by the author, and it is briefly described as it was used in some early test work. The latter EHD rig is dealt with in more detail as it was designed and commissioned by the author, for use in the current work. Sections 5.3 and 5.4 deal with the HFR rig and the disc machine respectively.

5.2 Elevated temperature optical interferometric test rigs

5.2.1 Optical interferometry

The EHD lubrication of a point contact, and the dependence of the film thickness on the prevailing inlet conditions, was described in § 1.4. The technique of optical interferometry is well suited to the investigation of EHD films - typical separations of hundreds or thousands of nanometers are found - as this is of the same order as the wavelength of visible light. The technique of optical interferometry is dealt with in detail in a number of text books [196] - [198]. A particularly good description of the application of the technique to the investigation of lubricant films, is given by Wedeven [199] and by Gentle [200]. The historical development of the technique in tribological applications is reviewed by Jackson [201]. This description includes the use of thin 'spacer-layers' of SiO_2, which were used to reduce the minimum film thickness observable from the limiting value of approximately 130 nm (which is imposed by the wavelength of light). The review also describes the use of transparent materials such as sapphire and diamond (which permit the use of much higher loads).

The operating ball on plate contact has a Hertzian diameter of the order of half a millimeter. As such the contact can be conveniently observed using a x 100 objective / eyepiece combination. However the interferometric process permits measurements of changes of film thickness - in the plane of the contact - of the order of tens of nanometers. It is therefore a very sensitive way to measure oil film thickness. The following section describes the basic technique, the requirements for good fringe visibility and so on, for a simple monochromatic source. The duochromatic and chromatic (white light) systems used in the current study, are then described. Calibration of fringes in terms of separation and of phase changes on reflection are included. The relative advantages and limitations of the various interferometric techniques are briefly discussed. Some improvements to the technique are described in chapter eight.

5.2.1.1 The monochromatic system - basic interferometry

The interferometric system is represented schematically in figure 5.1. The incident light undergoes a *division of amplitude* on reaching the semi-reflecting chromium layer. No width change occurs during this process. The two parts of the beam recombine within the disc; this results in the formation of *interference fringes*. The optical system for observing the fringes is focused at this point. In the case of a ball on plate contact the observed fringes consist of a series of concentric circles or '*Newtons rings*'. In figure 5.1 the angle of incidence (i) has been exaggerated for clarity. In practice the incident beam is very nearly perpendicular to the disc. The normal incidence and the similar refractive indices of glass and oil, ensure that the rays are nearly parallel i.e. that the angles of *incidence* (i) and *refraction* (r) are very similar. The semi-reflecting chromium layer thickness (~ 20 nm) is designed to ensure that the two parts of the beam are of approximately equal intensity, on recombination. The reflectivity / absorbance characteristics of the ball are essentially fixed.

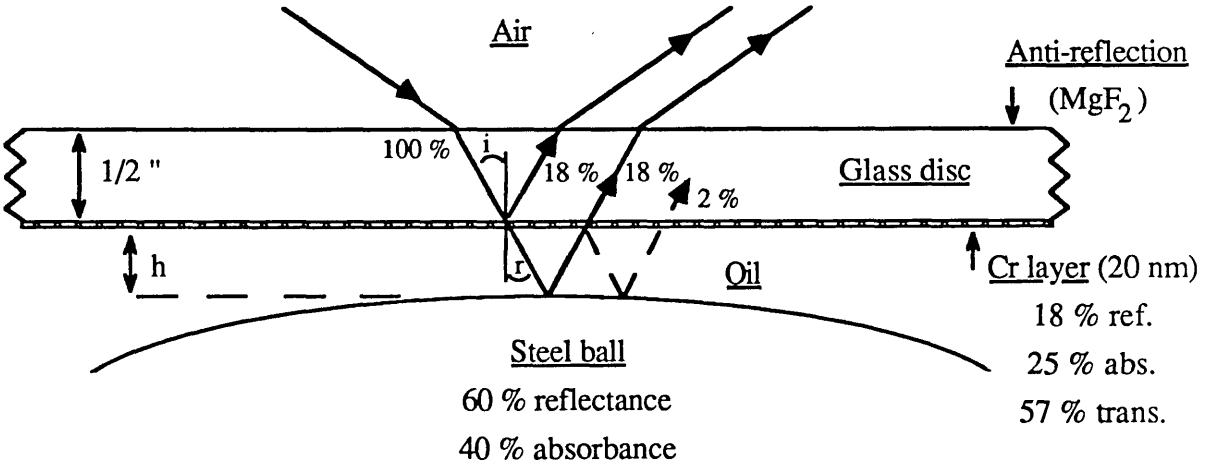


Figure 5.1 Basic interferometric system (two beam)

On recombining, the two parts of the beam have equal *intensity* i.e. they are of equal gross amplitude. However, the nature of their interference depends on the relative phase of the two beams. This in turn depends on the *optical path difference* (Δ) i.e. the respective path difference and the *refractive index* (n), of the medium separating them (n_{AIR} = 1.00029).

The importance of the refractive index of the separating medium is considered in § 5.2.1.6. The condition for *constructive interference* occurs when the optical path difference is an integer number of wavelengths (Nλ) as summarised in (I). In this case the component beams are in phase and the amplitudes add to give a 'bright fringe'. The derivation of this equation can be found in any of the standard texts recommended above.

$$\Delta = N\lambda = 2\,n\,h\cos i + \phi \qquad \text{(I)}$$

The parameters in equation (I) are as shown in figure 5.1. N is an integer (1,2,3 ...) called the *fringe order*. The correction factor (ϕ) is included to account for anomalous *phase changes* that occur on reflection at either or both of the reflecting surfaces. This is dealt with in § 5.2.1.3. The condition for *destructive interference* (dark fringes) occurs when the component beams are out of phase i.e. when the path difference is half a wavelength. This is summarised in equation (II). N is an integer (0,1,2 ...).

$$\Delta = \left(N + \frac{1}{2}\right)\lambda = 2\,n\,h\,\cos r + \phi \qquad \text{(II)}$$

5.2.1.2 Requirements for good fringe visibility

Fringe clarity was originally defined by Michelson [202] in terms of the *visibility* (V). This is defined in equation (III).

$$V = \frac{I_{max} - I_{min}}{I_{max} + I_{min}} \qquad \text{(III)}$$

It can be seen that (V) tends towards a maximum of one, when $I_{min} \rightarrow 0$. The following experimental parameters are important in ensuring this condition is achieved.

It was stated previously that clear fringes are obtained by adjusting the chromium layer thickness to ensure that the two beams are of equal intensity. This can be shown by applying the classical formula of Fresnel for *coherent* rays i.e. beams that are both in phase and of the same frequency. This formula is given in equation (IV).

$$I_{combined} = I_1 + I_2 + 2\sqrt{I_1}\sqrt{I_2}\cos\left(\frac{2\pi\Delta}{\lambda}\right) \qquad \text{(IV)}$$

The conditions for maximum and minimum intensity are summarised in scheme (V).

$$I_{max} = I_1 + I_2 + 2\sqrt{I_1}\sqrt{I_2} \text{ , when } \cos\left(\frac{2\pi\Delta}{\lambda}\right) = 1$$

$$I_{min} = I_1 + I_2 - 2\sqrt{I_1}\sqrt{I_2} \text{ , when } \cos\left(\frac{2\pi\Delta}{\lambda}\right) = -1 \qquad \text{(V)}$$

Substitution of the values for I_{max} and I_{min} into equation (III), gives the visibility as defined in equation (VI). It is apparent that the visibility tends to a maximum of one when $I_1 = I_2$, and that the intensity distribution follows a $\cos^2$ law.

$$V = \frac{2\sqrt{I_1}\sqrt{I_2}}{I_1 + I_2} \quad , \quad \therefore \; I = f\left(\frac{\cos^2 \pi\Delta}{\lambda}\right) \qquad \text{(VI)}$$

A second condition affecting the fringe visibility is the *degree of coherence* ($\gamma_{1,2}$); the affect on visibility is shown in equation (VII). $\gamma_{1,2}$ can vary between a maximum of one and minimum of zero, for mutually coherent and incoherent beams respectively. In the latter case no interference will be observed. The value of $\gamma_{1,2}$ is primarily a function of the light source used. A thermal source emits coherent wavetrains of fixed lengths (the *coherence length*). If this length exceeds the path difference, clear fringes will result. The coherence length is inversely related to the *spectral bandwidth*. Even so-called 'monochromatic' sources emit a finite range of wavelengths. Each component wavelength interferes successively to give light or dark fringes at different multiples of Δ. As h increases the constructive fringes of the shorter wavelength edge towards the destructive fringes of the longer wavelengths (and vice versa). This results in increased fringe widths - i.e. a decrease in V - as h increases. The use of a highly monochromatic source mitigates the decline in visibility with increasing separation. However the mutual interference associated with multi-chromatic and white light sources can be calibrated to give very accurate and closely spaced film thickness measurements at smaller values of h. This is described in § 5.2.1.4 - 5 below.

$$V = \frac{2\sqrt{I_1}\sqrt{I_2}}{I_1 + I_2}\gamma_{1,2} \qquad \text{(VII)}$$

In practice, the use of a light source or aperture of finite size, leads to the contact being illuminated by rays that deviate from the normal. This deviation is usually described as the *degree of collimation* of the source. A deviation from normal shifts the fringe to a position of greater thickness. Wedeven [199] developed an equation linking the maximum angle of deviation from the normal (θ), to the change in observed film thickness which results from the fringe shift. The author [199] showed that a typical commercial source ($\theta = 8^{o}$) resulted in an observed film thickness increase of less than 0.4 % (upto the maximum separation of ~ 2000 nm). This error can be ignored. Independent calibration of the fringes for a given light source - as described later in this chapter - avoids this complication altogether.

The final important consideration for good fringe quality is the nature of the surfaces present in the system i.e. their finish, absorbance / reflectivity characteristics etc. In two beam interferometry high *reflectivity* (R) is not essential; very good visibility can be obtained from low intensity beams for which $I_1 = I_2$. The reflectivity, for normal incidence, at the interface of two dielectric media (of refractive index n_1 and n_2) is given in equation (VIII). Since the reflectivity of the ball is largely fixed, the condition $I_1 = I_2$ is achieved by the use of a semi-reflecting dielectric chromium layer (see figure 5.1). However, thin metal layers lead to unusual intensity distributions and phase changes on reflection, as described in the following section. The influence of a thin metal layer (~ 20 nm), with a thickness much smaller than the typical Hertzian deformation [203], on the elastic properties of the glass substrate, can be ignored. The values given in figure 5.1 were measured by Wedeven [199].

$$R = \left(\frac{n_1 - n_2}{n_1 + n_2}\right)^2 \qquad \text{(VIII)}$$

Equation (VIII) predicts approximately 4 % reflection at an air / glass interface. The reflected light reduces the part of the light undergoing interference and it 'dilutes' the observed image. In practice the reflectivity is reduced to approximately 1% by coating the upper surface of the disc with an anti-reflection coating. Magnesium fluoride

(MgF_2, n = 1.38) is applied at a thickness of (λ' / 4 n). λ' is a wavelength in the middle of the visible spectrum (usually green light, for which $\lambda \sim 550$ nm). This is described in more detail in [199]. The optical components of the microscope were similarly, routinely-treated during manufacture.

Surface roughness and *surface geometry* will also affect fringe visibility, although in the set-up described in the current study, their influence can be ignored. A peak to valley height change of (λ' / 4 n) i.e. a thickness of approximately 95 nm, will shift the fringe intensity from light to dark (or vice versa). In practice, the surface finish of the discs and the balls used were very much better than this. In addition, the Hertzian pressures generated within the contact will cause elastic deformation of surface asperities, thereby reducing the values of the measured roughnesses. Geometric errors of form are only important if they exceed the Hertzian deformation (over the contact length). The EHD film thickness is determined solely by the operating inlet conditions and it will be unaffected by geometric irregularities of the ball or disc. Such irregularities simply result in a cyclic vertical displacement of the contact. However, since the displacement is typically less than the depth of focus, no loss of image results.

5.2.1.3 Calibration of monochromatic fringes and phase change on reflection

The phase change (ϕ) that occurs during a reflection at the interface of two dielectric media, is well understood. Reflection from an *optically rare* to an *optically dense* medium results in a phase change of π or 180^o. A dense to rare reflection leaves the phase unchanged. The optical density of a transparent medium is a measure of its refractive index (this is described in § 5.2.1.6). However metallic reflections, such as those from the ball and the chromium layer, do not obey this rule. This was simply demonstrated by Wedeven [199]. Wedeven observed the central fringe colour (h = 0) for the flat-on-sphere contact of various materials. The observed results are summarised in table 5.1.

Material		Phase change (ϕ)		First fringe
Flat	Sphere	flat / air	sphere / air	(h = 0)
Glass	Glass	0	π	destructive (dark)
Glass	Steel	0	π	~ destructive (dark)
Cr / Glass	Steel	$\neq 0$ or π	$\neq 0$ or π	neither (grey)

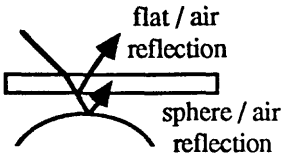


Table 5.1 Phase changes on reflection for the contact of a flat and a sphere (after Wedeven [199]).

It was stated earlier that the anomalous phase change on reflection affects both the fringe position and the fringe intensity distribution. The following calibration experiment was therefore conducted to measure the *relative* phase change between the light reflected from the ball surface and the chromium layer. The method of calibration is a modification of the technique used by Wedeven [199]. The calibration was repeated for a number of reasons. Firstly, the chromium plated discs and the steel balls used in the current study differed from those used in [199]. Secondly - as described in the following two sections - the technique was required to calibrate the coloured fringes that result from the duochromatic and white light systems used in the current study. Both of these light sources result in *unsaturated* coloured fringes. Their position is therefore highly 'observer-dependent'. Also their position depends on the *colour balance* of the light source used. Thirdly, the technique is important, for calibration purposes, in the improved interferometric techniques described in chapter 8.

The absolute thickness (h) corresponding to each fringe - in air - was calculated for two monochromatic sources as follows. The basic arrangement is shown in figure 5.2. This procedure avoided two potential sources of inaccuracy that were present in previous calibration procedures. Gohar and Cameron [195] allowed a steel ball of radius (R) to 'lightly touch' a chromium coated glass plate. The authors then measured the fringe diameters ($2\,r_f$) and calculated h from equation (IX). Equation (IX) is derived from the known geometry, when $r_f << R$. However, since h is of the order of hundreds of nanometers and it is proportional to r_f^2, two errors may result. Firstly, even a light load will result in a Hertzian deformation of radius (a), increasing the measured values of r_f and therefore h. Also, at very light loads, surface asperities or surface contaminants may

separate the surfaces reducing r_f and therefore h.

$$h = \frac{r_f^2}{2nR} \qquad \text{(IX)}$$

Foord, Hammann and Cameron [204] attempted to improve the procedure by using a chromed spherical lens, such that $R_{lens} >> R_{ball}$. However, the phase change on reflection from the chromed lens is unlikely to be the same as that on reflection from a steel ball.

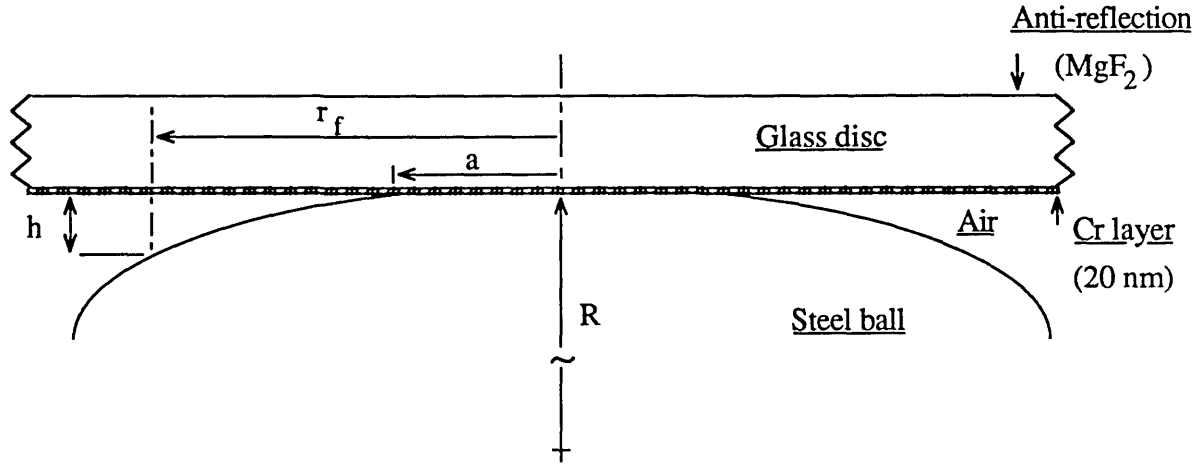


Figure 5.2 Ball on plate contact used for fringe calibration

In the current procedure, the ball used was of the type used throughout the current work. It was ultrasonically cleaned in toluene and acetone prior to use. The clean ball was placed on a balance (a second ball was used to counter balance the scales). A load of less than 0.1 g was found to unbalance the system. The ball was then loaded against the rigidly held disc by additional counter weights (in the range 500 - 1 g). The fringe diameters ($2 r_f$) were then measured, as described below. This differed from the procedure of Wedeven [199], in which a filar eyepiece was used.

Two monochromatic light sources were used. A green source (λ_{max} ~ 546 nm) and a red source (λ_{max} ~ 650 nm). In practice these 'monochromatic' sources were produced using narrow band filters. The spectral characteristics of the red filter (Wratten 25), the green

filter (Wratten 58) and a duochromatic red / green filter (Wratten 77A) are shown in figure 5.3. The green source was therefore obtained by using a white light source with the Wratten 77A and 58 filters. The red source relied upon the use of the Wratten 77A and 25 filters. The use of the duochromatic source is described in the next section. Typical 'Newtons rings' interference patterns are shown for a monochromatic (green) source in plate 5.1. Plates 5.2 and 5.3 show similar patterns for the duochromatic source and the white light source respectively.

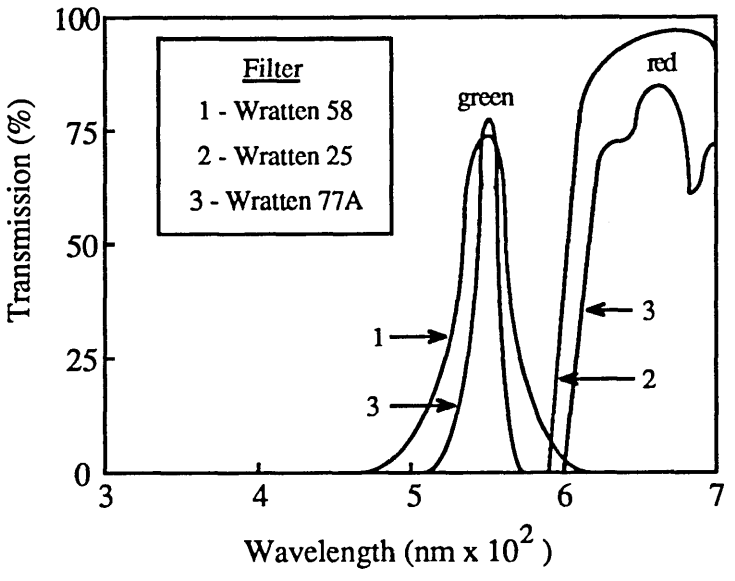


Figure 5.3 Spectral characteristics of monochromatic and duochromatic filters

The fringe patterns were photographed, for each of the monochromatic sources, at a series of known loads. During this procedure, the distance between the objective lens and the eyepiece was fixed. All photographs were taken at sharp focus (as observed through the viewfinder of a camera mounted on the optical system, in place of an eyepiece). This provided a series of plates from which the relative fringe diameters could be measured. However, calculation of the absolute fringe diameter (r_f) required an accurate knowledge of the magnification of the photographs. This calibration was achieved using a series of 'pinholes' (Ealing Beck Co.). These are small metal discs (diameter ~ 3 mm) each containing a very accurately machined pinhole (in the range 1000 - 5 μm). A number of the pinholes - covering the range of fringe diameters to be measured - were similarly

photographed. This was achieved by placing each of the pinholes, in turn, on the object ball and lightly loading it against the disc. This resulted in a series of photographs of pinholes of known diameter ($d_{pinhole}$). Direct measurement of the diameter of the pinhole on the photograph (d_{photo}), permitted a calibration graph to be plotted. d_{photo} was measured using a pair of dividers. Two measurements were taken, approximately at right angles, for each pinhole or fringe. The average of the two measurements was then used. A typical example of the calibration graph is given in figure 5.4. This calibration procedure was repeated before and after any measurements of fringe radii.

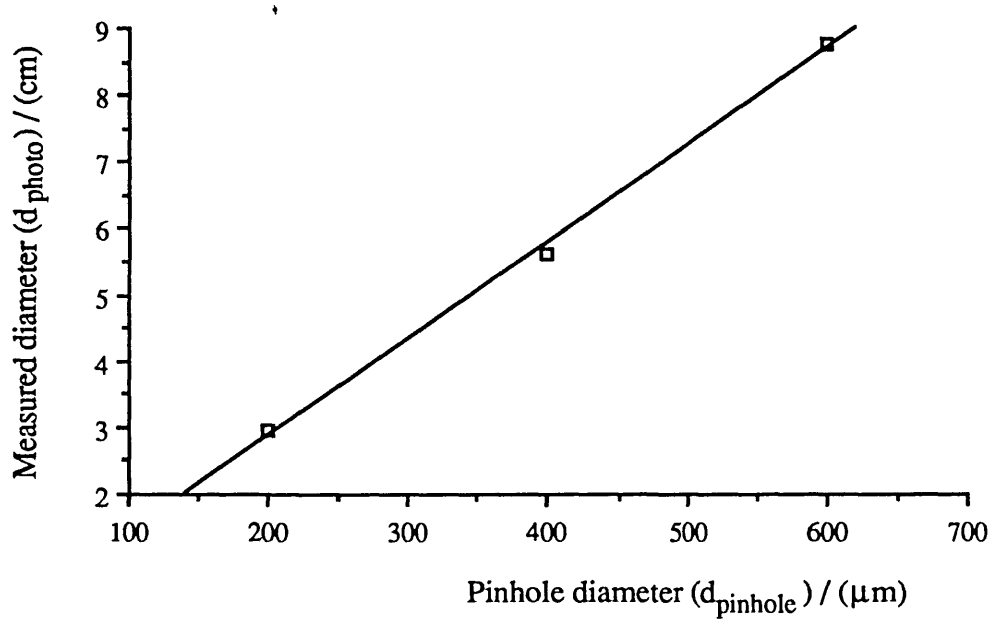


Figure 5.4 Fringe radius calibration graph

The calibration graph could then be used to find the absolute fringe radius (r_f) - for a required fringe - from its measured diameter on a photograph. Figure 5.5 shows a plot of r_f against the Hertzian radius - as a function of load - for the first seven dark fringes obtained using the red source. The Hertzian radius (a) was calculated from equation (X), using the material constants given in table 5.2. The reduced modulus is defined in the section on nomenclature. Figure 5.6 shows a similar graph obtained using the green source.

$$a = \left(\frac{3WR}{2E'}\right)^{\frac{1}{3}} \qquad (X)$$

Variable	Glass	Steel
Poissons ratio (σ)	0.22	0.293
Youngs modulus (E') / (N/m^2)	75.0×10^9	210.0×10^9
Reduced Youngs modulus (E') / (N/m^2)		1.13×10^{11}
Reduced radius (R) / (m)		0.0127
Load (W) / (N)		Variable

Table 5.2 Values for parameters used in calculation of Hertzian radius (a)

The shape of the curves in figures 5.5 and 5.6 results from the influence of the Hertzian deformation on the fringe radius (r_f). At high loads there is an appreciable Hertz radius (a). However as $W \rightarrow 0$, the Hertz radius $a \rightarrow 0$ and r_f approaches the asymptote r_f = constant. In practice, at very light loads, the measured values of r_f were less than predicted by the curve up to that point. This implied some spurious separation at low loads. This was observed as a change in the central fringe colour from grey to black. For this reason the

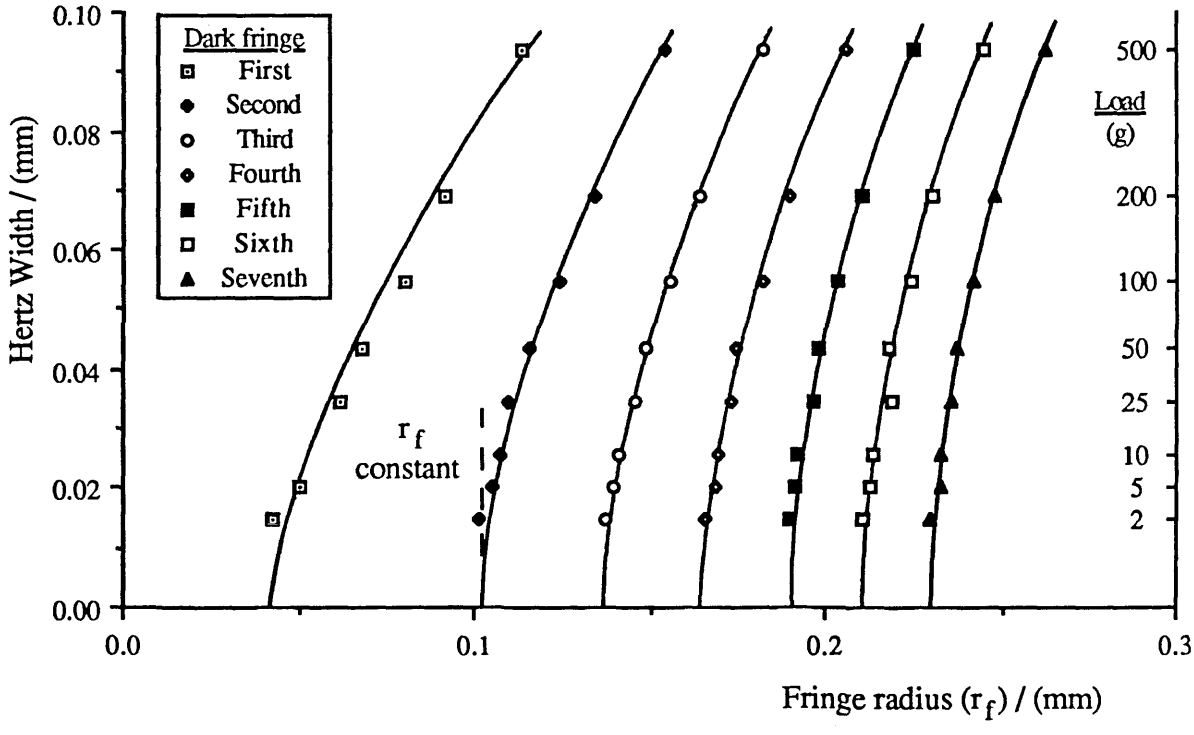


Figure 5.5 Fringe radius (r_f) as a function of load (red light source)

curves were drawn through the higher loads and carefully extended to zero, such that r_f = constant. The value of r_f - obtained for a given fringe - was then substituted into equation (IX), from which h was calculated. The separation (h) for each fringe was found in this way. The duochromatic and white light systems were similarly calibrated, as described in the next two sections.

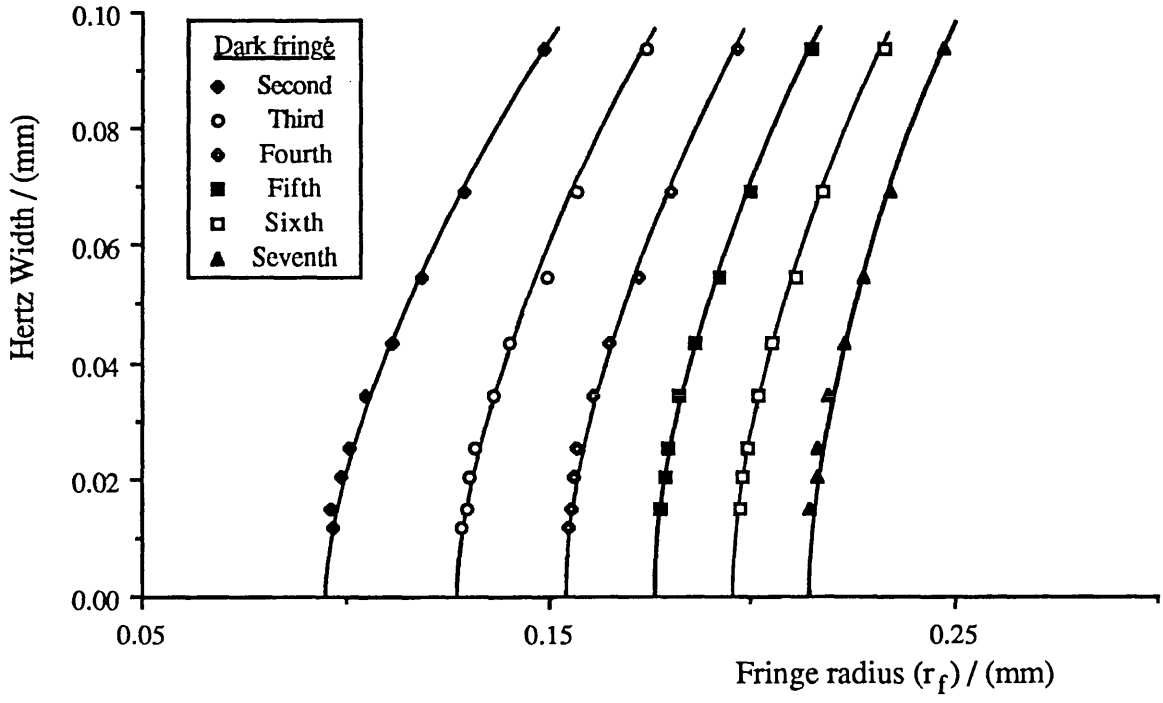


Figure 5.6 Fringe radius (r_f) as a function of load (green light source)

The shape of the curves was verified by Wedeven [199] using equation (XI). This equation predicts the shape of the separation extending away from the Hertzian contact. The equation was solved for r_f by trial and error. The procedure [199] was shown to verify the curve shape. P_{max} is the maximum Hertzian contact pressure.

$$h = \frac{a\,P_{max}}{E'} \left\{ -\left(2 - \frac{r_f^2}{a^2}\right) \cos^{-1} \frac{a}{r_f} + \left(\frac{r_f^2}{a^2} - 1\right)^{\frac{1}{2}} \right\} \qquad \text{(XI)}$$

where $P_{max} = \dfrac{3W}{2\pi a^2}$

Equation (XI) has also been used as the basis for a second method of fringe calibration. The ball is loaded against the disc and the required fringe radii are measured directly. The values of r_f are then substituted in to equation (XI), from which h is calculated for each fringe. An average value of h should be taken after repeating the procedure at a series of loads. This method was used by Gentle [200] to calibrate a white light source. However this method requires an accurate knowledge of the elastic properties of the materials involved.

The technique used by the current author to calibrate fringes can also be used to calculate the *relative* phase change (ϕ). This is achieved by plotting the calibrated fringe thickness against the fringe order (figure 5.7). The fringe order (N) is based on light fringes, as a light fringe will occur at zero order if no phase change occurs on reflection. The equations describing the curves shown in figure 5.7 were used to calculate the relative phase change i.e. the shift in the fringe order at h = 0. The values of ϕ calculated were 0.30 for the red source and 0.28 for the green source. λ_{max} was calculated, for each of the sources, by substituting the measured values of h and ϕ into equation (II); known values of n and N were used. This procedure gave λ_{max} = 578 nm for the green source and λ_{max} = 673 nm for the red source. The maximum transmission of gelatin dye filters is known to be highly dependent on age, ambient temperature, angle of incidence etc. From the graph it can be seen that the relative phase change was approximately $3\pi / 5$ radians, at zero thickness. The experiment summarised in table 5.1 indicated that the *absolute* phase change on reflection from the steel ball (ϕ_{ball}) was close to π. If ϕ_{ball} is assumed to be π, then the phase change due to the chromium layer ($\phi_{ch.}$) can be determined from equation (XII).

$$\phi = \phi_{ball} + \phi_{ch.} \qquad \text{(XII)}$$

Therefore, from equation (XII), $\phi_{ch.} = -2\pi / 5$ or $8\pi / 5$. This correlates well with the findings of Wedeven, who argues that $-2\pi / 5$ is more likely [199].

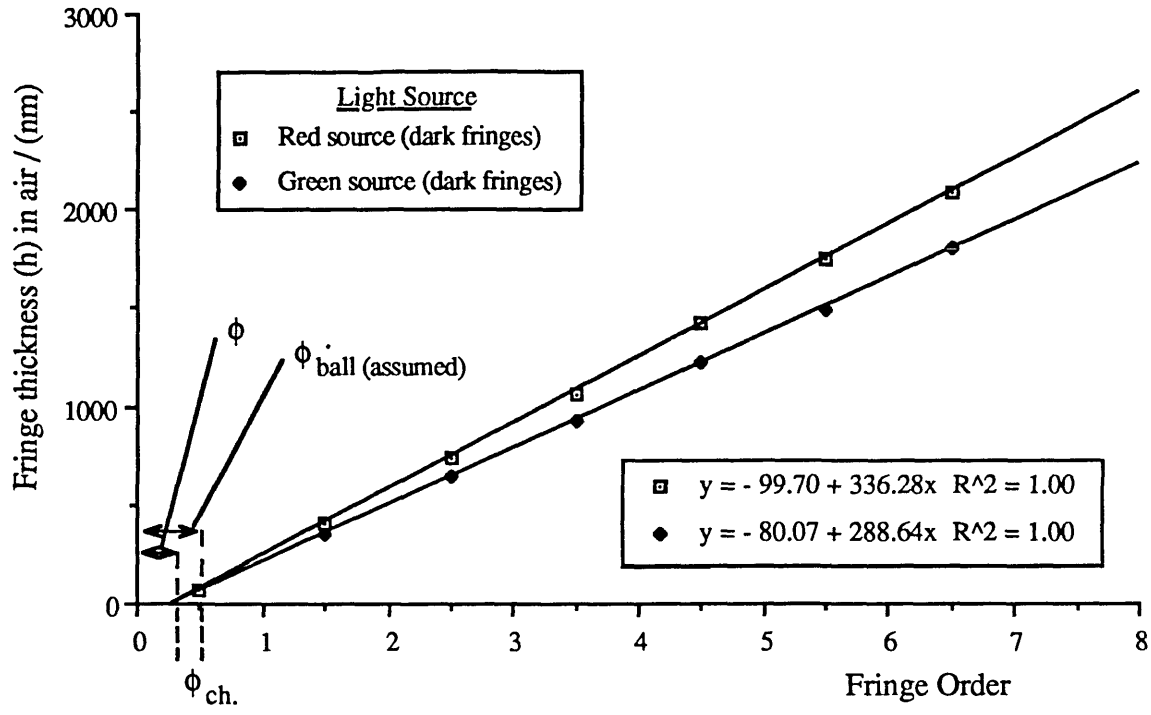


Figure 5.7 Fringe thickness vs. order - phase change (ϕ) on reflection

5.2.1.4 Duochromatic interferometry - calibration of fringes

The relative advantages and disadvantages of monochromatic, duochromatic and white light (chromatic) interferometry - and the circumstances in which each are preferred - are discussed in § 5.2.1.7. The duochromatic system requires two distinct wavebands, of good colour contrast. This was achieved using the Wratten 77A filter, which transmits red and green bands (see figure 5.3). The pattern of Newtons rings resulting from this source are shown in plate 5.2. The fringes observed originate from the superposition of the monochromatic fringes. The fringes due to the green source (λ_{max} ~ 546 nm) are more closely spaced than the red source (λ_{max} ~ 650 nm). The colour of the chromatic fringes - for a given separation - is simply the sum of the two monochromatic sources at that point.

As described previously, the observation of unsatured chromatic fringes is highly dependent on the observer. For this reason the calibration procedure described in the previous section was used to calibrate a number of the most easily observed fringes. Figure

5.8 shows a plot of Hertzian radius (a) against fringe radius (r_f).

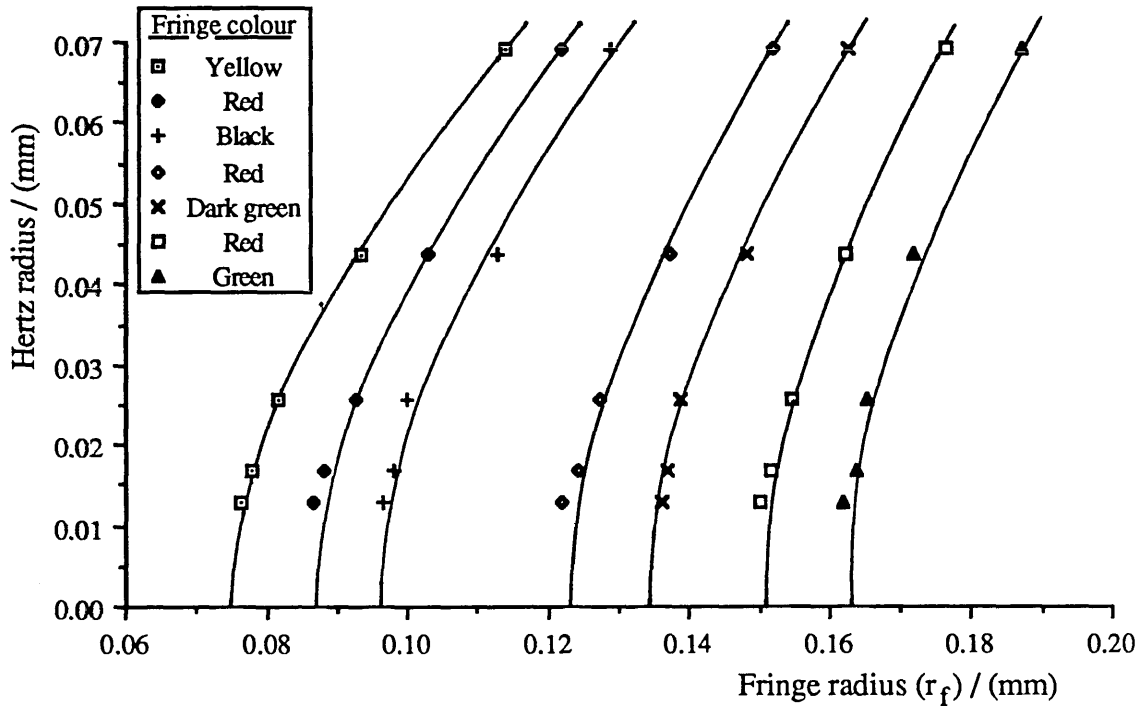


Figure 5.8 Fringe radius (r_f) as a function of load (duochromatic light source)

Table 5.3 compares the fringe separations (h) obtained by the author, with those obtained by Wedeven [199]. On average the current calibration agrees with that of Wedeven to within 4 %. Larger discrepancies tend to occur with the first few fringes, as extrapolation of the curves to the asymptote r_f = constant is more subjective in this region. As the accuracy was good, and it was found to increase with r_f (and therefore h) the calibration was limited to the first 50 % of the observable fringes. Measurement of oil film thickness, as a function of speed, usually relies on an average line drawn through 10 or more data points. For this reason any errors introduced as a result of differences in calibration, can be considered to be negligible within the accuracy of the technique.

Duochromatic - separation / (nm)			Chromatic - separation / (nm)			
Colour	Wedeven [199]	Author	Order	Colour	Gentle [200]	Author
black	813	-	1	yellow	200	-
yellow	243	221		orange	-	258
red	320	298		red	270	-
black	376	363		blue	340	370
yellow-green	538	-		green	430	-
red	622	596	2	yellow	470	494
dark green	711	707		red	560	572
green	812	-		blue	610	-
red	917	898		green	670	700
green	1084	1046	3	yellow	760	800
red	1181	-		red	860	870
green	1351	-		blue	900	-
red	1473	-		green	960	1000
green	1626	-	4	yellow	1050	-
dark red	1732	-		red	1150	1165
yellow-green	1895	-		blue	-	-
black	2019	-		green	1250	1300
yellow	2159	-				
black	2306	-				
yellow	2438	-				
black	2591	-				
yellow-green	2743	-				
red	2883	-				

Table 5.3 Comparison of fringe calibration with previous authors.
Duochromatic and white light sources

5.2.1.5 White light (chromatic) interferometry - calibration of fringes

A white light source may simply be considered to consist of a large number of monochromatic sources, each of which undergoes an interference process as described previously. The fringe colour, for any separation, results from the superposition of the

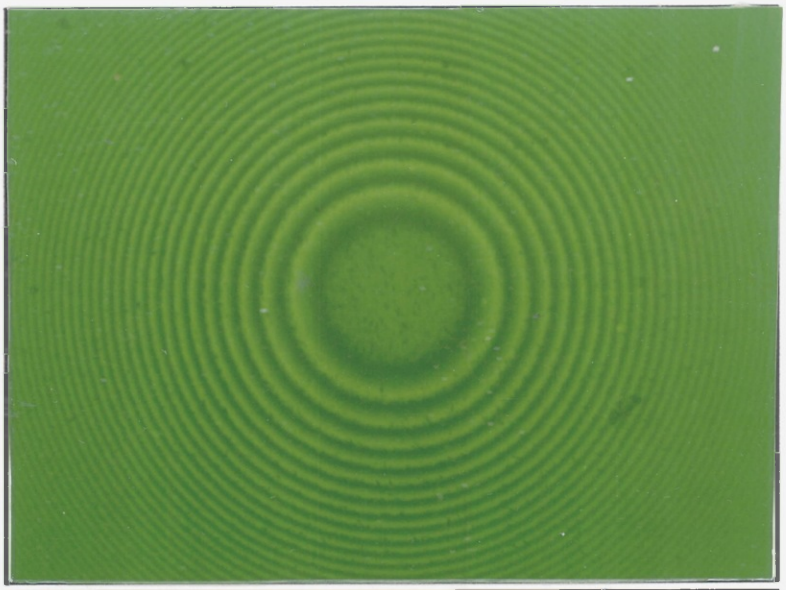


Plate 5.1
Monochromatic fringes in oil
(green source λ_{max} 546 nm).
Filters - Wratten 77A and 58.
Stationary contact.

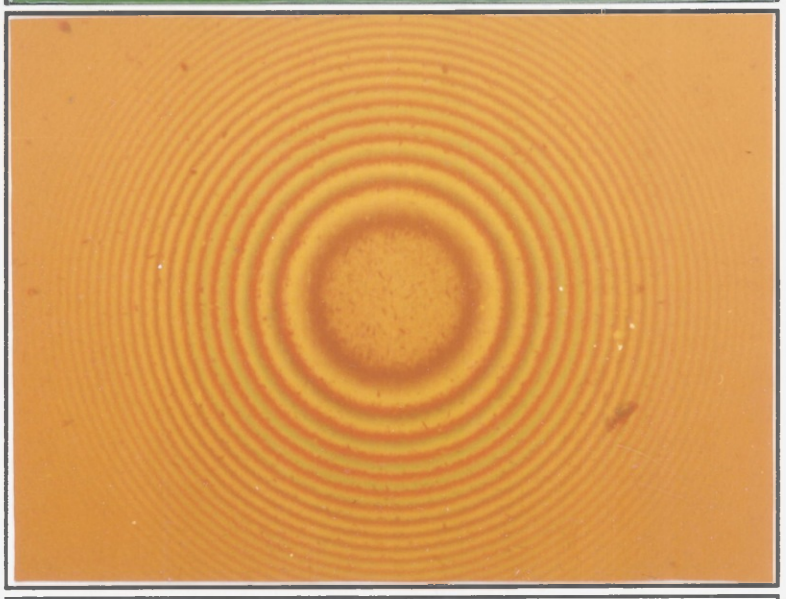


Plate 5.2
Duochromatic fringes in oil
(green and red sources).
Filter - Wratten 77A.
Stationary contact.

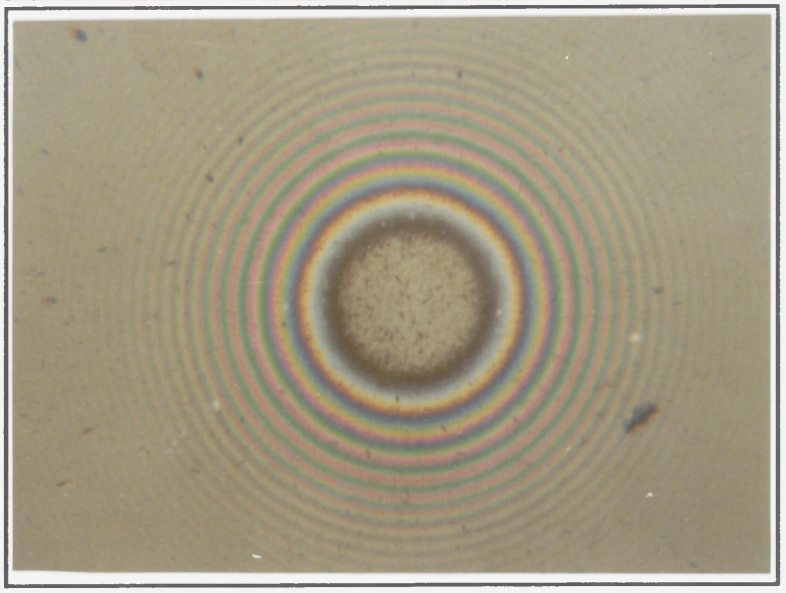


Plate 5.3
Chromatic fringes in oil.
(White light source).
Stationary contact.

intensities of the component monochromatic sources or individual wavelengths. Wavelengths that interfere destructively will be lost, those interfering constructively will be seen. For this reason a distinct series of interference colours are observed (and repeated for N = 2,3 ...) as h increases. No dark fringes are observed, as some component of the continuous spectrum is always interfering constructively. An example of a ball on disc contact, illuminated with a white light source, is shown in plate 5.3.

The component wavelengths present in the white light source, interfere to give a number of unsaturated colours that can be seen by the experimental observer. These colours require calibration to the eye of the observer. This was achieved as described previously. The white light source used was a 'cold' halogen lamp (Schott) as used in much of the experimental work. The fringes were calibrated from figure 5.9.

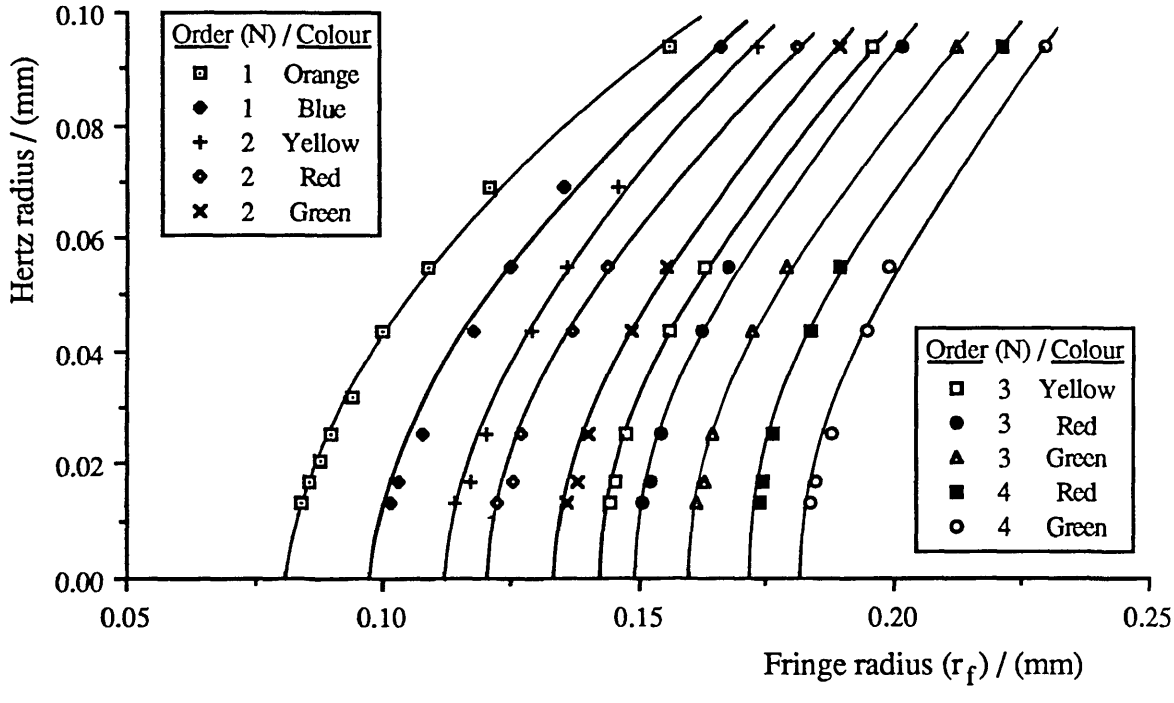


Figure 5.9 Fringe radius (r_f) as a function of load (white light source)

The separation (h) corresponding to each of the fringes calibrated, is given in table 5.3. The values are compared to those obtained previously by Gentle [200], using a different method and light source. It can be seen that the independent calibrations agree to within a few % in

most cases. As described in the previous section, differences of this size can be ignored. The good correlation also suggests that the 'colour balance' of the respective white light sources used, did not differ significantly. A number of white light sources used by the author to measure film thickness gave indistinguishable results.

5.2.1.6 Refractive index of the separating medium

The *refractive index* (n) or optical density of any optical medium is defined as in equation (XIII). The velocity difference in the two media results from a change in wavelength that occurs at the interface.

$$n = \frac{\text{speed in vacuum}}{\text{speed in medium}} = \frac{c}{v} \qquad \text{(XIII)}$$

All of the fringe calibrations described above were measured in air (n = 1.00029). The fringe thickness in any other medium (h_{medium}) is obtained by dividing the calibrated fringes by the refractive index of the medium used (according to equation XIV). The refractive index has been shown to have a negligible effect (± 2 %) on the phase change on reflection [199].

$$h_{medium} = \frac{h_{air}}{n\ (P,T)} \qquad \text{(XIV)}$$

The refractive index - in the above equation - should strictly be measured at the contact temperature and the prevailing fluid Hertz pressure. Refractive index usually increases with pressure and decreases with temperature. The variation with temperature can be simply measured using a commercial refractometer, such as the Abbe 60 used in the current study. The required temperature is achieved by circulating a polyglycol fluid, from a thermostatically controlled heating bath. Much of the work described in the current study used a synthetic hydrocarbon (SHC 234). The refractive index of this fluid was found to change from 1.4688 at room temperature, to 1.4440 at 100° C. Lacey [76] measured 16 formulated oils at 100° C and found n = 1.4440 ± 0.0002.

Measurement of the variation of refractive index with pressure - in the range of GPa's - is less easy. Paul and Cameron [205] developed a dropping ball device which simultaneously measured fluid density, pressure and viscosity. They showed that increasing the pressure from atmospheric to 1 GPa altered n by less than 10 %. An estimate can be made by combining the Lorenz-Lorentz equation (XV) with the empirical formula of Hartung [206] (XVI) for hydrocarbons. Equation (XV) gives the variation of refractive index with density (ρ). The subscripts o and p refer to atmospheric pressure and an elevated pressure P.

$$n_p = \frac{(1+2A)^{\frac{1}{2}}}{1-A} \qquad \text{(XV)}$$

$$\text{where } A = \frac{\rho_p}{\rho_o}\left(\frac{n_o^2 - 1}{n_o^2 + 2}\right)$$

Equation (XVI) gives the variation of density with pressure. ν is the kinematic viscosity in cSt.

$$\frac{\rho_p}{\rho_o} = 1 + b\,(P - P_o) \qquad \text{(XVI)}$$

$$\text{where } b = \frac{42.8 \times 10^{-6}}{\nu_{100^\circ F}^{0.0386}\; P^{0.25}}$$

In the current study the separating medium often consisted of a reacted polymeric layer plus some EHD film. The refractive index of the polymeric material could only be measured indirectly (§ 7.2.3.1). It was found to be close to that of the base stock (~ 1.444). Since the variation of n with pressure is small, the refractive index of the base stock at atmospheric pressure and the inlet temperature was used.

5.2.1.7 The interferometric systems - advantages and disadvantages

The relative merits of the various types of two beam interferometry may be understood by contrasting the monochromatic and white light systems. The duochromatic source

represents a compromise between these extremes.

The narrow bandwidth associated with a monochromatic source results in identical dark and light fringes separated by a constant relative spacing ($\Delta h = \lambda / 4n$). A knowledge of the wavelength means the relative spacing is therefore known automatically. The narrow bandwidth also ensures that the visibility remains good for much greater separations (h). However, this system is subject to a number of disadvantages. Fringe position is determined by monitoring the relative intensity; the human eye is much more sensitive to changes in colour (white light system). The relative spacing of the 'observable' separations (Δh) is fixed at a comparatively high value and a mistake in counting the fringes can lead to the wrong fringe order being ascribed to a given fringe.

Many of the advantages of the white light system are apparent from the paragraph above. A series of distinct colours appears for each spectrum order with a reduced relative spacing (Δh) i.e. there are more data points per spectrum order. The sequence of colours is easily recognisable and it shows the direction in which the separation is increasing. The relative intensities of the colours observed changes with fringe order (N); this means N is easily determined by an experienced observer. The main disadvantages of the system are firstly, that Δh is not constant and therefore careful calibration is required. Secondly, in the continuous spectrum, the colours merge as h increases. In practice, the maximum of four values of h per spectrum order can only be achieved for N = 1 and 2. At N = 3 and N = 4 the number of data points drops to 3 and 2 respectively.

In most of the current work the EHD films observed are of only moderate thickness (upto ~ 1000 nm). In this case the white light system provides the best compromise. However all of the conventional interferometric techniques described above remain subject to two restrictions. Firstly, the wavelength of visible light imposes a limit - of approximately 130 nm - on the minimum film thickness that can be measured. Secondly, at separations above this limiting value, the relative spacing of the measured film thickness is fixed. Chapter 8 describes some new techniques developed to improve upon these limitations.

5.2.2 Elevated temperature optical EHD rig used in early testwork

Figure 5.10 shows a sectional view of the EHD test rig used in some of the early testwork. It is similar in design and function to the optical rig that was designed and commissioned, by the author, for use in the current work (§ 5.2.3). The early test rig proved inadequate in a number of respects. Most notably it had severe vibrational problems, poor optical quality, a limited temperature range and a largely invariant slide / roll ratio. The problems associated with this rig, and the experience gained using it, were therefore considered prior to the design of a new test apparatus. Section 5.2.3 details the experimental procedure for the new rig; the similarities and the improvements are described with reference to the previous procedure. For this reason the use of the old rig is only briefly described here. A full account of its use, calibration etc is given in [76].

The rig employed chromatic interferometry to measure the optical separation between a steel ball running on a chromium plated glass disc. The materials used etc are described in section 5.2.3. The ball was loaded against the disc (figure 5.10) by placing a dead-mass on the pivoted loading arm. The ball position was fixed by two 'cotton-reel' rollers; the rollers were mounted in the loading arm on high-precision, miniature roller bearings. In addition to this, a modified loading arm was built in which the ball could be held stationary. This permitted the rig to be operated in pure sliding. This arrangement is described in more detail in section 7.2.2.1; a schematic diagram of the modified loading arm is given in figure 7.5.

The rig was run in either of two ways. If the disc alone was driven, it caused a freely rolling ball to be driven in nominally pure rolling. However, it was also possible to drive the ball at a different speed from the disc, to produce a required slide / roll ratio. This was achieved by accurately gluing a drive-shaft onto the test ball, in a lathe. A single motor was then used to drive both the disc and the ball, through a series of gearboxes and belt-driven pulleys. The power train layout is shown in detail in [76]. The degree of sliding could be altered smoothly during running by adjustment of a variable speed gearbox which was included in the ball-drive power train. The relative surface speeds were calculated from the measured shaft speeds, by accurately measuring the track radius at which the ball was running. The procedure for calibrating the track radius and for measuring the shaft speeds was similar to that described below (§ 5.2.3).

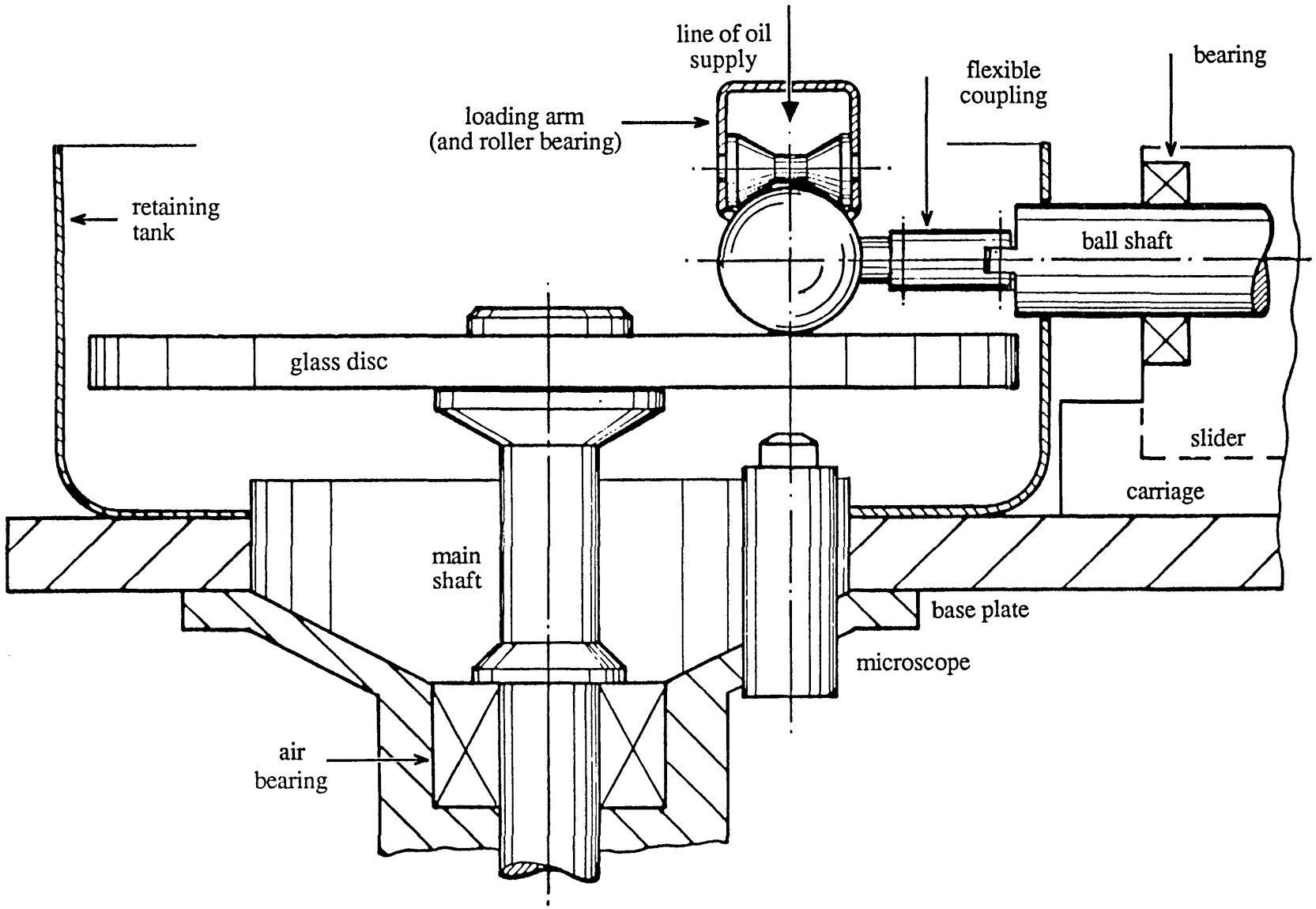


Figure 5.10 Sectional view of EHD rig used in early test work

In much of the test work the rig was required to operate at elevated temperatures. This was achieved by heating and circulating the oil supplied, and by blowing hot air into the chamber (as described in detail in § 5.2.3). In addition, the chamber was lagged and heating tape was used to provide a general, elevated background temperature. This was found to be unnecessary in the improved design, as the retaining tank volume was much reduced. The combination of the three heating methods enabled the contact temperature to be controlled at temperatures upto 140 ± 2^{o} C.

5.2.3 Elevated temperature optical EHD rig designed and commissioned for use in current work

Figure 5.11 shows a schematic representation of the EHD test rig. Plate 5.4 shows the rig in more detail. In this photograph the retaining tank, the lubricant circulation / heating system and the hot air blower have been removed for clarity. The rig is similar, in principle, to the rig described in the previous section. The contact is that of a one inch ball (RHP grade 20 AISI 52100) with a glass disc (6.5" diameter, 0.5" depth). The glass disc was coated with a MgF_2 anti-reflection coating on the upper surface and a semi-reflecting Cr layer on the lower surface. The coating specifications were as detailed previously (§ 5.2.1).

The current rig differed in design from the previous model in a number of respects. Firstly, the ball and plate contact has been inverted i.e. the plate runs on top of the ball. This facilitates observation of the contact. Secondly, a more powerful heating system has been used; this has increased the maximum operating temperature to approximately 200 ± 1^{o} C. The range of available slide-roll ratios, at which the ball and disc can operate, was improved by using independent motors to drive the ball and the disc. In addition to the above changes, the means of loading the ball against the disc was re-designed to avoid problems encountered with the previous rig. The various design improvements incorporated in the present set-up are detailed in the following sections.

The final major difference incorporated in the design of the new rig was the ability to measure traction. This was achieved by mounting the 1" deep base plate - on which the ball holder stands - on a system of three, near-frictionless air bearings (arranged at intervals of

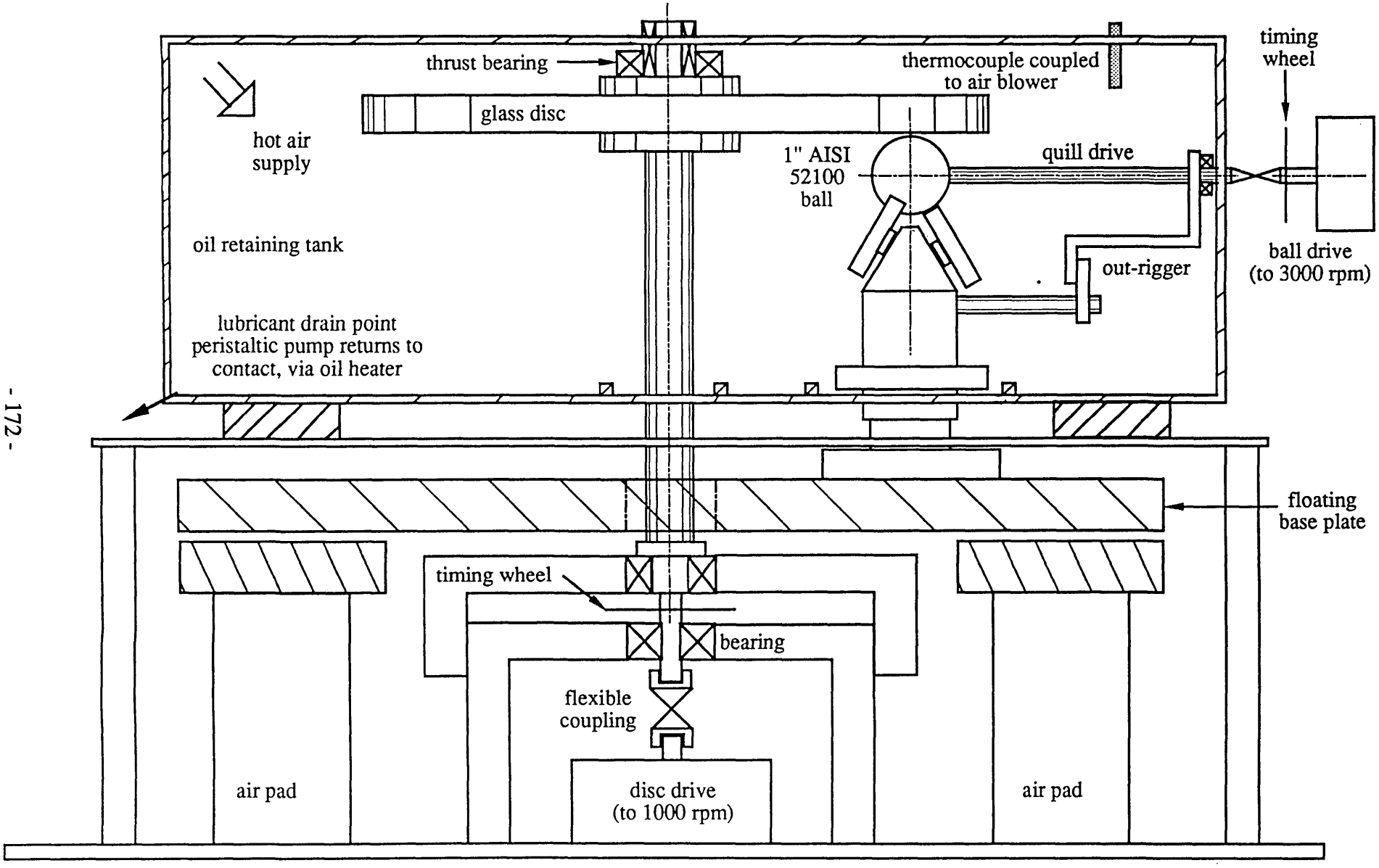


Figure 5.11 Schematic diagram of EHD test-rig

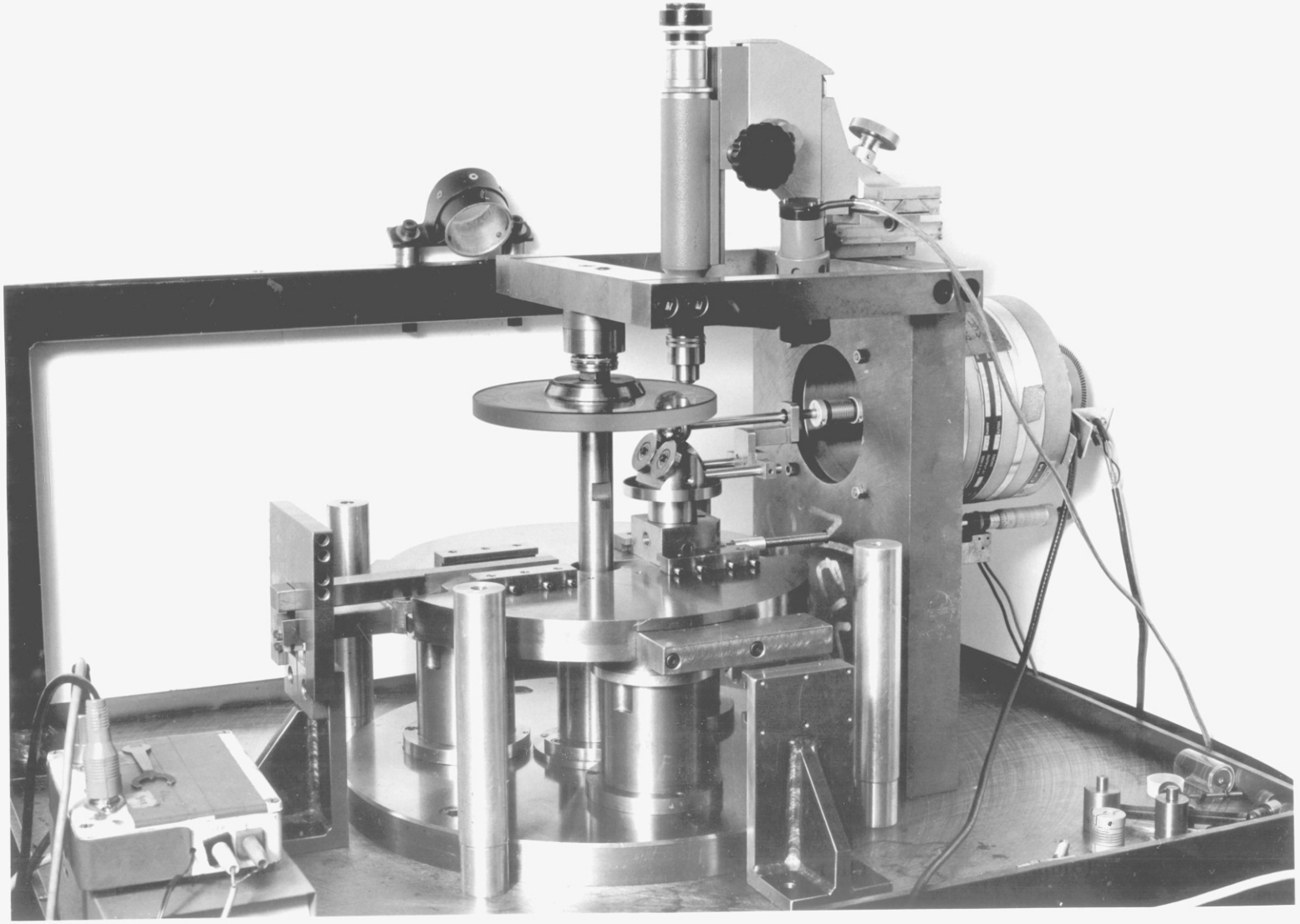


Plate 5.4 Optical interferometric test rig (variable slide-roll ratio and temperature)

120° when viewed from above). When the rig was operated with the air pads on, the base plate and ball mount assembly 'floated' approximately 0.0015" above the air pads. An additional 10 kg mass placed on the plate had no adverse affect on the 'frictionless' floating plate. The ball and plate assembly was therefore isolated from the rest of the rig except for the ball / disc contact and the ball-drive flexible coupling. Since the flexible coupling is designed to be stiff in torsion, but to bend easily, the only forces acting on the base plate are those emanating from the traction forces in the contact. The use of this system was limited to a feasibility study, during the current work, due to time constraints.

5.2.3.1 Temperature control and measurement

Two independent methods of heating were used to maintain the required chamber temperature and the required oil inlet temperature, respectively. The oil retaining tank, shown schematically in figure 5.11, consisted of a stainless steel chamber into which an aluminium lid was fitted. The enclosed volume (diameter 8", depth 5") was maintained at the required test temperature by a hot air supply. The air was supplied by a 1400 W 'turbo heat gun' (Costech Ltd.) linked to a CAL 7300 proportional and derivative controller (Controls and Automation Ltd). The controller had a digital display. The required test temperature was set on the display before start-up. During running the controller displayed the current chamber temperature as measured by an iron / constantan thermocouple sited on the opposite side of the chamber. During running the heat gun operated continuously, with the controller turning the heating element on and off as required. The blower thermocouple indicated an accuracy of ± 1° C upto the maximum test temperature of 200° C.

In addition to the above, a separate system was included for circulating and heating the test lubricant. The oil retaining tank was angled so that oil thrown from the glass disc by centrifugal force collected in one area. A length of glass tubing (6 mm O.D., 4 mm I.D.) was used to connect the drain point to a peristaltic pump. The pump used was a 17 series Masterflex 0 - 100 rpm model, with a flow rate of 2.8 ml per revolution. A typical test flow rate used was 28 ml / min i.e. a pump-head speed of 10 rpm. The pump was operated with silicon tubing (10 mm O.D., 6 mm I.D.), as this material has a very high temperature stability and elastic memory. Also it does not leach plasticisers into the test lubricant during running. The pump propelled the spent lubricant through a heater before returning it to the

contact. The heater consisted of a double walled glass cylinder with an inlet tube at the base and an upper outlet tube. The lubricant passed between the two walls; the inner tube contained a fully glass enclosed aquarium heater powered by a thyrister power controller (Gallenkamp Ltd). After heating, the lubricant re-entered the chamber via a glass tube fixed as close as possible to the contact inlet. A k-type thermocouple was attached to the inlet tube, with silicone sealant, to monitor the oil inlet temperature. This was displayed on an electronic thermometer (Comark). The oil circulating / heating system permitted temperature holding to ± 1 ^{o} C upto the maximum test temperature of 200^{o} C. Silicone rubber sheet sealed the oil inlet and the ball drive shaft. An extraction fan was used to remove fumes.

5.2.3.2 Ball loading systems - calibration of track radius

The previous rig employed two 'cotton reel' rollers and a dead mass loading system. This arrangement proved to be highly prone to vibration at high speeds. For this reason the following two systems were developed. In both cases, the track radius at which the ball was running, was dependent on the position of the floating base plate. In the majority of the test-work the rig was operated without the air pads i.e. with the base plate resting directly on the air pads. It was therefore important that the base plate was arranged concentrically with the drive shaft of the glass disc. This was achieved by accurately 'turning-down' a push-fit 'plug' which fixed the position of the base plate relative to the fixed shaft position. The 'plug' consisted of a cylinder machined to have an inside diameter equal to the shaft diameter, and an outside diameter equal to the central hole in the base plate. The cylinder was cut lengthways into two half cylinders. These were pushed into place to fix the plate / shaft positions. The half cylinders were removed prior to testing. The degree of concentricity was measured by replacing the glass disc with a steel disc and magnetically locking a clock gauge onto the disc. The disc / shaft was then rotated with the clock gauge set-up to measure changes in the radius of the base plate. The change in the radius of the base plate - which included machining errors - was found to be less than ± 0.0005" through 360^{o}. A second adjustment was required prior to running. This was made to ensure that the contact lay on an imaginary line drawn between the centres of the disc shaft and the drive shaft of the ball motor. The track radius could then be changed, as required - with the contact remaining on the imaginary line - by moving the ball loading assembly along a keyed slide-way cut into the base plate. The two ball loading assemblies and the track radius calibration are described in the remaining part of this section.

The first ball loading system used two 'cotton-reels' to fix the ball position, as previously, but it incorporated a pneumatic loading system (see figure 5.12). One cotton-reel was fixed on its mounting shaft, the other acted as a free-follower. The pneumatic system consisted of a pump, which filled a large volume reservoir, through a non-return valve. The reservoir loaded a rubber diaphragm and piston in the ball cage mounting. The piston resting on the diaphragm applied the load between the ball cage and the glass disc. The elastic diaphragm had the advantage of allowing a slight vertical displacement - which occurred as a result of slight fluctuations in the disc height during operation - whilst applying a constant load. The ball was traction-driven in nominally pure rolling, or at a required slide roll ratio by attachment of a quill drive (as shown in the figure). The means of mounting the quill drive is described below. Most fluids exhibit peak traction when the surface speeds differ by approximately 1%, after which the traction rapidly falls. Traction-driving the ball therefore implies the ball surface speed is within 1% of that of the disc. Any such minor difference will have a negligible affect on the film thickness (see §1.4).

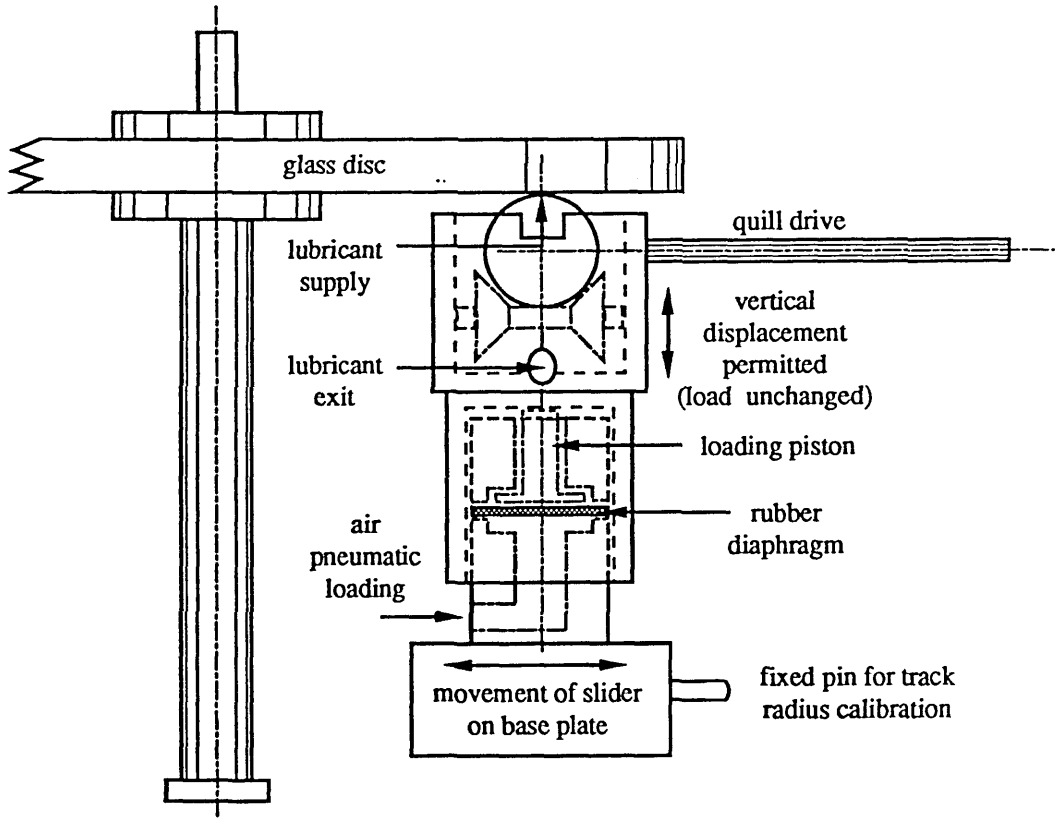
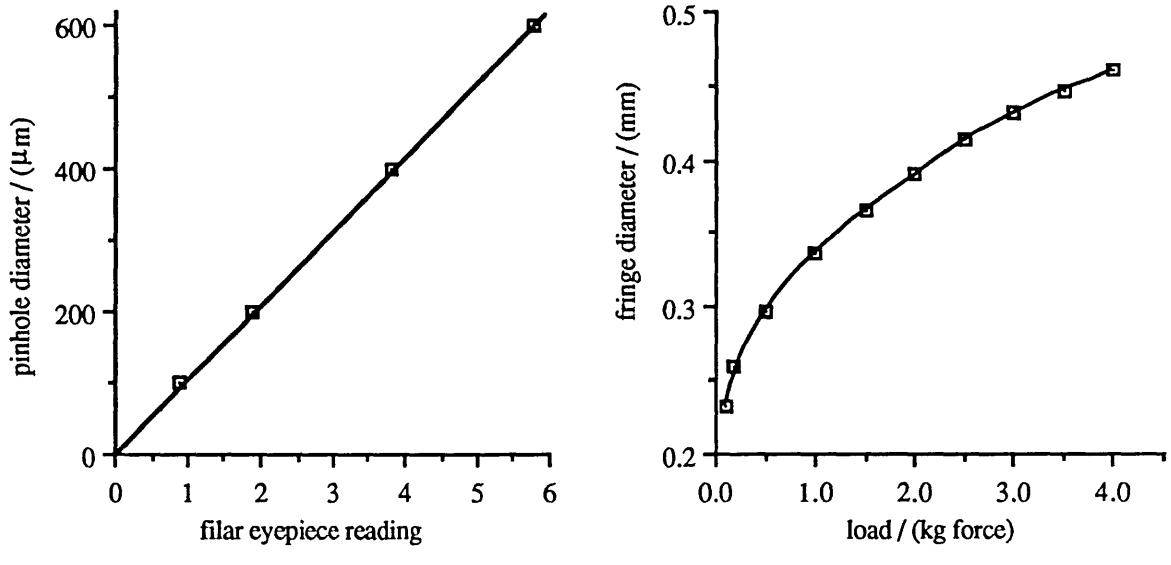


Figure 5.12 Pneumatic ball and cage loading assembly ('cotton-reel type')

The system was cross calibrated against a digital pressure gauge (John Watson and Smith Ltd., type 250) in two ways. Firstly, the dead mass required to depress the loading piston was measured as a function of the applied pressure (in the absence of the ball cage). The results are shown in figure 5.14. Secondly, a filar eyepiece was calibrated against a series of 'pin-holes' (as described in § 5.2.1.3). The eyepiece was used to measure the fringe diameter ($2\,r_f$) for the second dark fringe of the red monochromatic source (Wratten 25 filter). The loads were applied using a balance and a series of masses (§ 5.2.1.3). Figure 5.13 shows (a) the filar eyepiece calibration graph and (b) the measured fringe diameter, as a function of load.



(a) Filar eyepiece calibration

(b) Measured fringe diameter (static loading)

Figure 5.13 Filar eyepiece calibration and measured fringe diameter as a function of load

The fringe diameter measurements were repeated using the pneumatic loading system to load the ball cage assembly. Figure 5.13 (b) was used to relate the measured fringe diameter for a given pneumatic pressure (P / bar) to the equivalent dead mass load (Kg force). Figure 5.14 shows the applied pneumatic pressure against the equivalent mass load.

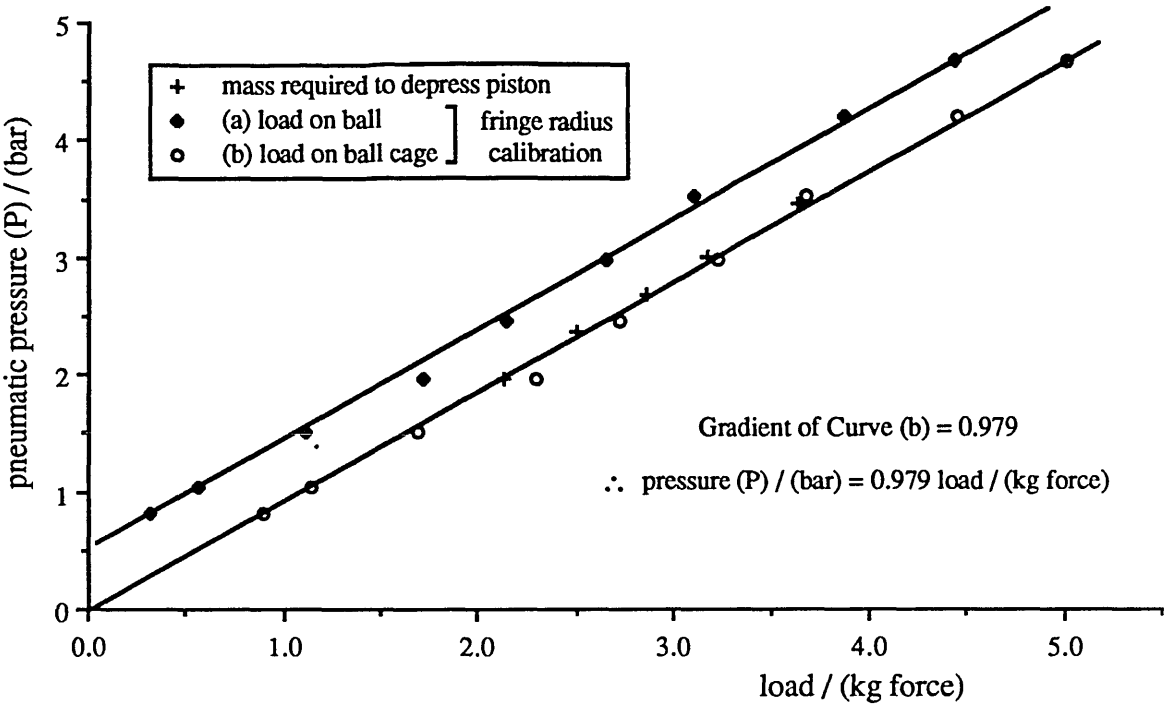


Figure 5.14 Calibration graph for pneumatic loading system

Figure 5.14 compares the two means of calibrating the applied pressure (P / bar) against the equivalent mass loading (Kg force). It is apparent that the two methods of calibration are in very good agreement. Two curves are plotted for calibration by fringe radius. A comparison of Figures 5.11 and 5.12 shows that the diaphragm / piston assembly loads the ball cage against the shaft / disc assembly, which pushes up against a thrust bearing. The ball cage assembly is therefore a 'free body' applying a force equal to its mass (0.577 kg) times g (the gravitational force constant), against the loading force. Curve (a) therefore relates the pneumatic pressure to the equivalent mass-load *on the ball.* Curve (b) - which is curve (a) displaced by + 0.577 kg on the x-axis - relates the pneumatic pressure to the equivalent mass load *on the ball cage assembly.* The force on the ball (N) is related to the applied pressure as shown in equation (XVII), which was taken from figure 5.14.

$$\text{Force on ball } /(\text{N}) = 9.81\left\{\left[\frac{\text{P(bar)}}{0.979}\right] - 0.578\right\} \qquad \text{(XVII)}$$

The track radius was calibrated against an attached micrometer in a similar way to that described in the following section. The calibration is given in equation (XVIII); R' is the micrometer reading (in inches). R_{rad} is the track radius in meters.

$$\text{Track radius } (R_{rad})/(m) = 0.0254\ (1.817 + R') \qquad \text{(XVIII)}$$

The ball loading system described above reduced the vibration associated with the previous design considerably. However the degree of accuracy required in positioning the precision bearings, upon which the cotton reels were mounted, proved to be unrealistic. A sphere is supported by contact at three points, some vibration remained as the ball alternated between three of the four ball / cotton reel contacts. For most purposes this vibration was simply a nuisance and many film thickness measurements were adequately taken using this set-up. However a more stable image was desirable, and if traction measurements were contemplated this would be essential. For this reason, the following design was adopted, in which the ball was constrained at three points and was effectively held in a fixed position. The ball holder is shown schematically in figure 5.15 and in detail in plate 5.4.

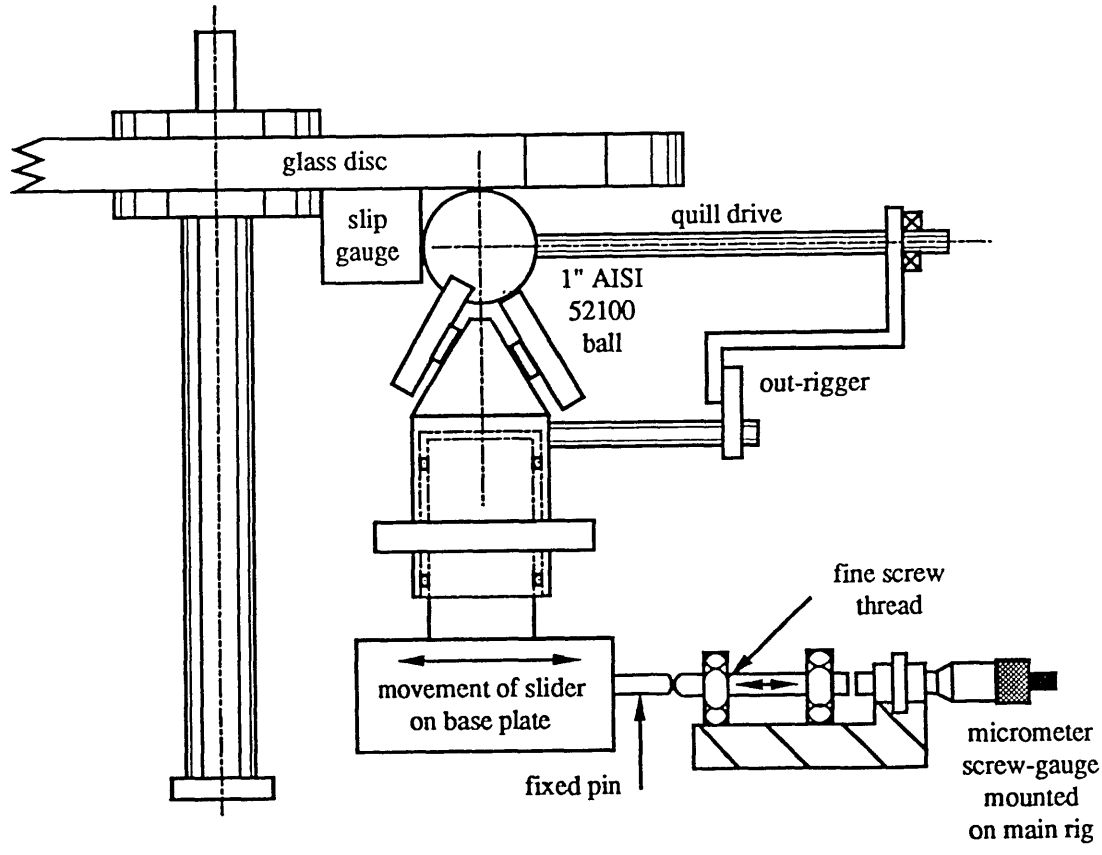


Figure 5.15 3-Disc ball mount assembly showing set-up for track radius calibration

The set-up shown above produced an extremely stable optical image. This system required the ball to be attached, through a quill drive, to a miniature precision bearing mounted on an 'out-rigger'. The out-rigger was necessary to prevent the unbalanced traction forces - which arose from the contact of the ball with the three disc-bearings - from causing the ball to spin. This also permitted the ball to be run 'skew' to the disc. This is of potential use in traction studies as an alternative way of shearing the oil film. As described previously, this system could be operated in nominally pure rolling by driving either the disc or the ball separately. Both surfaces were driven to achieve a required slide-roll ratio.

With this arrangement the applied load resulted simply from the mass of the disc and shaft (1.510 kg) and any additional masses added. Load changes due to friction in the shaft bearings may be ignored. Figure 5.15 shows the arrangement for calibrating the track radius (the previous set-up was similarly calibrated). The base plate was first set to the correct position (as described above). A slip gauge was then inserted between the shoulder of disc shaft and the test ball. The track radius was simply given by sum of the ball radius, the shoulder radius and the slip gauge width. This was calibrated against a micrometer screw gauge (which was permanently mounted on the rig). In practice a number of slip gauge widths were used and the average of the calibrations was taken. With the 3-disc ball mount a number of fixed pins (figure 5.15) were used to cover the available track radii. The track radius calibration, for a pin of length L, is given in equation (XIX).

$$\text{Track radius } (R_{rad}) / (m) = 0.0254 \ (3.183 + R' - L) \qquad \text{(XIX)}$$

Test balls were accurately mounted on quill drives using the jig shown in figure 5.16. A batch of test balls were individually held in a device designed to avoid scratching the rolling track, while a flat was ground onto the ball. A carbide tipped drill was then used to drill a 1/4" hole into the centre of the flat. However the holes were found to run off centre. For this reason the jig below was built. Firstly a 45^{o} angle was cut into the face of a solid, circular cross section block of mild steel. The central hole was drilled (7/32"), bored out using multiple passes (seven) and reamed to accept a 1/4" diameter silver steel shaft as a stiff push-fit. The end of the shaft entering the ball was turned down in a collet lathe to a loose-fit. The lathe head was then used to load the ball against the angle, which was concentric with the shaft hole. The loose-fit between the shaft and the ball was filled with

epoxy resin (Araldite) and the set-up was left overnight to set. A number of ball quill drives produced in this way were tested by rolling the shaft around in a V-block (on a surface plate) and measuring the ball eccentricity with a clock gauge. The eccentricities varied from an unmeasurably small value up to ± 0.00025".

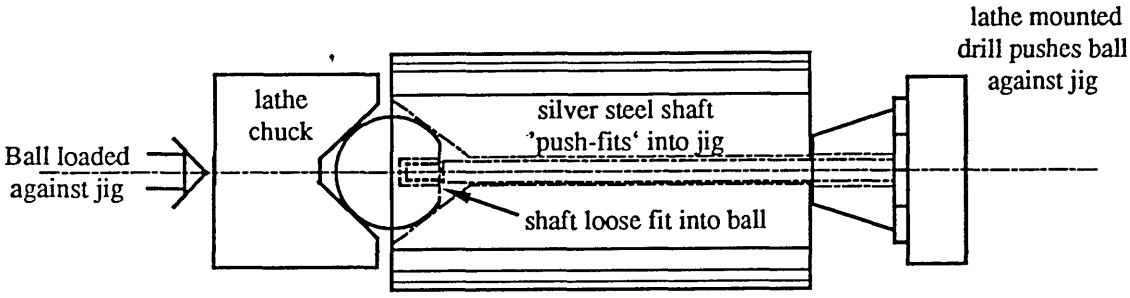


Figure 5.16 Schematic representation of jig for mounting ball on quill-drive

5.2.3.3 Motors - speed control and measurement

The ball and disc were independently driven using fast reacting regenerative 4-quadrant d.c. servo motors (Printed Motors Ltd, Borden, Hants). The maximum speeds were set to 3000 and 1000 r.p.m. respectively, by adjusting the potentiometer that controlled the motor supply reference voltages. Each motor had a back-mounted tacho-generator directly attached to the output shaft, to electrically measure the speed (BBC Brown Boveri, CEM, Dijon). This arrangement, for the ball drive, is just visible in plate 5.4. Each motors' speed was controlled and adjusted by means of an analogue servo-amplifier (Hauser Electronik, model SVC 206), powered by a mains transformer (Hauser ETS 206 V10) fitted with a current smoothing choke (Hauser 204 V10). The motor / controller assembly was put together, to the author's specifications, by HMK Technical Services Ltd, Congleton, Cheshire. Simply stated, the servo-amplifier compares the tacho output voltage (which is a highly linear function of the actual motor speed) with the reference voltage (which sets the required speed). The servo then rapidly applies the required braking or accelerating torque to match the actual speed, to that required. A ten turn helipot was used to obtain good resolution on the applied reference voltage.

The speeds of the ball drive shaft and the disc drive shaft - $(rpm)_B$ and $(rpm)_D$ respectively - were measured using an optical switch system and displayed on a digital counter. The optical switch consisted of an infrared source mounted opposite a phototransistor. A tachometer disc was mounted on each shaft; this consisted of alternate IR transparent and IR dark sections. When the shafts were driven the tacho-disc regularly interrupted the IR beam. A Schmidt trigger circuit [207] with a 9 V power source was used to operate the optical switches. The digital counter could be used to display either *shaft* speed, or the ratio of the two $[\ (rpm)_B / (rpm)_D\ ] = R_{rpm\ (B/D)}$. The *surface* speeds of the disc and the ball - U_D and U_B respectively - were calculated according to scheme (XX) below. $R_{U\ (B/D)}$ is the ratio of the surface speeds as defined below.

$$U_D/(ms^{-1}) = \left(\frac{2\pi R'}{60}\right)(rpm)_D \qquad U_B/(ms^{-1}) = \left(\frac{0.0254\ \pi}{60}\right)(rpm)_B$$

$$\therefore R_{U\ (B/D)} = \frac{U_B}{U_D} = \left(\frac{0.0127}{R'}\right)\left(\frac{(rpm)_B}{(rpm)_D}\right)$$

$$= \left(\frac{0.0127}{R'}\right) R_{rpm\ (B/D)} \qquad \text{(XX)}$$

When either the ball or the disc alone was used to traction-drive the rig in nominally pure rolling, speed holding was found to be constant within ± 0.1 rpm, i.e. ± 0.01% at 1000 rpm. Peak traction occurs when the surface speeds differ by approximately 1%. In practice it is often difficult to accurately maintain relative surface speeds within this range as one surface tends to 'drive' the other back into pure rolling. This problem was investigated for the current set-up by varying the surface speeds in this range and measuring the speed holding. Solution of the final equation in scheme (XX) - using R' = 0.0575 m and setting $R_{U\ (B/D)} = 1$ - predicts pure rolling when $R_{rpm\ (B/D)} = 4.529$. This condition was achieved, by driving the ball and the disc, and fixing U_D while U_B was varied in the range $U_B = U_D \pm 2\%$. During this operation U_D was found to vary by ± 0.06% and the ratio of the speeds was found to remain at a constant set value ± 0.06%. Therefore a maximum error in surface speeds of ± 0.12% was achievable. The relative surface speeds could therefore be controlled to within approximately 1/10 of the difference required to reach peak traction. The speed holding should therefore be more than adequate for traction studies.

5.2.3.4 Optical system

The optical system used for observing the contact interference fringes consisted of a x 10 objective lens (Leitz) and a x 10 eyepiece. Two white light (chromatic) sources were used during the current study. A tungsten filament lamp and a Halogen fibre-optic 'cold' light source (Schott). The two sources had different colour balances or 'temperatures' although this was not found to affect the colour of fringes observed with the eye. Tungsten sources have a 'warm' colour balance i.e. a bias towards the red end of the spectrum, when compared with daylight. The Schott source was supplied with a glass filter that restored a normal, daylight colour balance. With this arrangement the fringe colours could be accurately photographed using daylight colour balance film. In some cases a short duration Xe flash unit was used to photograph the 'frozen' contact; this light source also has a colour balance approaching that of daylight. The duration of the Xe flash was measured by coupling a silicon photovoltaic cell with a response time of approximately 50 ns (RS Components No. 303-674) to a digital storage oscilloscope (Gould OS 4000). Typical exposure times of 0.1 ms were found. The use of short duration flash photography is described in more detail in § 6.2.1.5.

The optical characteristics of the glass disc and the use of mono and duo-chromatic filters were described in § 5.12.1. Some typical examples of rolling contact interferograms for mono, duo and white light sources are shown in plates 5.5 - 5.7.

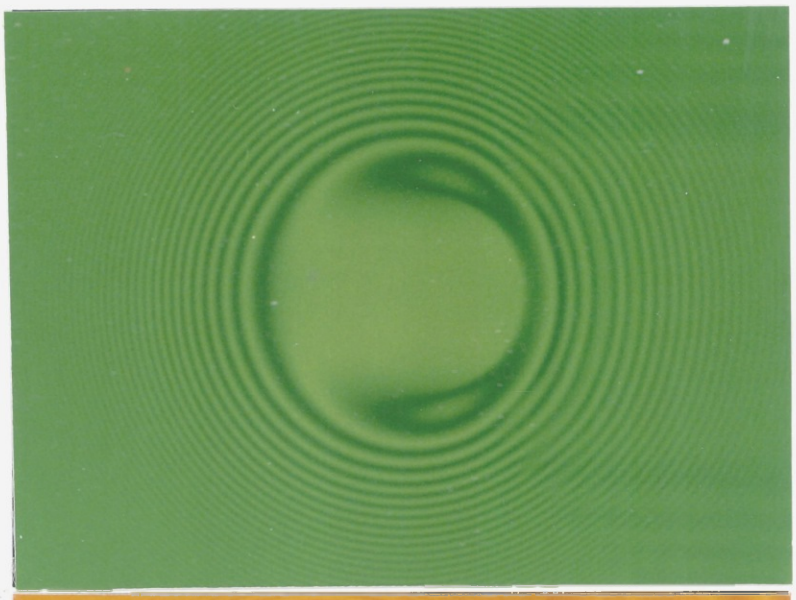


Plate 5.5
Monochromatic fringes in oil
(green source λ_{max} 546 nm).
Filters - Wratten 77A and 58.
Rolling contact.

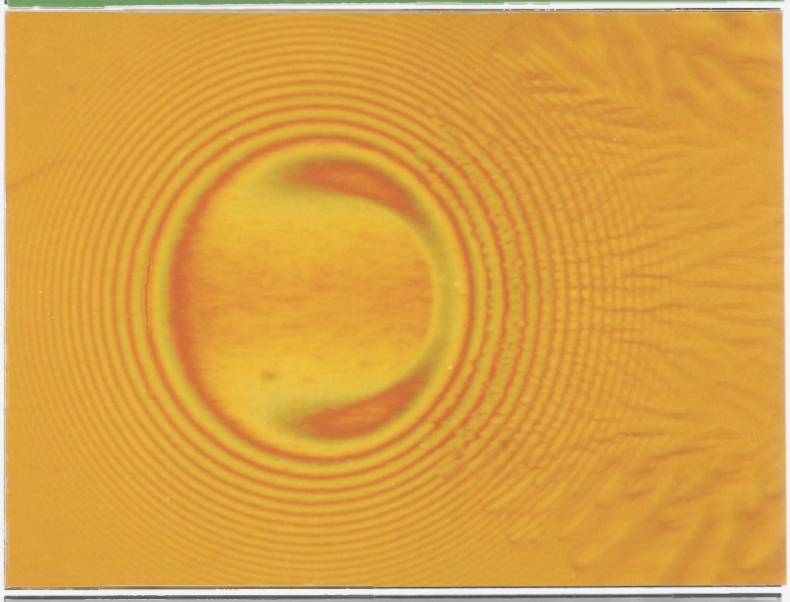


Plate 5.6
Duochromatic fringes in oil
(green and red sources).
Filter - Wratten 77A.
Rolling contact.

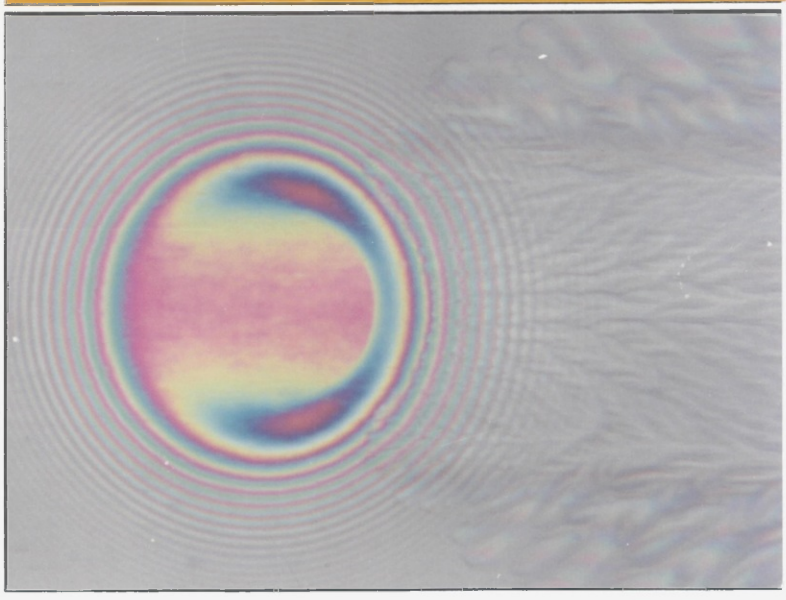


Plate 5.7
Chromatic fringes in oil.
(White light source).
Rolling contact.

5.2.3.5 Lubricant preparation - viscosity / shear rate measurement

Base stock / additive solutions were prepared by weighing the required amounts of the two components into a glass beaker and heating the mixture, with stirring. The solution was then added to the rig at the required test temperature (as described in § 5.2.4). Section 1.5 described the extreme dependence of viscosity on temperature and section 1.4 described the relationship between the EHD film thickness and the viscosity of the fluid, at the prevailing inlet temperature. An accurate knowledge of the temperature / viscosity characteristics of test fluids was therefore necessary. These measurements were taken using a rotating cone on plate viscometer (Ferranti-Shirley). This device rotates a shallow cone on a flat plate. This geometry possesses the dual advantages of a constant shear rate across the whole sample, whilst requiring a very small volume of test lubricant. The plate is connected to a thermostatically controlled glycol bath via a pump. Viscosity was therefore accurately measured, as a function of temperature. The sample temperature was indicated by a thermocouple embedded in the surface of the plate. An electronic thermometer (Comark) was used to display the sample temperature.

A series of cone sizes were used depending on the viscosity of the test fluid being measured and the required shear rate. The cone constants are given in table 5.4. Equation (XXI) gives the dynamic viscosity (η / Pa.s) as a function of the cone speed (rpm), the cone constant, and the arbitrary reading and scale setting on the viscometer.

$$\text{Viscosity /(Pa.s)} = 0.1\left(\frac{\text{cone const . x reading x range}}{\text{speed}}\right) \qquad \text{(XXI)}$$

The shear rate (D) is a function of the angular velocity (Ω) of the cone (rad / sec) = (2 π rpm / 60) and the cone angle (Ψ) measured in radians. The relationship is given in equation (XXII). These equations were used for the shear rate / viscosity measurements described in § 7.2.3.1.

$$\text{Shear rate (D) / (sec}^{-1}) = \frac{\Omega}{\Psi} = \frac{2\pi\,\text{rpm}}{\Psi.60} \qquad \text{(XXII)}$$

The temperature viscosity characteristics of a number of lubricants used in the current study are given in appendix A1.

Cone (diameter / cm)	Cone constant	Cone angle (Ψ) / (rads)
large (7)	1.1975	0.005895
medium (4)	6.7361	0.0061488
small (2)	54.9056	0.00626488

Table 5.4 Cone constants used in viscosity and shear rate calculations

5.2.4 General experimental procedure - commissioning tests for EHD rig

The rig was solvent-cleaned at the end of a test, in preparation for the next run. This was achieved by draining the previous lubricant, while hot, and pumping toluene around the rig when it had cooled. Any remaining base stock went into solution in the toluene; this solution was discarded. The procedure was then repeated, firstly with toluene and then with acetone, to remove any toluene residue. This procedure ensured that the oil retaining tank and the circulating system were completely clean. The acetone present after draining rapidly evaporated. The ball loading assembly was further solvent-cleaned in a shallow bath of toluene and then acetone (to ensure the removal of test-lubricant retained in the bearings).

A new 1" AISI 52100 ball (RHP 20 grade) was used for each test. This was ultrasonically cleaned in toluene and acetone, before re-assembling the rig and fitting the aluminium lid. The load was set to the required value, either pneumatically or through additional masses, depending on which ball mounting assembly was used. The required test temperature was set on the CAL controller and the blower was turned on. The rig was deemed to have reached equilibrium when the oil inlet thermocouple reading matched that of the CAL thermocouple. During this equilibration period the test lubricant was heated, with stirring, to the required test temperature.

A plug in the aluminium lid was removed so that the lubricant could be introduced into the chamber. The peristaltic pump was started up. The aquarium heater and the drive shaft were switched on as the oil reached the heater and the disc, respectively. The time was noted and the various experimental parameters - oil film thickness, shaft speed, temperature etc - were set to their required values. A record of the variation in these values was kept

during the course of the test. The oil film thickness was monitored, as required, by viewing the contact through a second plug-hole in the aluminium lid.

The following sections describe some commisioning tests carried out on the rig. These demonstrate some of the typical uses of the rig. The final section describes the two main test procedures used to follow the build-up if thick anti-wear films from solutions of phosphorus based additives in oil.

5.2.4.1 Effective pressure viscosity coefficient (α value) as a function of temperature

The effective pressure-viscosity coefficient (α value) can be measured, as a function of temperature, for any test lubricant, by comparison with a reference oil of known α value. The procedure used is described below. A knowledge of the variation of the viscosity and the effective pressure-viscosity coefficient with temperature is essential if the EHD film thickness is to be calculated from theory. It therefore provides valuable design data. Equation (XXII) is the Dowson and Hamrock formula [9] for calculating the central film thickness (h_c). Throughout the current work all separations (h) referred to, unless otherwise stated, are *true* central film thicknesses i.e. the optical separation (as listed in table 5.3) divided by the refractive index of the lubricant being tested. The constituent parameters in equation (XXII) were detailed in § 1.4 and in the section on nomenclature.

$$\frac{h_c}{R'_x} = 2.69 \left(\frac{U\eta_o}{E'R'_x}\right)^{0.67} (\alpha E')^{0.53} \left(\frac{W}{E'R'^2_x}\right)^{-0.067} (1 - 0.61\, e^{-0.73k}) \qquad \text{(XXII)}$$

Equivalent α values can therefore be found by comparing plots of log (h) vs. log ($\eta_o U$) for a reference oil ($\text{Oil}_{\text{REF.}}$) of known α value, and a test oil (Oil_{TEST}).

At constant ($\eta_o U$), W, E' and R_x' the film thickness is related to the α value as in scheme (XXIII). k is a constant.

$$h_{TEST} = k\,(\alpha_{TEST})^{0.53}$$
$$h_{REF.} = k\,(\alpha_{REF.})^{0.53} \qquad \text{(XXIII)}$$

Combined, these equations can be arranged to give equation (XXIV).

$$\alpha_{TEST} = \alpha_{REF.} \left(\frac{h_{TEST}}{h_{REF.}} \right)^{\frac{1}{0.53}} \qquad \text{(XXIV)}$$

The experiment was carried out as follows, on an oil (OEP 215) used by the project sponsors (MOD). The reference oil used was a mineral oil (Shell) for which $\alpha = 21.75$ GPa^{-1} at 25° C. All measurements were made in nominally pure rolling, i.e. with the disc only driven. In this case, since $U_B = U_D$, the rolling speed is simply referred to as U. The central film thickness was measured as a function of rolling speed, for the test lubricant, at a series of fixed temperatures (22, 50, 76.5 and 100 ± 1° C). A similar measurement was made on the reference oil at 24° C. In all cases a pneumatically applied load of 50 N was used (approximately 0.6 GPa maximum Hertz pressure). The temperature-viscosity characteristics for the two oils were measured using the Ferranti-Shirley viscometer (as described above). A full plot is given in appendix A1. Table 5.5 briefly summarises the temperature / viscosity data and the refractive indices measured at room temperature.

OIL	Refractive Index	Viscosity / (Pa.s) 40° C	100° C
OEP 215 (TEST)	1.4883	0.172	0.014
SHELL (REF.)	1.4890	0.020	0.004

Table 5.5 Refractive indices and viscosity data used in α value calculations

Figure 5.17 shows a plot of log h vs. log U. The values of log U were measured, for each curve, at the high and low extremes of log h. For example the curve for OEP 215 at 50° C gave the values listed in table 5.6. The viscosity information was obtained from appendix A1.

log h / (m)	log U / (ms^{-1})	$\therefore$ log ($U\eta_o$) / (N/m)	since
- 6.872	- 0.87	- 1.899	η / (Pa.s) = 0.0935
- 6.190	+ 0.128	- 0.901	logη / (Pa.s) = - 1.029

Table 5.6 α value calculation - data from figure 5.17 and appendix A1

Each of the curves in figure 5.17 was similarly treated. The data obtained was used to plot log U vs. log (η_oU) for the oils at each temperature. This is shown in figure 5.18.

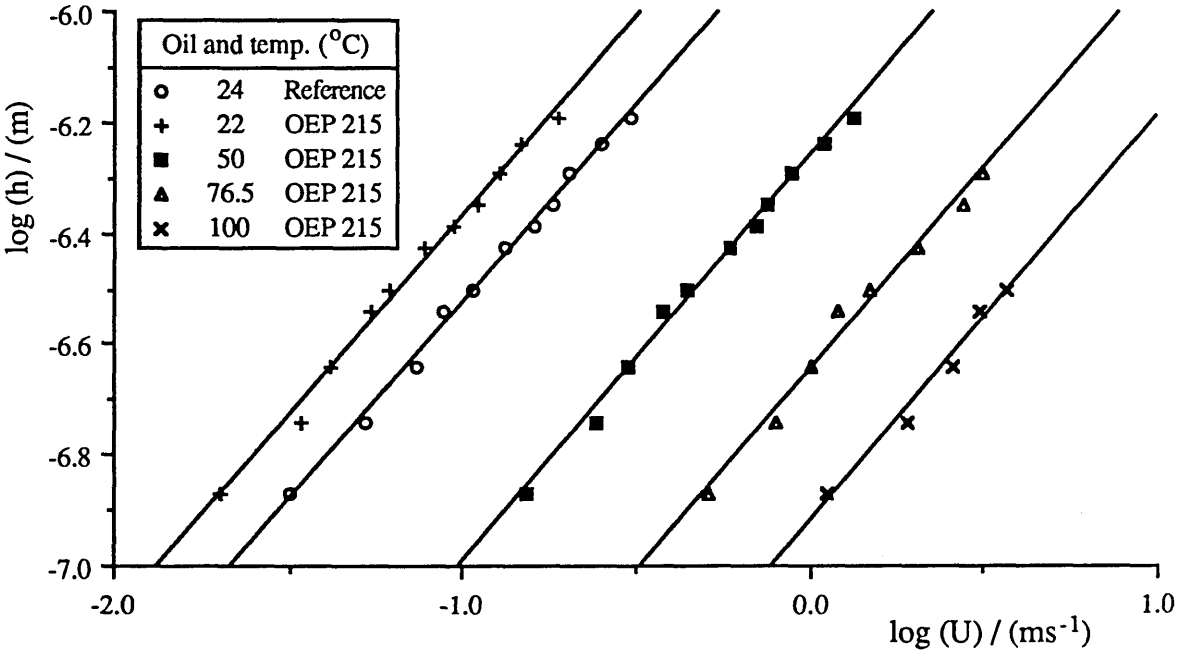


Figure 5.17 Log (h) vs. log (U), as a function of temperature (OEP 215 and Ref. oil)

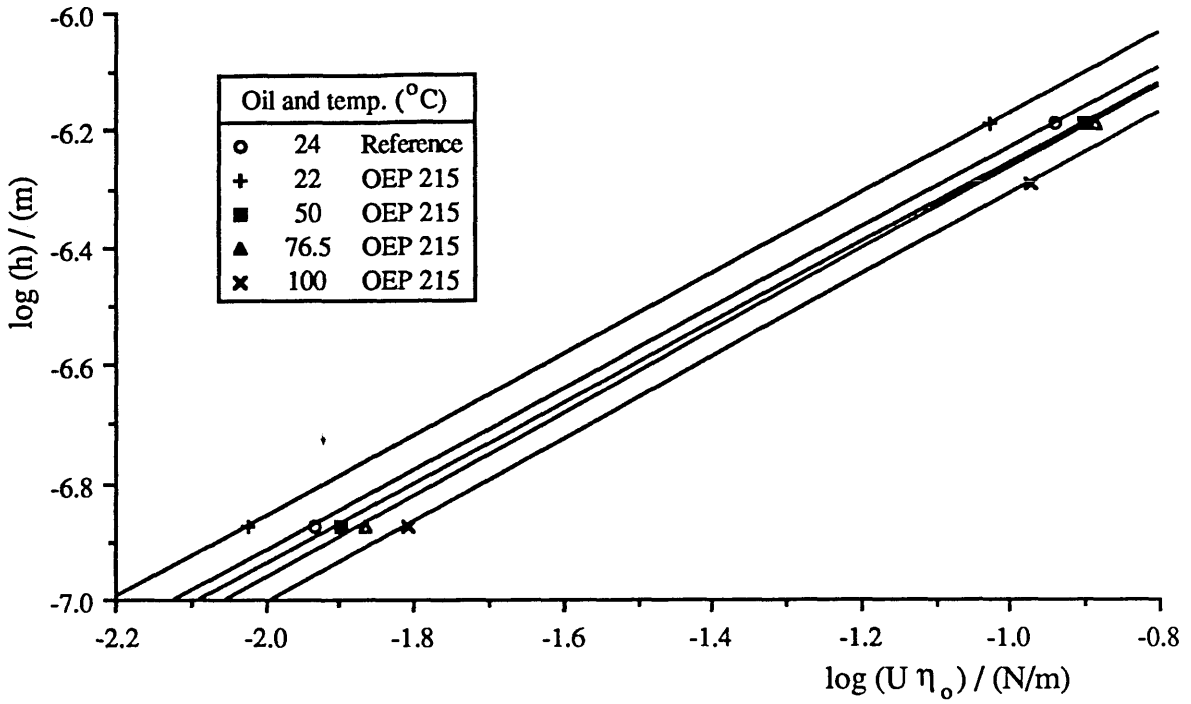


Figure 5.18 Log (h) vs. log (U η_o), as a function of temperature (OEP 215 and Ref. oil)

The curves in figure 5.18 were used to calculate the effective values of α_{TEST} (as shown in table 5.7). The values of log h given in the table were measured, from the curve, at the fixed value of $\log(\eta_o U) = -1.5\ Nm^{-1}$. It should be noted that in plotting figure 5.18 the viscosity of the reference fluid at the test temperature (24° C) was used. In calculating α_{TEST} - from equation (XXIV) - the value of $\alpha_{REF.}$ at 25° C was used as an approximation. This is reasonable since viscosity changes much more rapidly than effective α value over this temperature region.

Oil	Temp. (°C)	log h / (m)	∴ h / (nm)	$\left[\frac{h_{TEST}}{h_{REF.}}\right]$	$\left[\frac{h_{TEST}}{h_{REF.}}\right]^{1/0.53}$	α_{TEST} / (GPa^{-1})
Shell	24	- 6.574	266.6	-	-	-
OEP	22	- 6.516	304.8	1.14	1.287	28.0
OEP	50	- 6.600	251.2	0.94	0.894	19.4
OEP	76.5	- 6.617	241.5	0.905	0.830	18.0
OEP	100	- 6.658	219.8	0.824	0.695	15.1

Table 5.7 Evaluation of α values as a function of temperature (data from figure 5.18)

Figure 5.19 shows the effective α values for OEP 215 as a function of temperature. During the course of the current work a number of oils were similarly evaluated. This data is given in appendix A 1. This graph includes a plot of the synthetic hydrocarbon (SHC 234) used as the base stock in much of the current test-work. Similar measurements were made, by the author, to investigate the speed / separation characteristics and thence the pressure-viscosity coefficients of various fluids under unusual operating conditions. This included a range of simple low-viscosity fluids at cryogenic temperatures (where their viscosities were sufficiently high to produce EHD films that could be measured using conventional interferometry), a range of high performance base stocks blended to have the same viscosity at a single test temperature (to compare relative α values) and a range of low viscosity fluids using an improved interferometric technique (as described in chapter eight). Not all of these studies have been included in the current work. Full details can be found in the list of author's publications that follows the references section.

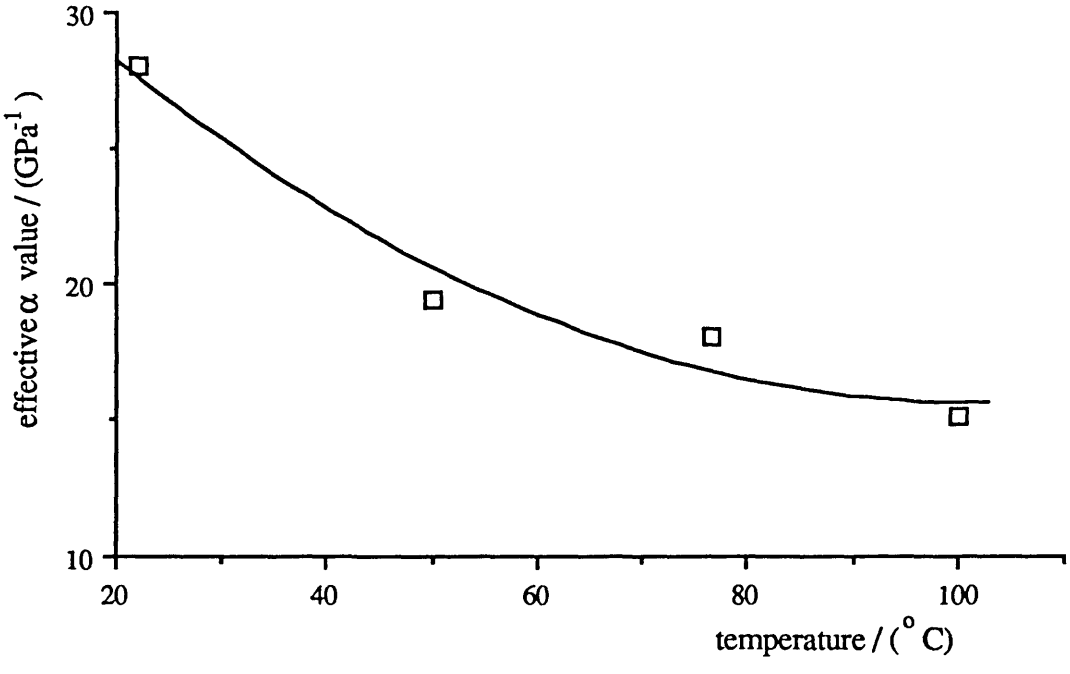


Figure 5.19 Alpha value as a function of temperature (OEP 215)

5.2.4.2 Separation as a function of slide-roll ratio (SRR)

The test rig, as described previously, may be run with the ball and the disc driven, to achieve an accurately variable degree of sliding. The relative speed of the contacting surfaces is often defined in terms of the slide-roll ratio (SRR). The SRR in turn, is defined in terms of the ball and disc speeds, as in equation (XXV).

$$SRR = \left[\frac{U_B - U_D}{U_B + U_D} \right] \qquad (XXV)$$

As explained previously, chromatic interferometry permits the film thickness to be measured at a series of discrete separations. In practice, the film thickness is a simple function of the observed central film colour - in order of increasing separation the colours are yellow, red, blue and green. As the separation increases the sequence is repeated as second order fringes and so on (this method was described in detail in § 5.2.1.5). The fringe calibration, in air, was given in table 5.3. Observation of the variation of film thickness with speed - at a constant relative speed (SRR) - would therefore require observation of the first discrete separation (yellow ~ 135 nm) at a chosen SRR. The ball and disc speeds would then have to be increased to the next observable separation (red ~ 180 nm) whilst maintaining a constant SRR. In practice, it is very difficult to maintain a constant SRR, whilst independently adjusting the ball and disc speeds.

For this reason an indirect method was developed to measure the film thickness as a function of the slide-roll ratio. It uses the relationship between the SRR and the speed ratio ($R_{U\,(B/D)}$) derived in scheme (XXVI) below.

$$SRR = \left[\frac{U_B - U_D}{U_B + U_D}\right] = \frac{U_B/U_D - 1}{U_B/U_D + 1} = \frac{R_{U(B/D)} - 1}{R_{U(B/D)} + 1}$$

$$\therefore \; (R_{U(B/D)} + 1)\,(SRR) = (R_{U(B/D)} - 1)$$

$$(R_{U(B/D)}.SRR) + (SRR) = (R_{U(B/D)} - 1) \qquad \text{(XXVI)}$$

$$1 + (SRR) = R_{U(B/D)} - (R_{U(B/D)}.SRR)$$

$$1 + (SRR) = R_{U(B/D)}(1 - SRR)$$

$$\therefore \; R_{U(B/D)} = \left(\frac{1 + SRR}{1 - SRR}\right)$$

Table 5.8 shows the derived values of the speed ratio ($R_{U(B/D)}$) obtained by substituting various slide-roll ratios into the final equation in scheme (XXVI).

Let SRR =	+ 0.5	+ 0.4	+ 0.3	+ 0.2	+ 0.1	0	- 0.1	- 0.2	- 0.3	- 0.4	- 0.5
$\therefore R_{U(B/D)}$ =	3.00	2.33	1.86	1.50	1.22	1.00	0.82	0.66	0.54	0.43	0.33

Table 5.8 Relationship between slide-roll ratio (SRR) and speed ratio ($R_{U(B/D)}$)

Central film thickness and rolling speed measurements were taken at a fixed temperature (75 ±1° C) with three mineral oils of similar viscosity. Only one is included here, as an example of the use of the rig. The oil is referred to as oil A; its viscosity / temperature characteristics are included in appendix A1. A ball-load of 50 N was used. The refractive index of oil A was measured as 1.4670.

The central film separation was measured - as a function of speed - with the ball running in nominally pure rolling ($R_{U(B/D)} = 1$). This was achieved by driving the disc alone. The resultant curve is not included, but it was of the same form as those given in figure 5.17. The surface speeds required to achieve each measured separation are summarised in table 5.9. The ball drive was then attached, and the oil was tested as follows. It should be noted that during the sliding / rolling measurements, the speed ratio recorded from the digital display was that of the shaft speeds i.e. $R_{rpm\,(B/D)}$. The surface speed ratio ($R_{U(B/D)}$) was

calculated according to equation (XX). The experiment was run at a track radius of 0.0555 m, therefore pure rolling ($R_{U\,(B/D)} = 1$) occurred when $R_{rpm\,(B/D)} = 4.368$.

The disc speed (U_D) was adjusted to that at which the first yellow fringe was observed in pure rolling, and the ball speed (U_B) was adjusted so that $R_{U\,(B/D)} = 1$. With U_D fixed, U_B (and therefore $R_{U\,(B/D)}$) was increased until the next observable separation was reached i.e. first order red. The surface speed ratio was noted at this point. This procedure was continued on through, blue, green etc. U_D was then reset and fixed at the speed at which the next fringe - first order red - was observed, in pure rolling. U_B was gradually increased through the sequence of chromatic fringes i.e. first yellow ($R_{U\,(B/D)} < 1$); first red ($R_{U\,(B/D)} = 1$), first blue ($R_{U\,(B/D)} > 1$) and so on. This procedure was repeated for each of the chromatic fringes. The crude data obtained (and the data obtained for oil A in pure rolling) is summarised in table 5.9.

ROLLING	Order (N)	1	1	1	1	2	2
	Colour	yellow	red	blue	green	yellow	red
	U_D/ (ms^{-1})	0.609	0.976	1.328	-	1.938	2.76
	log U_D/ (ms^{-1})	- 0.215	- 0.011	0.123	-	0.287	0.440
ROLLING / SLIDING	(N) / Colour	$R_{U\,(B/D)}$ (U_D fixed as above, U_B varied to fringe shown)					
	1 yellow	**1.00**	0.28	0.07	-	-	-
	1 red	2.30	**1.00**	0.42	-	0.09	0.00
	1 blue	3.73	1.72	**1.00**	-	0.43	0.16
	1 green	-	2.71	1.60	-	0.73	0.32
	2 yellow	-	3.10	1.83	-	**1.00**	0.50
	2 red	-	-	-	-	1.72	**1.00**

Table 5.9 Oil A - crude data for pure rolling and rolling / sliding studies

The data given in table 5.9 was used to plot a graph of the form shown in figure 5.20.

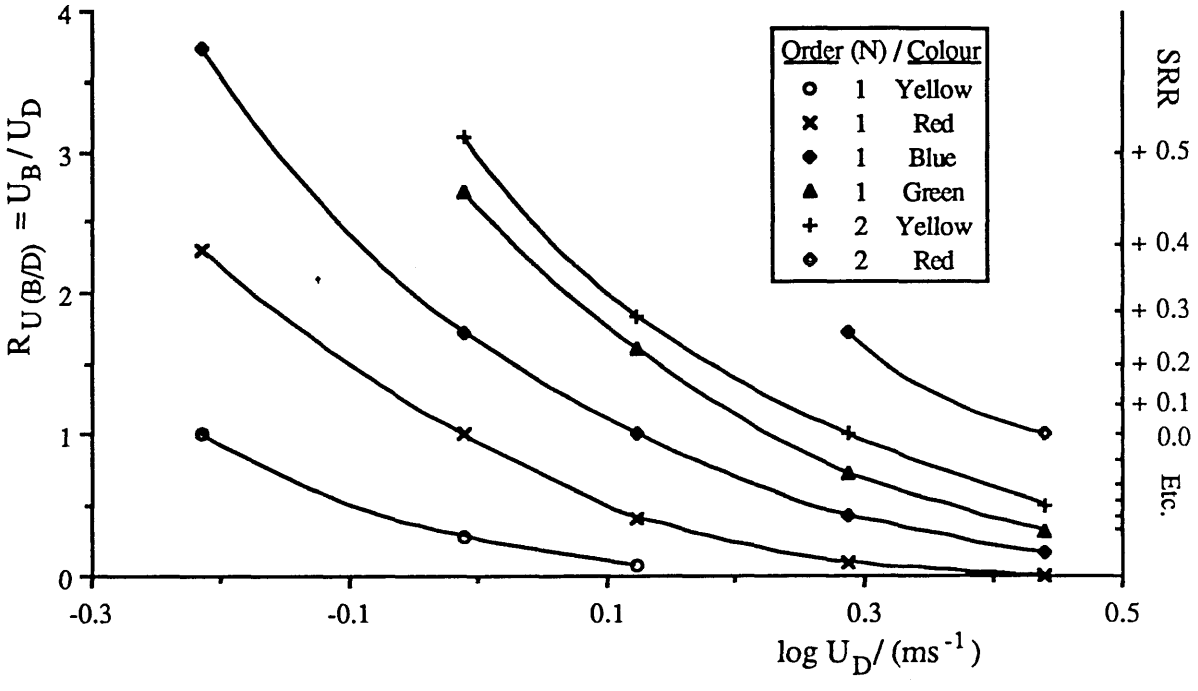


Figure 5.20 Oil A - speed ratio ($R_{U\,(B/D)}$) vs. log speed

A log separation vs. log rolling speed graph, at a series of fixed SRR, could then be generated from figure 5.20 by employing the derived relationship between $R_{U\,(B/D)}$ and SRR. For example, from scheme (XXVI), a SRR of - 0.1 corresponds to $R_{U\,(B/D)} = 0.82$ (see table 5.8). A horizontal line drawn at $R_{U\,(B/D)} = 0.82$ crosses in turn the first order yellow contour where U_D would lead to a separation corresponding to first order yellow, then the first order red contour and so on (in all cases with SRR = - 0.1). Setting $R_{U\,(B/D)} = 1.22$ generated a similar line for SRR = + 0.1. The data obtained from figure 5.20 is summarised in table 5.10.

		log (U_D) / (ms^{-1} x 10^{-2}) as a function of SRR (data from figure 5.20)										
		SRR										
(N) / Colour		+ 0.5	+ 0.4	+ 0.3	+ 0.2	+ 0.1	0	- 0.1	- 0.2	- 0.3	- 0.4	- 0.5
1	yellow	-	-	-	-29.4	-25.5	-21.6	-17.7	-14.2	-10.7	-6.5	-3.5
1	red	-29.5	-21.6	-16.0	-10.9	-6.2	-1.8	2.3	6.0	9.7	13.9	17.0
1	blue	-16.0	-9.0	-3.2	2.4	7.5	12.2	16.6	20.8	24.9	29.2	33.0
1	green	-3.6	2.5	8.3	13.4	18.2	22.5	26.6	30.6	34.7	39.5	43.0
2	yellow	0.5	5.7	11.8	17.6	23.3	28.2	33.1	38.1	4.25	47.2	50.5
2	red	-	-	25.6	32.1	38.2	44.0	-	-	-	-	-

Table 5.10 Log (U_D) as a function of SRR (data from figure 5.20)

The data in table 5.10 was used to plot the variation of log separation vs. log speed, at a series of fixed slide-roll ratios (figure 5.21).

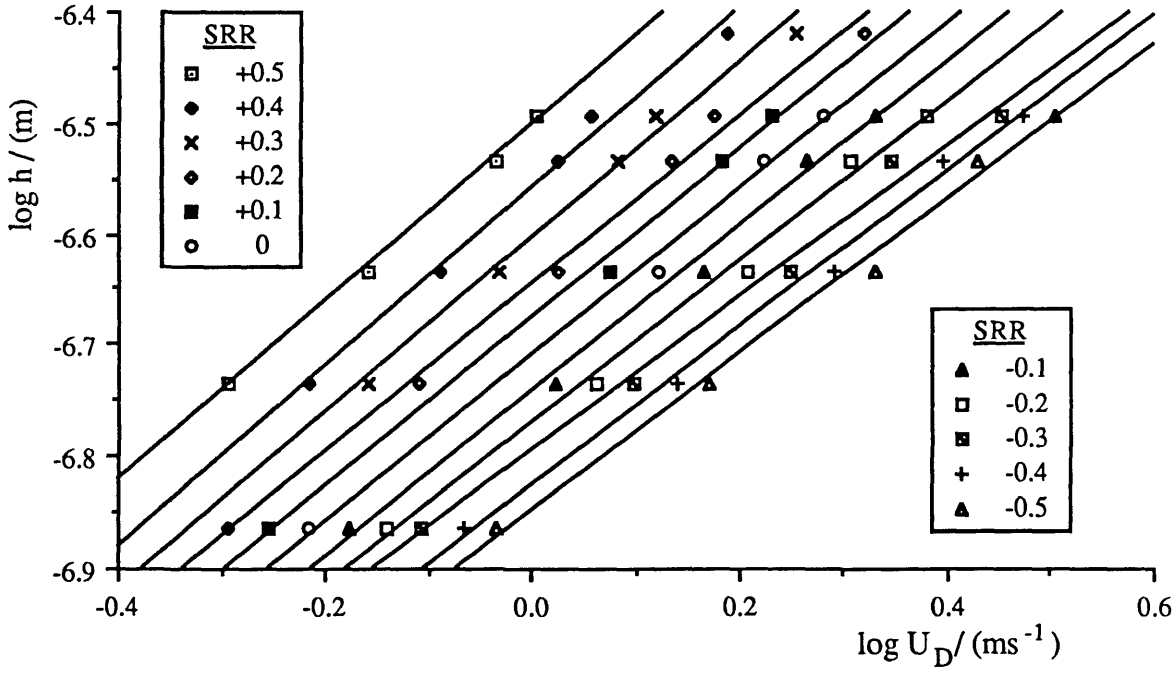


Figure 5.21 Oil A - log (separation vs. speed) as a function of SRR

EHD theory (§1.4) predicts film thickness to be a function of the *average rolling speed* [(U_B+U_D) / 2)] and to be independent of the *degree of sliding* (U_B - U_D). The relationship below (equation XXVII) allowed this to be tested.

$$R_{U(B/D)} = \left(\frac{U_B}{U_D}\right)$$

$$\therefore \left[\frac{(U_B + U_D)}{2}\right] = \left[\frac{(R_{U(B/D)} \cdot U_D + U_D}{2}\right] \qquad \text{(XXVII)}$$

Equation (XXVII) was used to calculate the values of [$(U_B+U_D) / 2$] at a series of fixed separations or fringe colours, over a wide range of U_B and U_D. This calculation was done for each data point shown on figure 5.20. Table 5.11 contains an example of the calculation of average speed, for the various combinations of U_B and U_D at which the first order red fringe was observed. The film thickness corresponding to this fringe was (270 nm / 1.4670) = 184 nm, i.e. log h = - 6.743). The data obtained was used to plot a graph of log separation against log (average speed); the data is shown graphically in figure 5.22. In figure 5.22 and table 5.11 the symbols refer to the at the fringe colour observed at the current value of U_D, but with $R_{U\,(B/D)} = 1$ i.e. in pure rolling. This is consistent with figure 5.20 from which the data was taken. The graph shows the theory to hold good within the experimental errors involved. [$(U_B+U_D) / 2$] can be seen to be largely constant, at any given separation, for widely varying U_B and U_D.

Symbol	$U_D / (ms^{-1})$	$R_{U\,(B/D)}$	$\left[\frac{R_{U(B/D)} \cdot U_B + U_D}{2}\right] / (m)$	$\therefore \log\left[\frac{U_B + U_D}{2}\right] / (m)$
o	0.609	2.30	1.005	0.0021
×	0.976	**1.00**	0.976	- 0.011
◆	1.328	0.42	0.943	- 0.023
-	-	-	-	-
+	1.938	0.09	1.056	0.023
◇	2.760	-	-	-

Table 5.11 Calculation of average speed at which first red fringe was observed

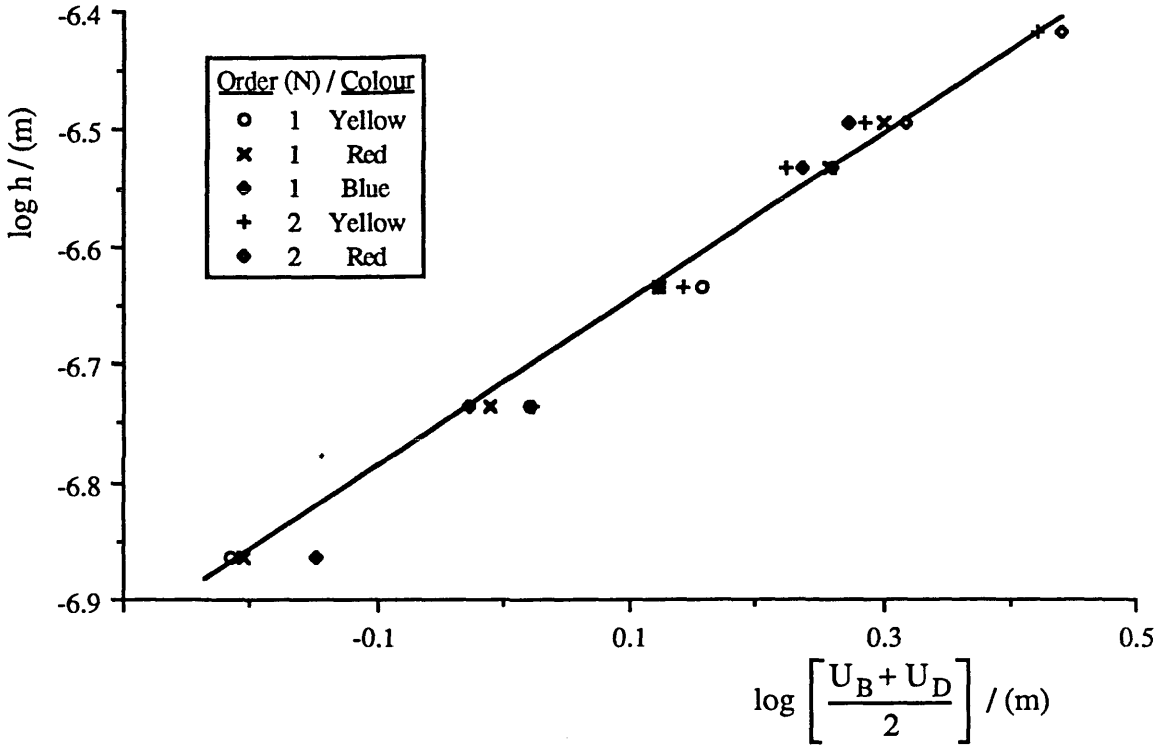


Figure 5.22 Oil A - log separation vs. log average speed

5.2.4.3 General test procedure for monitoring thick film formation

In general, two distinct procedures were used to follow the build-up of thick reacted layers within the EHD contact. The two procedures are referred to as *constant separation* (h) and *constant speed* (U) respectively. Chapter six contains numerous examples of the two procedures.

In the first procedure, a constant central film thickness or colour was maintained throughout the test. The film thickness (h_o) was set at the start of the test - in the absence of any reacted layer - and this separation was maintained throughout the test by reducing the rolling speed (U) as required. Initially, the separation (h_o) resulted from an EHD generated film (h_{EHD}). However, as the test continued, a thick chemically reacted film (h_{CHEM}) formed in the contact. If the assumption is made that the chemical film thickness is independent of the oil film thickness - and the oil inlet conditions remain unaltered - then the EHD film thickness can be calculated from equation (XXVIII). This assumption is shown to be valid in § 6.2.1.4. The subscripts o and t refer to the start of the test (at time = 0) and a time t during the test, respectively.

$$h_{EHD\ t} = h_o \left(\frac{U_t}{U_o} \right)^{0.67} \qquad \text{(XXVIII)}$$

The thickness of the reacted layer (h_{CHEM}), any time t, may then be calculated from equation (XXIX).

$$h_{CHEM\ t} = h_o - h_{EHD\ t} \qquad \text{(XXIX)}$$

The procedure described above is to be preferred, since it provides a continuous measurement of film build-up. However, as Lacey et al point out [28], this method does give rather higher scatter than the constant speed technique. This results from the fact that optical interferometry gives the film thickness to ± 15 %, which corresponds to a change in speed of ± 22 % [28].

In the constant speed technique, the inlet conditions were fixed and a known, initial film thickness (h_o) was set by adjusting the speed. The inlet conditions were then fixed for the remainder of the test, so that any additional film thickness resulted from a reacted, chemical layer in the contact. The chemical film thickness could then simply be calculated by subtracting the initial film thickness (h_o) from that observed at some time t (h_t). This technique suffered from the dual disadvantages of providing relatively few data points and of increasingly poor visibility at very high film thicknesses (§ 5.2.1.2). These limitations are both imposed by the technique of chromatic interferometry, although a reduced scatter does result.

It is clear that the chemical film thicknesses observed are dictated by the physical properties of the film under the extreme conditions present in an EHD contact. For example, the presence of mixed EHD / chemical film will alter the refractive index of the separating medium (from that of the base oil). However, changes in the refractive index alone could not produce the observed film thickness variations. In fact the chemical films have been shown to have refractive indices close the base oil (§ 7.2.3.1). The physical properties of the film material are considered in more detail in chapters 6 and 7.

5.3 High frequency reciprocating (HFR) test device

The optical rig described above permitted continuous observation of the chemical film growth in the contact zone. However, the technique used to monitor the film growth - optical interferometry - requires one transparent surface and a minimum film thickness of the order of hundreds of nanometers. For this reason, two test rigs were used that employed a more realistic contact metallurgy, and which operated in the boundary regime. The rigs used were a high frequency reciprocating (HFR) rig, as described below, and a mini-disc machine (§ 5.4).

The HFR rig is shown schematically in figure 5.23. The rig may be operated with any required contact geometry. Figure 5.23 shows the contact used in the current work - the point contact of a moving ball, on a stationary flat. The ball was oscillated, repeatedly over a chosen stroke length, at a pre-set frequency. The small volume of test lubricant (~ 3 cm^2) was enclosed in an oil bath, so that the reciprocating contact ran fully-flooded. The temperature of the test lubricant was increased, as required, by heating elements in a retaining / heating block. The ball was loaded against the flat by a dead-weight hung from the vibrator-arm. The electrical contact resistance (ECR) and the coefficient of friction (μ) were monitored continuously during operation in two ways. The variation within each stroke was displayed on an oscilloscope. This permitted any breakdown of the insulating film or any stick-slip within the stroke to be observed. In addition, a chart recorder (Rikadenki) was used to keep a permanent record of changes in the 'average' ECR and coefficient of friction, during the course of a test. Contact wear was monitored by measuring the wear scar, on the flat, after testing. A stylus profilometer (Talysurf IV, Taylor-Hobson Ltd) was used for wear scar measurements.

The following section briefly describes the calibration of the HFR rig. The experimental variables (vibrator stroke length / frequency, temperature etc) were set using an electronic control system built specifically for the rig. The measurement of ECR and coefficient of friction was incorporated in this set-up. Full details of the controlling 'logic' are not included here; these can be found in [208]. The experimental work carried out using the rig is detailed in chapters six and seven.

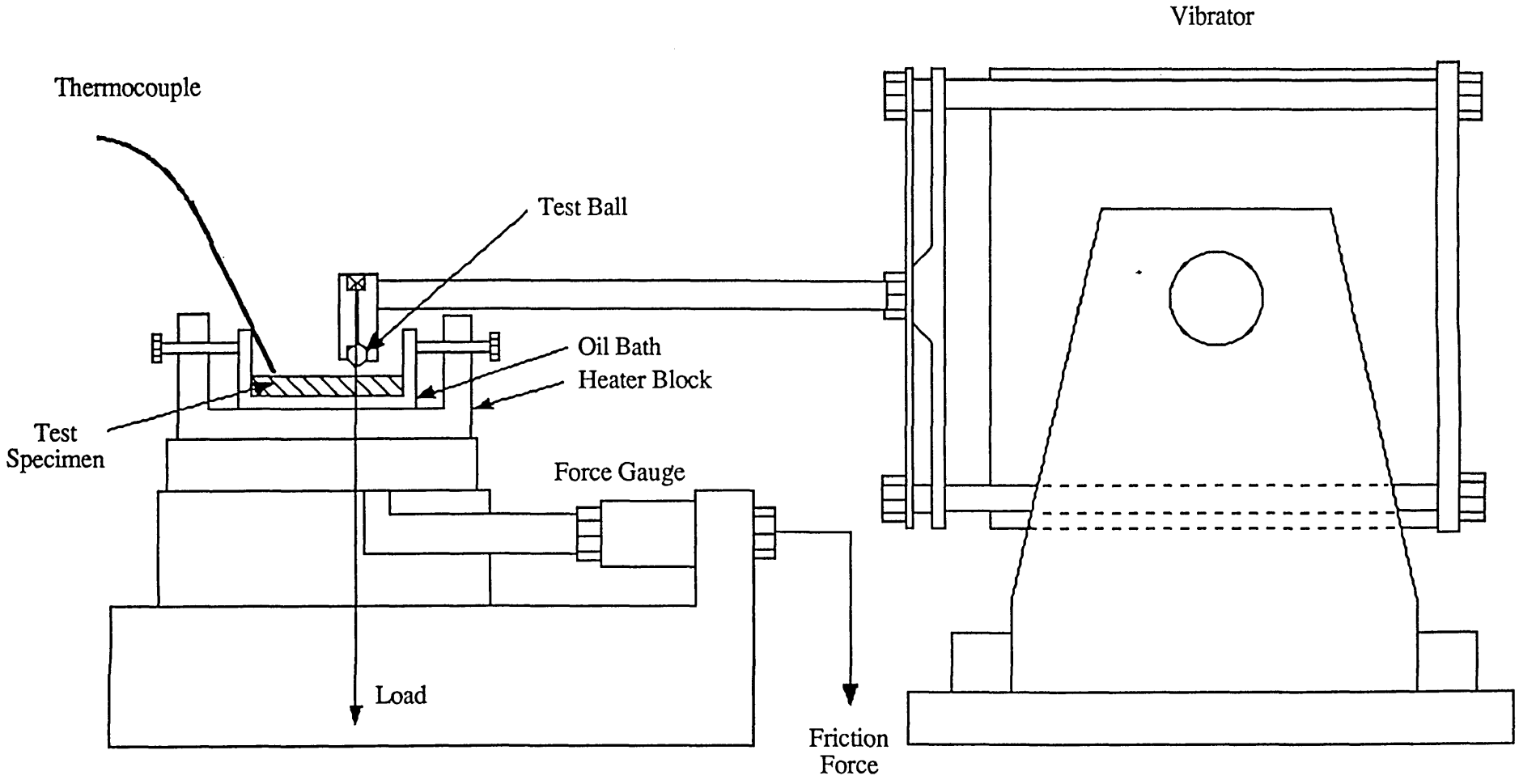
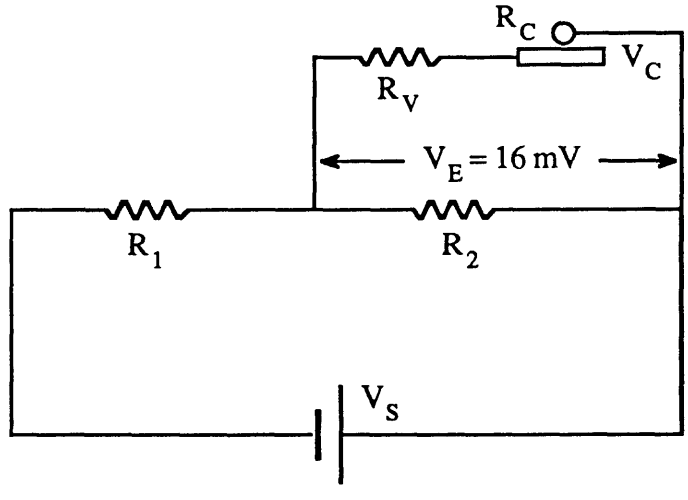


Figure 5.23 - Schematic diagram of High Frequency Reciprocating (HFR) Rig

5.3.1 Calibration of HFR rig

Electrical contact resistance (ECR) may be used as a qualitative measure of thick film growth within a rubbing contact. The rapid development of a high contact resistance has been shown to occur at a particular, repeatable temperature for a number of phosphorus and sulphur based additives [209], [210]. An increased ECR has also been shown to correlate well with reduced wear [209], [211]. For this reason an increased ECR has been tentatively concluded to imply the formation of a separating film of reacted material. However, it is impossible to infer separations from the measured ECR due to the extremely variable resistivities of reacted films [212].

The set-up used to measure ECR in the HFR rig is shown in figure 5.24. The supply voltage (V_S) and the resistors R_1 and R_2 were fixed such that $V_E = 16$ mV. According to Crook [213] the voltage applied across the contact should be kept well below 0.5 V, to avoid voltage discharge or 'tunneling'. The HFR controller included a variable resistor (R_V) in series with the contact. In practice this consisted of two calibrated, independently variable resistors (0 - 10 and 0 - 100 KΩ). The controller simultaneously displayed V_E, V_C and R_V from which the contact resistance could be calculated according to scheme (XXX).



$$\frac{V_C}{V_E} = \frac{R_C}{R_V + R_C}$$

$$V_C(R_V + R_C) = R_C V_E$$

$$V_C R_V + V_C R_C = R_C V_E$$

$$R_C(V_C V_E) = -V_C R_V$$

(XXX)

$$\therefore R_C = \left(\frac{R_V + V_E}{V_E - V_C}\right)$$

Figure 5.24 Schematic representation of set-up used to monitor electrical contact resistance (ECR) in high frequency reciprocating test-rig

The stroke length was calibrated against the arbitrary setting on the controller as follows. The rig was set up and run, at a series of fixed loads, at various controller stroke length settings. The distance traversed by the ball was measured by observing the movement of a point on the ball holder with a filar eyepiece. The eyepiece was calibrated as described previously (§ 5.2.1.3). Figure 5.25 shows the distance travelled by the ball as a function of the controller setting, at a series of loads. From figure 5.25, a stroke length of 1 mm (i.e. ± 0.5 mm) corresponded to a stroke length setting of 0.22 (at a load of 0.5 kg).

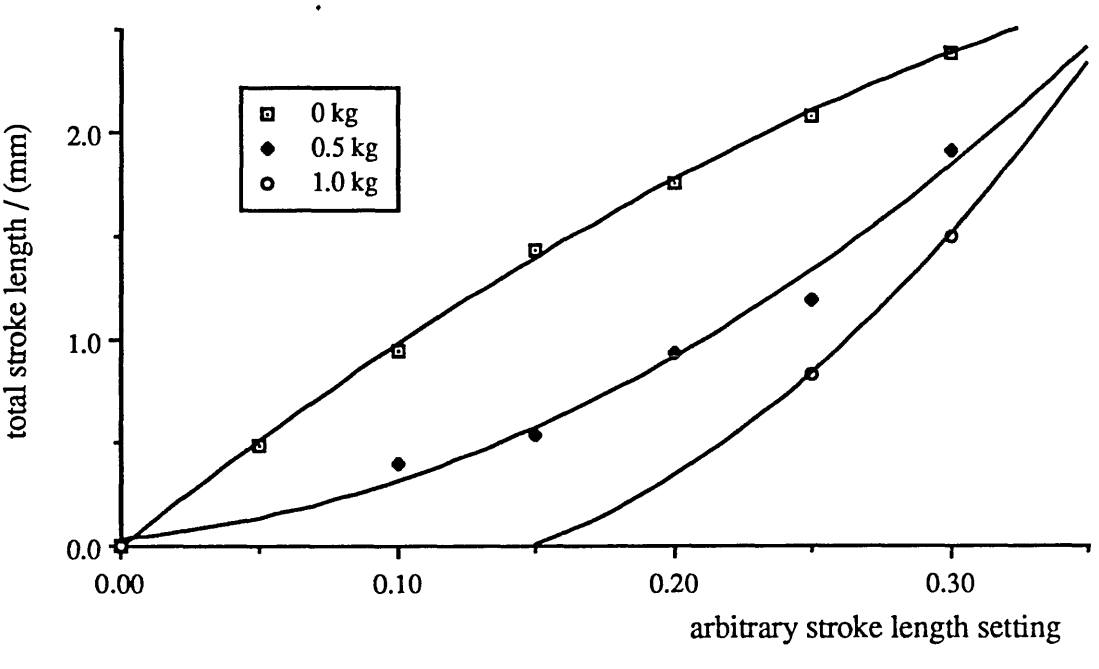


Figure 5.25 HFR rig - calibration of stroke length

The operating temperature was selected by setting a digital readout in the controller. The controller powered heating elements in the retaining block. A thermocouple mounted in the block switched the power in and out to maintain the required temperature. However, if was found that a second thermocouple placed directly in the test lubricant consistently under-read the block temperature (by ~ 6° C at 40° C and by ~ 14° C at 220° C). For this reason a slight 'over-temperature' was set on the block as required. In the HFR tests the temperature referred to is that of the test lubricant.

The stroke frequency was also selected via a digital readout on the controller. The frequency was shown to be accurate by cross-checking with an oscilloscope.

The coefficient of friction (μ) was measured via a pre-calibrated [214] piezo-electric force gauge. When loaded, a piezo-electric crystal produces a charge proportional to the applied load. This charge was measured by the control unit and converted into an output voltage.

5.3.2 Sample preparation and test procedure

The ball, flat, vibtator arm and oil bath were solvent cleaned in toluene and acetone prior to testing. A 6.35 mm diameter AISI 52100 ball was used. The flat consisted of a piece of EN 31 steel bar (3/4 x 1/8"). AISI 52100 and EN 31 are equivalent US and UK steel specifications (see table 7.3). The flats were cut into approximately 3/4" squares prior to sequential grinding on a metaserve polishing wheel. The specimens were ground to a mirror finish on two cloth-covered polishing wheels impregnated with 6 μm and 1 μm diamond powders respectively. The final polishing processes employed a circular motion, against the rotation of the wheel, to ensure that a randomly distributed roughness resulted. This process produced a surface finish of 0.1 μm R_a (CLA), when measured using a cut-off of 0.25 mm i.e. approximately a contact width.

The test procedure used was as follows. The flat was secured in the oil bath and the test lubricant (3 cm^2) was added. The ball was secured in the vibrator-arm and this assembly was left resting on the flat until the lubricant reached the required test temperature. The ball was then loaded against the flat and the vibrator was started. The ECR and friction were monitored throughout the test. The ball was typically oscillated over a horizontal stroke length of 1 mm (i.e. $\pm$ 0.5 mm) at 50 Hz, under a load of 0.5 kg. Wear scar analyses were performed after cooling and solvent cleaning, at the end of the test.

The results of the HFR testing and the details of the test lubricants used etc are given in chapter six (§ 6.2.1.3 and 6.3.1.1).

5.4 Mini-disc machine

A capacitance bridge set up was used to measure film thickness in a mini-disc machine, in an attempt to study phosphonate ester film formation under realistic contact conditions. The experimental set up is shown schematically in figure 5.26.

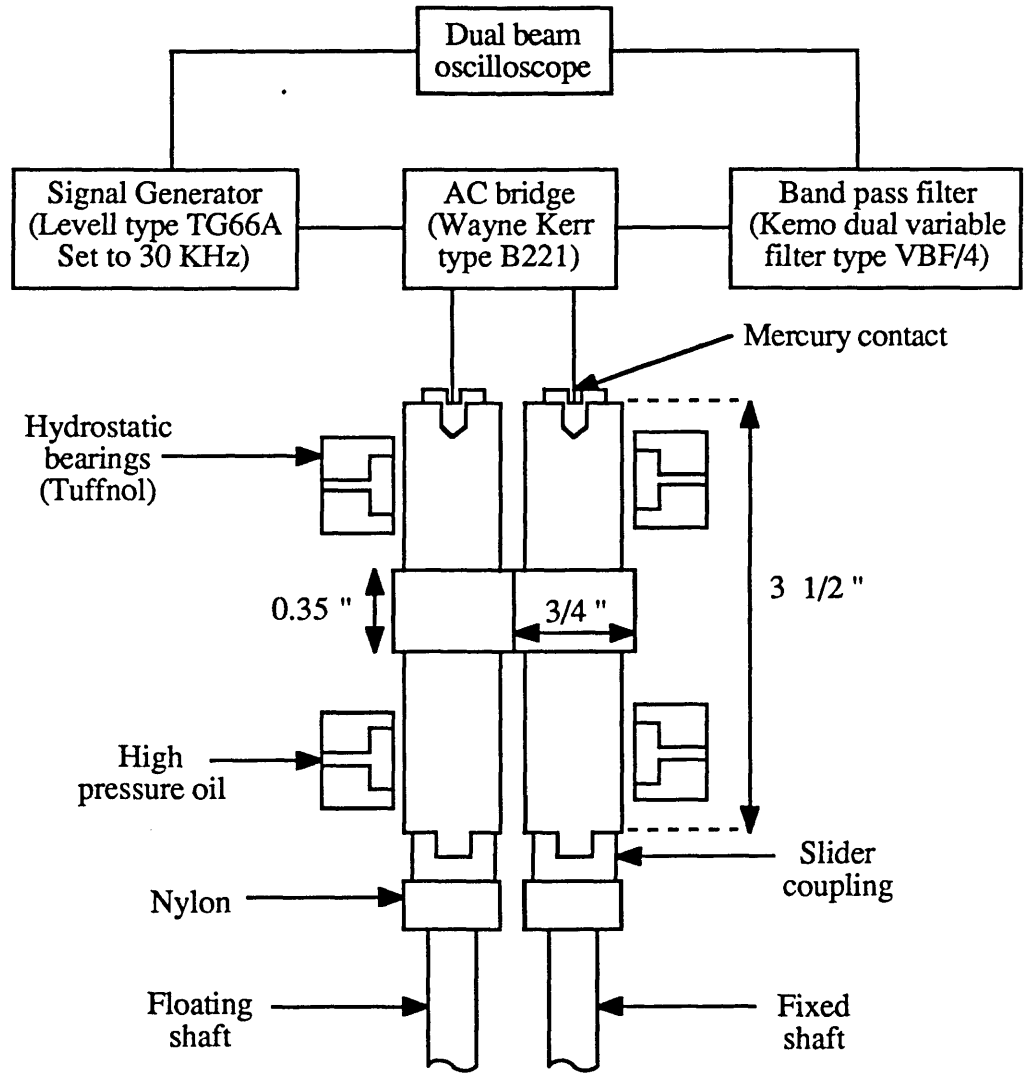


Figure 5.26 - Schematic diagram showing mini-disc machine and capacitance bridge set-up

The specimens were loaded together at 180° by hydrostatic 'pad' bearings (through which the test lubricant was supplied at high pressure). The discs speeds were variable over the

range 0 - 3000 rpm (~ 0 - 3 ms^{-1}) upto a maximum slide-roll ratio of 0.66 (i.e. one disc rotating at half the speed of the other). Electrical isolation was achieved by using a nylon coupling and 'Tuffnol' hydrostatic bearings. The rig typically operated with oil inlet temperatures in the range 30-40° C. A minimum of 5 litres of oil was required to run the test-rig.

Capacitance was converted to film separation as described in [215] and [216]. In all cases, the viscosities and dielectric constants used to calculate the film thickness were those of the bulk oil at the prevailing temperature, as measured by a trailing thermocouple. Variation of dielectric constant with pressure was not investigated, but neglect of this is considered to lead to an underestimate of film thickness of 10 - 20 % [216]. Two sets of tests were run, at a series of slide-roll ratios, on the base stock and the base stock plus 1 % mono-dodecyl phosphonate (synthesised as described in chapter 4). Details of the contact conditions and the measured film thicknesses are given in § 6.2.2.1. Only brief experimental details have been included here as the experiment was carried out by a final year student, on the authors behalf. Full details may be found in the students final report [216].

CHAPTER 6 - PERFORMANCE TESTING OF ORGANOPHOSPHORUS ESTERS

6.1 Introduction

The following chapter describes the testing of a range of organophosphorus esters in a number of test rigs (see chapter 5). The test devices were chosen to represent the range of lubrication regimes encountered in practical situations. The aim of the studies described in the current chapter was to demonstrate the presence and test the effectiveness of reacted layers generated in the presence of additives. The physical and chemical properties of the films formed are the subject of chapter 7.

The work described in this chapter is organised along the lines of chemical type. Section 6.2 deals with esters derived from phosphonic acid $(HO)_2P(O)H$; section 6.3 deals with esters based on phosphoric acid $(HO)_3P(O)$. The performance of each of the 'families' that constitute these two broad groupings is then described for a range of operating conditions, lubrication regimes etc. Synthetic details of the additives produced by the author and the sources of the other additives used, can be found in chapter 4.

6.2 Esters of phosphonic acid - $(HO)_2P(O)H$

6.2.1 Di-alkyl / aryl phosphonates $(RO)_2P(O)H$

The work of Lacey [76] consisted of a systematic study of the build-up of thick films with a range of di-alkyl and aryl phosphonates. However this work [76] was limited to full fluid-film EHD contacts (at elevated temperature). The following tests extended this study to examine the importance of other additives typically included in fully formulated oils (§ 6.2.1.2). The maximum additive-film thickness obtained previously was shown to be depletion controlled (§ 6.2.1.1). The role of these additives in boundary lubrication was also investigated (§ 6.2.1.3). In addition, the physical nature of the film material was investigated within an operating contact (§ 6.2.1.4 and § 6.2.1.5) and by indirect means after testing (see § 7.2).

6.2.1.1 Maximum film thickness / depletion of additive (BOPP)

The maximum additive-film thickness observed optically, at elevated temperature, was reported in [76] to be of the order of 300 nm. This was further investigated using the early EHD rig described in § 5.2.2. A 'constant U' test (see § 5.2.4.3) was run, in nominally pure rolling, using a 3 % w/w solution of BOPP in a synthetic hydrocarbon base stock (SHC 234). The viscosity and the effective pressure-viscosity coefficient (α value) were measured, as a function of temperature, by the author. This data is summarised in appendix A1 and table 6.1. The experimental conditions were chosen to match those used by Lacey [76]. The experiment was run at 100° C using approximately 65 g of lubricant and a supply rate of approximately 25 cm^3 / min. A load of 15 N was used. When the oil inlet temperature was stable at 100° C the rolling speed was fixed to ensure a constant oil-film thickness. Any additional separation was therefore due to an additive-generated film. Full details of the experimental procedure were given in sections 5.2.2.1 and 5.2.4.3.

The results of the test were similar to those observed previously by Lacey [76]. A gradual increase in film thickness up to approximately 200 nm was observed over a period of approximately 100 minutes. No further increase occurred after this time. An identical, unused ball was then substituted for the original ball. The test was continued at 100° C, using the original lubricant. No further film growth was observed. The absence of further film formation could be explained in a number of ways. Depletion of the 'active' thick film forming agent would account for the observed absence of further growth; although depletion of bulk additive is unlikely (as explained below). Further polymer formation might also be limited by the rate of formation / diffusion of Fe (III) species at the surface. However, further growth might be expected, if this were the case, with an untreated ball. Finally, the severe conditions of shear etc. present in the contact might limit the maximum surviving film thickness. The following experiment was designed to determine which of these alternatives was operating.

The experiment above was repeated using 0.85 g of BOPP in 65 g of SHC 234 i.e. a 1.29 % solution w/w. A single, new ball was used. The results are shown in figure 6.1. A rapid additional film thickness of approximately 150 nm was observed to build-up during the first 100 minutes of the test. This value gradually increased to the limiting value of

~ 200 nm during the second 100 minutes of the test. At this point an additional 1.01 g of BOPP was directly added to the lubricant sump. Over the next 45 minutes the film thickness increased very rapidly to exceed 730 nm. Chromatic interferometry is not well suited to the observation of very thick films (see § 5.2.1.7) and at this point the image became unclear, although the film thickness increase appeared to continue. The poor image quality may also be explained by the non-uniform film distribution (see § 6.2.1.4 and § 7.2). During the test the film thickness increased from the initial EHD film thickness of ~ 187 nm (observed as the first order red fringe) up to a maximum of ~ 730 nm (fourth order yellow fringe) i.e. a chemical film thickness of ~ 540 nm plus.

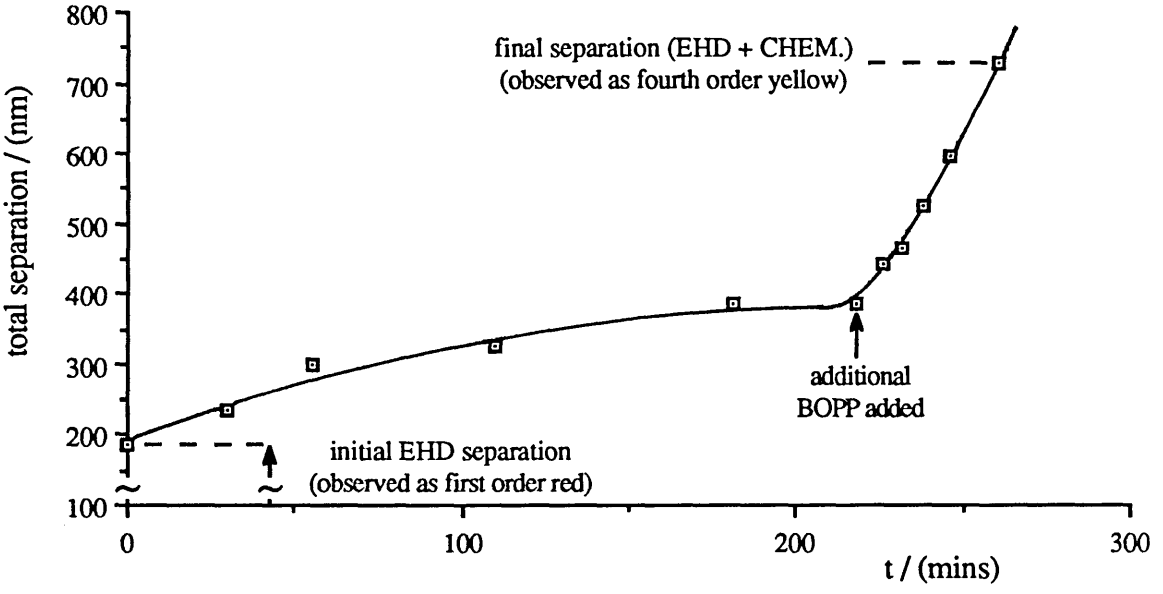


Figure 6.1 Maximum film thickness (BOPP) - separation vs. time

The experiment above shows the maximum film thickness to be depletion controlled in some way. However, the following argument shows that depletion of bulk additive cannot occur. If BOPP is assumed to have a density of 1 g / cm^3 the average chemical film thickness (h_{CHEM}) over the whole ball surface can be calculated from equation (I). Substitution of the volume of additive ($Vol._{ADD}$) and the ball radius ($r_B = 0.0127$ m) into equation (I) permits calculation of the radius of the ball plus a uniform coating of additive (r_{B+CHEM}).

$$\text{Vol.}_{ADD} = \frac{4\pi}{3}\left(r^3_{B+CHEM} - r^3_B\right) \qquad (I)$$

$$\therefore \quad r_{B+CHEM} = \sqrt[3]{\left(\frac{3 \times \text{Vol.}_{ADD}}{4\pi}\right) + r^3_B}$$

The chemical film thickness can then be simply calculated from equation (II).

$$h_{CHEM} = r_{B+CHEM} - r_B \qquad (II)$$

If 2 g of additive is used i.e. Vol._{ADD} is approximately equal to 2×10^{-6} m^3 the above equations give $h_{CHEM} = 3.2$ mm; the use of 0.85 g of BOPP gives $h_{CHEM} = 0.41$ mm. The above analysis was based on a uniformly coated ball. In practice, film formation was almost entirely confined to the EHD contact between the ball and its supporting rollers (§ 7.2.2.3). If the maximum film thickness were controlled by depletion of bulk additive the limiting film thickness should be of the order of millimeters not hundreds of nanometers as observed. The design of the rig (§ 5.2.2.1) ensured that the additive could not be lost by surface reaction elsewhere in the system. This evidence suggests that the maximum film thickness was determined by depletion of some active, thick film-forming component, or impurity, present in the bulk additive.

The curves shown in figure 6.2 provide further evidence for this theory. The plots show the chemical film build-up with time for a mixture of 'constant U' and 'constant h' tests run by the author. All of the tests were run under identical conditions using ~ 65 g of a 3 % w/w solution of BOPP in SHC 234, at 100° C. The chemical film thickness (h_{CHEM}) was extracted from the total film thickness ($h_{CHEM} + h_{EHD}$) as described in § 5.2.4.3. The individual tests are identified by their type and the date on which they were performed.

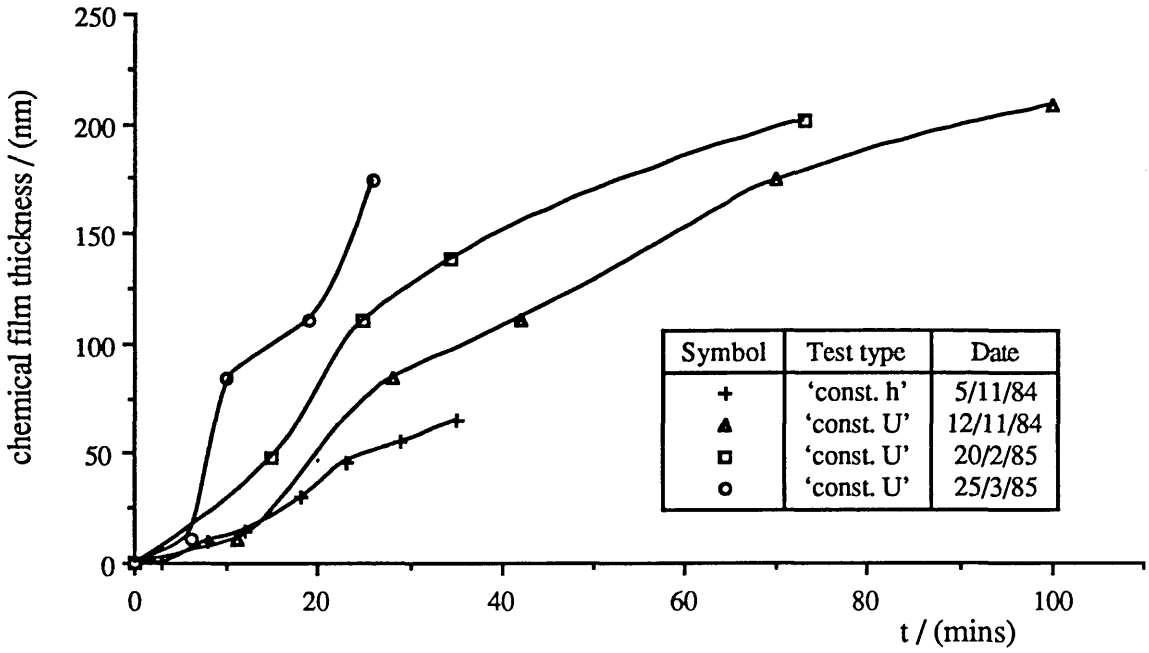


Figure 6.2 Film build-up with time - 3 % BOPP in SHC 234

It is clear from figure 6.2 that there was considerable variation in the rates of film build-up, even in tests conducted under apparently identical conditions. However, there appeared to be a systematic, chronological increase in the build-up rate as the BOPP got older. The material was produced as a single batch by Lacey [76] as described in § 4.3.1.2. This may imply a slow decomposition with time to form a more reactive species, perhaps as a result of hydrolysis. The evidence presented in § 7.3.1.3 suggests that the predominant break-down mode is hydrolytic. However no change in the IR spectrum was detected during this period. The variable build-up rates observed previously by Lacey [76] were attributed to catalysis as a result of differences in the rig-cleaning procedure applied between tests. This may also have been the cause in the current experiments, although the cleaning procedure was standardised as immersion in toluene and acetone. The observation of Lacey remains consistent with the author's view of an important thick film-producing impurity.

6.2.1.2 Rate of film build-up with other additives present

Modern formulated oils contain a wide range of additives included to extend the operating capability of the oil into more extreme environments than otherwise possible (§ 1.7). The following experiment was designed to provide information on the effects of other additives in the package, on the known thick film forming behaviour of BOPP. A 'constant U' test was run on a 3 % w/w solution of BOPP in SHC 234, plus a full additive package. The temperature, flow rate and mass of lubricant were fixed as described previously. The formulation used is given in table 6.1. This formulation is representative of a typical mixed package. It differed however, in the use of a single anti-wear / extreme pressure additive. A more typical formulation might have been expected to contain two AW / EP agents of differing stabilities / activation temperatures, to cover the range of circumstances met in practice. The fully formulated solution was observed to be slightly 'hazy.' This was because the quantities of polar additives used slightly exceeded the limited solubility of the non-polar base stock.

FUNCTION	% MASS	FORMULATION DETAILS
Synthetic hydrocarbon (base stock)	96	η (Pa.s) = 0.359 40 ^{o}C, 0.035 100 ^{o}C $\alpha_{100^{o}C}$ = 8.56 GPa^{-1}
Anti-oxidant	1.0	Alkylated phenyl-α-naphthylamine
Corrosion inhibitor	0.2	Antimony dithiocarbamate
Storage stabilizer	0.2	2,6 di-tert-butyl- α-dimethyl amino p-cresol
Corrosion inhibitor	0.05	Benzotriazole
Foam inhibitor	~ 1 ppm	Silicone (60,000 cSt)
Anti-wear additive	3.0	bis-tert-octyl phenyl phosphonate (BOPP)

Table 6.1 Fully formulated additive package

The chemical film thickness is shown, as a function of time, in figure 6.3. The rate of build-up is contrasted with that observed by Lacey [76] in a 'constant U' and a 'constant h' test. The figure shows good agreement between the rate of film build-up in the 'constant U' tests of Lacey [76] in pure base stock and the author with a full additive package. The latter experiment was performed approximately five years after the work of Lacey [76], (on 4/8/88). The results described in section 6.2.1.1 (figure 6.2) predict a much increased build-up rate in the more recent experiment. Thus the additive package appears to reduce the rate, perhaps by competition for surface sites. However, comparison of the 'constant h' and 'constant U' tests performed by Lacey [76], at about the same time, demonstrate the variation in observed rates of build-up. Thus the full additive package may slightly reduce the growth rate, but it remains of the same order. The final film thickness is greater in the more recent experiment than that observed previously by Lacey [76] or the author. This provides further evidence of the importance of an active thick film producing impurity, which increases in concentration with time.

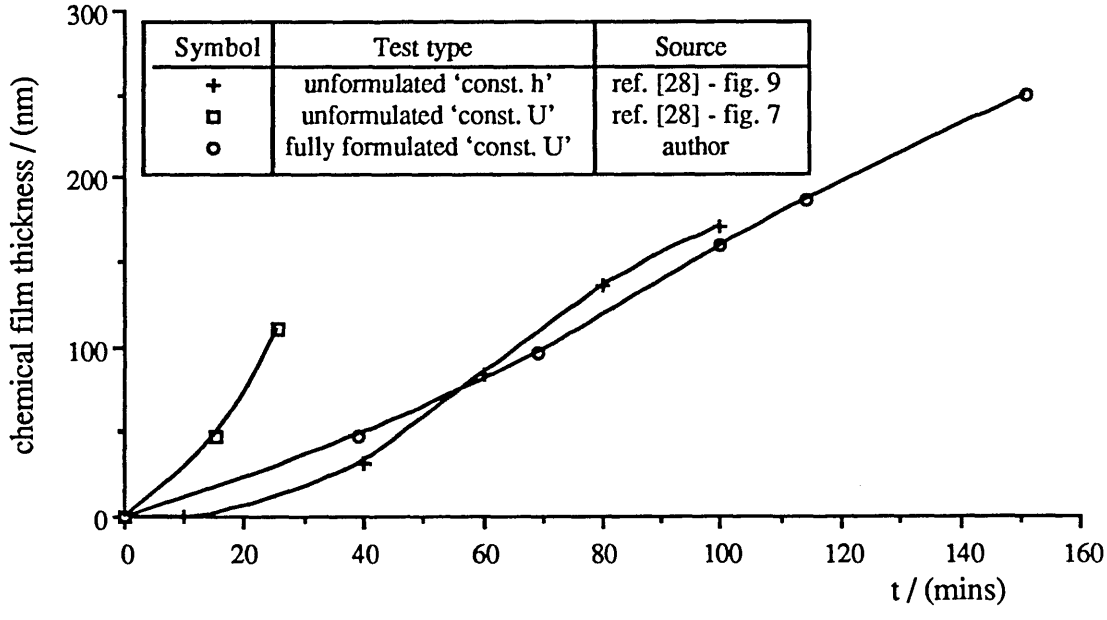


Figure 6.3 Film build-up with time - 3 % BOPP ± full additive package

6.2.1.3 Performance in high sliding, boundary lubricated contact - HFR testing of BOPP

Optical interferometry was used by Lacey [76] and the current author to show that phosphonate ester anti-wear additives from thick polymeric films in pure rolling and low slide / roll ratio EHD contacts. These films continue to separate the surfaces when the EHD component of the separation falls to zero i.e. in the stationary contact (§ 6.2.1.4). It is of great practical importance to investigate how these additives would operate under initial conditions of low specific film thickness, when considerable metal to metal contact occurs. Clearly for many practical applications anti-wear additives need to be effective in high sliding conditions and in boundary lubrication. The standard optical interferometric ball on plate rig was used to indirectly demonstrate the build-up of thick film material in a pure sliding test (§7.2.2.1). The following experiment monitored the film behaviour in a high frequency reciprocating (HFR) test rig (see § 5.3). This set-up employs a more realistic steel on steel contact metallurgy, operating under boundary lubricated conditions.

Details of the test procedure, sample preparation and so on were given in section 5.3.2. The lubricant used in the following tests was hexadecane ($C_{16}H_{34}$). This was stored over a mixture of activated alumina and silica gel, to remove polar impurities and to dry the liquid respectively. The performance of the base stock was contrasted with a 3 % solution w/w of BOPP. The tests were run for thirty minutes each, at a series of fixed temperatures. New specimens were used for each test.

The results are shown in figures 6.4 - 6.6. Figure 6.4 shows the average electrical contact resistance (ECR) during each test. In tests with additive present, the ECR was found to gradually increase at temperatures exceeding 80^{o} C. Accurate measurement of the ECR proved difficult as considerable variation occurred within each test and often within each stroke. However, the average ECR - as measured from the chart recorder - rose rapidly at 100^{o} C. A near infinite ECR i.e. a fully insulating layer was observed at 120^{o} C.

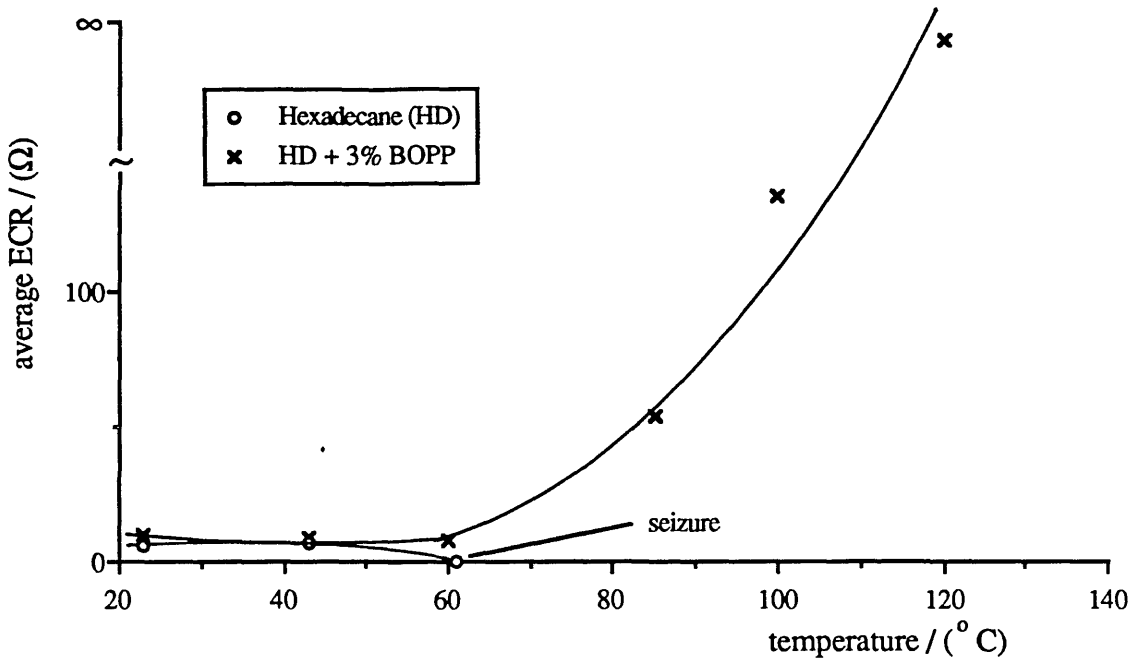


Figure 6.4 Electrical contact resistance vs. temperature - hexadecane ± 3 % BOPP

Figure 6.5 shows the variation in the coefficient of friction with temperature for hexadecane ± 3 % BOPP. In the absence of additive the contact seized at 60° C. Even at 40° C the coefficient of friction was highly variable during the test showing some stick-slip, in the absence of BOPP. The measured wear scar at 40° C was smooth with BOPP present, but highly rough and irregular for hexadecane alone. The additive considerably reduced the coefficient of friction at all temperatures.

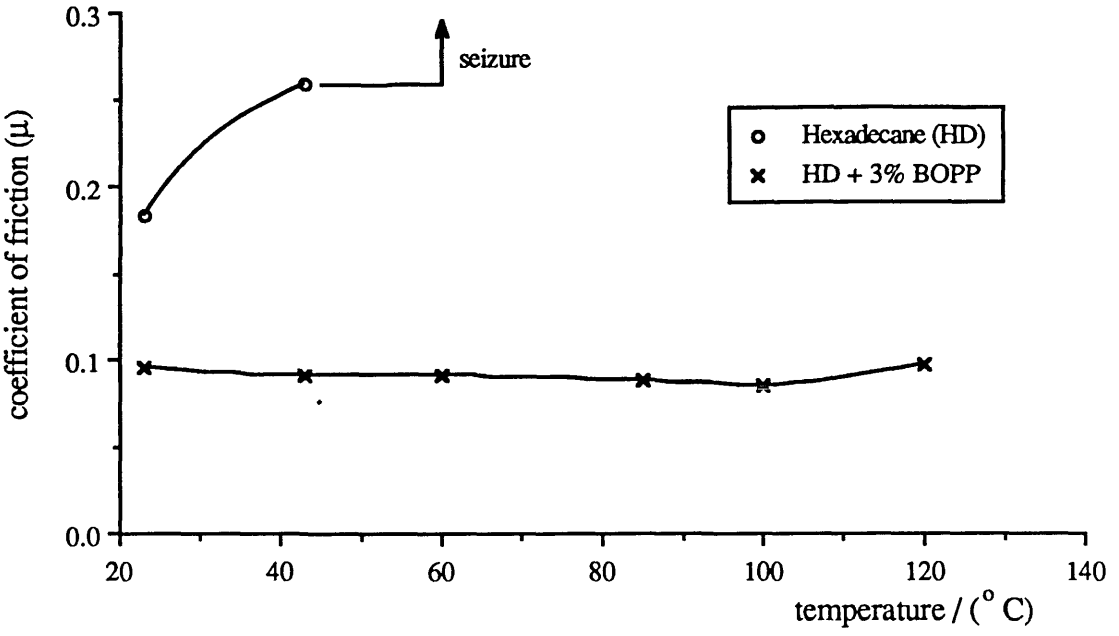


Figure 6.5 Coefficient of friction (μ) vs. temperature - hexadecane ± 3 % BOPP

Figure 6.6 shows the maximum scar depth for hexadecane ± 3 % BOPP as a function of temperature. This was determined from three profiles measured perpendicular to the direction of sliding and one profile measured along the wear scar. In all of the experiments with pure hexadecane the initial 'mirror finish' of the flat specimens was retained after the test. With BOPP present at temperatures below 60° C, an easily removable, white material coated the surface. The talysurf stylus 'ploughed' through this material, giving a measurement of the surface profile of the metal substrate. However, at 60° C this material was tough enough to be measured by the talysurf. At temperatures exceeding 60° C, with additive present, optical examination of the steel surface after rubbing showed the presence of a semi-transparent film. This material largely filled the wear scar preventing measurement of the scar depth.

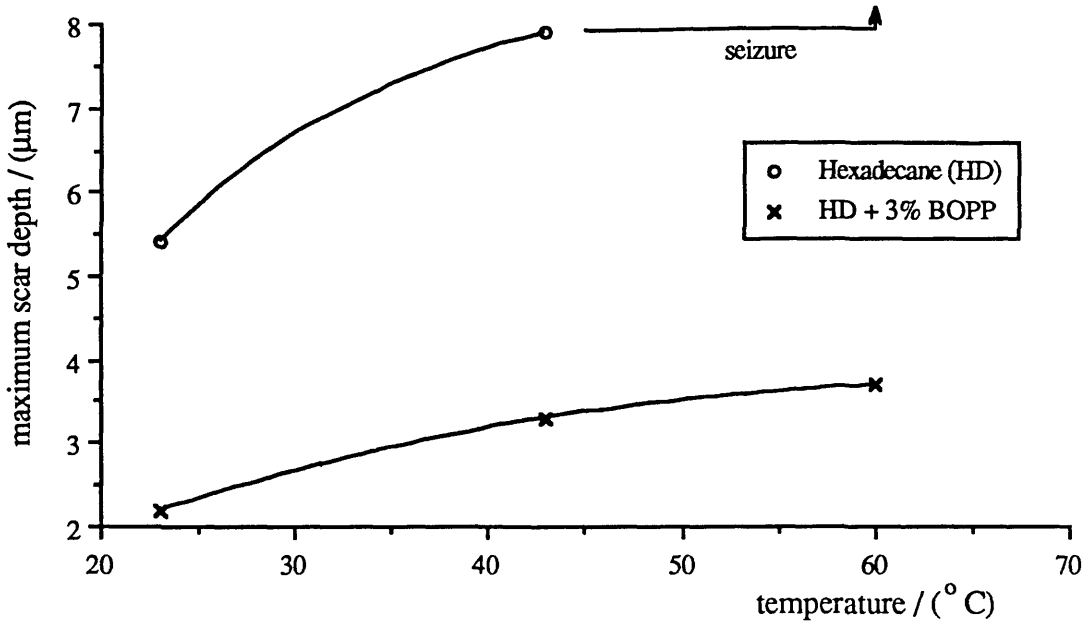


Figure 6.6 Maximum scar depth vs. temperature - hexadecane ± 3 % BOPP

The above tests extend earlier work to show that a di-substituted phosphonate ester anti-wear additive formed thick surface films not only in low slide-roll ratio EHD contacts, but also under high sliding, boundary lubricated conditions (see sections 7.2.1 - 7.2.2 also). This suggests that its anti-wear action is likely to be effective in high sliding gears and similar components. The rate of film formation and the temperature at which it occurred correlated well with that observed previously in pure rolling. At temperatures of 80 - 100° C a film formed, causing transition from boundary, through mixed, to almost full separation of the sliding surfaces.

6.2.1.4 Physical nature of the film material - high viscosity liquid or solid ?

The scriber tests described in section 7.2 suggest that at room temperature the inner layer of thick film material - which survived ultrasonic cleaning in toluene and acetone - is quite hard. In principle the surface polymeric material may be highly viscous, viscoelastic, plastic or elastic. The physical nature of the material may also be temperature-dependent. In practice, the important consideration is the physical properties of the material when operating under the conditions prevailing in an EHD contact. However, in all cases, so long as the material is considerably more viscous than the base oil, it is likely to promote surface separation at speed.

Two extremes of film behaviour may be hypothesised. Firstly, that the chemical film forming with time has a thickness which is totally independent of speed, varying only with elapsed test time. This would happen if the film were behaving as a solid. Secondly, that the film formed has a thickness which is dependent upon viscosity and rolling speed in a classical EHD manner i.e. proportional to $(\eta U)^{0.7}$. This would happen if the material were behaving as a viscous Newtonian liquid. In the following analysis the physical nature of the film is investigated by comparing the rates of film build-up in constant speed, variable film thickness test and a constant film thickness, variable speed test (using the same additive, temperature etc.). On the basis of each of the two hypotheses, the chemical fraction of the film formed in the 'constant h' test can be extracted mathematically, as a function of test time. The calculated rate of film build-up is then compared with that observed in the 'constant U' test to see which model gives the best prediction. The expressions for the chemical film thickness - for each of the two models - were derived as follows.

Viscous liquid model

The derivation below was based on the assumption that the thick film material behaves as a *viscous liquid.* Therefore - for a fixed load and fixed inlet conditions - the following speed / viscosity relation applies in a 'constant h' test. The subscript (h) denotes a constant h test; the subscripts o and t refer to the start of the test and a time (t) during the test.

(i) At constant h, (with W and α fixed) :-

$$U_{o(h)} \cdot \eta_o = U_{t(h)} \cdot \eta_t$$

$$\therefore \quad \eta_t = \frac{U_{o(h)} \cdot \eta_o}{U_{t(h)}} \qquad \text{(III)}$$

(ii) A constant U plot may be obtained from the constant h data by employing the following relationship. This relationship holds true if the only change with time is in the viscosity of the chemical film, and therefore in its contribution to the total separation ($h_{t\,(liquid)}$). $h_{o\,(u)}$ refers to the initial separation in a constant U test.

$$\frac{h_{t\,(liquid)}}{h_{o(u)}} = \left(\frac{U_t \cdot \eta_t}{U_o \cdot \eta_o}\right)^{0.7}$$

Since, in constant U tests $U_t = U_o$

$$\therefore \quad h_{t\,(liquid)} = h_{o\,(u)} \left(\frac{\eta_t}{\eta_o}\right)^{0.7}$$

Substitution for η_t, from equation (III), gives equation (IV). This equation predicts the total separation at any time ($h_{t\,(liquid)}$) - in a 'constant U' test - from the experimental data of a 'constant h' test, on the assumption that the film material *behaves as a viscous liquid.*

$$h_{t\,(liquid)} = h_{o\,(u)} \left(\frac{U_{o(h)}}{U_{t(h)}}\right)^{0.7} \qquad \text{(IV)}$$

Rigid solid model

The following derivation is a similar treatment to that above, based on the assumption that the *film material behaves as a rigid solid.* The total separation (h) is split into its component parts i.e. the contribution due to the EHD film (h_{EHD}) and the contribution due to the solid, chemical film (h_{CHEM}). The other subscripts are defined as previously.

(i) At constant h the following expressions apply, since the oil viscosity is constant during the test. W and α remain constant, as described previously.

$$h_{EHD\,(t)} = k\,(U_{t(h)})^{0.7}$$

$$h_{o(h)} = k\,(U_{o(h)})^{0.7}$$

$$\therefore \quad h_{EHD\ (t)} = h_{o(h)} \left(\frac{U_{t(h)}}{U_{o(h)}} \right)^{0.7} \qquad (V)$$

If the film behaves as a rigid solid in a constant h test, the following expression applies : -

$$h_{CHEM\ (t)} = h_{o(h)} - h_{EHD\ (t)}$$

Substituting for h_{EHD} from equation (V) gives : -

$$h_{CHEM\ (t)} = h_{o(h)} - h_{o(h)} \left(\frac{U_{t(h)}}{U_{o(h)}} \right)^{0.7}$$

$$\therefore \quad h_{CHEM\ (t)} = h_{o(h)} \left[1 - \left(\frac{U_{t(h)}}{U_{o(h)}} \right)^{0.7} \right] \qquad (VI)$$

(ii) A <u>constant U</u> plot may be obtained from the constant h data using the following relationship : -

$$h_{t\ (SOLID\ )} = h_{o(u)} + h_{CHEM\ (t)}$$

Substituting for $h_{CHEM\ (t)}$ from equation (VI) gives : -

$$h_{t\ (SOLID\ )} = h_{o(u)} + h_{o(h)} \left[1 - \left(\frac{U_{t(h)}}{U_{o(h)}} \right)^{0.7} \right]$$

At the start of the test the separation is due to the oil film only and $h_{o\ (u)} = h_{o\ (h)}$.

$$h_{t\ (SOLID\ )} = h_{o(u)} \left[2 - \left(\frac{U_{t(h)}}{U_{o(h)}} \right)^{0.7} \right] \qquad (VII)$$

Thus equation (VII) predicts the shape of a 'constant U' test-plot, from the experimental data of a 'constant h' test, on the assumption that the *film material behaves as a rigid solid.*

Figure 6.7 shows the variation in the total separation ($h_{TOTAL} = h_{EHD} + h_{CHEM}$) as a function of the *rolling speed ratio* ($U_{t(h)} / U_{o(h)}$). The curves were generated by choosing a series of rolling speed ratios and calculating the film thicknesses predicted by each of the two models. Equation (IV) was used to calculate the separation based on the viscous liquid model; equation (VII) was used for the solid model. In figure 6.7 the total separation is given in terms of the increase in the initial separation (h_o). Both models predict a similar film build-up when the rolling speed ratio is close to unity i.e. when the chemical film thickness is close to zero. However, with thicker chemical films present - at reduced values of the rolling speed ratio - the two models predict quite different total film thicknesses.

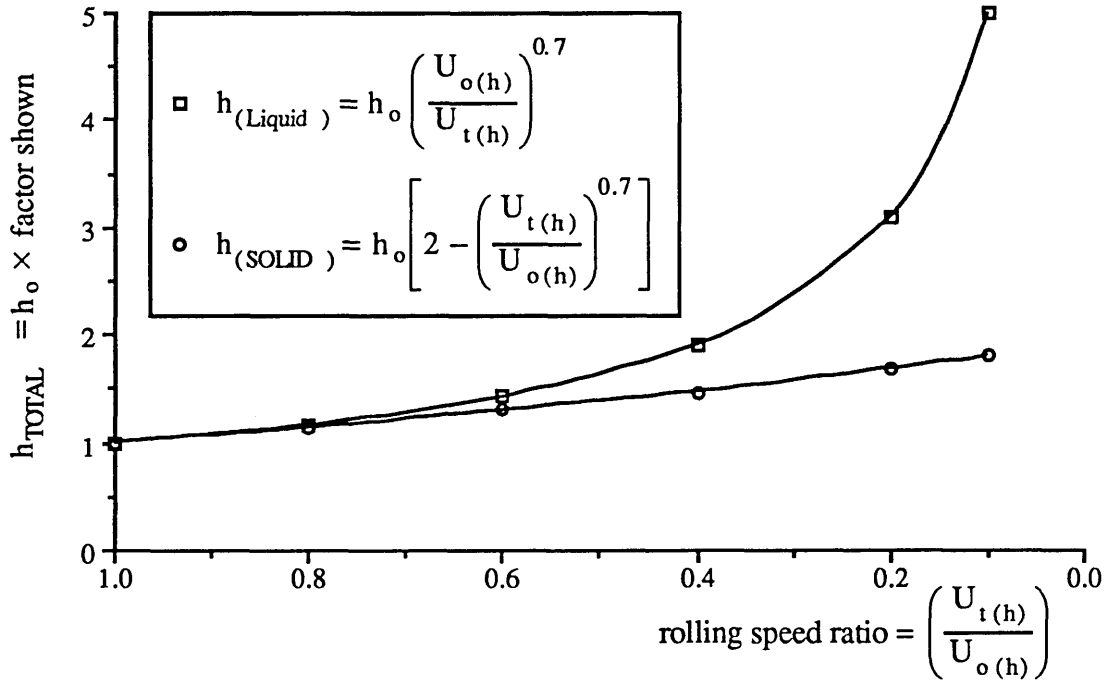


Figure 6.7 Film thickness predicted in a 'constant U' test
as a function of rolling speed ratio

It is apparent from figure 6.7 that the variation of the rolling speed ratio with time - as measured in a constant h test - can be used to predict the shape of the curve in a constant U test. Comparison with the actual build-up observed in a constant U test (under the same conditions) should show which model best represents the physical properties of the film.

Figure 6.8 shows the change in the total separation with time, in a constant U test, using BOPP as additive. The actual build-up observed in the constant U test of 12/11/84 is compared with that predicted by the solid model and the liquid model. The predicted curves were calculated from equations (IV) and (VII) using the constant h test-data of 5/11/84. The initial separation in the constant h test - and the change in the rolling speed ratio with time - were used to calculate the constant U curves. The value of $h_{o\,(h)}$ (observed as the first order blue fringe at 235 nm) was substituted for $h_{o\,(U)}$ in equations (IV) and (VII).

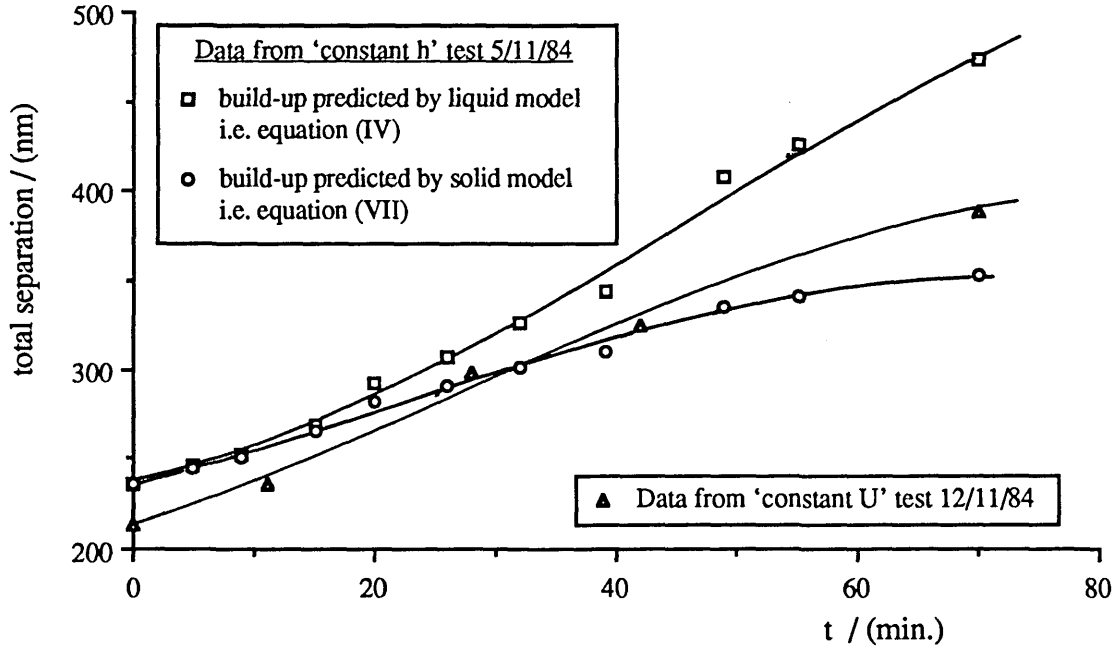


Figure 6.8 Observed and predicted film thickness increase in a 'constant U' test - 3 % BOPP in SHC 234

The constant U test shown in figure 6.8 was run at a slightly reduced initial film thickness. However, the shape of the film build-up may be compared with the predicted curves. In the initial stages of the constant U test the build-up seemed to most closely resemble that predicted by the viscous liquid model. The more rapid build-up may also have been due to the general increase observed over time (§ 6.2.1.1). In the latter stages of the test the film thickness increase was much closer to that predicted by the solid model.

Although the curves in figure 6.8 suggested that the film material behaves as a solid, the evidence was not clear cut. For this reason a similar analysis was carried out on data obtained for the build-up of a chemical film from a 3% solution of di-dodecyl phosphonate (DDDP) in SHC 234, at 100° C [76], [28]. The build-up predicted by the two models was calculated from the constant in test data in figure 3 [28] and compared with that obtained in a constant U test (figure 4 [28]). The two tests were conducted under identical conditions of temperature, load etc. A reduced initial film thickness was used in the constant U test. The curves are shown in figure 6.9. It is clear from figure 6.9 that the chemical film material is augmenting the EHD film in a solid, speed independent manner, under the conditions present in the operating contact.

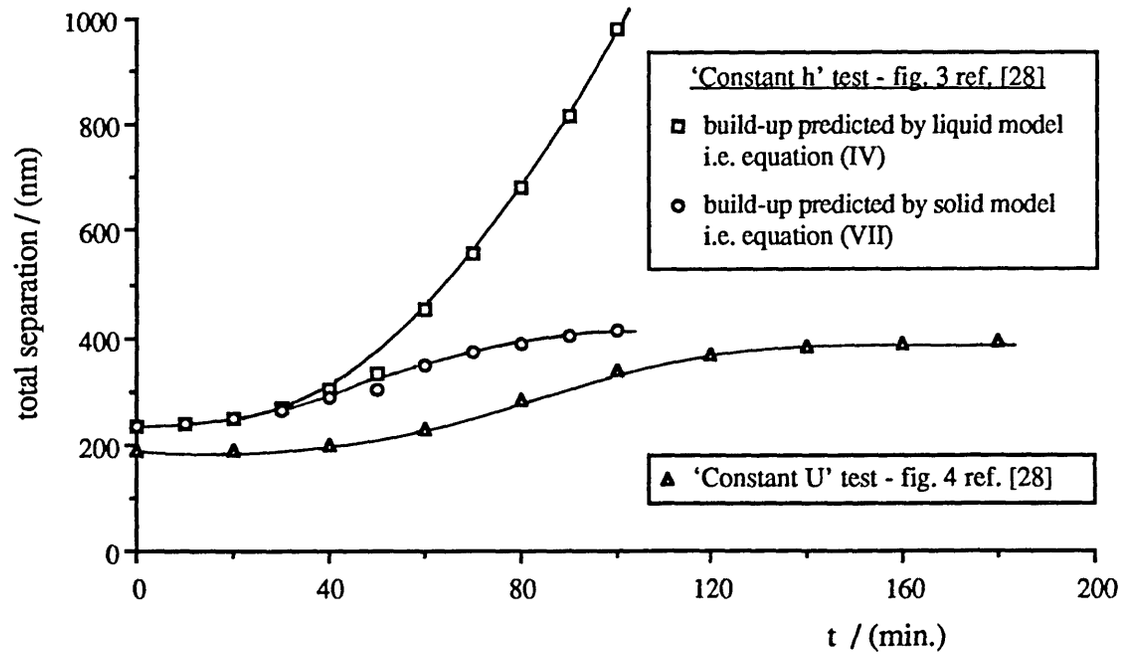


Figure 6.9 Observed and predicted film thickness increase in a 'constant U' test - 3 % DDDP in SHC 234

6.2.1.5 Behaviour of chemical film material in a rolling contact and in a stationary contact - high speed photography

The quality of the image observed in rolling tests was found to deteriorate as the test progressed when thick film forming additives were present. However, the quality of the image of the stationary contact, at the end of the test, was good. This suggested that the thick film material was disrupting the film thickness. If this were the case a time-averaged central film thickness / colour would be observed, although short term fluctuations were occurring. A short duration, Xenon flash unit was therefore used in an attempt to 'freeze' the rolling contact. It was hoped that this might provide evidence about the distribution and the physical properties of the film material within the rolling contact.

A number of short duration photographs were taken using a Xenon flash unit built in the author's laboratory. The duration of the flash is defined as the period during which the intensity exceeds two thirds of the maximum [199]. The flash duration was measured by linking a silicon photodiode (RS Components Ltd, Nº 303-674) to a Gould OS 4000 digital storage oscilloscope. The photovoltaic cell specified a rise time (from 10 % to 90 % of maximum output voltage) of ~ 50 ns, across the visible spectrum. The oscilloscope permitted the signal intensity (arbitrarily measured as the diode output voltage) to be measured as a function of time, and to be stored. By altering the time base the intensity / time trace could then be plotted out - in real time - on a chart recorder (Rikadenki). A typical example is given in figure 6.10. The duration was found to be highly consistent at approximately 0.1 ms. If the flash duration is known the maximum rolling speed that can be effectively rendered stationary or 'frozen,' can be calculated as described below.

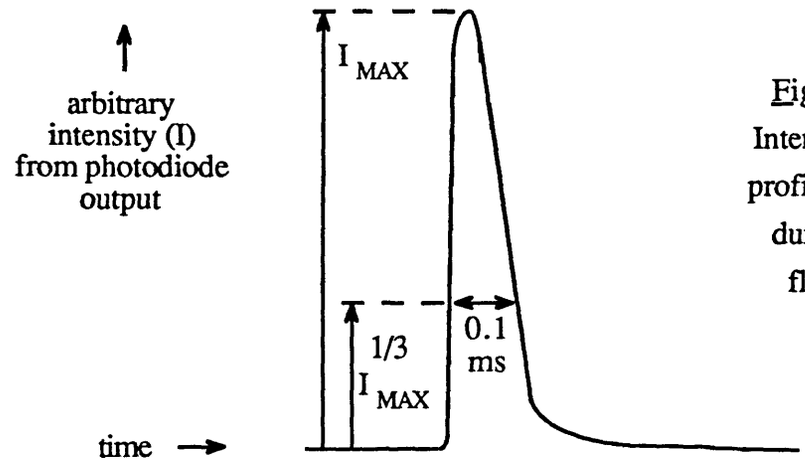


Figure 6.10
Intensity / time profile for short duration Xe flash unit

The following experiment describes the use of short duration photography to investigate the behaviour of a thick, reacted film in a rolling contact. A constant h test was run, with 3% BOPP, under the conditions summarised in § 6.2.1.1. The experiment followed the first order blue fringe at approximately 235 nm. Plate 6.1 was obtained by manually opening the camera shutter and illuminating the contact with the Xenon source. At the time of taking the photograph the rolling speed had been reduced from its initial value of 1.29 ms^{-1} to 0.789 ms^{-1}. Thus a solid, chemical film thickness of approximately 68 nm was predicted using equation (XXIX) chapter 5. The central film thickness - as observed by the naked eye - remained first order blue. In plate 6.1 the oil inlet is on the left. Some cavitation is apparent in the lubricant in the outlet.

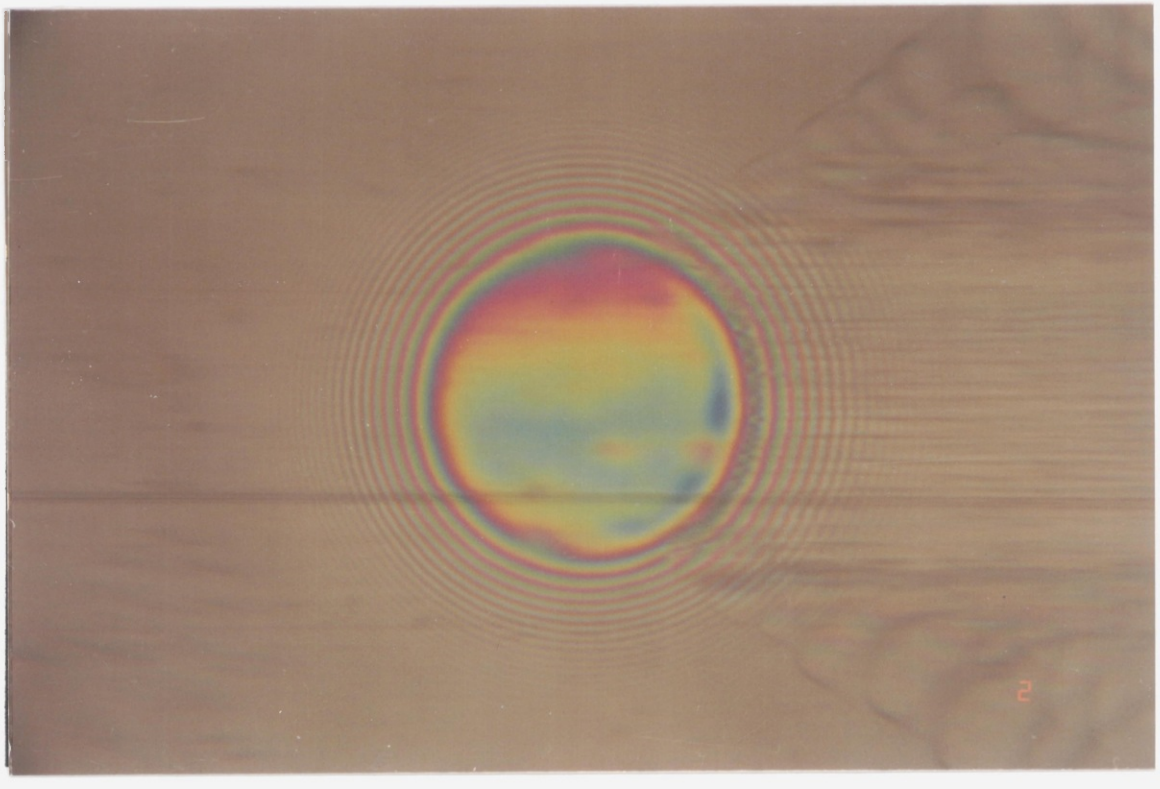


Plate 6.1 Short duration exposure of BOPP-generated
film in rolling contact (U = 0.789 m/s)

The characteristic 'horse-shoe' shape contact is barely visible in plate 6.1, although it could still be seen with the naked eye. The 'average' central film thickness therefore varied considerably over a short time scale. Two localised irregularities of the order of 1/4 the contact width are visible within the blue area. Since the variation in film thickness with

fringe colour is yellow < red < blue, the order in which the fringe colours change towards the centre of the irregular areas identifies them as 'lumps' with a thickness less than the average film thickness. This provides further, indirect evidence of the solid nature of the film since a viscous liquid might not be expected to produce such a local variation. The Hertzian contact diameter was calculated to be 0.275 mm (equation (X) chapter 5). The time required for the ball to rotate one Hertzian diameter can be obtained by dividing the Hertzian diameter by the rolling speed. This gave a value of 0.35 ms. Since the flash duration is 0.1 ms, the ball should rotate 0.1 / 0.35 = 0.28 of the contact diameter during the exposure time. This correlated well with the observed local film thickness changes.

Plate 6.2 shows the hot, stationary contact at the end of the test. It is apparent that the material is not evenly distributed, but it continues to separate the surfaces in the absence of an EHD film. The contact was maintained at the test temperature of 100° C for a further period of approximately 60 minutes. No change in the image was observed over this time. This proved that the separation was not due to a pressured oil entrapment or 'squeeze-film.' It also provided further indirect evidence of the solid nature of the film since even a highly viscous liquid might have been expected to leak away during this time.

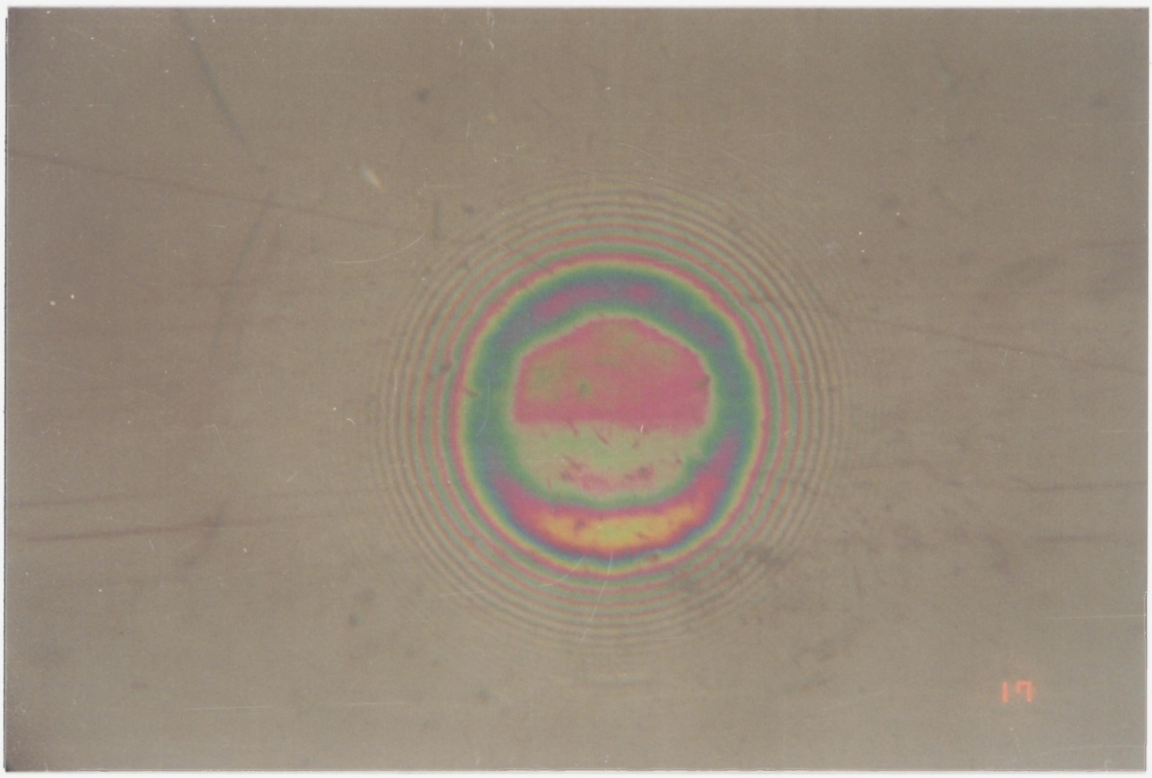


Plate 6.2 BOPP film in loaded contact at end of test (temperature = 100° C)

6.2.1.6. Miscellaneous esters - short chain di-alkyl phosphonates

During the course of the current study thick, reacted layers were found to build-up with di-alkyl phosphonates containing alkyl groups ranging from hexyl (C_6H_{13} -) to dodecyl ($C_{12}H_{25}$ -). However many commercial formulations include shorter chain length di-alkyl phosphonates. Similar tests to those described above i.e. 3 % w/w additive in SHC 234 at 100° C, were therefore completed with di-*iso*-propyl phosphonate (i-$C_3H_7O)_2P(O)H$ and di-*n*-butyl phosphonate (n-$C_4H_9O)_2P(O)H$ as additive. No thick film formation was observed after periods of 4 and 3 hours respectively, nor could any thinner films be detected by reflection infra red analysis of the balls after testing (see chapter 7). This suggests that the short chain versions either failed to react with the ball surfaces, or the films formed did not remain in the contact and contribute measurably towards surface separation.

The work described in chapter seven shows the thick film material can be generated 'in vitro' at elevated temperatures. The 'model compounds' were formed by direct reaction of the additive with iron containing species. In these studies it was found that model compound formation occurred faster and at lower temperatures, with di-alkyl phosphonates, as the alkyl chain length fell. This implied that film material was formed in the contact and subsequently lost. In general, the melting point of the model compounds was found to increase with increasing chain length. A model compound generated with di-methyl phosphonate i.e. the shortest chain length was found to melt in the range 198 - 200° C. The di-hexyl version melted at approximately 250° C. Thus the absence of a film with short chain lengths could not be due to the film material 'melting out' of the contact.

It seems probable that the absence of a separating film with short chain length phosphonates may have resulted from differences in the physical properties of the film material. Transmission infra red analyses of solids are usually carried out by grinding the material in an inert carrier fluid (see § 4.4.1.3.).

This procedure was used to analyse a range of model compounds derived from di-alkyl phosphonates (see chapter 7). During these analyses it was found that compounds having a chain length of five carbon atoms or less were easily ground i.e. they behaved as crystalline solids. However, model compounds derived from longer chain length di-alkyl

phosphonates, and from BOPP, were found to deform plastically during the grinding process. This suggests that the physical properties of the short chain compounds did not encourage their retention within the rolling track.

A short chain phosphite - tri-*iso*-propyl phosphite $(i\text{-PrO})_3P$: - was also tested in the optical EHD rig. No film build-up was observed after 100 minutes at 100° C.

6.2.2 Mono-alkyl phosphonates (RO)(HO)P(O)H and their amine salts

The following section considers the behaviour of mono-alkyl phosphonates and their octadecylamine salts. Preparative details for these compounds were given in section 4.3. The build-up of reacted layers was investigated in a boundary lubricated, mini-disc machine (§ 6.2.2.1) and in an EHD contact (§ 6.2.2.2). Some reflection infra red studies of the films formed are given in chapter 7.

6.2.2.1 Mini-disc machine testing - mono-dodecyl phosphonate

The mini-disc machine and the capacitance bridge method of film thickness evaluation were discussed in § 5.4. Full details of the method can be found in [216]. The contact conditions used in the current experiment are summarised in table 6.2. A solution of mono-dodecyl phosphonate $(C_{12}H_{25}O)(HO)P(O)H$ was employed, at a concentration of approximately 1 % w/w, in a hindered ester gas turbine oil conforming to Eng. RD 2497. The base stock used is a pre-formulated commercial product containing a mild boundary additive package. 1 % additive was chosen so as not to affect the bulk oil properties (dielectric constant, viscosity etc) too greatly. However approximately 1 % w/w in a total oil volume of approximately 5 litres should ensure sufficient additive for surface reaction.

CONTACT CONDITIONS	
Load / (N)	1800
Max. Hertz pressure / (GPa)	1.25
Mean rolling speed / (m/s)	0.75 - 3.0
Slide-roll ratio	0 - 0.66
Axial CLA / (μm)	0.16
Circumferential CLA / (μm)	0.08
LUBRICANT	
Formulated turbine oil	Eng. RD 2497
Viscosity (20° C) / (Pa.s)	6.15×10^{-2}
Viscosity (100° C) / (Pa.s)	4.93×10^{-3}
Alpha value (20° C) / (GPa^{-1})	20.3
Additive (1 %)	(DodecO)(HO)P(O)H

Table 6.2 Contact conditions for capacitance measurements in mini-disc machine

A comparison of table 6.2 and figure 6.11 shows that the surface roughness is of the same order as the film thickness. The capacitance technique can be used to measure the separation within such a boundary lubricated contact by employing a bridge to balance the capacitive and resistive components of the oil film [216]. The rig was run for 30 minutes at 2 ms^{-1}, in the absence of additive, until the disc temperature was stable at 39° C. The film thickness was then measured - at a series of speeds - in pure rolling, at 20 % sliding and at 66 % sliding. The additive was then added to the sump. An initial decrease in film thickness was observed, possibly as a result of a slight viscosity drop. The film thickness was then observed to increase gradually over a period of approximately 30 minutes. The film thickness measurements were repeated when no further film growth was observed. Figure 6.11 show the film thicknesses determined with and without additive present.

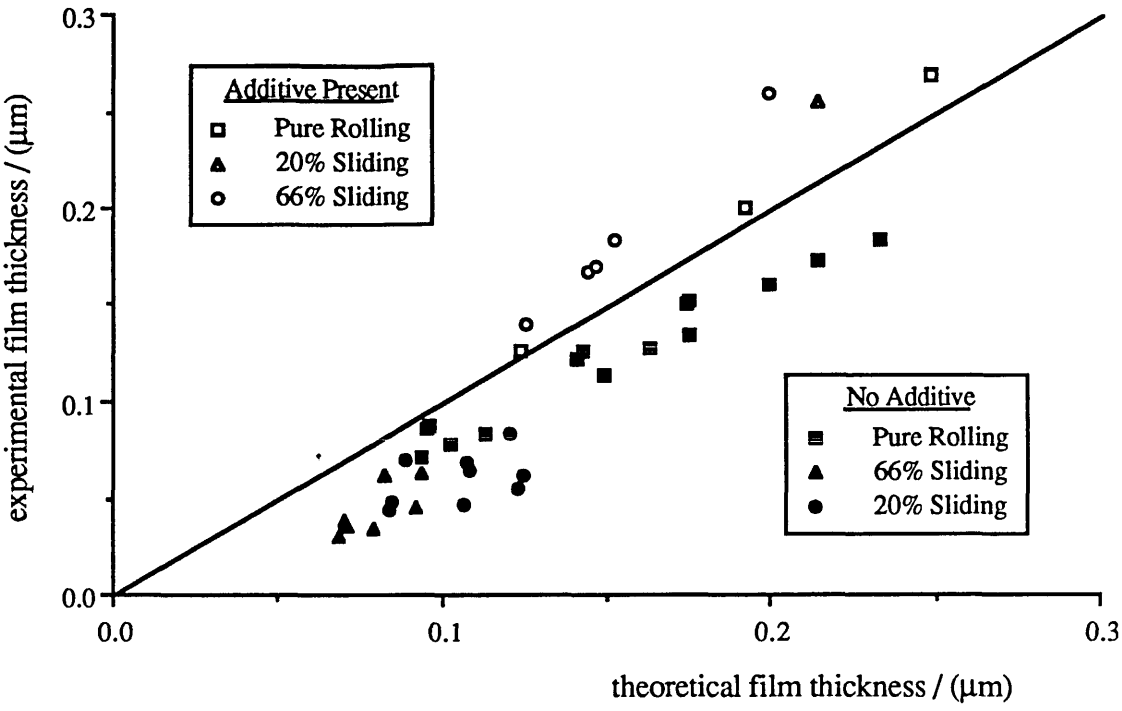


Figure 6.11 Disc machine experimental vs. theoretical film thickness (± additive)

Figure 6.11 is a plot of the film thicknesses determined from capacitance readings against the film thicknesses calculated from EHD theory. The bold line on the figure represents the theoretical line of measured equals calculated film thickness. In the absence of additive, the film thicknesses were typically 20 % less than predicted. This was probably due to variation of the dielectric constant with pressure (see § 5.4). However, with the mono phosphonate ester present the film thickness typically rose by 0.1 μm to exceed the theoretical film thickness.

It is apparent from figure 6.11 that a greater increase was observed with sliding (6 results) than in pure rolling (3 results), when additive was present. This may have resulted from increased build-up in the sliding contacts, in which some additional shear heating would be expected. Lacey et al observed similar behaviour with di-alkyl / aryl phosphonates [28]. Alternatively some part of the additional separation may have been due to an increase in bulk viscosity resulting from reduced frictional heating. This would be expected if the additive were producing a weak film of low shear strength. However, if this were the case an immediate film thickness increase would have been expected. The presence of reacted layers was confirmed by reflection infra red spectroscopy, after running (§ 7.3.2).

6.2.2.2 Mono alkyl phosphonates - testing in EHD rig

Initial testing carried out in the EHD rig identified some problems in following the build-up of reacted layers generated with mono-alkyl phosphonates. Two tests were carried out at 100° C using 3 % w/w solutions of additive in SHC 234. A 20 N load was used in both cases. The additives used were mono-butyl and mono-dodecyl phosphonate. In both cases the image quality was found to deteriorate with time. The image was totally lost after approximately fifteen minutes with the butyl ester and thirty minutes with the dodecyl ester. However, an increasing film thickness was observed with the dodecyl ester before the image was lost. The tests were continued for approximately 100 minutes, after which the balls were removed for reflection IR analyses . In both cases thick reacted layers were visible on the balls after testing. The IR analyses suggested that the material generated with mono-dodecyl phosphonate was similar to that obtained previously with di-dodecyl phosphonate. The material was similarly concentrated within the rolling tracks. The butyl ester produced a wide spread 'white' film which appeared, from IR analyses, to consist mainly of a mixture of corroded metal and unreacted ester. The IR evidence is discussed in more detail in chapter 7.

At the end of the test conducted with the dodecyl ester, the ball cage was moved so that the ball contacted the disc at a different track radius. This restored the image quality to that observed before testing. A thick film was observed in the contact. No image was observed at the original track radius with an untested ball. Thus it appeared that the acidic additive was removing the thin, sputtered layer of chromium in the rolling contact. This was confirmed by microscopic examination of the cleaned disc, after testing.

The problems of image loss associated with highly acidic additives led to the use of neutral amine salts of mono-alkyl phosphonates (see § 3.7). The experiments above were repeated with two octadecylamine salts of mono-alkyl phosphonates - $[CH_3(CH_2)_{17}NH_3O](RO)P(O)H$, where R = hexyl and dodecyl. No film formation was observed, in a constant U test, with the hexyl ester, after running for 220 minutes at 100° C. Although the test was conducted at a higher load (50 N on the ball) no deterioration in image quality was observed. The test was run using approximately the same concentration of additive - based on phosphorus - as the test conducted by Lacey with

$(HexO)_2P(O)H$ [28]. In the current test 3.5 g of additive was used in the total mass of 65 g of additive solution. This represents 3.5 / 435 = 8 x 10^{-3} moles of phosphorus; the molecular weight of $[CH_3(CH_2)_{17}NH_3O](HexO)P(O)H$ = 435 g/mol. Lacey [28] used 2 g of $(HexO)_2P(O)H$ (molecular weight = 250 g/mol) i.e. 2 / 250 = 8 x 10^{-3} moles of phosphorus in a total of 65 g of additive solution.

The constant U experiment described above was repeated at the same phosphorus concentration i.e. 4.2 g of the mono-dodecyl amine salt (molecular weight = 519 g/mol). No increased separation was observed after 100 minutes. At this time mono-dodecyl phosphonate was directly added to the sump (1.25 g, molecular weight = 250 g/mol). This represented a phosphorus concentration - based on the mono-dodecyl phosphonate only - of 1.25 / 250 = 5.0 x 10^{-3} moles in approximately 65 g of lubricant. The separation had been steady at approximately 139 nm (observed as the first order yellow fringe) prior to the addition of the mono-dodecyl ester. After addition a rapid increase in film thickness was observed. However the film build-up was only monitored as far as the first red fringe (after approximately 30 minutes). After this time the image rapidly degraded due to loss of the semi-reflective chromium layer.

Figure 6.12 compares the initial build-up observed by the author, using mono-dodecyl phosphonate, with that observed by Lacey [28] with di-dodecyl phosphonate. In both cases the chemical film thickness has been extracted from the total film thickness (as observed in constant U tests) by the method described in section 5.2.4.3. Time zero is taken to be the time at which the additive was introduced. The data for di-dodecyl phosphonate is taken from figure 4 of reference [28]. In the di-dodecyl phosphonate test 2 g of additive was used i.e. a concentration of 2 / 418 = 4.8 x 10^{-3} moles of phosphorus in 65 g of SHC 234 (molecular weight of $(DodecO)_2P(O)H$ = 418 g/mol).

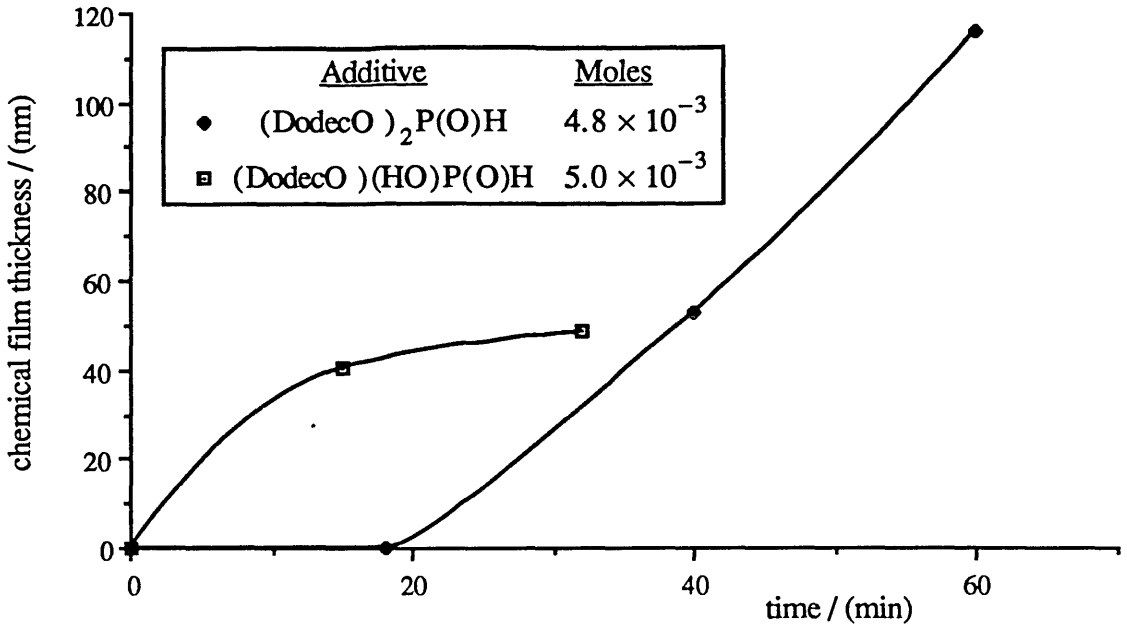


Figure 6.12 Chemical film build-up - mono and di-dodecyl phosphonate

Figure 6.12 shows a similar rate of film build-up for the mono and the di-dodecyl ester, although the build-up occurs much sooner with the mono-substituted version. This implies that the film build-up with di-alkyl phosphonates is determined either (i) by the rate at which they break-down into mono-esters (hydrolysis or pyrolysis) or (ii) the rate of dissolution of iron from the surface (which would be expected to occur earlier with the acidic mono-esters). However, since the standard optical method is restricted to the observation of the early stages of film build-up any conclusions should be tentatively drawn.

6.2.2.3 Discussion - film build-up with mono-alkyl phosphonates / amine salts

Some film formation was observed with both long and short chain length mono-alkyl phosphonates, although this material seemed to consist largely of corrosion products with the short chain versions. The conventional method of monitoring film build-up is not well suited to the measurement of films formed by such acidic compounds (due to the loss of the semi-reflective chromium layer). However, the initial build-up occurred after a shorter 'initiation period' - but at a similar rate thereafter - with a longer chain length mono-phosphonates (compared to a di-alkyl phosphonate of the same length). This may imply

break-down of the di-ester into the mono-ester, by hydrolysis (§ 7.3.1), is the rate limiting step.

The use of neutral amine salts overcame the problems associated with image loss. However, a complete absence of reacted layers was observed with the neutral salts. This may have resulted either from (i) a much reduced dissolution of iron at the surface, (ii) from direct inhibition of the active thick film forming component or (iii) from inhibition of formation of the active thick film forming component. This is to be expected if the molecule exists as the neutral salt in solution, since (i) implies the presence of the free acid and (ii) and (iii) imply the presence, or formation, of the probable 'active' thick film forming species i.e. the phosphonate anion [$(RO)HPO_2^-$].

No further testwork was undertaken to distinguish which of these mechanisms was involved, since the acidic mono-phosphonates were only produced in an attempt to probe the mechanism by which the di-esters form thick, reacted layers. The mono-esters are far too acidic to be used in practice, in an unmodified form. The use of a silica spacer layer (as described in chapter 8) would have overcome the problems associated with loss of optical quality. However, it is apparent from the work described in § 6.2.1.5 that film formation is not uniform over the whole of the ball surface and the technique described in chapter 8 monitors the film thicknesses present, for short periods, at various positions on the ball surface.

6.3 Esters of phosphoric acid - $(HO)_3P(O)$

The following section describes test work conducted with a range of esters derived from phosphoric acid. Section 6.3.1 describes tests conducted with tri-cresyl phosphate (TCP). TCP $(CH_3.C_6H_4.O)_3P(O)$ is commonly included in commercial formulations and although its behaviour has been the subject of much research its role remains nuclear (see § 2.4.1). Section 6.3.2 deals with di-alkyl acid phosphates $(RO)_2(HO)P(O)$ and their amine salts.

6.3.1 Tri-cresyl phosphate (TCP)

Section 2.4.1 summarised previous studies into the mode of action of TCP. Although no clear, single mechanism has yet emerged many of these studies identified an 'activation temperature' of 200 - 220° C.

A 6 % solution of TCP in SHC 234 was tested in the optical rig, by the author. No evidence of film build-up was found after 3 hours at 200° C. However, electrical contact resistance (ECR) measurements made during the HFR tests described below (§ 6.3.1.1) suggested that some film formation was occurring, although the film thickness could not be measured directly by this method (§ 5.3). These results suggested that a film - with a thickness less than one half the wavelength of light - was formed with TCP at elevated temperatures. Direct measurements of films of this thickness can be achieved either by a spacer layer technique (chapter eight) or by indirect optical means. As the spacer layer method was undergoing evaluation at the time of the testing, the latter technique was used (§ 6.2.1.2 - § 6.2.1.3). The same grade and source of TCP was used in all of the test-work described in this section (tri-tolyl phosphate, BDH Chemical Co. Ltd., technical grade).

6.3.1.1 HFR testing of TCP

In the following test a 7 % w/w solution of TCP in SHC 234 was compared with the base stock alone. The test procedure, sample preparation etc. was as described in § 5.3.2. Two sets of fixed duration tests (120 minutes each) were carried out (i) at room temperature and (ii) at 250 ± 5° C. Very similar results were found for the base stock with and without additive present, at room temperature. Wear scar analyses - carried out as described in

§ 6.2.1.3 - showed very little difference in the observed wear rates. The electrical contact resistance remained very low, for both lubricants, implying no reacted layers. Because of their similarity these results are not included. It was also difficult to obtain a homogeneous TCP / SHC solution, at room temperature, due to the poor relative solubility. The results obtained at 250° C are presented and discussed below.

The variation of the coefficient of friction (μ) and the electrical contact resistance (ECR) with time is shown in figures 6.13 and 6.14 respectively.

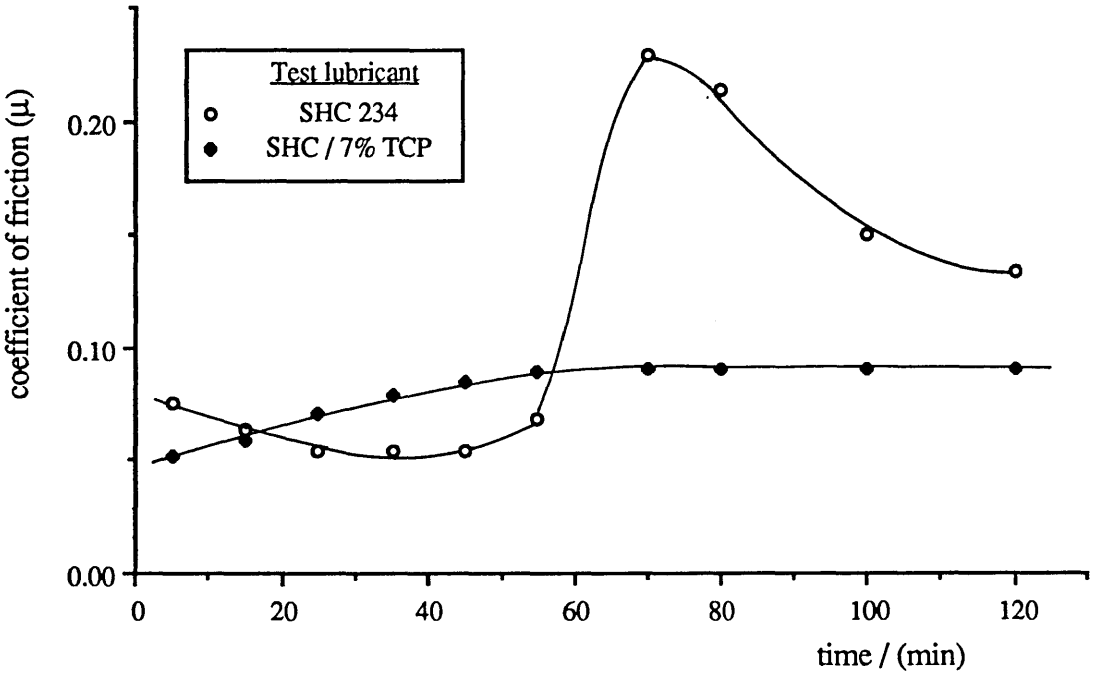


Figure 6.13 HFR rig - coefficient of friction (μ) vs. time (SHC 234 ± 7% TCP)

In the absence of additive, the coefficient of friction was found to drop soon after starting the test. This correlated well with a slight increase in the observed average ECR. The correlation implied some oxidation of the unformulated base stock. The average ECR increase suggested that polar species formed during oxidation were producing a reacted surface layer. However, considerable ECR break-down / asperity break-through was apparent within the stroke (from the ECR displayed on the oscilloscope). The failure of the oil-generated, reactant layer is obvious from the rapid increase in μ and decrease in average ECR later in the test. This corresponded to a period of severe stick-slip.

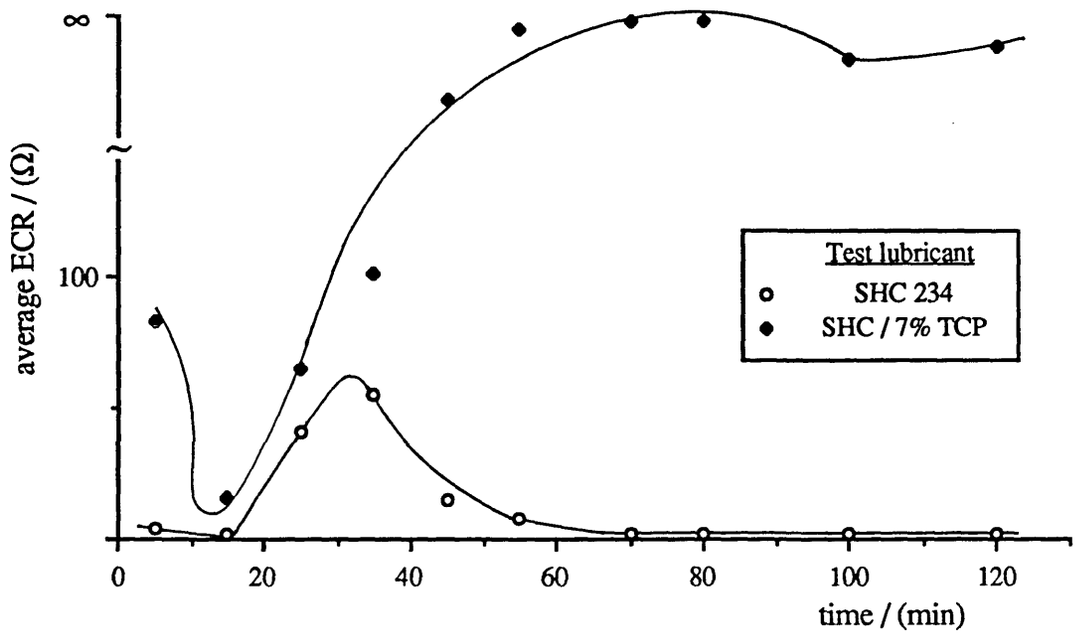


Figure 6.14 HFR rig - electrical contact resistance vs. time (SHC 234 ± 7% TCP)

The ECR was initially high, with TCP present, although it fell rapidly in the rubbing contact. This correlated with a low coefficient of friction initially which suggested the presence of an adsorbed or similar layer. As the test progressed the adsorbed layer was lost. This was gradually replaced by an insulating, reacted layer. A slight increase in μ was observed during this period. In the latter half of the test a near infinite ECR i.e. a fully insulating layer was present. This material displayed highly consistent frictional behaviour. The ECR as observed on the oscilloscope showed very little asperity penetration within the stroke.

After testing, the flat specimens were cooled and solvent-cleaned prior to optical examination and wear scar profilometry. The TCP-tested specimen had a slightly dulled, brown finish. Optical microscopy identified the presence of lumps of reacted material, on the surface of the specimen. The specimen tested in base stock alone retained a 'mirror' finish. The various measurements made on the wear scar are shown - in the form of a bar chart - in figure 6.15. A considerable reduction in wear is apparent with TCP present.

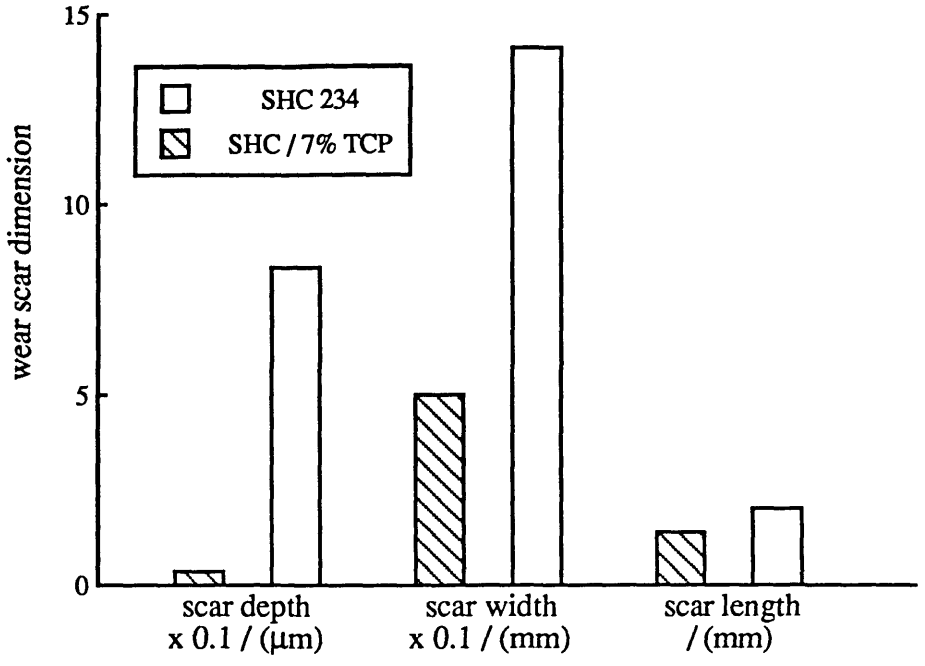


Figure 6.15 HFR rig - wear scar profilometry (SHC 234 ± 7% TCP)

6.3.1.2 Static (in vitro) pretreatment with TCP

The following indirect method was used to measure the thickness of films generated with TCP, at elevated temperature. Four one inch balls (AISI 52100) were subjected to various pretreatments. The conditions of pretreatment are given in table 6.3. Test balls A, B and C were pretreated in boiling tubes containing approximately 40 cm^3 of lubricant. The boiling tubes were immersed in a thermostated heating bath. The temperatures in the table refer to the temperature of the test lubricant.

Ball	Solution	Pretreatment
A	Pure TCP	220° C for 6 hours
B	3% TCP in SHC	220° C for 6 hours
C	Pure SHC 234	220° C for 6 hours
D	Solvent clean only	None

Table 6.3 Static pretreatment conditions (SHC ± 3% TCP)

After pretreatment and partial cooling, the test balls were removed from their respective solutions and left to drain until no observable solution remained. The test balls were then left to cool to room temperature, prior to testing in the optical EHD rig. Identical conditions of load, base oil, track radius etc. were employed during the film thickness measurements. Untreated SHC 234 was used as base stock in all cases. The results are shown as a standard log separation versus log speed curve in figure 6.16. No curve is shown for ball D as this was indistinguishable from ball C.

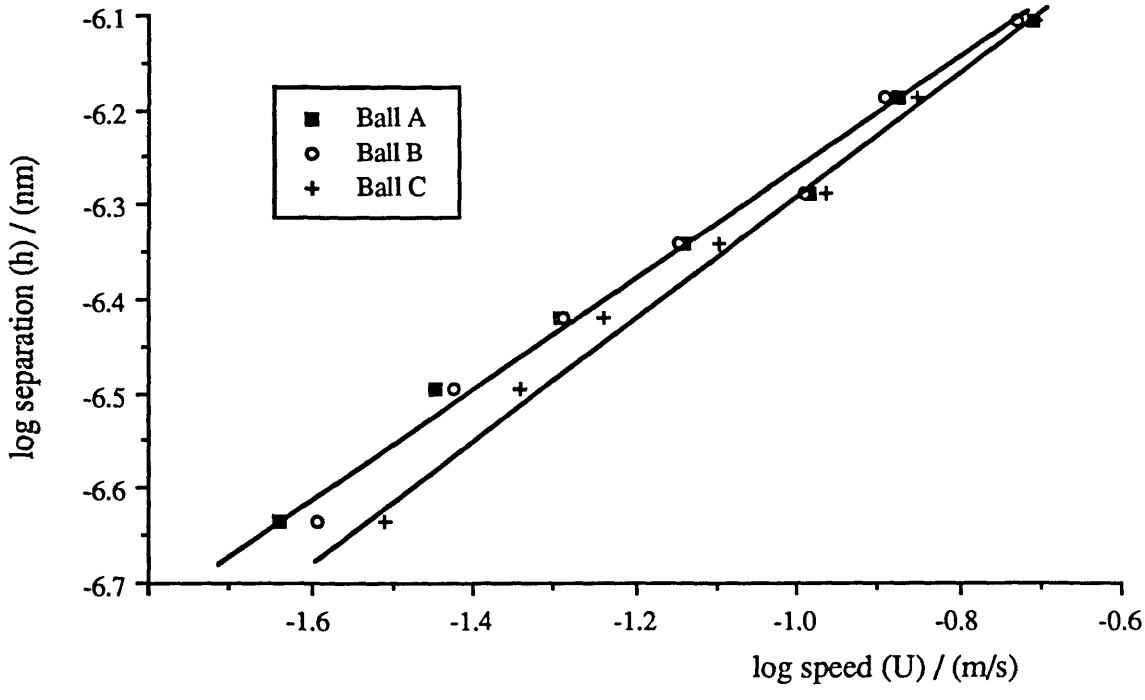


Figure 6.16 Log h vs. log U - static pretreatment SHC 234 ± 3% TCP

The curves shown in figure 6.16 are of two distinct types. The balls that were pretreated in the absence of TCP (C and D) show conventional log h versus log U behaviour i.e. a gradient close to that predicted by EHD theory (§ 1.4). However, the balls that were pretreated with TCP show a reduced gradient. In the interests of clarity a single line was drawn through the data points generated with balls A and B. The results have been replotted as observed central film thickness versus disc speed in figure 6.17. Plotting the results in this form makes it easier to observe any additional separation that may have resulted from the formation of a reacted layer.

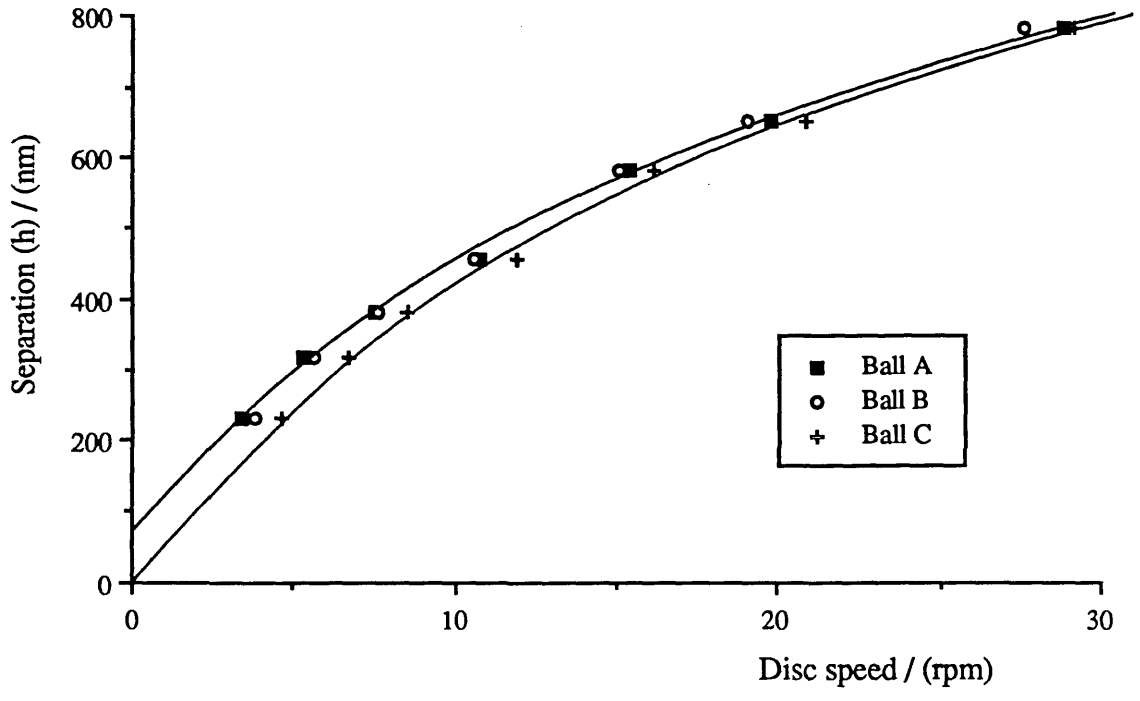


Figure 6.17 Separation vs. disc speed - static pretreatment SHC 234 ± 3% TCP

At first sight figure 6.17 implies an additional film thickness of approximately 75 nm. The graph assumes the refractive index of any additional, TCP-generated film material is the same as that of the base oil. This has been shown to be true for phosphonate generated films (§ 7.2.3.1). Careful observation of figures 6.16 and 6.17 shows that the additional separation falls as the total separation increases. This is consistent with the formation of an additive generated film, which loses significance as the total separation far exceeds that of the additive film thickness. Alternatively, the reduced gradient observed in figure 6.16 could have resulted from a reduced relative phase change (ϕ) with the TCP treated surfaces. The film thickness values in the figures assume $\phi = 3 / 5\pi$ (see § 5.2). The relative phase change depends on the phase change at the chromium coating (which is unlikely to change) and the phase change at the ball (which is approximately π in the absence of a film). The fact that a film was visible with the naked eye after pretreatment (ball A) provides further, indirect evidence of the presence of a film in the EHD testing. The gradient observed in figure 6.16 with ball C shows that no phase change occurred when a ball was heated in base stock alone. This rules out oxide formation for example.

The results above suggest that TCP can form a tenacious film with a thickness far exceeding that conventionally accepted, and that it is able to withstand the shear of an EHD contact. Only the material close to the ball exhibits this sort of physical behaviour. After draining, ball A had a thicker, loosely-held covering. This material could be seen with the naked eye. When ball A was run in the EHD rig much of this material was quickly lost to yield the residual film measured. Similar behaviour was observed when a ball was pretreated in pure BOPP at 100° C. Very thick films were initially found to be present, but much of the film material was rapidly lost from the contact during running in the EHD rig.

6.3.1.3 Dynamic pretreatment with TCP (in EHD rig)

The experiment described in the previous section showed that the physical nature of the material generated with TCP is greatly influenced by the conditions under which it is formed. The material generated 'in vitro' with pure TCP was eliminated from the contact, during testing in the EHD rig. For this reason, the following experiment was conducted. The balls were pretreated directly in a high shear, high pressure EHD contact. Two balls were pre-run at elevated temperature in the EHD rig. The conditions are summarised in table 6.4. At the end of the pretreatment no films exceeding the minimum film thickness observable by interferometry i.e. approximately 140 nm were visible. The maximum oil inlet temperature was limited to 180° C. However, the temperature in the contact may have exceeded the 'activation' temperature of approximately 200° C, due to heating effects within the contact [51]. After pretreatment the experiment described in the previous section was repeated. The test balls were removed from their respective solutions and left to drain until no observable solution remained. Both balls were then retested at ambient temperature using the same base oil, in the optical EHD rig.

Ball	Solution	Pretreatment
X	5% TCP in SHC	3 Hours at 180° C
Y	Pure SHC 234	3 Hours at 120° C

Table 6.4 EHD rig - pretreatment conditions (SHC ± 3% TCP)

Ball Y was also preheated, although the previous experiment suggested that no anomalous phase changes occur on heating. The observed separation is shown as a function of the rolling speed in figure 6.18. The graph suggests some formation of a reacted layer.

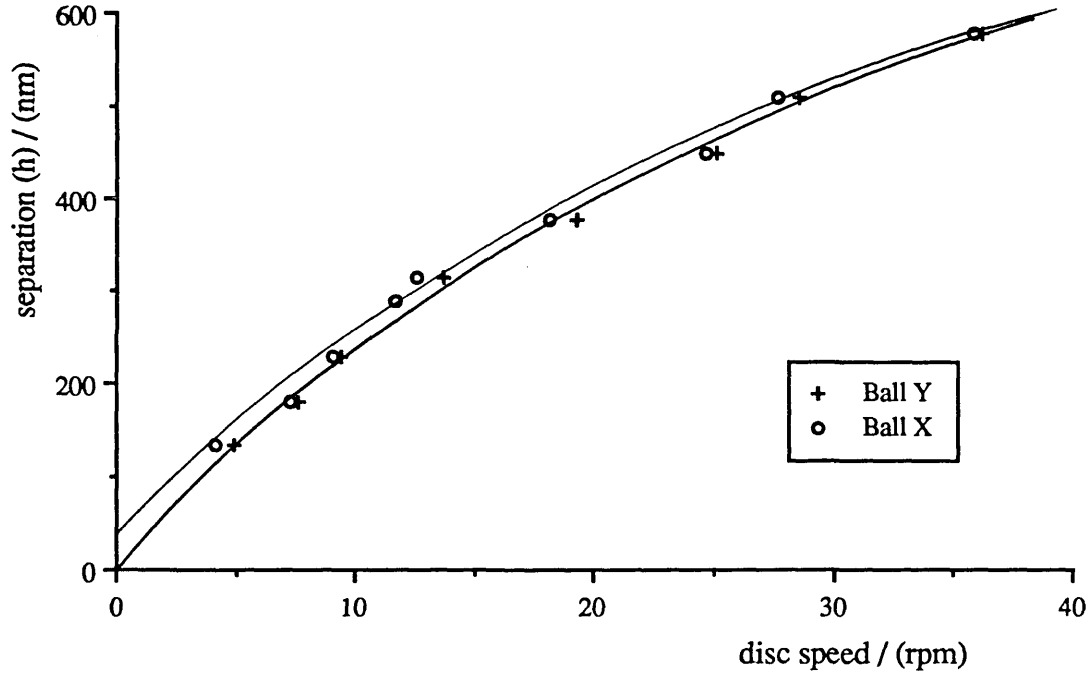


Figure 6.18 Separation vs. disc speed - dynamic pretreatment SHC 234 ± 5% TCP

6.3.2 Phosphoric acid esters and their amine salts

Two observations led to the synthesis of a range of phosphoric acid esters and amine salts as described in chapter 4. Firstly, the acid esters are known to act as bridging ligands [95] and they were believed to be important in polymer formation [76], [29]. Secondly, a commercial amine phosphate tested by the author in the EHD rig showed some signs of polymer film formation. No film formation was observed at 100° C, but some indirect evidence of film formation was obtained at 180° C. The film build-up could not be monitored directly by optical interferometry, because of the inability of conventional lubricants to form sufficiently thick films at this temperature. The evidence of film build-up came from reflection infra-red studies of the ball surface after testing. A slight shift of the phosphoryl bond vibration was observed with the amine phosphate, which may have indicated partial co-ordination and thence polymer formation. However, considerable oxidation of the base oil occurred at the test temperature and this partially masked the

phosphoryl vibration. For this reason the reflection infra-red studies proved inconclusive.

The work of Lacey et al [76], [29] suggests that the bridging species is mono-alkyl phosphate, which results from oxidation - and, presumably, partial hydrolysis - of the di-alkyl phosphonate. This seems unlikely in view of the known oxidation stability of di-alkyl phosphonates, and their reactivity towards nucleophilic attack at phosphorus. This stability is evident from the very powerful oxidising agents required to produce di-alkyl acid phosphates from di-alkyl phosphonates (as described in chapter four). If oxidation of phosphonate is the first step in polymer formation, then the use of the primary oxidation product - the di-alkyl acid phosphate - should result in the build-up of a thick reacted layer at a minimum rate equal to that observed with the phosphonate. Indeed, according to the mechanism proposed previously [76], the rate of polymer build-up must be limited either by the oxidation of phosphonate or the dissolution / oxidation of the iron surface. The use of a di-alkyl acid phosphate might be expected to increase the oxidation / dissolution rate also. This hypothesis was tested as follows.

A 3% w/w solution of di-dodecyl acid phosphate in SHC 234 was tested in the optical EHD rig. No film formation was observed after 4 hours at 100° C. Some oil breakdown was evident. The ball removed from the rig retained a highly reflective appearance, indicating the absence of any reacted layer. This was confirmed by reflection infra-red analysis. When the experiment was repeated at 180° C the identification of a reacted layer was complicated by considerable oil breakdown. Reflection IR analysis of the decomposition products present on the ball surface indicated oil breakdown, with almost no change in the position of the phosphoryl bond vibration. Because of the problems in following film build-up at the required test temperature and the constraint of time no further studies were conducted into film formation within a rolling contact. The compounds were shown to form polymeric, model compounds with iron stearate (§ 7.3.1).

The primary oxidation product of di-dodecyl phosphonate failed to form a reacted layer. This may be compared with the rapid film build-up observed with the hydrolysis product - mono-dodecyl phosphonate (see § 6.2.2). It should be noted that the mono phosphonate was of limited purity (in contrast to the di-alkyl acid ester). This suggests that hydrolysis, not oxidation, precedes polymer formation with di-alkyl phosphonates. Some further evidence from mechanistic studies using model compounds is presented in chapter seven.

CHAPTER 7 - PHYSICAL AND CHEMICAL NATURE OF ORGANO-PHOSPHORUS ADDITIVE / IRON REACTION PRODUCT

7.1 Introduction

The following chapter describes studies into the physical and chemical nature of the material resulting from the reaction of phosphorus-based anti-wear additives and iron containing species. In general terms the material is formed in two distinct environments. It can either be generated in an operating contact or it can result from the static reaction of iron, or an iron containing material, with pure additive (or a solution of additive in oil). The resulting material may be described as having been formed '*in lubro*' or '*in vitro*' respectively.

In chapter one it was shown that the successful operation of many lubricated contacts depends upon the formation of protective, chemical layers on the rubbing surfaces. It is apparent that the physical properties of the material formed will determine whether it functions successfully, and that the physical properties required will depend upon the prevailing Lambda value, that is the operating regime. For many years AW and EP additives were believed to function by the formation of thin layers of metal inorganic, or more recently organic, salts. These films were thought to reduce adhesion and promote load-sharing by chemically smoothing or 'polishing' the surface. However it is apparent from much of the work described in chapter 2 that much thicker films are often formed. Developments in EHD theory have shown that bodily separation of contacting surfaces is not restricted to rigid solids. Any viscous or visco-elastic material with a viscosity exceeding that of the base stock, will augment the conventional hydrodynamic or EHD film, at normal running speeds. The slow acceptance of the latter mechanism resulted, at least partly, from the heavy solvent cleaning required by the high vacuum environments employed in most surface analytical techniques. The physical nature of the polymeric material formed by reaction with additive would be expected to vary with its proximity to the surface. Rigorous solvent cleaning would therefore remove much of the loosely-held organic material. For this reason, wherever possible, non-intrusive techniques have been used in the current work to determine the physical properties of the material 'in lubro'. The

high shear rate, temperature and pressure found in an operating contact would also be expected to be important in determining the physical properties of the film material. These studies are detailed in § 7.2. Some further attempts to determine the physical nature of the film material in an operating EHD contact were described in § 6.2.1.4 and § 6.2.1.5.

The chemical composition of the iron / additive reaction product generated 'in vitro' and 'in lubro,' is the subject of § 7.3. Static solution studies have been used both to produce well-defined, model compounds for further chemical analyses, and to investigate the mechanism by which the additives react with iron.

7.2 Physical nature of the iron / additive reaction product

The following two sections detail studies into the physical nature of the material resulting from the reaction of additive with steel surfaces (§ 7.2.1 - 7.2.2) and with iron-containing powders and compounds (§ 7.2.3).

7.2.1 Reaction films generated on steel surfaces

The test-work described in the following section was completed after testing a solution of *bis*-(*t*-octyl-phenyl) phosphonate (BOPP) in hexadecane, in a High Frequency Reciprocating (HFR) rig (this work was described in detail in § 6.2.1.3). During the HFR testing, it was observed that the fine scale surface roughness present prior to testing was replaced by a low frequency, 'globular' roughness after testing (when the additive was present). This suggested that the additive was altering the surface profile by either : -

(i) chemically polishing the surface
(ii) or reacting with the surface to produce a thick reacted coating that obscured the original surface roughness.

The following experiment was designed to find out which of these mechanisms was operating, firstly at a location distant from the contact and secondly within the contact itself.

7.2.1.1 Chemical polishing vs. thick film formation
Talysurf relocation - out of contact

Two flat test-pieces - denoted A and B in the following description - were produced from a piece of EN 31 bar (3/4 x 1/8"). The specimens were cut into approximately 3/4" squares prior to sequential grinding on a rotary polishing wheel (Metaserve). The specimens were ground in water using 220, 600 and 800 grade carborundum paper. The final grinding process employed a circular motion against the rotation of the wheel to ensure that a randomly distributed roughness resulted. Unlike the HFR tests described in § 6.2.1.3, no further polishing was used in the current experiment, as an easily 'observable' roughness was required. The lubricant used was hexadecane ($C_{16}H_{34}$). This had previously been stored over a mixture of activated alumina and silica gel, to remove polar impurities and to dry the liquid respectively. Specimen B was tested using a solution of BOPP in hexadecane (3% w/w).

The relocation device, shown schematically in figure 7.1, was built to distinguish between the chemical polishing and the thick film mechanisms. The device was intended to relocate the specimens so that the surface profile could be measured - over the same region on three successive occasions - prior to testing, after testing with additive and after removal of the film material (by treatment with a vigorous solvent). The device was mounted on a magnetic block which was permanently locked onto the Taylor-Hobson talysurf IV during testing. The test-pieces were scratched prior to testing, to provide a constant datum from which subsequent profiles could be matched.

The specimens were ultrasonically cleaned in toluene and then in acetone prior to each measurement of the surface profile. The flats were placed in the HFR rig, 3 ml of lubricant was added and the temperature was maintained at 108 ± 3° C for thirty minutes. The HFR rig and the test procedure were described in detail in chapter 5. After HFR treatment the specimens were removed, ultrasonically solvent-cleaned and then treated as follows with dry di-methyl sulphoxide (DMSO). DMSO [$(CH_3)_2S=O$] is a highly hygroscopic, aprotic liquid. The DMSO was dried, prior to use, using size 4A molecular sieve [218]; this was essential as it rapidly absorbs enough atmospheric moisture to rust the specimens. The specimens were refluxed for one hour in a round-bottomed flask containing DMSO. The

attached condenser was fitted with a drying tube containing calcium carbonate as drying agent, to prevent water absorbtion during reflux. The specimens were again cooled and ultrasonically solvent-cleaned before the surface profile was remeasured.

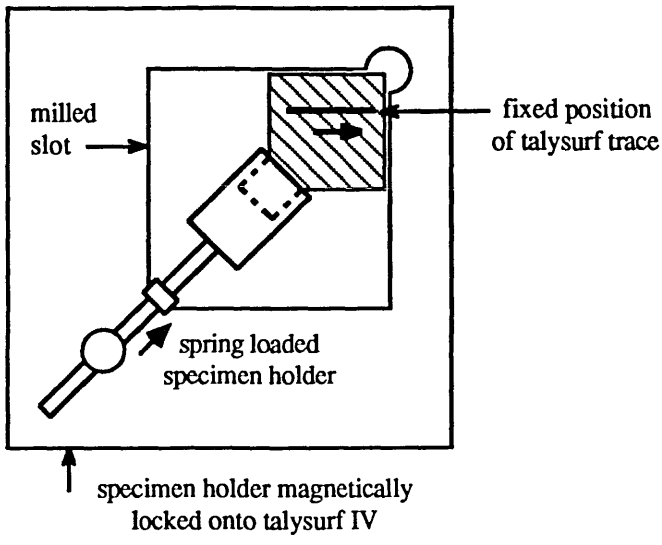


Figure 7.1 Schematic diagram of test-piece relocation device

Figure 7.2 shows a representative section from the relocated surface profiles of specimen A, after various treatments. The vertical and horizontal magnifications are x 10,000 and x 100 respectively. The surface profile (I) was measured prior to testing. Profile (II) was recorded after removal and replacement of the specimen to test the accuracy of the relocation device. The two profiles were found to be virtually identical, implying relocation to within one asperity width. Specimen A was then heated with pure hexadecane, solvent-cleaned and the surface profile was remeasured. It was found to be indistinguishable from profiles (I) and (II), and for this reason it was not included in figure 7.2. The effects of DMSO treatment were investigated by recording the surface profile after DMSO treatment / solvent-cleaning - this is shown in profile (III). The relocation again appears to be good and the surface is almost unchanged by the DMSO treatment. However, careful observation shows that a few asperity heights have increased slightly, presumably as a result of some surface deposition or very slight rusting. Profile (IV) was recorded after removal and replacement of the specimen, to further demonstrate the accuracy of the relocation device and to show that the surface was not rendered friable by the DMSO treatment.

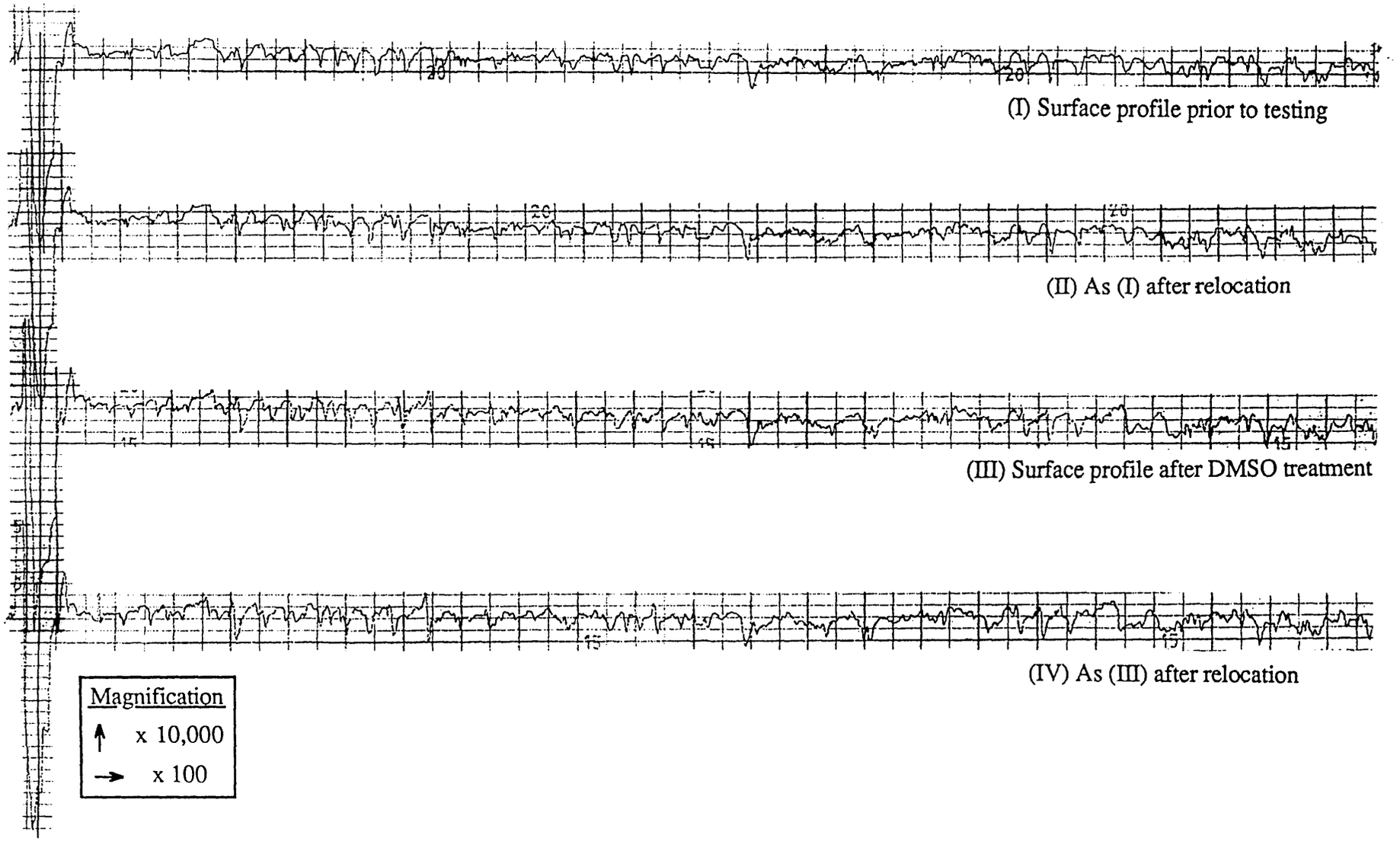


Figure 7.2 Relocation of surface profiles - untreated test piece (A)

The measurements on test piece A, as summarised in figure 7.2, demonstrated the high accuracy of the relocation device and the absence of gross changes in the surface profile as a result of the various treatments used. It was necessary to demonstrate this before testing with additive. The previous test procedure was repeated for specimen B, except that a solution of BOPP in hexadecane (3% w/w) was used in the HFR rig. The results are summarised in figure 7.3. The surface profiles (V) and (VI) were recorded for successive relocations of the untested specimen and they are very similar. Profiles (VII) and (VIII) were recorded for successive relocations of specimen B after testing with hexadecane / BOPP (in both cases after ultrasonic cleaning in toluene and acetone). The fine scale roughness was been replaced by a lower frequency, globular roughness. Surface profile (IX) was recorded after DMSO treatment to remove the film material.

A comparison of profile (V) and profile (IX) shows that the original surface roughness was recovered after removal of the additive-generated film. This clearly demonstrates that the additive produced the low frequency roughness distribution by the growth of a thick film and not by chemically polishing the surface. An estimate of the maximum thickness of the coating can be made by measuring the height of the tallest 'asperity' situated to the right of the datum scratch. It varies in height from approximately 8 - 11 mm i.e. 800 - 1100 nm. The original profiles were photocopied on to clear acetate. Overlaying the profiles measured before and after treatment with BOPP suggested an average additional film thickness of the order of 200 - 500 nm. This is greater than the typical peak to valley heights of commercial bearing finishes. A comparison of profiles (VII) and (VIII) shows a slight deepening of some of the valleys in the latter profile, suggesting that some of the material generated outside of an operating contact is removed by successive passes of the talysurf stylus. Later work will show that this is not the case for material generated within a contact. However, even the statically generated material was found to be sufficiently tenacious as to be unaffected by ultrasonic cleaning in toluene / acetone. Only a very vigorous solvent such as boiling DMSO was found to remove the film.

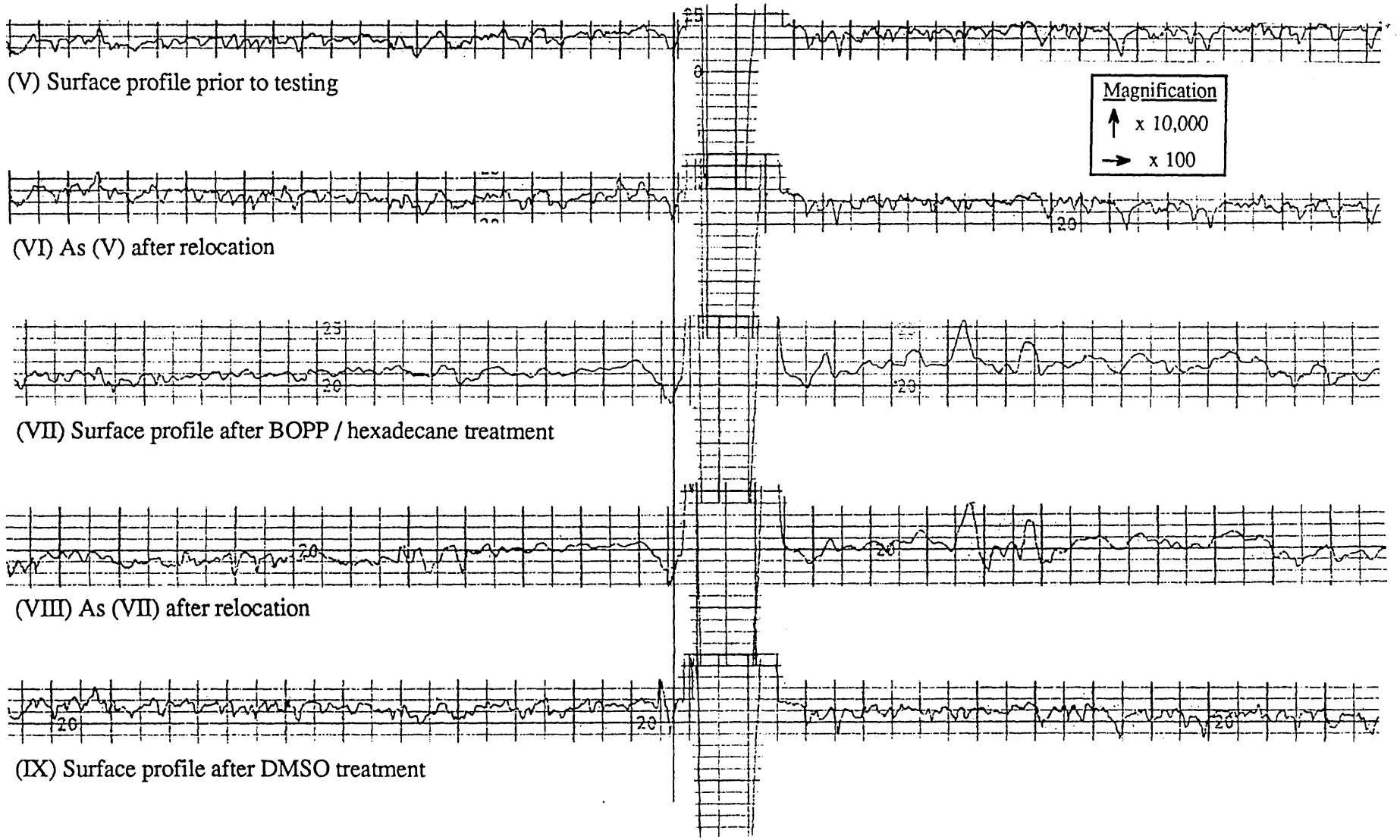
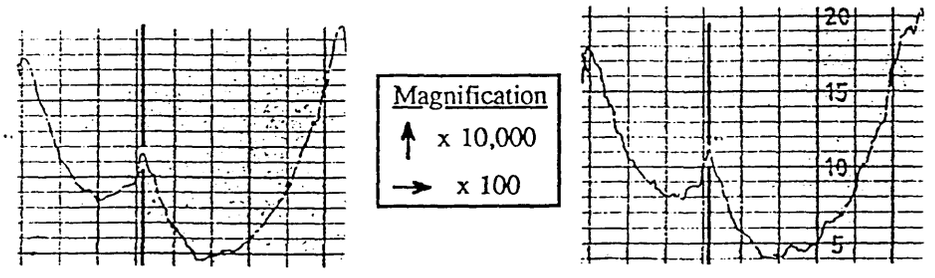


Figure 7.3 Relocation of surface profiles - BOPP / hexadecane treated test piece (B)

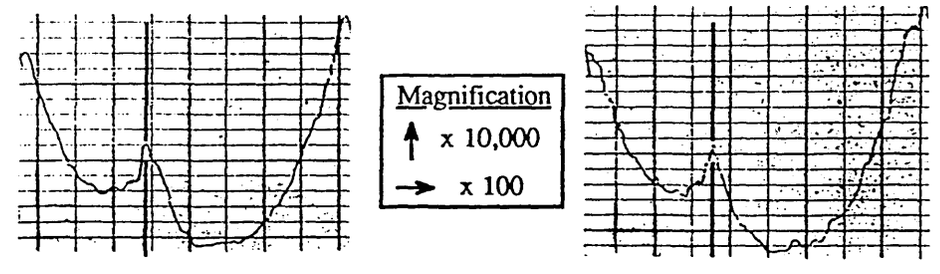
7.2.1.2 Talysurf relocation - within the wear scar

The test procedure described for specimen B (above) was repeated in the following experiment. In this experiment, however, a 1/4" (6.35 mm) AISI 52100 diameter ball was rubbed on the stationary, flat test-piece. EN 31 and AISI 52100 are equivalent bearing steels conforming to English and American steel specifications. Their respective compositions are given in table 7.3. A test temperature of 115 ± 3° C was employed. The ball was oscillated over a stroke length of ± 0.5 mm at an operating frequency of 50 Hz (the procedure is detailed in § 5.3).

Figure 7.4 shows relocated surface profiles measured through the wear scar, in a direction perpendicular to the direction of sliding. Profiles (X) and (XI) are successive relocations recorded after ultrasonic cleaning with toluene / acetone, but prior to DMSO treatment. Profiles (XII) and (XIII) are successive relocations recorded after DMSO treatment and further solvent cleaning.



(X) Wear scar post HFR testing (XII) Wear scar post DMSO treatment



(XI) As (X) after relocation (XIII) As (XII) after relocation

Figure 7.4 Relocated wear scar surface profile after HFR testing in BOPP / hexadecane - pre and post DMSO treatment

Comparison of the two profiles recorded before DMSO treatment and the two profiles recorded after DMSO treatment show that good relocation was achieved. Treatment with DMSO has resulted in a similar alteration of the surface profile to that observed with specimen B. The smooth profile observed immediately after testing with additive present, is replaced by a rougher profile when the material is removed with boiling DMSO. A comparison of the depth of the wear scar before and after DMSO treatment shows the latter to be of the order of 1 mm on the figure i.e. 100 nm deeper. Thus the additive appears to operate by formation of a thick, protective layer and not by chemical polishing within the contact as well on the bulk material. Further supportive evidence for this mechanism was presented in chapter six. This section details the results of a full programme of HFR tests including friction, wear and electrical contact resistance data.

The previous experiments have produced evidence that BOPP acts by the formation of a thick, protective layer even in boundary lubricated contacts. The following section provides further evidence for this mechanism.

7.2.2 Physical nature of film material generated in an EHD rig

The optical interferometric studies of Lacey et al [76], [28] showed that di-alkyl / aryl phosphonate esters form thick polymeric films in pure rolling and low slide / roll ratio EHD contacts. The films formed continued to separate the surfaces in the absence of an EHD film i.e. in the stationary contact. The following two sections describe studies aimed at investigating the physical nature of the films formed in a pure sliding contact (§ 7.2.2.1) and in a pure rolling contact (§ 7.2.2.2). The optical EHD rig used by Lacey was used in a modified form, to produce the films tested here. Full details of the rig design and the test procedure are given in § 5.2.

7.2.2.1 Physical nature of material generated in pure sliding

The wear scar relocation tests described in the previous section suggested that BOPP is an active thick film forming agent, even under initial conditions of low specific film thickness when considerable metal / metal contact occurs. The optical interferometric technique described in chapter five requires a thin semi-reflecting layer of chromium to be sputtered onto the glass disc which contacts the steel ball, to split the beam prior to its recombination

and interference. However, the chromium layer, is invariably scraped off under sliding, boundary conditions. To overcome this the following modified optical technique was used.

The loading arm used previously by Lacey [76], as described in chapter five, was rebuilt so that the ball could be held stationary. The redesigned loading arm is shown schematically in figure 7.5. The rig was lubricated with a solution of BOPP in synthetic hydrocarbon (SHC 234, 3% w/w) at 100° C. The test was run holding the 25.4 mm AISI 52100 ball stationary and rotating the disc at a sliding speed of 0.924 ms^{-1}, under a load of 15 N, for 150 minutes. During the first minute or so of the test, before the chromium was removed, an interference pattern could be seen which indicated that the film thickness was less than the limit measurable by optical interferometry (that is approximately 140 nm). The EHD central film thickness (h_c) and the minimum film thickness (h_o) were calculated using the Dowson and Hamrock formulae [9] (see chapter one equations (V) and (VI), and the section on nomenclature). The values of the various parameters used in the calculation are summarised in table 7.1. The viscosity and the effective pressure-viscosity coefficient (α value) were measured by the author (as described in chapter 5). These variables are plotted as a function of temperature for SHC 234 in appendix A1. The calculated film thicknesses were h_c = 109 nm and h_o = 67 nm. As such no image was seen after the first minute of the test, nor was one visible at the end of the test.

Variable	Glass	Steel
Poissons ratio (σ)	0.22	0.293
Youngs modulus (E') / (N/m^2)	75.0×10^9	210.0×10^9
U / (m / s)	0.924	0
Reduced Youngs modulus (E') / (N/m^2)		1.13×10^{11}
$U_{mean} = (U_1 + U_2 / 2)$ / (m / s)		0.462
η (100°C) / (Pa.s)		0.0351
α (100°C) / (GPa^{-1})		8.56
R'_x / (m)		0.0127
W / (N)		15

Table 7.1 Values for parameters used in EHD film thickness calculation

At the end of the test, with the disc stationary, the ball and its holder were gently raised and moved radially outward onto a part of the disc where the chromium layer was intact. When the microscope was focused on this new contact a thick, globular film was observed to be separating the surfaces. The contact appeared similar to that shown in plate 6.2. The separating film was not an oil entrapment as it survived tangential movement of the disc. The distribution and appearance of the material around the contact were investigated using a rotary talysurf and scanning electron microscope (SEM) analysis.

The ball loading arm was removed from the rig, cooled and ultrasonically solvent-cleaned in toluene and acetone. The arm was then relocated on the rotary talysurf so that the distribution of the film could be measured. This set up is shown schematically in figure 7.5. The ball holder was designed to accommodate a 1" ball in a 'push-fit' to give accurate location. The ball was held in place by two grub screws. The loading arm, carrying a new ball, was mounted on a magnetic block, onto which it could be accurately relocated after removal for testing. The talysurf stylus was raised and lowered, in the plane of the page (figure 7.5), and the height was fixed at the point at which the stylus was farthest from the ball centre. This ensured that the measured surface profile ran through the centre of the contact. The apparatus was then set up so that the talysurf stylus traversed an arc with a radius equal to the ball radius i.e. the curved surface was effectively rendered flat. The speed at which the stylus traversed the profile was set to give a magnification of x 100 in

the traversed direction. The loading arm / ball combination was then removed and tested in the EHD rig, as described previously. After testing, the arm was solvent-cleaned and replaced on the rotary talysurf.

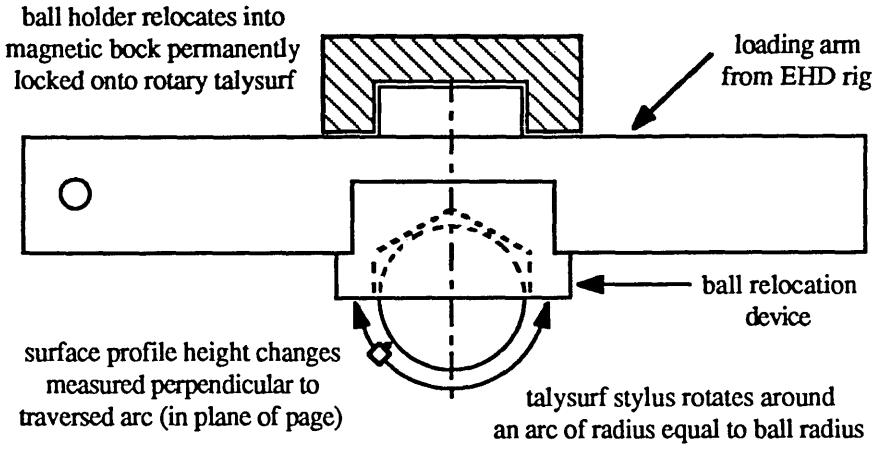


Figure 7.5 Schematic diagram of ball surface profile relocation device

Figure 7.6 (XIV) shows the surface profile after testing; the direction of sliding is from left to right. The figure includes a section of a typical profile for an untested ball (XV inset) for comparison. The magnifications are given on the figure. This shows a maximum deposit depth of approximately 36 mm on the figure i.e. 36 x 10^{-3} / 5,000 = 7.2 μm in the inlet. The right hand end of the profile shows a flat, depositless region. If this is assumed to be the ball surface it can be seen that wear has occurred, in the contact, to a depth of approximately 7 mm on the figure (that is 1.4 μm on the ball). The wear is concentrated over a distance of approximately 3 cm on the figure, with some reduced wear occurring over a 5 cm long region. These two values correspond to 0.3 mm and 0.5 mm distances on the ball surface. Substitution of the parameters given in table 7.1 into equation (XIX) permits calculation of the Hertzian radius (a). The calculated Hertzian radius is 0.136 mm i.e. a diameter of 0.272 mm, which correlates well with the observed wear.

$$a = \left(\frac{3W R_x'}{2E'} \right)^{\frac{1}{3}} \qquad \text{(XIX)}$$

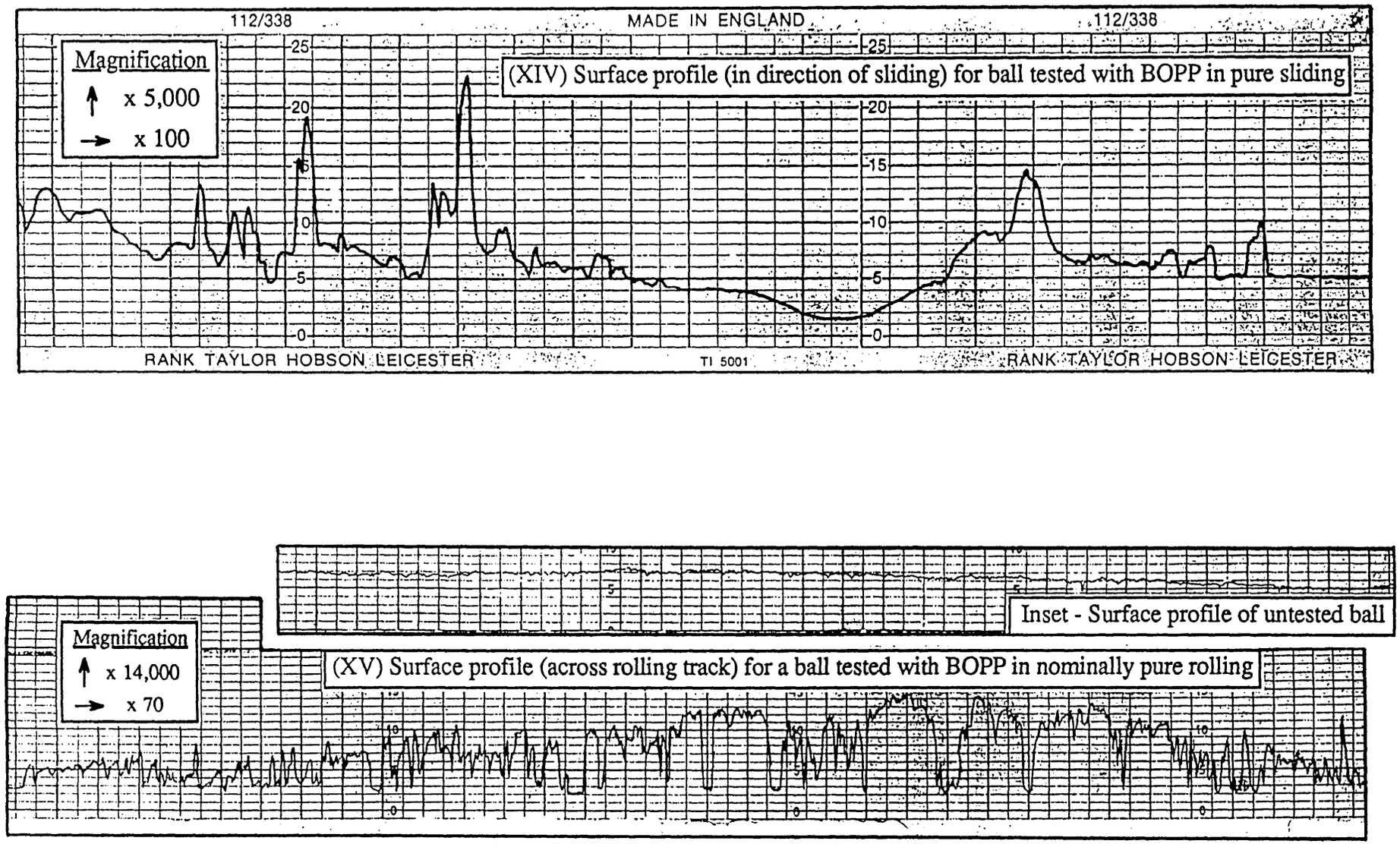


Figure 7.6 Surface profile of ball after testing with BOPP - in pure sliding (XIV) and in nominally pure rolling (XV)

7.2.2.2 SEM / EDAX analysis of material generated in pure sliding

The specimen described in the previous section was subjected to Scanning Electron Microscopy (SEM) analysis to determine whether the additive was producing a thick reacted layer in the wear scar. Before being placed in the SEM, the wear scar was scribed using a glass rod that had been melted and drawn to a fine point. If thick film material were present the scribing process would be expected to clear a channel through the film (presuming the material to be softer than drawn glass) and the contrast should be observable with the SEM.

The SEM used was a JEOL JSM T-200 fitted with an energy dispersive analysis of X-rays (EDAX) facility. The SEM gives a magnified three dimensional image which can be recorded photographically as follows. The sample is scanned by a parallel beam of electrons. The secondary electrons emitted from the surface of the sample are focused by a magnetic or electrostatic 'lens' to give a magnified image. The incident electron beam also causes the elements present at the surface to emit X-rays. The energy of an emitted X-ray is characteristic of the element from which it originated. Thus the EDAX facility gives a guide to the elements present and their respective concentrations (from the number of signals of a fixed energy that are received). The detector plots the number of X-rays counted as abscissa against the energy of the X-ray (in k eV) as ordinate. However the EDAX facility suffers from the dual disadvantages of only recording elements of atomic number greater than 10 (this limit is imposed by the detector) and of giving an average surface composition to a depth of 200 - 500 nm. A detailed description of SEM and EDAX analysis can be found in [219] and [220] respectively.

Plate 7.1 is a SEM photograph of the scribed specimen. The specimen was solvent-cleaned as described previously, before insertion into the SEM chamber and vacuum evacuation. Non-conducting films usually require a thin sputtered coating of gold or carbon to improve the image quality; this was found to be unnecessary. The ball was placed in a 'pool' of silver loaded paint, on the sample stage. This ensured a good electrical contact, which prevented the specimen charging up (this would lead to a reduced image quality). In the photograph the direction of sliding is from upper right to lower left. The SEM magnification was x 35 (this was increased to approximately x 80 during printing). A close

examination of the scribed line clearly demonstrates the presence of a thick, reacted layer at the front of the wear scar. However it is not clear whether similar material is present further into the scar, as the contrast is less well defined on the left side of the scribed line.

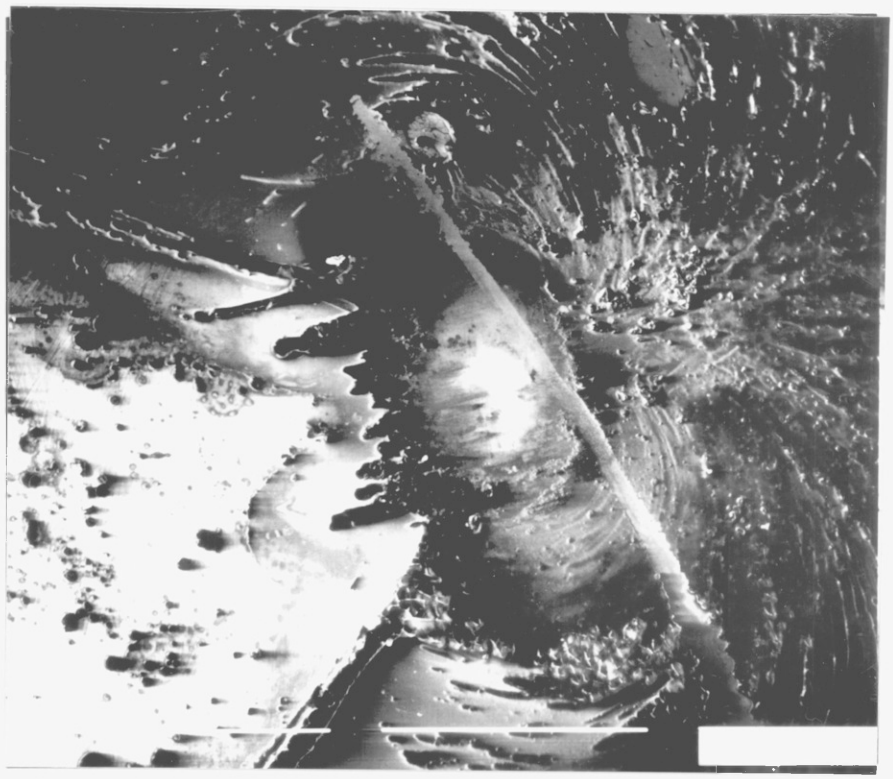


Plate 7.1 Appearance of film material around contact after pure sliding test with a 3% w/w solution of BOPP in SHC 234

To overcome this problem the EDAX facility was used to compare the elemental composition of the centre of the scar (the white region in plate 7.1) with the thick film material i.e. the black region in the exit of the scar. The conditions used for the EDAX analysis were the same as those used by Lacey [76] and are summarised in table 7.2. The preset count total refers to the number of counts required for the machine to acquire a spectrum, within a given energy range or 'window.'

Magnification	x 1000
Electron beam energy	10 k eV
Preset count total	25000
Preset window	2.68 - 3.2 k eV
Resolution	20 eV / channel

Table 7.2 Experimental conditions used for EDAX analysis

The results of the EDAX analyses are shown in figure 7.7. It can be seen that the wear scar contains a high level of phosphorus. The strong iron signal results from the steel substrate, as the EDAX technique is not truly surface sensitive. An EDAX analysis of the film material out of the contact has a higher phosphorus content, as might be expected. Also, because it is much thicker, it has effectively masked the steel substrate.

In combination, the image observed optically after testing, the EDAX data and the less clear-cut SEM photograph suggest that even under initial conditions of low film thickness the additive can produce a thick, protective layer capable of contributing towards surface separation.

7.2.2.3 Physical nature of material generated in a rolling EHD contact

The following measurements were made on the thick-film material generated on a 25.4 mm AISI 52100 ball running in nominally pure rolling. The reacted layer was generated from a solution of BOPP in SHC 234 (3 % w/w) at a test temperature of 100^{o} C and a load of 15 N. The test was conducted at constant speed for 100 minutes. During this time the observed separation went from first order blue (~ 235 nm) to second order blue (~ 422 nm). The experimental procedure was discussed in detail in § 5.2. Thus an additional separation of approximately 290 nm was observed optically. This resulted from the formation of a thick, reacted layer in the contact. The material was observed to continue to separate the surfaces, after testing, in the absence of an EHD film (as shown in plate 6.2). After cooling, the ball was ultrasonically cleaned in toluene and acetone. The ball was then placed in the rotary talysurf relocation device so that a series of surface profiles could be measured. Figure 7.6 compares a section of the surface profile of a ball after testing with

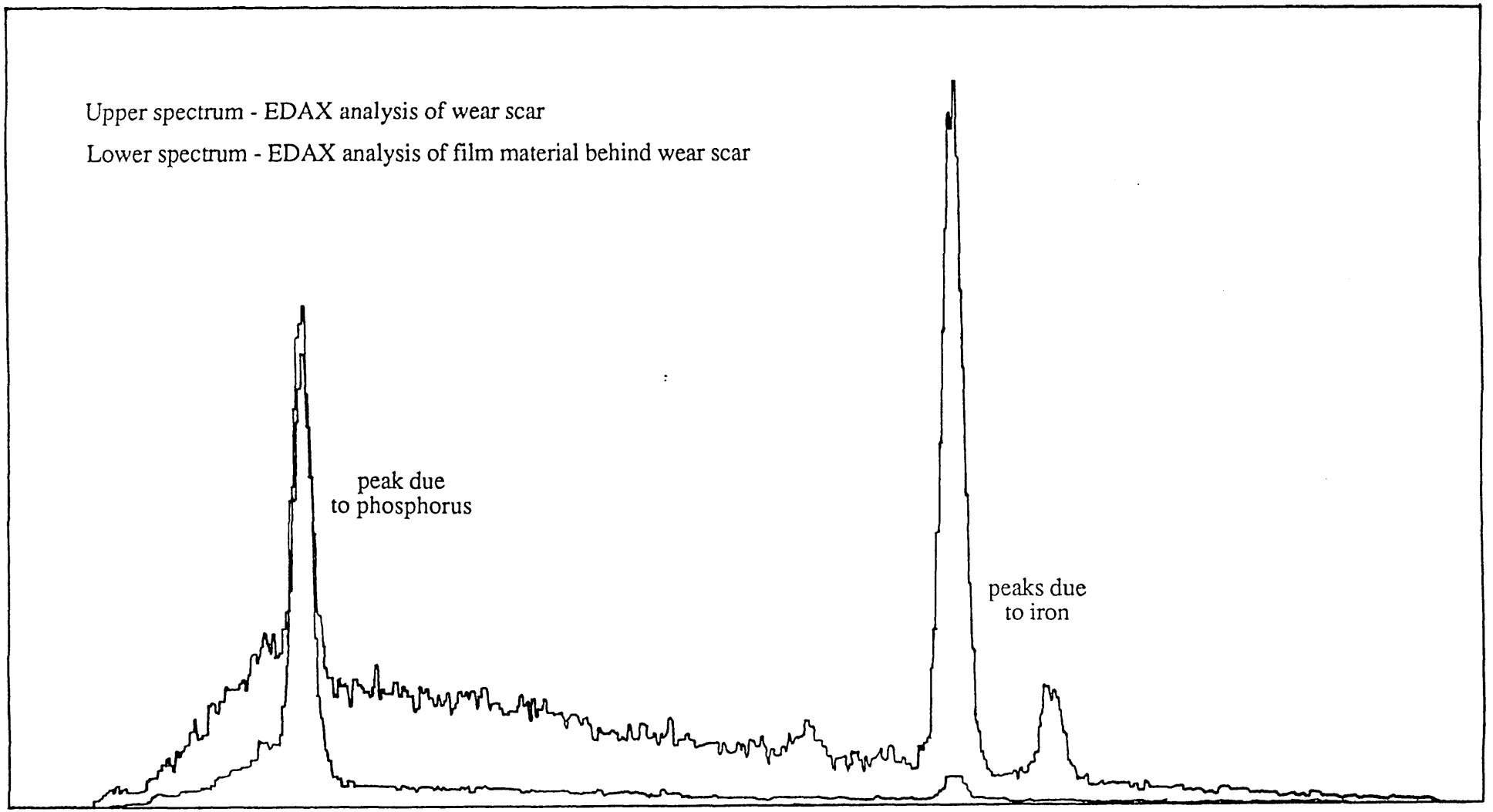


Figure 7.7 EDAX emission spectrum - ball run in pure sliding with BOPP / SHC 234

BOPP (profile XV) with an untested ball (inset). The original magnifications were x 20,000 vertically and x 100 horizontally. These magnifications were photo-reduced by 70 %, to give the values shown on the figure. The surface profile (XV) in figure 7.6 was measured across the central rolling track (i.e. perpendicular to the direction of rolling). Going from left to right the region measured is from out of the central rolling track (where little material was present), across the rolling track (where most of the material is deposited) and beyond (where the amount of deposited material falls off). It is apparent from the figure that the film distribution is not even over this region. The minimum deposit thickness appears to be consistent throughout the profile at approximately 2 - 2.5 units above zero (as read from the scale of the talysurf paper). It seems reasonable to assume that this represents the original i.e. the deposit-free ball surface. If this assumption is made, the maximum deposit thickness is approximately 14 mm on the figure. This represents a measured film thickness of 1 μm or 1000 nm. This should be contrasted with the average chemical film thickness observed in the rolling EHD contact - at 100° C - of approximately 290 nm. Thus it appears that at elevated temperature the high pressures present in the contact (of the order of 0.4 GPa) elastically deform the thick film material. An indirect measurement of the hardness of the material is described in § 7.2.2.4. The maximum Hertzian contact pressure (P_{max}) was calculated from equation (XX) to be 0.387 GPa.

$$P_{max} = \left(\frac{3W}{2\pi a^2}\right) \qquad \text{(XX)}$$

The film distribution, viewed from left to right, starts with a depositfree region. This is followed in turn by a gradual build up of material for approximately 10 cm (1.4 mm on the ball surface). This gives way to a 10 cm long (1.4 mm on the ball) plateau region of relatively constant height (this region contains the central rolling track). The gradual build up is then reversed. This distribution correlates well with the distribution that can be seen in plate 7.2 below.

The loading arm of the EHD rig used to generate the thick film material, employs two 'cotton reel' rollers to locate the ball (as described in § 5.2). This means that as well as the single EHD point contact between the ball and the plate, the ball is in EHD contact with the two rollers (at up to four points). The local conditions of high shear, pressure and elevated

temperature prevailing in these contacts, result in film build-up being concentrated in the rolling / sliding regions. This is shown in plates 7.2 and 7.3. These photographs are both of films generated with BOPP in pure rolling. Plate 7.2 shows the film material generated around the central rolling tack (the rolling direction is left to right). The material was scribed using a glass capillary drawn to a fine point. The ball was photographed using a Vickers photoplan M 41 microscope fitted with a Vickers J 35 automatic exposure unit. A magnification of x 25 was used. The photograph shows a horizontal yellow band approximately 35 mm high (i.e. 35 / 25 = 1.4 mm on the ball surface) of near constant film thickness. This region is the area around the rolling track and it is bounded on either side by a blue / green region, which gives way to an orange / red band. This correlates well with the talysurf profile (XV) discussed above. Plate 7.3 shows the concentration of thick film material in the EHD contacts (the rolling direction was from top to bottom). The central region represents the ball and plate rolling track; the concentrations of material to either side result from the contact of the ball with the 'cotton reel' rollers.

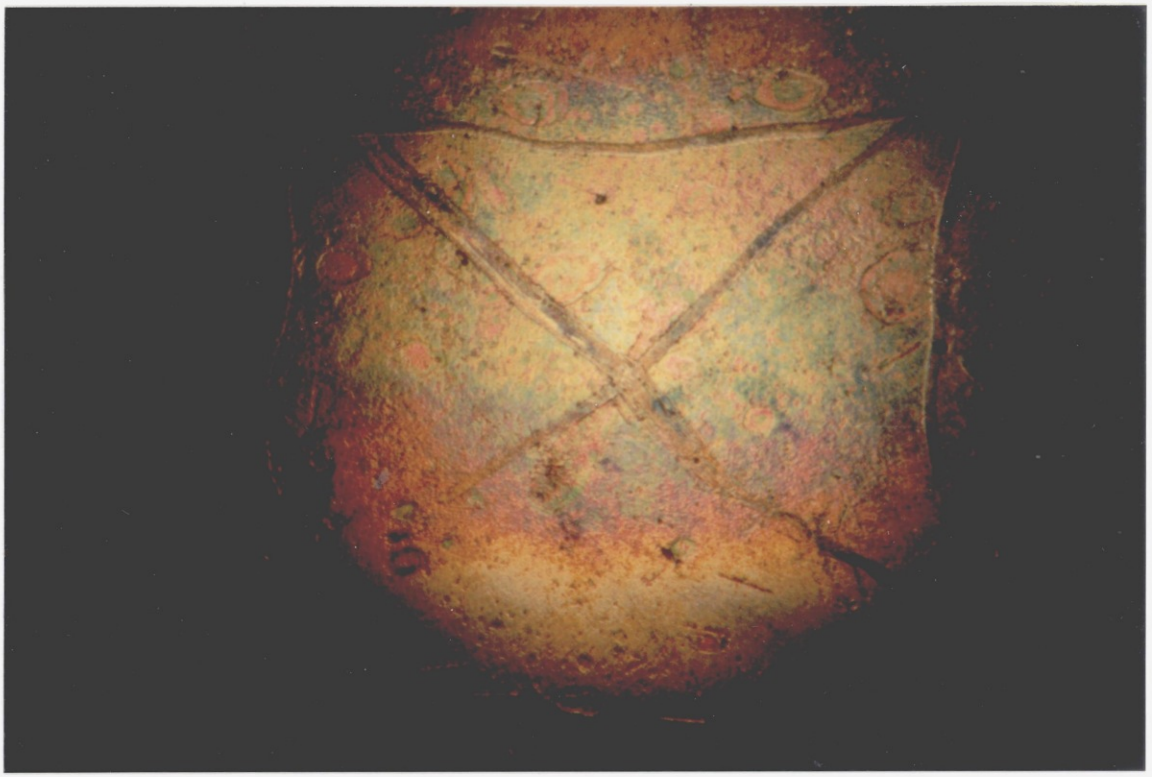


Plate 7.2 Scribed film material generated in central rolling track with BOPP



Plate 7.3 Surface distribution of thick film material

7.2.2.4 Hardness of material generated in a rolling EHD contact

An attempts was made to measure the hardness of the film material using a conventional micro-hardness indenter (a Vickers diamond pyramid hardness indenter). Direct measurement of the hardness of a film of the order of one micron thick, was found to be impossible. The hardness measured was dominated by the hardness of the substrate. However the measurements did show an apparent hardness increase to have occurred in the rolling track after running with additive. The test ball described in the previous section was also measured here. The *diamond pyramid hardness* (DPH) or *Vickers hardness number* (VHN or VPH) was measured as follows. A diamond pyramid indenter, ground to ensure that the angle between the faces equalled 136^{o}, was loaded against the ball with a load (P / Kg) of 50 Kg. The average length of the diagonals (L / mm) was then measured by observing the dent using a microscope fitted with a pre-calibrated eyepiece graticule. The DPH was then calculated as in equation (XXI). The DPH was measured within the rolling track and out of the track. The average measured values of L were 0.320 and 0.327 mm (the ball may be considered 'flat' over this distance), this gave calculated values of 906 ± 3

and 867 ± 3 respectively for the DPH. The apparent hardness increase may have resulted from work hardening caused by elastic deformation of the contact during testing. A second ball run with BOPP gave values of 872 ± 3 in the track and 864 ± 3 out of the track. A ball measured after running at elevated temperature, in the absence of additive, gave values of 872 ± 3 in the ball / 'cotton reel' track and an unchanged 864 ± 3 out of the track. However the hardness measured originally was complicated by the presence of a reacted layer (approximately one micron thick). If the reacted layer is assumed to be very much softer than the substrate - ignoring any work-hardening effects - the difference in measured hardness due to the film can be estimated. A soft film might be expected to be 'squeezed' out of the depression caused by the indenter, giving a depression of the same shape but 1 μm deeper. A simple analysis based on the geometry of the indentations would predict an increase in L from 0.327 to 0.332 mm, i.e. an decrease in DPH from 867 to 841. The measured increase in DPH must therefore have resulted either from work-hardening in the rolling track, or from the film having an appreciable hardness. If the material extruded to the edge of the indenter were appreciably hard and elastic it might be expected to 'back-fill' the depression when the indenter was removed. This would result in a reduction of the measured value of L and an increased measured hardness number.

$$DPH = \left[\frac{2P \sin\left(\frac{\theta}{2}\right)}{L^2} \right] \qquad \text{(XXI)}$$

Because of the problems discussed above, the following indirect method was devised to get some measure of the hardness of the material grown in a rolling EHD contact. The ball described previously was solvent-cleaned and permanently locked into the rotary talysurf relocation device. The ball was arranged so that the surface profile was measured along the central rolling track (i.e. in the direction of rolling). A series of profile measurements were made after scraping the surface with a number of scribers of increasing hardness. A selection of the profiles are shown in figure 7.8. Profile (XVI) shows the film distribution prior to scribing.

The surface film was first scraped with a piece of hard wood cut to a fine point and the surface profile was remeasured. The resulting profile was indistinguishable from profile (XVI). The procedure was repeated with a perspex and then an annealed glass scriber; the surface profile remained unaltered. The surface profile (XVII) was measured after scribing the film with a glass capillary drawn to a fine point and thus work hardened. This resulted in the permanent removal of a section of the film (as indicated on the figure). It should be noted that the profiles in figure 7.8 have been traced over by hand (to improve the definition). This process has produced very slight changes in the profiles shown, but the only changes in the originals were due to the action of scribing the film material (as indicated on the figure). The scribing procedure was repeated with work hardened glass, steel and tungsten carbide (the profile was measured between each treatment). Profile (XVIII) shows the resulting film distribution - the changes resulting from each treatment are shown on the figure. The glass and steel scribers both resulted in the removal of film material (the latter to the level of the ball surface). The tungsten carbide scriber formed a deep and permanent track in the ball surface.

It should not be inferred from this that the whole of the effective thick film material has a hardness approaching that of work hardened glass. Ultrasonic cleaning with toluene and acetone will have removed any softer, outer layers of polymeric material. These, although soft and only weakly held on the surface, might well contribute to film formation in rolling or sliding concentrated contacts where pressure and speed combine to generate EHD films from viscous material, even at quite low speeds. The difference between the time-averaged chemical film thickness measured optically in an EHD contact, and the film thickness measured with the talysurf, suggests that the film is elastically deformed in the former case or that it swells during solvent treatment. In principle the layer may be viscous, visco-elastic, plastic or elastic. The rolling tests presented in § 6.2.1.4 contain evidence that the film augments the EHD film in a solid (i.e. in a speed independent) rather than a viscous liquid manner.

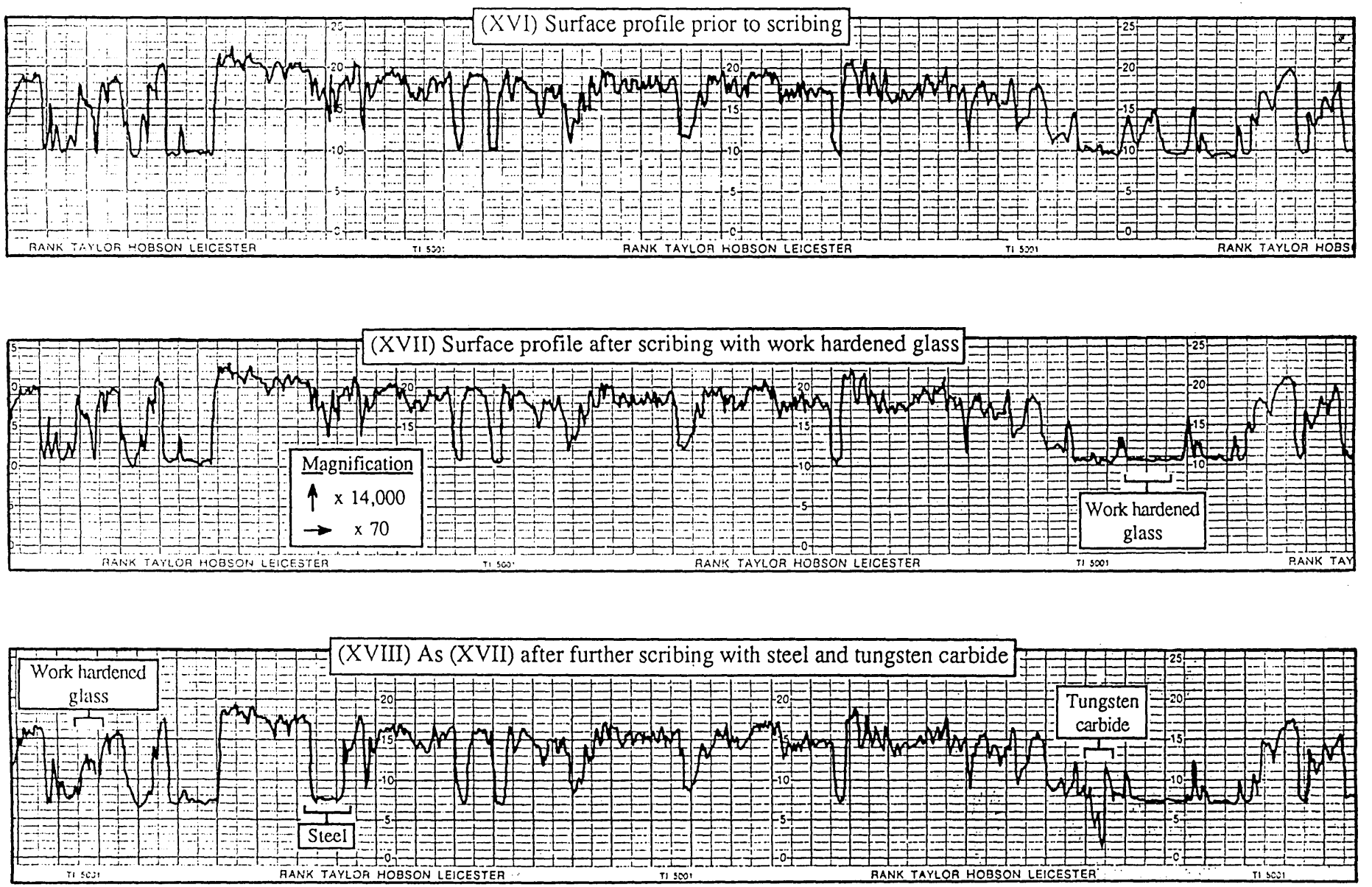


Figure 7.8 Surface profiles (along rolling track) for a ball tested with BOPP in nominally pure rolling - effect of scribing film material

7.2.3 Physical nature of material generated 'in vitro'

The following section describes experiments conducted to investigate the physical nature of the polymeric material formed by the reaction of additive with iron-containing species in test-tube rather than contact conditions. Section 7.2.3.1 investigates the reported rheopecticity [76] displayed by the polymeric material formed by the reaction of di-alkyl phosphonate and iron powder. Section 7.2.3.2 discusses the importance of surface pretreatment of samples in the light of anomalous results obtained with occasional batches of test balls and powders. Section 7.2.3.3 describes experiments designed to investigate the life cycle / history of the thick film material.

7.2.3.1 Rheopecticity / refractive index of polymeric material

The thick film polymer grown onto a ball in a dynamic, rolling test can be produced in bulk by reacting iron powder with either pure phosphonate or phosphonate / base stock solution, at elevated temperatures. Chemical analyses have shown the structure of the two forms to be very similar [78].

The polymer produced statically is reported in [76] to exhibit rheopecticity i.e. to demonstrate an increase in viscosity at increased rates of shear. The following tests were conducted on a series of samples removed after varying intervals from (i) mixtures of iron powder / pure di-hexyl phosphonate (DHP) and (ii) iron powder / 3% DHP in liquid paraffin. The di-hexyl phosphonate was purified by distillation prior to use (as described in § 4.3.1.2). The experimental procedure was designed, as far as possible, to follow the procedure used by Lacey [76] . The iron powder and liquid paraffin used were the same batches as those used in [76]. The iron powder used was supplied by Goodfellows Metals Ltd as 99%+ purity milled Fe, sieved into the particle size range 75 - 53 μm. This material has an estimated median diameter of 64 μm and an estimated median surface area per gram of 11.9×10^{-3} m^2 [76]. The liquid paraffin used had dynamic viscosity of 0.0133 Pa.s at 40° C and 0.00308 at 100° C; it was stored over alumina prior to use to remove polar impurities. The reaction vessel employed was a three necked 100 cm^3 capacity 'pear shaped' flask. This was immersed in a heating bath containing liquid paraffin and the latter was heated, with stirring, on a hot plate. A bath temperature of 164° C was found to give

the required vessel temperature of 155 ± 5° C. Iron powder (1.35 ± 0.01 g) was weighed into the reaction vessel and DHP or DHP / paraffin solution (15 g) was added. The reaction mixture was agitated by oxygen which was supplied to the bottom of the reaction vessel through a finely drawn pipette, at a supply rate of 100 ± 5 cm^3 / min. Samples were removed after various intervals. The dynamic viscosity of each sample was then measured, at a series of shear rates, at an ambient temperature of 24.5° C. The viscosity was measured using a Ferranti-Shirley viscometer (as described in detail in § 5.2.3.5). The variation of viscosity with time - at a series of shear rates - is shown for pure DHP in figure 7.9 and for DHP / liquid paraffin in figure 7.10.

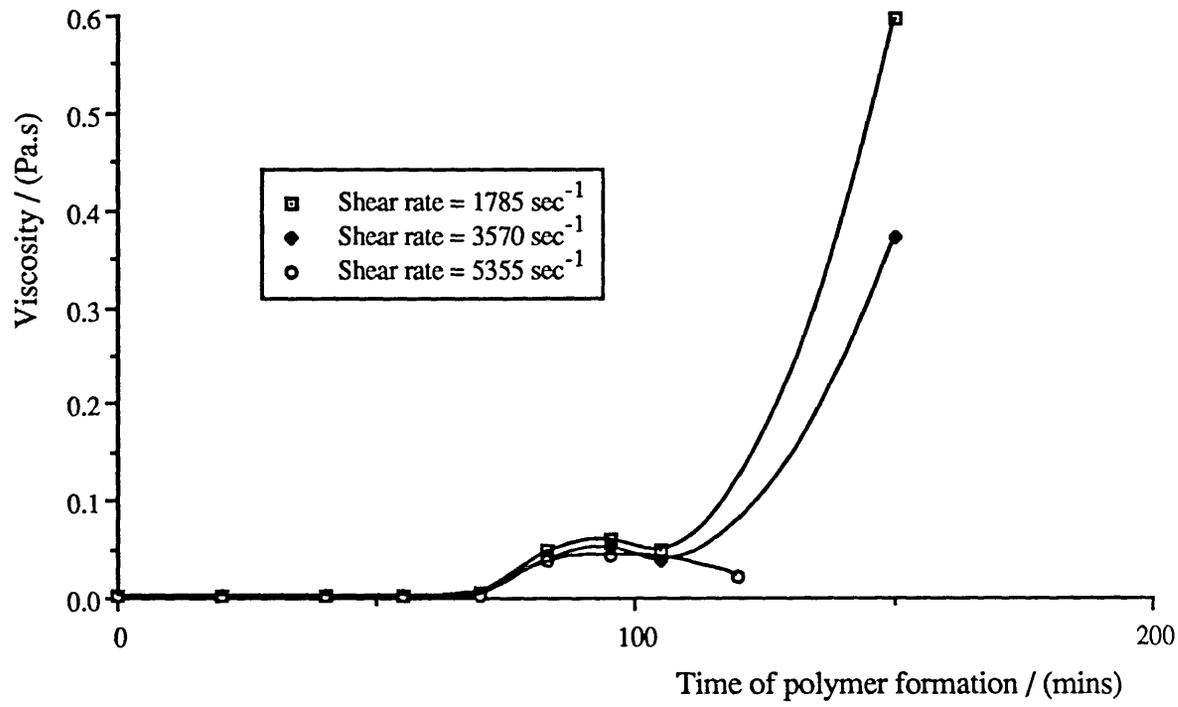


Figure 7.9 Polymer viscosity as a function of time / shear rate - pure DHP

Although both solutions demonstrated increasing viscosity with time, due to the formation of polymer, all sample viscosities were shear independent (for moderate rates of shear). The practical importance of this in terms of energy loss in bearing systems is evident. At higher shear rates some shear thinning occurred.

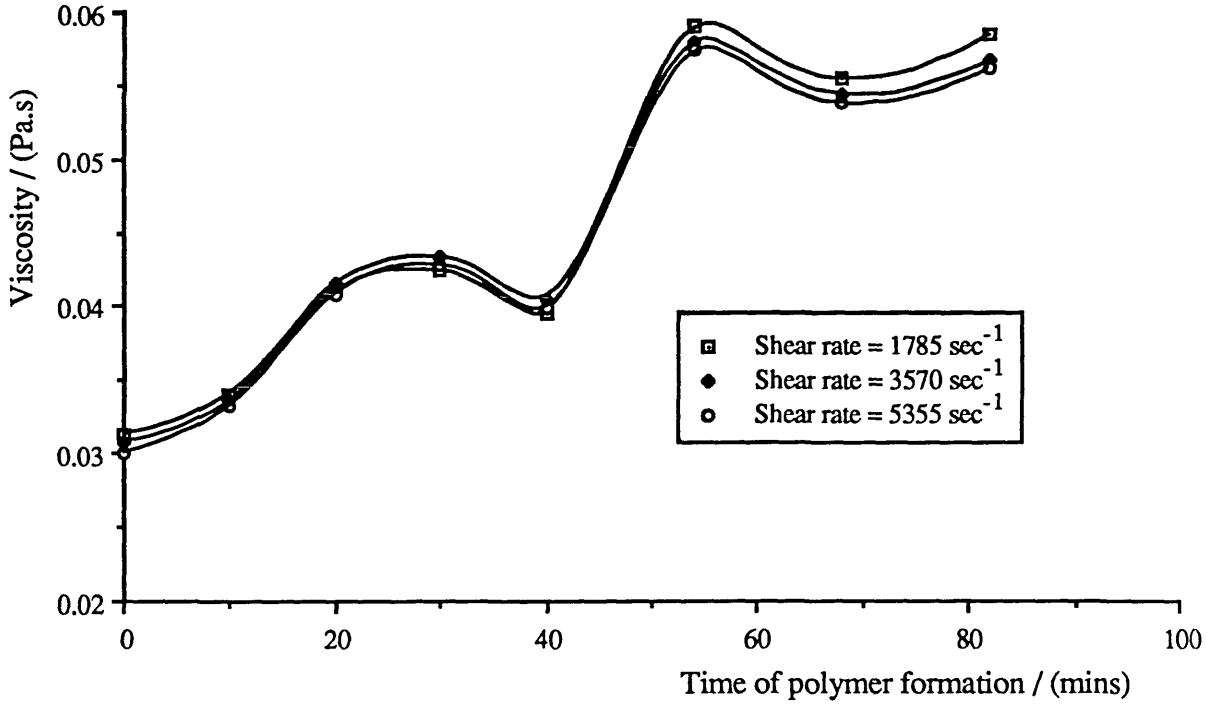


Figure 7.10 Polymer viscosity as a function of time / shear rate - 3% DHP / liquid parrafin

Bulk, static preparation of the polymer also permitted its refractive index to be measured directly. This is important in the optical measurement of film thickness (as described in chapter 5). The refractive index of the base oil / additive / iron powder reaction product was measured as 1.432 which is very similar to that of the base oil justifying previous assumptions made in optical film thickness calculations.

7.2.3.2 Importance of surface pretreatment

In the current studies erratic results were obtained using bearings and iron powders produced by different manufacturers. Occasional ball and powder batches showed a complete absence of reaction with additives in both test tube and dynamic test-work. The results discussed below have important consequences for the use of anti-wear additives in practice. The unusual results have been traced not to any component of the formulation, but to a rust / corrosion inhibitor used to pre-treat steel surfaces.

Two bearing steel metallurgies were used, EN 31 and its replacement AISI 52100. As the table below shows these are of very similar composition, the latter having a slightly increased chromium content. Chromium is known to inhibit thick film formation [76].

ELEMENT	EN 31	AISI 52100
C	0.90 - 1.20	0.90 - 1.20
Si	0.10 - 0.35	0.10 - 0.35
Mn	0.30 - 0.75	0.30 - 0.75
S	0.050 Max.	0.050 Max.
P	0.050 Max.	0.050 Max.
Cr	1.00 - 1.60	1.30 - 1.60

Table 7.3 Elemental composition of EN 31 and AISI 52100 steels

A number of different sets of balls were obtained from a range of bearing suppliers. Normal reaction was observed with all but one brand of 52100 ball (Fag Bearing Co. Ltd.), with which no thick film formation occurred. The balls were investigated using the SEM / EDAX facility described previously. This permitted observation of the ball surface and determination of its elemental composition, respectively.

EDAX analysis proved inconclusive, as it is limited to elements with atomic numbers greater than 10 and is not truly surface sensitive (it gives an averaged analysis to depth of 2000 - 5000 Angstroms). However it did demonstrate the bulk composition of the balls used to be very similar.

It appears from a private communication that the problem arises from the use of a barium based rust inhibitor [221]. This is not removed by boiling solvent or ultrasonic cleaning, and can only be removed by electrocleaning. The practical implications of this sort of pretreatment are evident. The thick film mechanism requires dissolution of iron prior to the

formation of insoluble polymer that coats the surface. If iron removal is prevented then so is the beneficial anti-wear activity. More conventional anti-wear additives may also be prevented from acting as a result of competition for surface sites with the rust inhibitor. A similar phenomenon was observed by Klaus and Bieber [62] with TCP. The phosphorus content of the wear scar dropped to zero when a barium sulphonate rust inhibitor was used.

The experiments described in sections 7.2.3.1 and 7.2.3.3 used milled iron powder of 99%+ purity in the size range 75 - 53 μm. However, a different iron powder of similar size distribution and reportedly 99.9% + purity failed to give any reaction. These powders were also investigated using the SEM / EDAX combination.

The two types of surface appeared very similar (this is important since high frequency surface convolutions can greatly increase the real area available for reaction). In addition, thin surface oxides which are known to be very important in film formation [29], would not have been detected. It is probable that a rust inhibitor was responsible.

In both cases XPS or ESCA (X-ray photoelectron spectroscopy and electron spectroscopy for chemical analysis) would have been more suitable, as all elements above atomic number 1 can be 'viewed' and the surface sensitivity is down to 10 - 20 Angstroms.

7.2.3.3 Life cycle / history of thick film material. Dissolved iron content - Atomic Absorption Spectroscopy (AAS)

Much of the test work described in chapter six - in which thick film build-up was monitored in a rolling EHD contact - used a viscous synthetic hydrocarbon (SHC 234). The static solution studies of Lacey [76] and those described in § 7.2.3.1, employed a low viscosity liquid paraffin as base stock. In the latter case [76] the polymer build-up was monitored by atomic absorption spectrophotometry (AAS), which gives the dissolved iron content - an effective measure of the amount of polymer formed - as a function of time. This test procedure used is described below. In chapter six it was shown that the maximum film thickness in a contact was depletion controlled and that it could exceed 600 nm. The influence of base oil type on the dispersion of material into solution is of obvious practical importance since gross loss of polymer could lead to filter-blockage, oil starvation and failure. For this reason the dissolved iron content tests described in [76] were repeated with

the more representative synthetic hydrocarbon base stock.

The samples for AAS analysis were generated using the experimental procedure described in § 7.2.3.1, with the following variations. The agitant gas used was nitrogen supplied at 100 cm^3 / min. A solution of DHP in SHC 234 (3% w/w, 25 g total) was placed in the reaction vessel and iron power (0.3008 ± 0.0001 g) was added. The DHP and iron powder were from the same source as described previously. Samples of the reaction mixture (approximately 0.4 ± 0.0001 g) were removed by pipette after varying intervals. Care was taken to ensure that no iron powder was removed with the samples. The polymer / base oil samples were then subjected to chemical digestion by strong acids, to provide an aqueous solution suitable for AAS analysis. Each sample was accurately weighed into an Erlenmeyer flask (250 cm^3 capacity) to which analar nitric acid (HNO_3, 50 cm^3) and analar perchloric acid ($HClO_4$, 5 cm^3, 87 %, ρ = 1.54 g / cm3) were added. The mixture was heated at a gentle boil for approximately 3 hours. After cooling, the digested mixture was placed in a 100 cm^3 volumetric flask and diluted to volume with distilled water. In some cases a slight 'oily' residue remained; the flask was shaken to ensure all iron ions were extracted into the large aqueous phase. A control solution was prepared in the absence of an iron-containing sample. The procedure was designed to follow the method of Lacey [76] as closely as possible.

The iron content of the resulting solutions was measured using a Baird Alpha 3 spectrophotometer. The machine was made 'iron selective' by using an iron element hollow cathode lamp. The wavelength at which iron atoms absorb was selected (approximately 248 nm) and the absorbance was set to zero. The acetylene burner was ignited and aligned with the lamp emission. The machine was then re-zeroed after flushing with de-ionised water. The spectrophotometer was calibrated using samples prepared by dilution of a 1000 ppm Fe standard solution (ferric nitrate) to the absorbance range of the machine. The standard solutions (0 - 10 ppm Fe) were introduced to the flame via a sampling tube. The absorbance was recorded as a digital readout. De-ionised water was introduced between readings to purge the previous sample and to check the zeroing. The calibration graph is shown in figure 7.11.

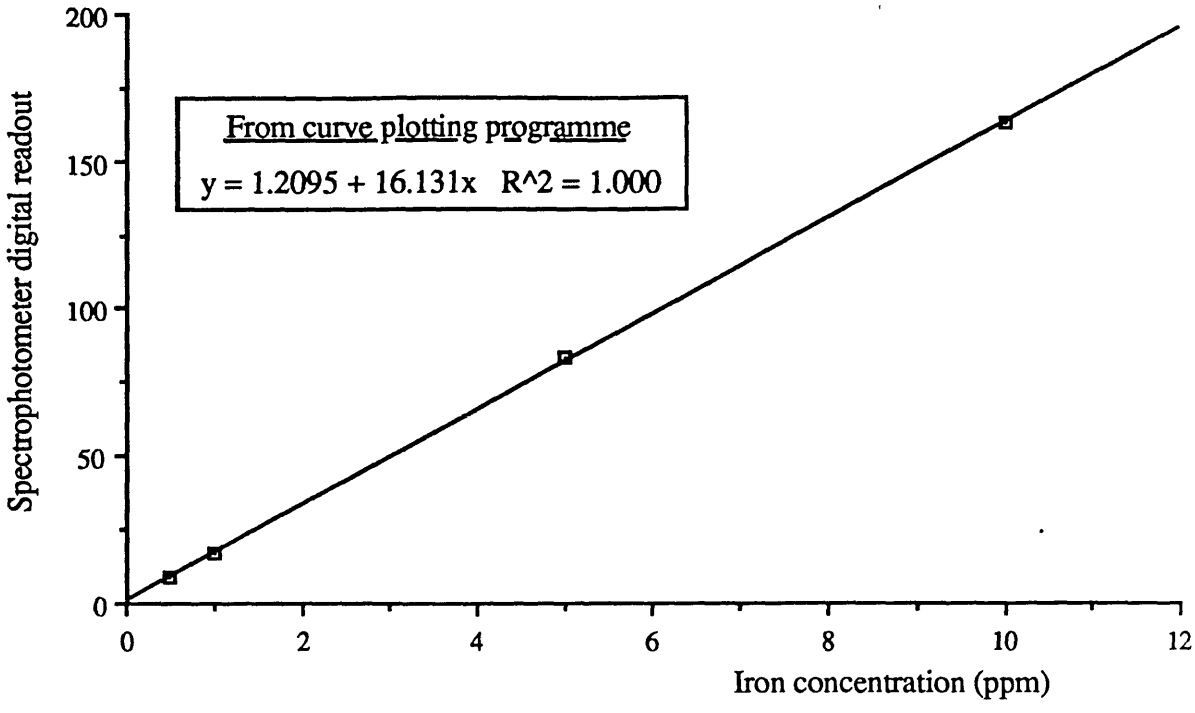


Figure 7.11 AAS calibration curve - spectrophotometer readout vs. iron concentration

1 ppm of iron is equivalent to 1mg / litre, i.e. 1 x 10^{-3} g of iron in 1 litre or 1 x 10^{3} g of water. Therefore a diluted / digested sample (100 cm^3) having an iron concentration of 1 ppm contains 1x10^{-4} g of iron. The iron concentration of the original sample (% Fe) is obtained from the weight of sample used (w), as shown in equation (XXII).

$$\%\ \mathrm{Fe} = \left(\frac{\mathrm{ppm} \times 10^{-4}}{w}\right) \times 100 \qquad \text{(XXII)}$$

$$= \left(\frac{\mathrm{ppm} \times 10^{-2}}{w}\right)$$

Figure 7.12 compares the iron content, after varying intervals, for pure DHP and 3% DHP / liquid paraffin (LP), as measured by Lacey [76], with those for SHC 234. From the graph it can be seen that a drop in iron content occurs with DHP in solution. With liquid paraffin the maximum iron content is lower in the 3% solution. This suggests that depletion of additive may be important. In the early stages of the reaction short chain length and partially co-ordinated oligomers - with a relatively high solubility in base stock - would be expected to predominate. As the reaction proceeds the polymer solubility would be expected to fall as the average chain length increases giving rise to the observed fall in iron content. The solubility argument is supported by the behaviour observed with the increasingly non-polar SHC 234 (the drop occurred sooner and at lower iron content in this case). After testing, the SHC reaction mixture showed three distinct phases. The solid iron powder was 'glazed' with a thick, viscous material; the bulk liquid phase remained largely unchanged. Thus as the reaction progressed the polymer material became increasingly concentrated around the iron, with very little of it dissolving into the bulk SHC.

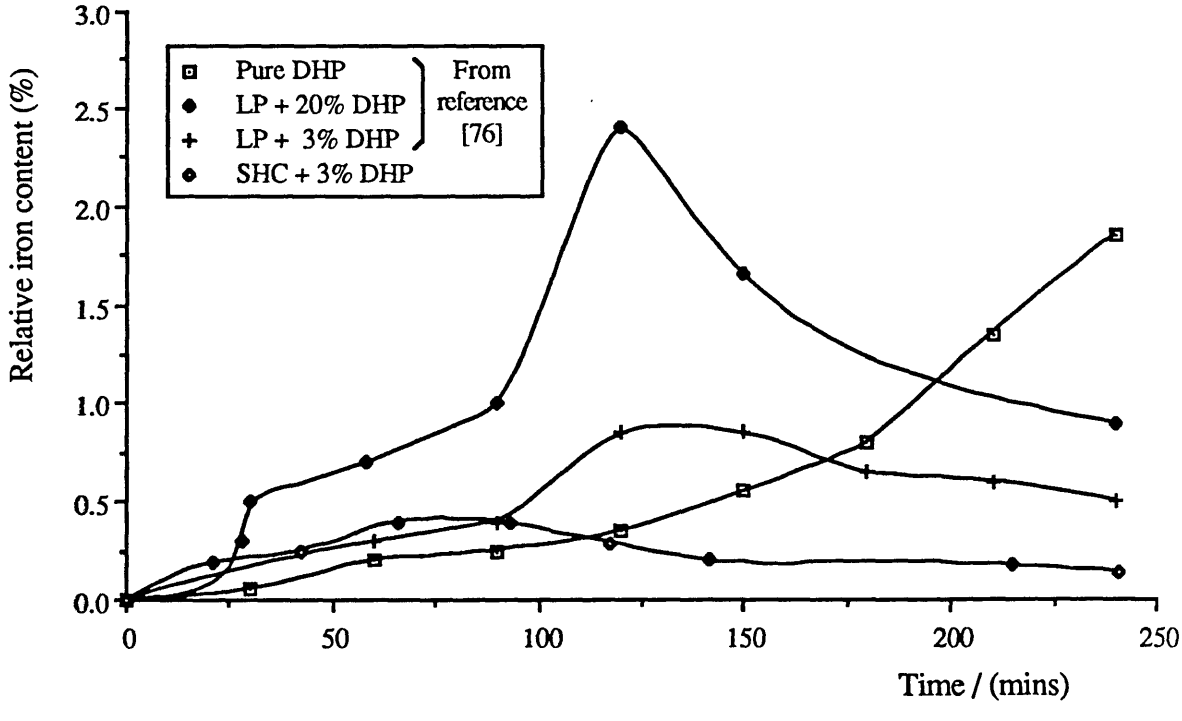


Figure 7.12 Atomic absorption spectrophotometry (% iron content vs. time)

The experimental results presented in this chapter so far have important practical implications. The dissolution of iron required prior to polymer formation will occur predominantly in areas of concentrated contact. In these areas, depending on the prevailing Lambda value, conditions of high shear, temperature, pressure and wear combine to increase the additive reactivity. The absence of these operating conditions will limit film formation elsewhere in the operating environment e.g. gearbox. The material has been shown to form on rolling / sliding surfaces and to contribute towards their separation even under initial sliding, boundary conditions. Once formed, and particularly if formation occurs in an EHD contact, the polymeric material is very difficult to remove. As such, loss of material back into solution seems unlikely; this is important as it could lead to filter blockage, starvation and therefore failure. The thick film material generated in an EHD contact has been shown to be very hard and extremely tenacious. Much if not all of it is unaffected by ultrasonic cleaning in a range of solvents. To date the only method found of removing the film is by boiling in dry DMSO, a very vigorous solvent.

7.3 Chemical nature of iron / additive reaction product

The following section describes studies into the chemical nature of the material resulting from the reaction of iron or iron-containing species with phosphorus-based anti-wear additives. Section 7.3.1 considers the nature of the material formed 'in vitro.' Section 7.3.2 deals with the material formed on metal surfaces.

7.3.1 Chemical nature of reaction product formed 'in vitro'

7.3.1.1 Introduction - experimental procedure / additives tested

Many workers have investigated the interaction of anti-wear additives and iron / steel surfaces or powders (see chapter two). A disadvantage of this approach is the restricted dissolution of iron, which limits the extent of product formation. There is very strong evidence that the iron present in the polymeric material generated in the current study is $Fe^{(III)}$ [76], [29]. For this reason an iron (III) salt was used in much of the following work. An oil-soluble salt was chosen - iron stearate $Fe[O_2C.(CH_2)_{16}.CH_3]_3$. Direct reaction of this salt with pure anti-wear additives or a solution of the additive in base stock

gave well defined, model compounds for chemical analyses and permitted some insight into the mechanism by which the additives function.

Table 7.4 summarises the additives used to prepare polymeric materials with iron stearate. In general a small quantity of iron stearate was heated - at 100° C for 1 hour - in excess liquid additive. Excess additive was employed to ensure that the central Fe $^{(III)}$ species could achieve maximum co-ordination. The precipitates formed were filtered and washed with toluene and acetone to remove excess additive. Infra-red (IR) spectra were recorded by producing a 'Nujol' mull of the precipitates as described in § 4.4.1.3. No reaction was observed with tri-cresyl phosphate (TCP) under the conditions detailed above. The work described in § 2.4.1. identified an 'activation temperature' of approximately 220° C for TCP. The TCP-generated material described in table 7.4 was formed after 3 hours at 240° C using an oxygen supply to agitate the mixture. Llopis et al [71] identified the importance of oxygen in the reaction of TCP and iron surfaces. However the role of oxygen is almost certainly oxidation of the iron surface since the phosphate cannot be oxidised. This is discussed in more detail in § 7.3.1.3. below.

7.3.1.2 Experimental observations

The following section describes general observations made during production and analysis of the model compounds. Although largely qualitative in nature, these observations provide some insight into the mechanism of formation of the polymeric material, and the means by which this contributes towards surface separation, in practice. Some more detailed mechanistic studies are included, with IR spectra, in § 7.3.1.3.

CLASS	ALKYL GROUPS	COMMENTS
Phosphonate $(RO)_2P(O)R^1$	$R^1 = H$ R = Me, Et, i-Pr	Finely divided white powder
	$R^1 = H$ R = Hex, Oct, Decyl, Phenyl, t-Octyl-Phenyl	Lumps of solid globular material. Plastic behaviour when stressed
	$R = R^1$=Me	Finely divided white powder
Phosphate $(RO)_3PO$	R = Et, Bu	Finely divided white powder
	R = Cresyl	Black crystalline precipitate
Phosphite $(RO)_3P$	R = Me	Finely divided white powder
Phosphinic acid $RR^1P(O)OH$	R = H R^1 = Phenyl ; R = R^1 = Phenyl	Finely divided white powder
Phosphonic Acid Dialkyl Ester $(RO)_2P(O)OH$	R = Dodecyl	Finely divided white powder

Table 7.4 Anti-wear additives reacted with Fe (III) stearate

The clearest evidence of additive / iron interaction came from changes in the phosphoryl (P=O) bond vibration. As polymer formation occurred, the lone pair on the phosphoryl bond co-ordinated to the central Fe $^{(III)}$ species. This resulted in loss of double bond character and a shift in the bond vibration towards lower wavenumber (ν / cm^{-1}). The polymeric material is believed to contain the species X_2PO^{2-} (where X is any species attached to phosphorus) which has two intermediate single / double Fe—O bonds. Further

evidence of the polymeric nature of the reaction product comes from its insolubility in base oil, toluene and acetone which implies a compound of high molecular weight. After draining, the crude polymer product had two distinct phosphoryl vibrations due to the co-ordinated polymer and the remaining additive. The latter was lost after solvent cleaning. The spectra obtained for the model compounds generated with di-alkyl phosphonates were very similar to those obtained from films generated in the EHD rig (§ 6.2) and [76]. Although better peak definition was observed with the model compounds. Model compounds generated with pure additive and with solutions of additive in base oil had indistinguishable IR spectra.

The source of iron was found to be important in determining the chemical and physical nature of the polymer. In all cases polymer formation occurred faster and at a lower temperature with Fe $^{(III)}$ than with iron powder. Adding iron stearate to pre-heated di-alkyl phosphonates produced a hard, polymeric precipitate almost immediately. When this procedure was repeated with iron powder a soft, polymeric agglomeration was slowly formed. This material displayed poorly defined peaks when subjected to infra-red analysis. Soluble iron (II) salts demonstrated intermediate behaviour. This suggested that the formation of iron (III) and not additive decomposition was rate-limiting under these conditions. No similar reactions were observed when Fe_2O_3 was heated with di-hexyl phosphonate or di-ethyl phosphonate. This implied that free or complexed Fe^{3+} was necessary for polymer formation.

The physical nature of the materials generated 'in vitro' correlate well with the behaviour observed in the EHD rig (see § 6.2.1.6.) With di-alkyl phosphonates the rate of polymer formation 'in vitro' was found to increase with decreasing chain length. However, di-alkyl phosphonates with chain lengths of less than 5 carbon atoms did not give rise to thick, reacted layers in the EHD rig. Model compounds produced with these additives were hard, 'crystalline' substances that were easily ground for IR analysis. The longer chain length versions consisted of solid globular lumps which behaved plastically when stressed. Thus any polymeric material formed in the rolling contact with the shorter chain compounds would not be retained and would fail to contribute towards surface separation. The melting points of this group of model compounds (see § 6.2.1.6) was found to increase with chain length. However, in all cases, the melting points were too high to permit substantial 'melting-out' of any reacted layers.

7.3.1.3 Mechanism of polymer formation

The following section considers the mechanism of formation of polymeric material with di-alkyl / di-aryl phosphonates. Brief consideration is given to the mechanism by which TCP produces a polymeric product with iron.

Section 4.3.1.2 contains indirect evidence of the hydrolytic break-down of di-alkyl phosphonates (some further, indirect evidence is given in § 6.2.2) The three means of break-down and the resulting products were summarised in scheme (VI) in chapter four. Oxidation yields the respective acid phosphate, thermolysis gives the mono-phosphonate plus an alkene, and hydrolysis gives the mono-phosphonate plus the respective alcohol. Thus analysis of the reaction mixture - after polymer formation - may give an insight into the mechanism. Previous studies [29], [76] (see summary § 2.4) suggested the bridging species to be either acid phosphonates or mono-alkyl acid phosphates (with the latter predominating in most circumstances). The structure was shown in figure 1.7.

The hydrolytic break-down was confirmed in the following experiment. Figure 7.13 shows the IR spectra of (i) mono-dodecyl phosphonate (RO)(HO)P(O)H, (ii) di-dodecyl phosphonate $(RO)_2P(O)H$ and (iii) di-dodecyl acid phosphate $(RO)_2(HO)P(O)$.
R = dodecyl in all cases. Figure 7.14 shows the spectra of the respective polymeric products (iv) - (vi), formed by reaction with iron stearate. Table 7.5 summarises the bond vibrations present in figures 7.13 and 7.14.

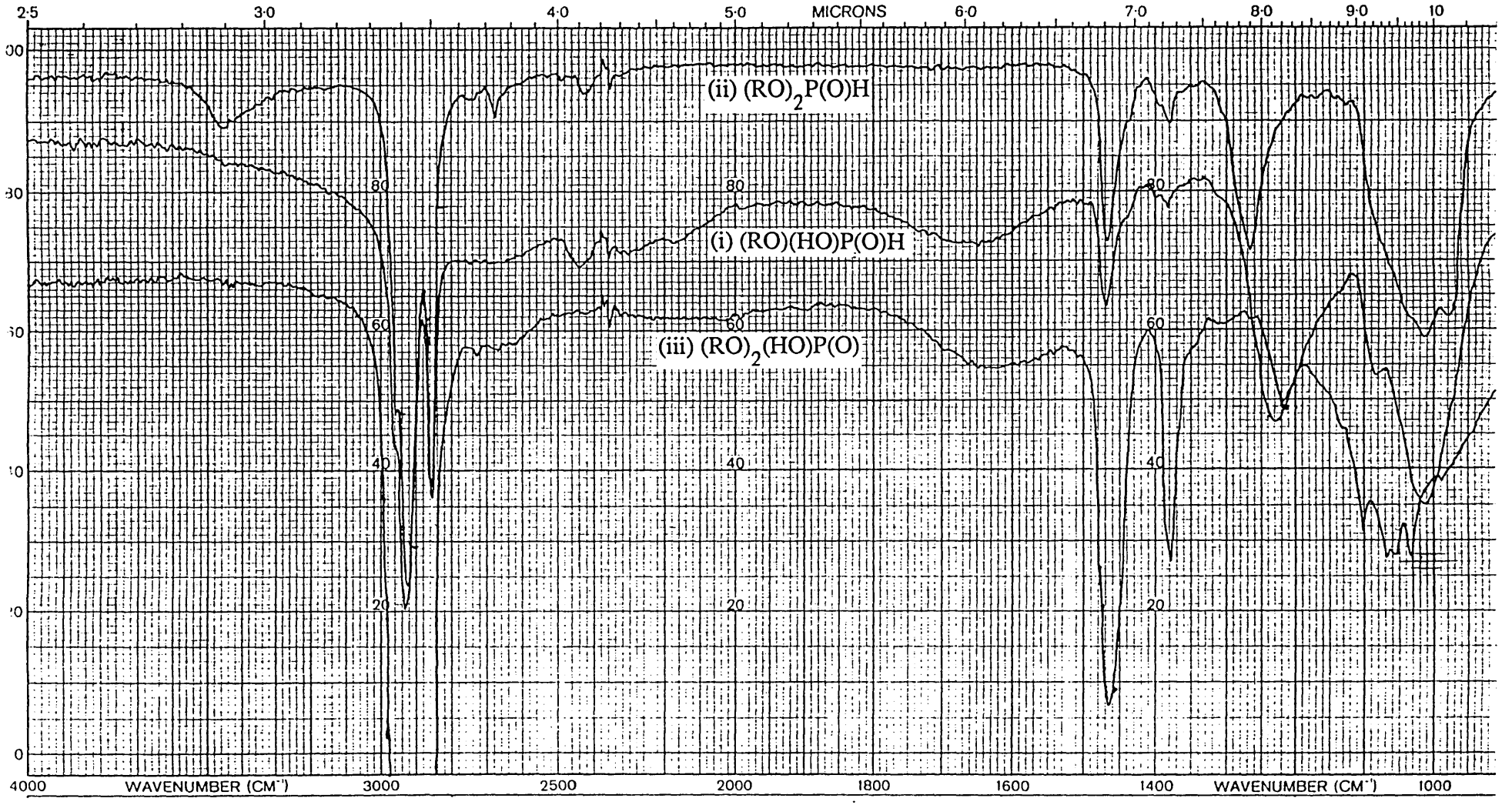


Figure 7.13 Infra-red spectra of dodecyl esters

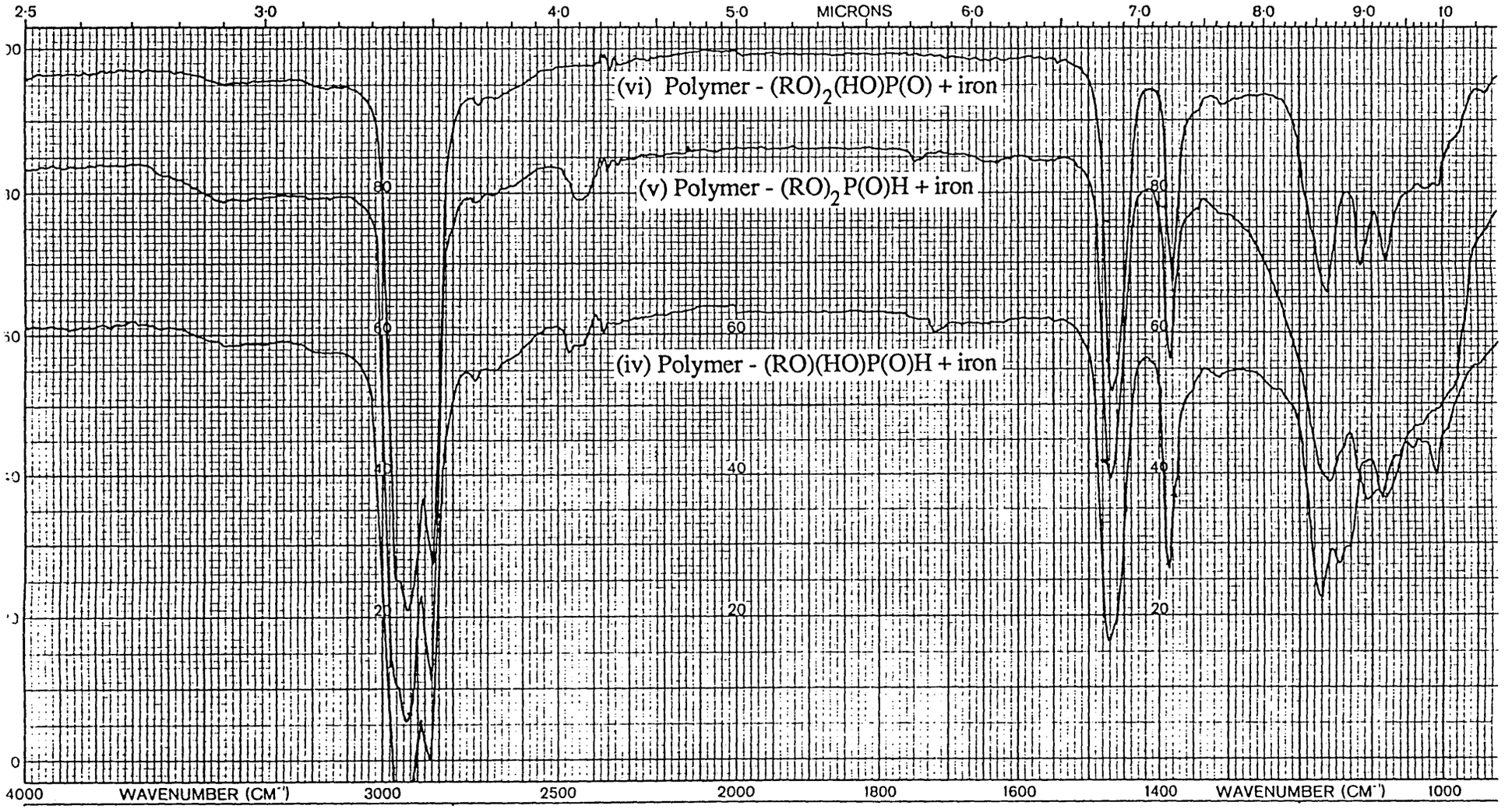


Figure 7.14 Infra-red spectra of polymers formed with dodecyl esters and iron

	Approximate Group Frequencies / cm^{-1}				
	P(O)OH	P-O-H	P = O	P-H	P-O-C-
COMPOUND	~ 2620 ~ 2250 ~ 1680	~ 1020	~ 1270 to ~ 1150	~ 2440	~ 900 to ~ 1100
(i) (RO)(HO)P(O)H	x	x (1005)	x (1227)	x	x
(iv) Iron polymer of (i)	-	-	x (1163)	x	x
(ii) $(RO)_2P(O)H$	-	-	x (1267)	x	x
(v) Iron polymer of (ii)	-	-	x (1158)	x	x
(iii) $(RO)_2P(O)OH$	x	x (1030)	x (1218)	-	x
(vi) Iron polymer of (iii)	-	-	x (1161)	-	x

x band present ; - no band in spectrum

Table 7.5 Presence of peaks and approximate group frequencies - dodecyl esters and polymers formed with iron stearate

Some indirect evidence of hydrolysis was apparent from the presence of parent alcohol in the di-alkyl ester. This is confirmed by the spectra and the data in table 7.5. In all three cases the co-ordinating species was X_2PO^{2-}. The phosphoryl bond vibration moved towards lower wavenumber in each case. The mono-phosphonate (i) co-ordinated through the phosphoryl oxygen / acid group by loss of the acidic proton and therefore loss of the P—O—H vibration. This was confirmed by the presence of a peak at 1700 cm^{-1} (which was due to stearic acid formed by combination of the proton and the stearate anion, as explained below). The P—H bond vibration was retained. The di-dodecyl ester (ii) reacted similarly, with retention of the P—H bond; this ruled out oxidation prior to co-ordination. The break-down was confirmed as hydrolytic by the new peaks present at ~ 1740 and ~ 1060 cm^{-1} in the polymeric product (v). These peaks resulted from the formation of dodecyl stearate ester, which contaminated the product. This is explained in more detail below. The acid phosphate ester (iii) co-ordinated through the phosphoryl oxygen / acid group. Some evidence of stearic acid formation can be seen; no evidence of ester formation was found in (vi). The decomposition products stearic acid (~ 1700 cm^{-1}) and dodecyl stearate ester (~ 1740 cm^{-1}) were present as low level impurities in the polymeric products (iv)/(vi) and (v) respectively. The majority of the impurities remained in the bulk of the respective additive solution. Their presence was confirmed by running the IR spectra of the

remaining additive solutions. The acid and ester impurities were identified as follows.

Figure 7.15 shows the IR spectra of pure stearic acid (vii), and two esters produced by heating stearic acid with butan-*1*-ol (viii) and dodecan-*1*-ol (ix), in the presence of a few drops of mineral acid (HCl) as catalyst. Spectrum (vii) shows that the peaks observed previously at ~ 1700 cm^{-1} (C = O) and ~ 2550 cm^{-1} were due to stearic acid. Butyl stearate ester (viii) was formed by heating approximately equi-molar quantities of stearic acid and butan-*1*-ol, with the HCl catalyst. The C = O bond in the ester can be seen at ~ 1740 cm^{-1} (the presence of some free stearic acid can be seen from the shoulder at ~ 1700 cm^{-1}). The absence of free alcohol is indicated by the absence of R—OH vibration (~ 3300 cm^{-1}). Dodecyl stearate ester (ix) was produced by reacting a slight excess of dodecan-*1*-ol with stearic acid. The resulting ester displayed a (C = O) bond vibration at ~ 1740 cm^{-1} and a C—O bond vibration at ~ 1060 cm^{-1} (as observed in (v) previously). This showed that the (C = O) bond vibration in the ester was effectively independent of the chain length of the parent alcohol. This bond vibration was observed in the solutions remaining after reaction of di-alkyl phosphonates, of all chain lengths, with ferric stearate, thus confirming hydrolytic break-down of the phosphonate. An esterification-type reaction between the —OR groups present on the bridging phosphonate anion (in the polymer oligomers) and the stearate can be ruled out. Firstly, the majority of the ester was present in the excess additive solution i.e. not in the polymer, and secondly, no ester was observed in the solution remaining after formation of polymer (iv).

Polymers of the type discussed above can, potentially, cross-link through hydrolysis of —OR groups on the bridging phosphonate anions (see figure 1.7) and co-ordination into a second Fe $^{(III)}$ centre. This possibility was investigated by comparing the products formed with two compounds in which cross-linking could not occur, with one in which it could. The compounds chosen were di-phenyl phosphinic acid $(\phi)_2P(O)OH$; phenyl phosphinic acid $(\phi)HP(O)OH$ and di-phenyl phosphonate $(\phi O)_2P(O)H$ respectively. ϕ = phenyl C_6H_5—. Figure 7.16 shows the IR spectrum of $(\phi)HP(O)OH$ (x) and the polymeric product formed on reaction with ferric stearate (xi). The main peak assignments are summarised in table 7.6. A number of broad peaks can be seen in the spectrum of the parent acid (x), presumably as a result of hydrogen bonding. The much improved peak definition in (xi) implies a well-ordered structure. The loss of the O = P—O vibration, movement of the phosphoryl vibration and retention of the P-H vibration all suggest

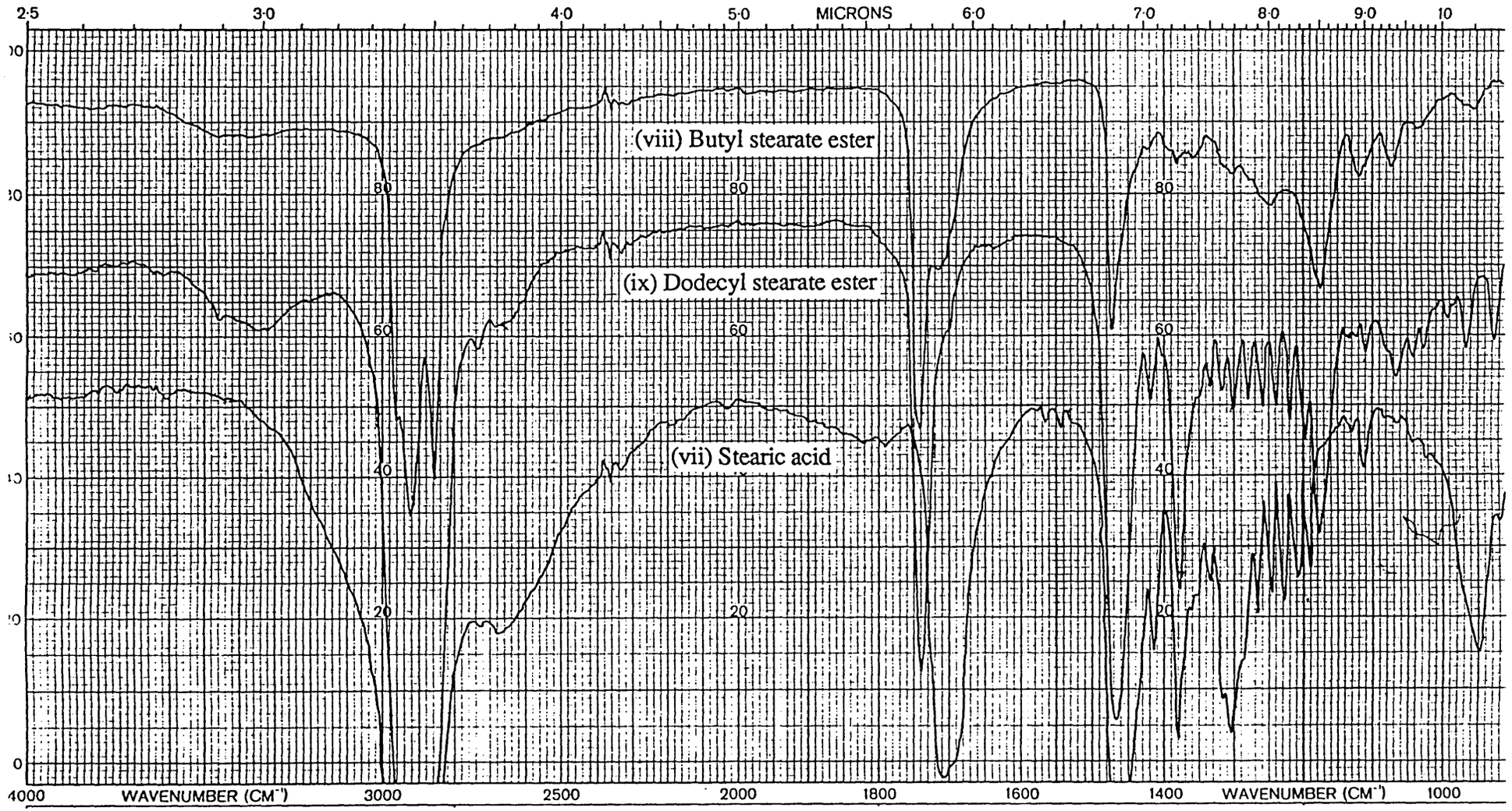


Figure 7.15 Infra-red spectra of stearic acid and two stearate esters

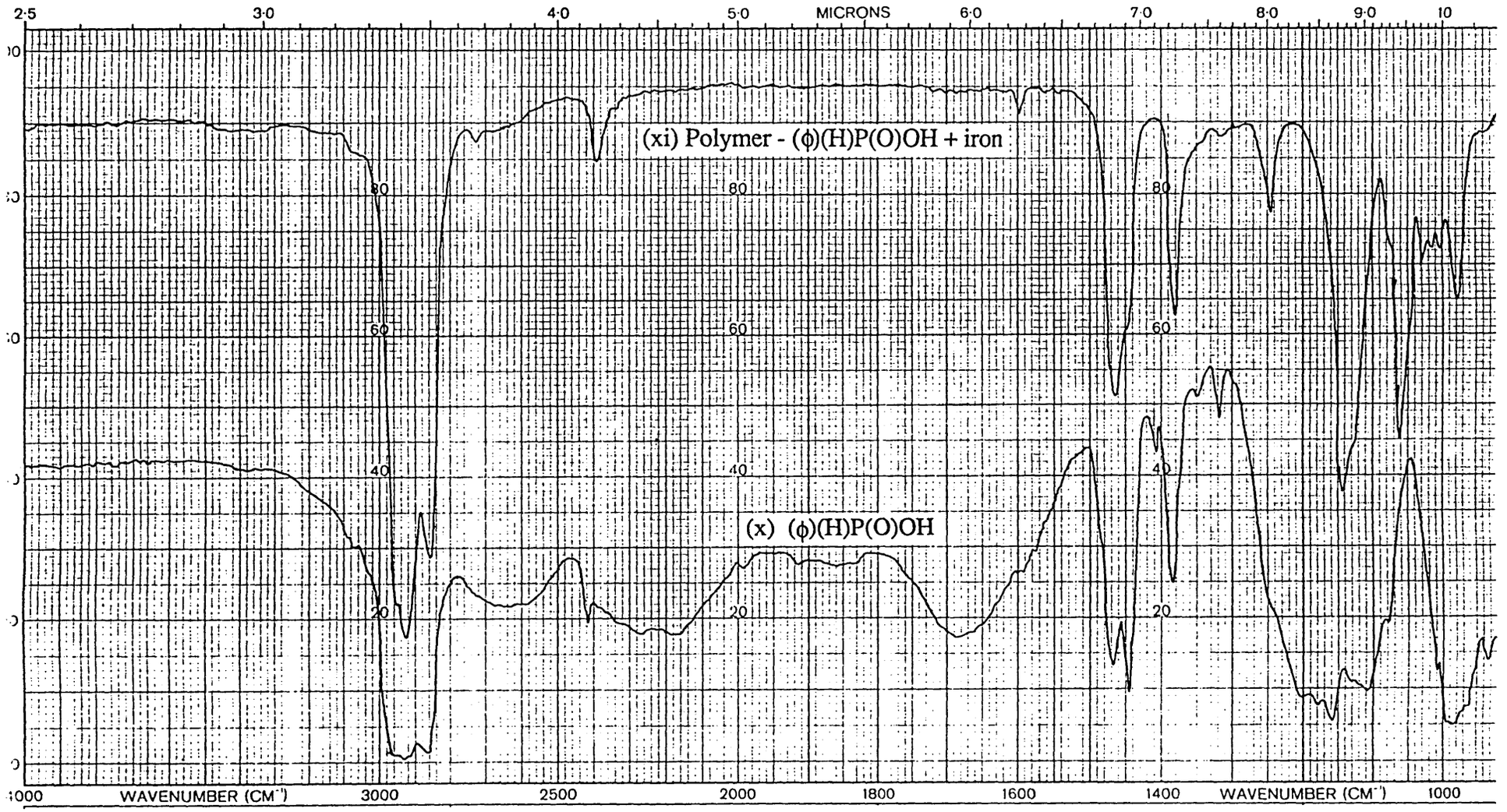


Figure 7.16 Infra-red spectra of phenyl phosphinic acid and polymer formed with iron

co-ordination to a central iron species as explained above. Stearic acid was found in the solution remaining after formation of (xi). Similar, although less clear cut, evidence was obtained with (ϕ)HP(O)H. Evidence of hydrolytic break-down, prior to reaction with iron, was found with $(\phi O)_2P(O)H$.

	Approximate Group Frequencies / cm^{-1}					
	P(O)OH	P-O-H	P = O	O = P-ϕ	P-H	P-ϕ
COMPOUND	~ 2620 ~ 2250 ~ 1680	~ 1020	~ 1300 to ~ 1100	~ 1315	~ 2450	~ 1380 and ~ 1460
(x) (ϕ)(H)P(O)OH	x	x	x	x	x	x
(xi) Iron polymer of (x)	-	-	x	-	x	x

x band present ; - no band in spectrum

Table 7.6 Presence of peaks and approximate group frequencies - phenyl phosphinic acid and polymer formed with iron stearate

Figure 7.17 shows IR spectra of pure TCP (xii) and the black, crystalline material (xiii) that remained after a 5% TCP / hexadecane solution was reacted with ferric stearate at 270° C for 3 1/2 hours. Oxygen was used as to agitate the mixture. A TCP / hexadecane solution heated in the absence of iron was unchanged after this period (TCP is a known anti-oxidant). A hydrolysis / co-ordination process similar to that described previously is evident from the IR spectra. The shift in the phosphoryl vibration shows co-ordination. Some stearic acid / phenyl stearate ester, resulting from hydrolysis, can be seen from the peaks at ~ 1700 - 1750 and ~2700 cm^{-1}. The hydrolytic mechanism was also supported by a more rapid polymer formation observed when water was added. Some slight —OH vibration is evident in spectrum (xiii) at $\nu > 3000\ cm^{-1}$. This may result from phenol formed during hydrolysis, or from OH groups produced by further hydrolysis in the bridging phosphate anions.

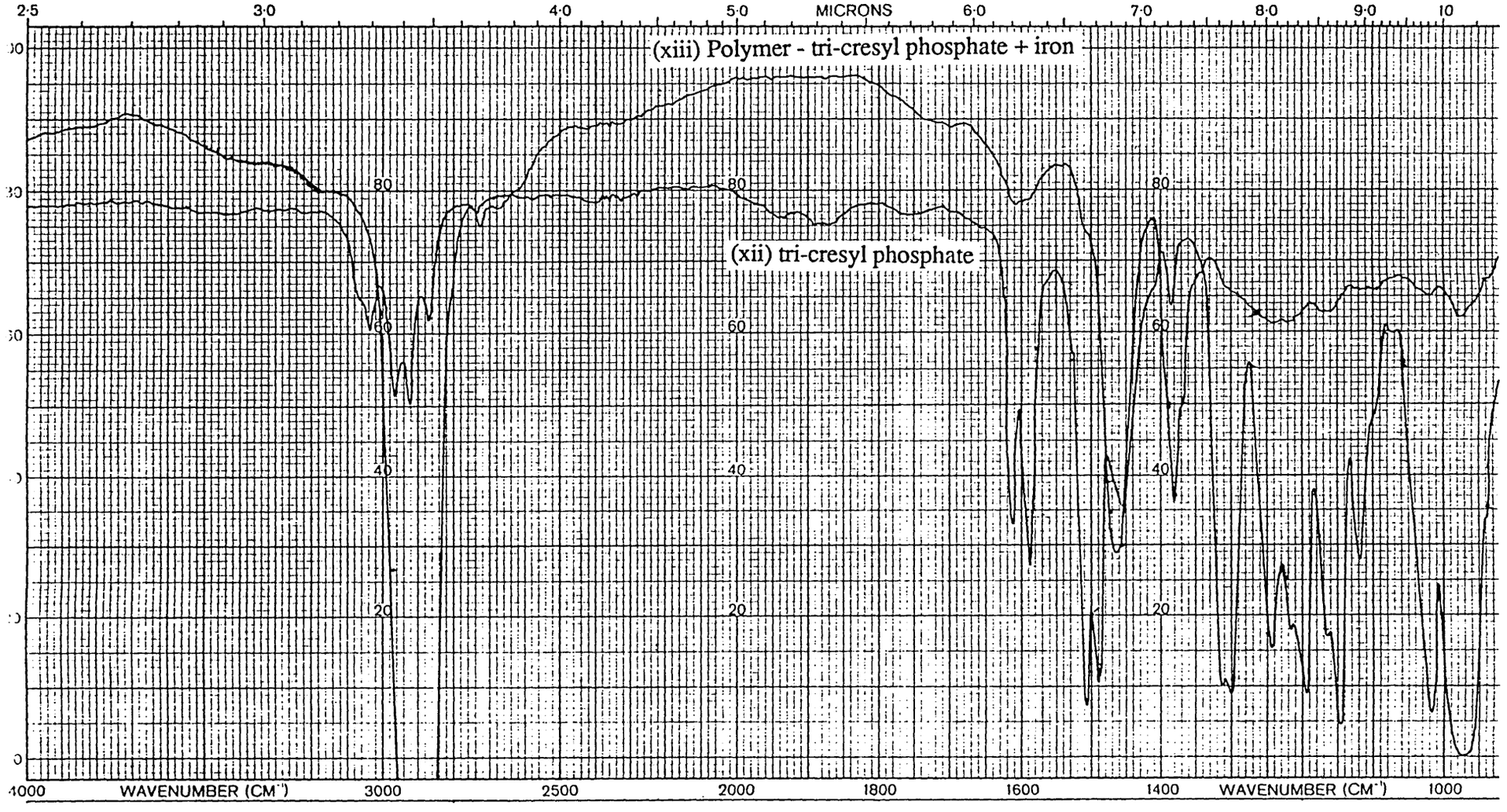


Figure 7.17 Infra-red spectra of tri-cresyl phosphate and polymer formed with iron

7.3.1.4 Discussion

The evidence described above suggests that di-alkyl phosphonates form polymeric compounds by hydrolysis which creates two P—O ligand groups for co-ordination into the central iron (III) species. It is probable that this co-ordination occurs through bridging, rather than chelation. Di-alkyl acid phosphates and di-alkyl / aryl phosphinates have been shown to undergo similar reactions. There is evidence in the literature that latter two groups bridge preferentially [95], [97]. A similar mechanism appears to operate with TCP.

The mechanistic evidence from the 'in vitro' studies provides a guide to the mechanism of film formation in a lubricated contact. Removal of an alkyl chain, during hydrolysis, will reduce the solubility of the additive in the base stock and will lead to its preferential accumulation in the boundary layer coating the rubbing surfaces. The hydrolysis products react with $Fe^{(III)}$ produced by oxidation in the rubbing contact; good evidence of the availability of oxygen can be found in reference [29]. Bridging reactions result in the formation of an insoluble viscous or solid film, which is retained in the contact and which contributes towards surface separation.

7.3.2 Chemical nature of reaction product formed on surfaces

Reflection infra-red spectroscopy was frequently used in the course of the current work to confirm the presence of reacted polymeric films on rolling / rubbing surfaces after testing. It is a very sensitive technique and it can provide evidence about the chemical nature of films with thicknesses below the limit detectable by conventional interferometry. In the current study the presence of a polymeric film was demonstrated by shifts in the phosphoryl bond vibration (as explained above).

A single example of the use of the technique is included here. Table 7.7 summarises the spectra presented in figure 7.18 (the IR spectra are limited to the 800 - 1400 cm^{-1} region, which includes the phosphoryl bond vibration). The pure phosphonate esters (xiv), (xv) and the model compounds (xvi), (xvii) were measured using conventional transmission IR

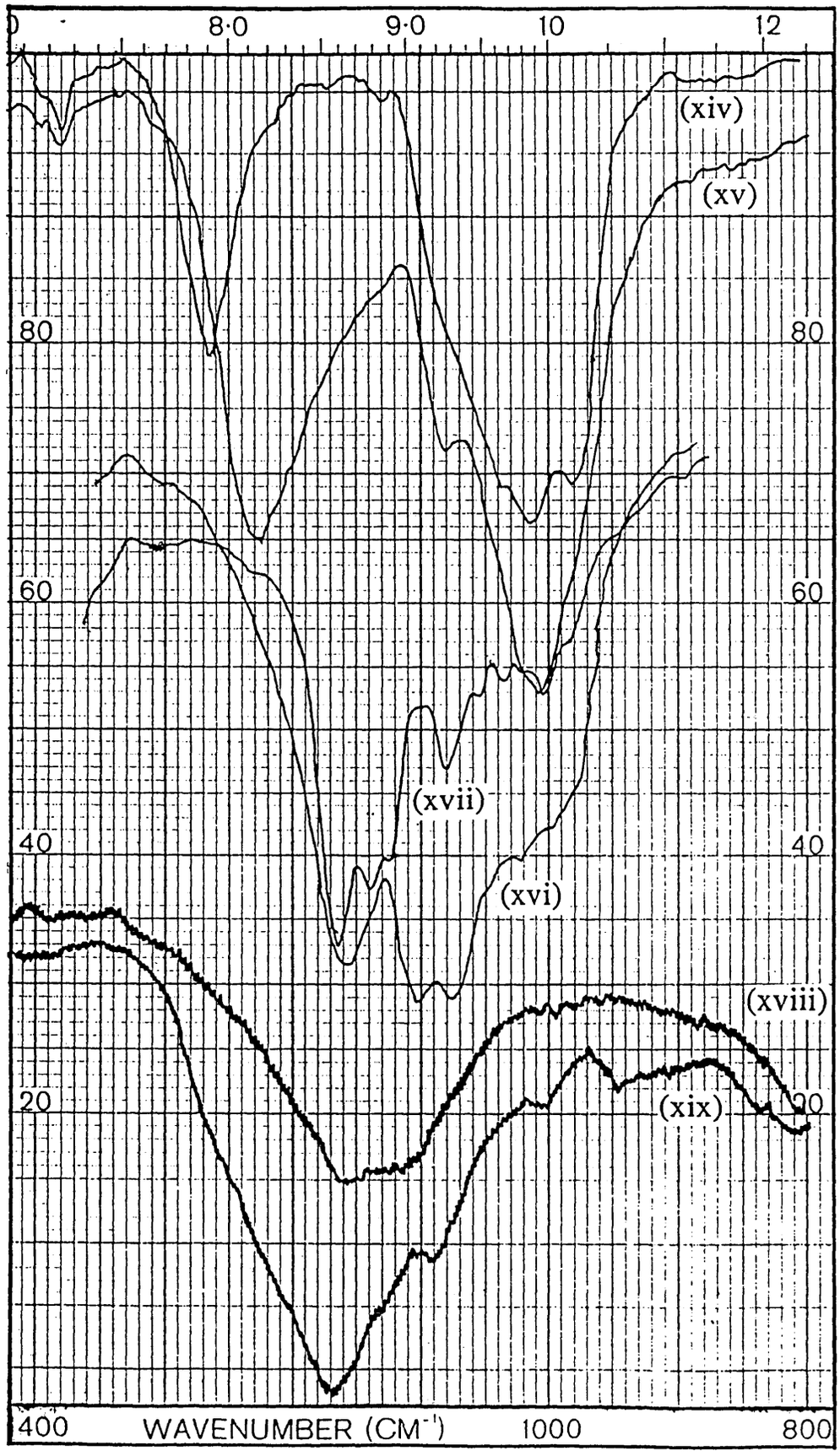


Figure 7.18 Phosphoryl bond vibration

spectroscopy. The reflection infra-red spectra (xviii) and (xix) were measured on the surfaces of the mini-disc machine specimen (§ 6.2.2.1) and the ball tested in the EHD rig (§ 6.2.2.2), respectively. In both cases mono-dodecyl phosphonate was used as additive. The spectra were recorded after solvent cleaning.

N º	COMPOUND (R = dodecyl)	$\nu_{(P=O)}$ / cm^{-1}
(xiv)	$(RO)_2P(O)H$	1267
(xv)	(RO)(HO)P(O)H	1227
(xvi)	Iron polymer of (xiv)	1158
(xvii)	Iron polymer of (xv)	1163
(xviii)	Polymer film (disc machine)	~ 1155
(xix)	Polymer film (EHD rig)	~ 1165

Table 7.7 Approximate group frequencies - dodecyl esters and polymers formed with different iron sources

The similarity in the polymeric material generated from the di and mono-alkyl esters - formed both statically and in operating contacts - is apparent from figure 7.18. Lacey [76] produced polymeric material by reacting iron powder with di-dodecyl phosphonate.The phosphoryl bond vibration occurred at 1160 cm^{-1} indicating the similarity of this product to the model compounds. The shoulder on the phosphoryl peak (xvi) resulted from contamination by ester as described previously. The reflection infra-red spectra of the polymer material generated in operating contacts i.e. (xviii) and (xix) show a slightly reduced P—O—C vibration (~ 1100 - 900 cm^{-1}). This may result from greater hydrolysis of alkyl groups in the bridging phosphonate anions. This would be expected to increase under the more severe conditions found in an operating contact.

A comparison of the reflection infra-red spectra of a ball tested in the EHD rig with mono-butyl phosphonate (§ 6.2.2.2) showed no change in the position of the phosphoryl bond vibration. This confirmed the absence of a reacted, polymeric layer.

CHAPTER 8 - DEVELOPMENT OF OPTICAL INTERFEROMETRIC METHOD. THE MEASUREMENT AND STUDY OF VERY THIN LUBRICANT FILMS IN CONCENTRATED CONTACTS.

8.1 Introduction

In § 5.2.1.7 the interferometric method was shown to be subject to two severe limitations. Firstly, the method cannot be used to measure film thicknesses of less than approximately 100 nm and secondly, measurements can only be made at a series of discrete, fixed separations spaced at intervals of approximately 50 nm.

The following chapter describes improvements to the conventional technique aimed at overcoming these limitations (§ 8.2). Spectroscopic analysis of interference fringes has permitted continuous measurement of film thickness. These measurements have been extended to very thin films by applying the spectroscopic to analysis glass discs covered with a thin, sputtered 'spacer layer' of silica (SiO_2).

Combination of the spectrometer and spacer layer methods has permitted measurement of the film forming abilities of very low viscosity fluids, at very low speeds (§ 8.3). For example, the separation / speed characteristics of hexadecane (η = 0.003 Pa.s) were measured down to 1 ± 1 nm thickness, permitting calculation of the pressure-viscosity coefficient (α value) in an operating contact. The contribution of a boundary / oiliness additive (stearic acid) has been measured directly (§ 8.3.2.2). Deviation from EHD theory - which is based on continuum fluid mechanics - has been observed with film thicknesses of less than approximately 15 nm.

8.1.1 Previous studies

The two important limitations of conventional optical interferometry can be seen from equation (I). This was explained in chapter 5 (θ is the angle of incidence of the light). In monochromatic interferometry the first destructive interference fringe occurs at approximately 75 nm in air and 55 nm in oil (using a red source for which λ is

approximately 675 nm). However the next fringe i.e. the first constructive fringe occurs at 245 nm in air and 175 nm in oil. These values were calculated from equations (I) and (II) (chapter 5) using the measured net phase change $\phi = 0.28$, and assuming $\theta = 0^{o}$ and $n_{oil} = 1.4$. Monochromatic interferometry is limited by the relatively poor ability of the human eye to determine intensity levels. With chromatic interferometry the minimum observable separation occurs as a constructive fringe at approximately 200 nm in air and 130 nm in oil. This represents the minimum film thickness easily measurable by the method. A number of ways of overcoming this limitation have been attempted. The minimum can be brought down to about 60 nm by using an angle of incidence greater than 0^{o} but total internal reflection limits any further reduction [222].

$$h_{oil} = \frac{\left(N + \frac{1}{2} - \phi\right)\lambda}{2\, n_{oil} \mathrm{Cos}\,\theta} \qquad N = 0, 1, 2 \qquad \text{(I)}$$

The most successful approach to overcoming the problem, which has been incorporated in the current study, has been to use a "spacer layer." The principle behind this is shown in figure 8.1. A coating of transparent solid, typically silica, of known thickness, is deposited on top of the semi-reflecting chromium layer. This solid thus permanently augments the thickness of any oil film present and is known as a "spacer layer". Hence destructive interference now obeys equation (II). Strictly, n_{oil} should be a weighted-average of n_{oil} and n_{sp}. In practice, as explained previously, n_{oil} and n_{sp} are very similar.

$$h_{oil} + h_{sp} = \frac{\left(N + \frac{1}{2} - \phi\right)\lambda}{2\, n_{oil} \mathrm{Cos}\,\theta} \qquad N = 0, 1, 2 \qquad \text{(II)}$$

Therefore the first interference fringe occurs at at a separation reduced by h_{sp}, where h_{sp} is the optical thickness of the spacer layer. With a flat spacer layer, Westlake was able to measure an oil film of only 10 nm thickness using optical interferometry [223].

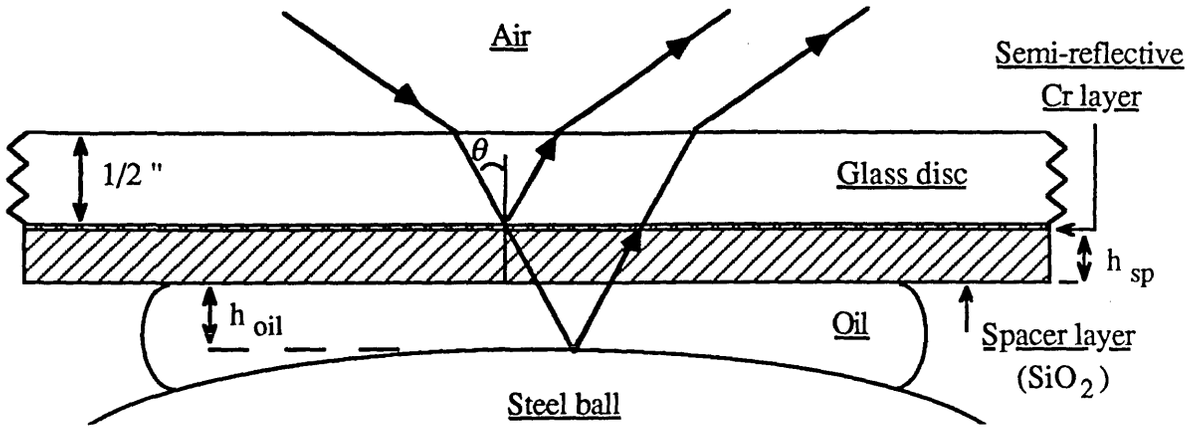


Figure 8.1 Schematic representation of spacer layer method

The use of a spacer layer does not overcome the second problem of optical interferometry which is the limited resolution and accuracy of film thickness measurement. This limitation can be seen in table 5.2, which shows that the thicknesses that can be measured are 50 nm apart and, due to the inability of the human eye to perceive colours precisely and accurately, are ± 20 nm. When monochromatic interferometry is used, resolution is worse, at λ/4, although multiple beam interferometry does provide very high precision.

One method of overcoming this limitation, first postulated by Westlake [223], has recently been described by Guangteng and Spikes [224].They used an alumina (Al_2O_3) spacer layer whose thickness varied in the shape of a stepped-wedge, over the transparent flat surface, in an optical rig. This meant that, with no oil film present, fringes were produced at certain locations on the surface, where the spacer layer was an appropriate thickness to cause interference. However when a thin oil film was formed it had the effect of moving these interference fringes a short distance around the disc, to a position of lower spacer layer thickness. Measurement of fringe movement then yielded oil film thickness. The method was able to detect oil film thicknesses of less than 10 nm. A problem encountered using this technique was the difficulty of obtaining regular spacer layer wedges. Also, low viscosity oils, which require high speeds to generate films, needed high speed recording equipment to chart the continuously changing interference fringe colours.

In the early stages of development of the current system the author used a similar set-up. This was calibrated, with test lubricant in the contact, in a similar manner to that described in chapter five. Although this system reduced the minimum film thickness measurable, it remained subject to the limitation of discrete, well-spaced fringes. In addition, extraction of the oil film thickness required a highly consistent spacer layer which was well characterised in terms of its thickness and refractive index. This work is not included in view of the subsequent improvements.

8.2 Development of optical interferometry - experimental method

In the following study, the two limitations of optical interferometry - the one-quarter wavelength of light limit and the low resolution - were addressed by using a combination of a fixed-thickness spacer layer (see § 8.2.2) and spectral analysis of the reflected beam (§ 8.2.1). The first of these overcomes the minimum film thickness that can normally be measured and the second addresses the limited resolution of conventional interferometry. The conventional optical test rig was employed (figure 5.11). A 25.4 mm diameter superfinished steel ball (Fag bearing Co.) was loaded against the flat surface of a float-glass disc. In most of the work described in the following chapter the ball was driven by a shaft and the disc was driven, in nominally pure rolling, by traction forces in the contact. This permitted much slower surface speeds to be achieved, as the ball speed could be controlled down to approximately 2.6 rpm i.e. 0.0035 ms^{-1}.

8.2.1 Spectral analysis of central film thickness

The system used to monitor the film thickness is shown schematically in figure 8.2. A small area of the central plateau region of the EHD contact was 'observed' by the optical system (as shown in figure 8.3(a)). The light entering the spectrometer was restricted to a thin, rectangular strip of the central fringe image (running in the rolling direction) by a narrow grating (500 - 100 μm) mounted on the spectrometer. This light was dispersed by the grating / spectrometer system. The dispersed spectrum was observed as the output from a black and white video camera. The video output consisted of a band spectrum spread horizontally on a television screen, with the intensity of the spectrum, at each wavelength, indicating the extent of interference. This is shown schematically in figure 8.3(b). The

vertical axis of the spectral band mapped across the centre of the contact. This image was screen-dumped into a microcomputer which drew an intensity profile of the spectrum as a function of wavelength. The micro-computer sub-divided the screen horizontally into a 0 - 256 array. The screen position at which maximum intensity occurred (x_{Max}) was displayed automatically (by fitting a parabola to the intensity profile). The wavelength at which maximum constructive interference occurred (λ_{Max}) was calculated from a calibration of the spectrometer micrometer position and the displayed value of x_{Max} (see § 8.2.1.1). The film thickness was then calculated in the absence of a spacer layer as described in § 8.2.1.2, or with a spacer layer present as described in § 8.2.2.3. In practice the band spectrum and the intensity profile were displayed on separate screens.

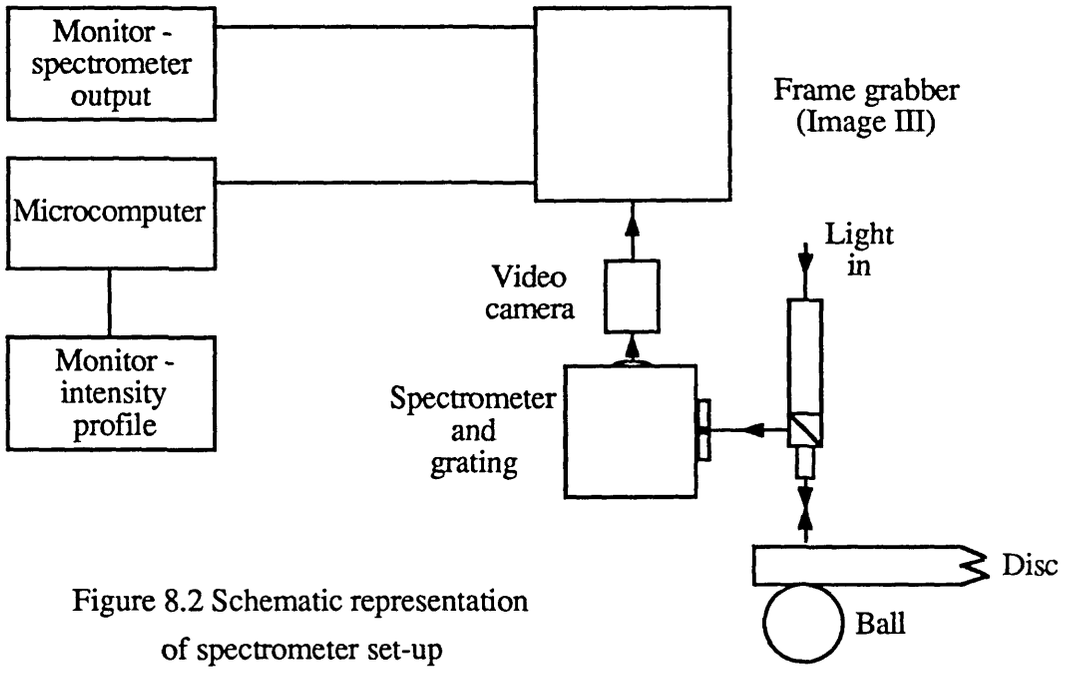


Figure 8.2 Schematic representation of spectrometer set-up

8.2.1.1 Calibration of the spectrometer

To increase spectral resolution, the magnification was arranged so that only a portion of the spectrum fitted on the screen. The spectrometer grating was rotated, using a micrometer, to scan the whole spectrum. The spectrometer was calibrated with respect to micrometer reading (MR in inches) and screen position (x_{Max}) by passing the light from a mercury lamp, with known wavelength emission, into the spectrometer. In test work a cold halogen white light source employed. The calibration is described below.

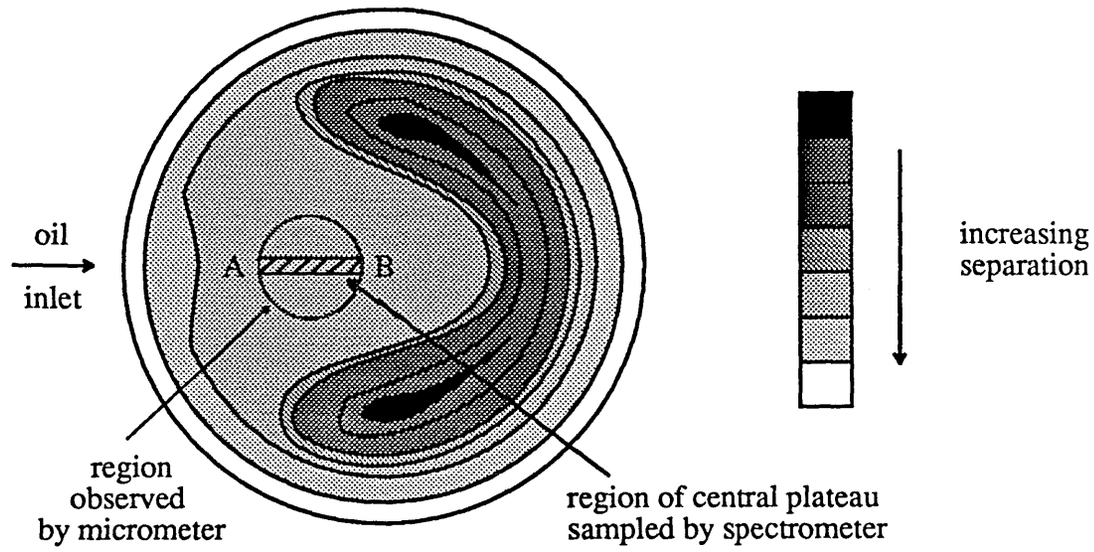


Figure 8.3(a) Schematic map of EHD point contact
showing region observed by spectrometer

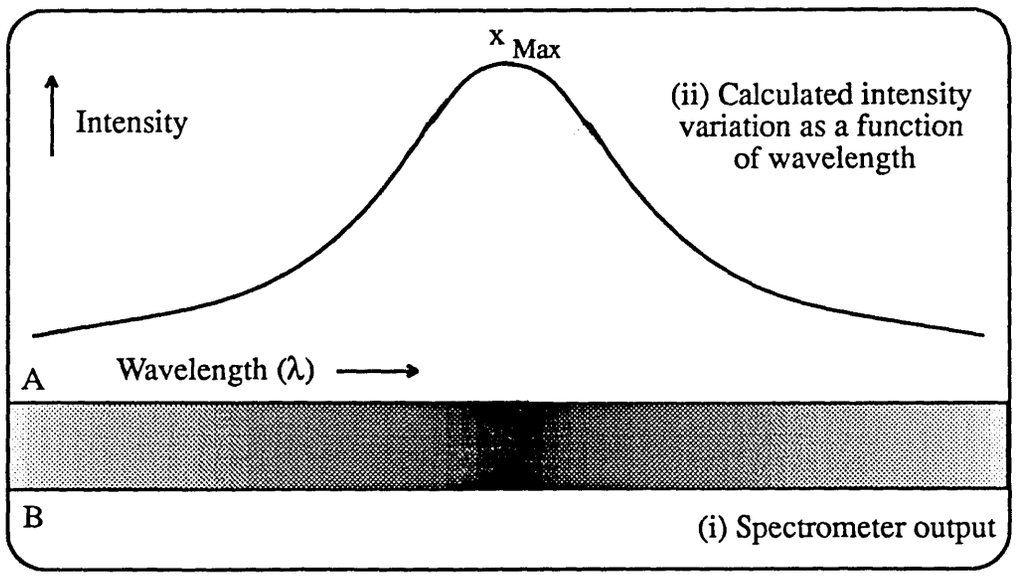


Figure 8.3(b) Schematic representation of screen display showing (i) the
spectrometer output and (ii) the calculated intensity variation

The spectrometer was calibrated against wavelength by adjusting the micrometer so that each discrete waveband in the Hg source was placed at the screen position $x_{Max} = 128$. This is shown in figure 8.4, which includes the equation of the 'best fit' line.

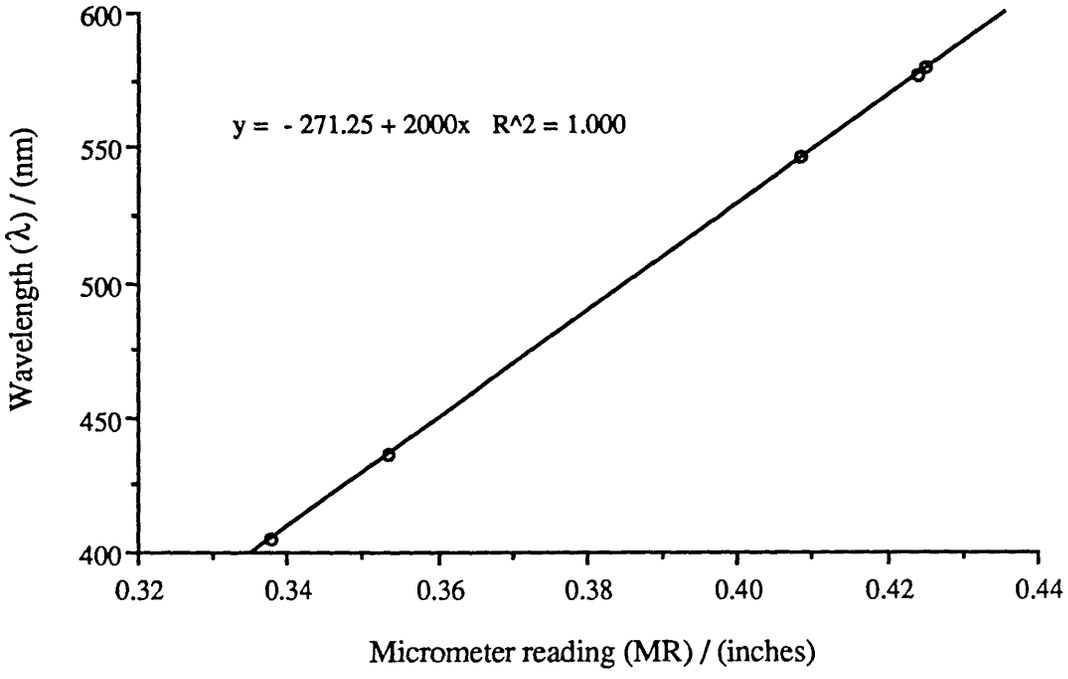


Figure 8.4 Spectrometer calibration - wavelength against micrometer reading

A calibration with respect to screen position was achieved by noting the variation in screen position for each spectral line, as a function of the micrometer setting. This is shown for three of the spectral lines in figure 8.5.

It is apparent from figures 8.4 and 8.5 that 1 screen dot corresponds to a change in wavelength of 0.47 nm, and that 256 screen dots corresponds to a change in micrometer reading of 0.0602 inches. Thus λ_{Max} can be calculated from the measured value of x_{Max} (for a pre-set MR) according to equation (III). The system was found to measure λ_{Max} to $\pm$ 1 - 2 screen dots i.e. $\pm$ 0.5 - 1 nm depending on the number of readings taken (§ 8.3.2). This represents an error of $\pm$ 0.2 - 0.4 % in λ_{Max} for a typical mid-range wavelength of 500 nm.

$$\lambda_{Max}\,(nm) = 2 \times 10^3 \left[(MR - 0.0301) + 0.0602 \left(\frac{x_{Max}}{256} \right) \right] - 271.25 \qquad (III)$$

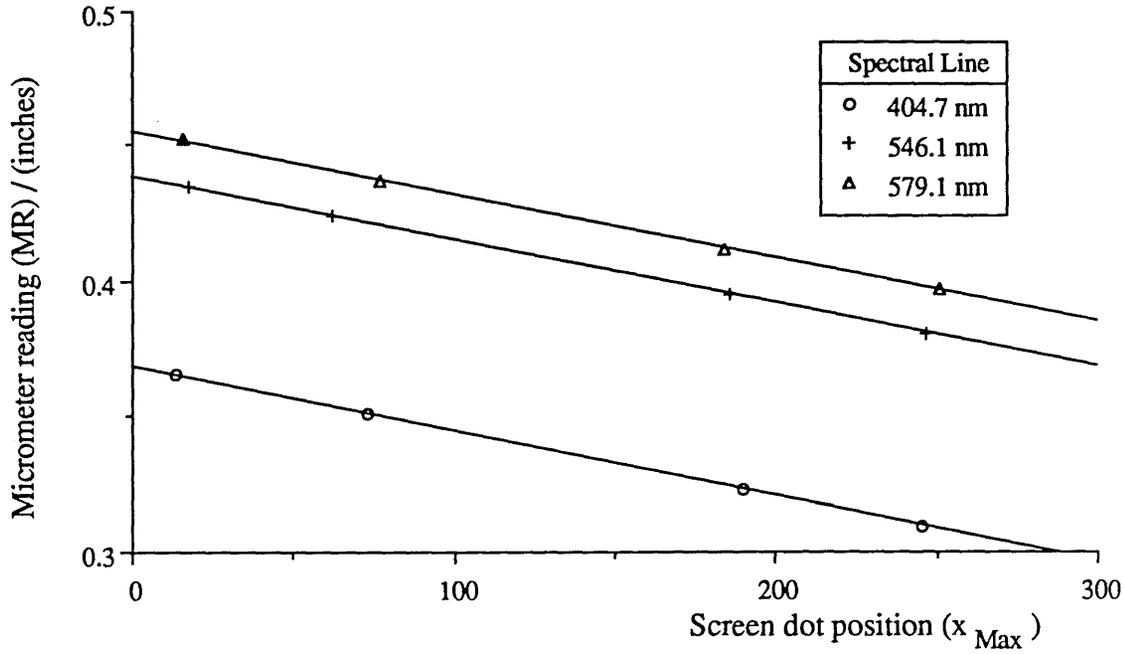


Figure 8.5 Spectrometer calibration - micrometer reading against screen dot position

8.2.1.2 Spectral measurement of film thickness - conventional disc

The spectroscopic method can be used to calculate the film thickness / speed characteristics using a conventional disc i.e. a disc bearing a semi-reflective coating only. As speed is increased x_{Max} moves left to right across the screen, towards longer wavelength, as the EHD separation increases. A further increase in speed causes this process to be repeated as second order fringes (N = 2) and so on. The film thickness, for a given speed, is calculated according to equation (IV) from the measured value of x_{Max}. λ_{Max} is calculated from x_{Max} according to equation (III).

$$h_{oil} = \frac{(N - \phi)\lambda_{Max}}{2\, n_{oil}} \qquad (IV)$$

The phase change (ϕ) was measured as described previously (§ 5.2.1.3). An example of this method is given in § 8.3.1.

8.2.2 Spacer layer method

The following section describes the evaluation of the refractive index of the silica film and the film depth as a function of disc radius. An example of its use in measuring an oil film is given in § 8.3.1.

8.2.2.1 Evaluation of silica film thickness as a function of disc radius

Initial work used a disc sputtered with a relatively thin silica spacer layer of approximately 100 nm. The thickness of silica was determined in two ways. When the spacer layer was sputtered, a thin radial strip of the disc was masked, so that a shallow silica-free groove was obtained. The thickness of silica on either side of this was then measured by passing a talysurf stylus across the groove in a circumferential direction. The spacer layer thickness was measured as a function of the disc radius. The results are shown in figure 8.6.

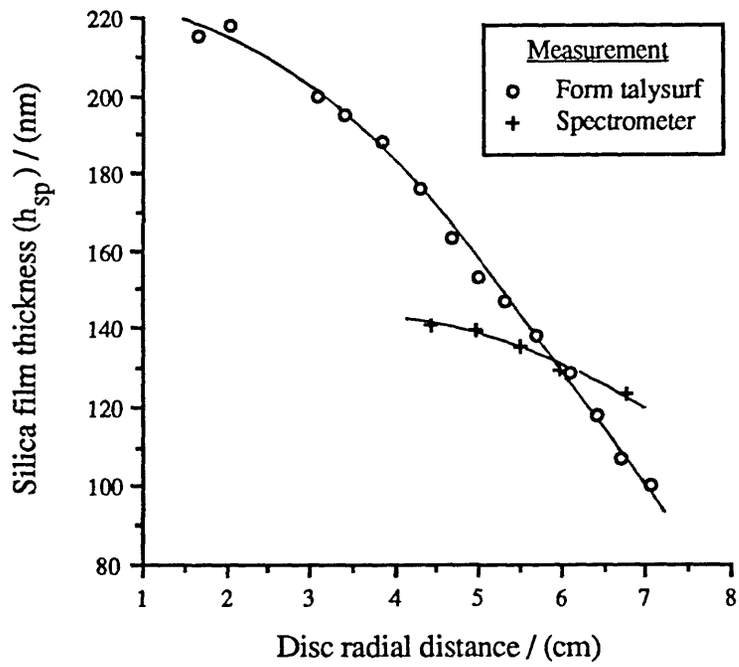


Figure 8.6 Measured film thickness - thin spacer layer

The silica film thickness was also determined, as a function of the disc radius, by an optical interference method (using the spectrometer). A steel ball was loaded against the silica surface which gave an interference pattern of a central, circular Hertzian area with

surrounding circular fringes due to the air gap between deformed ball and flat. The thickness of the silica layer in the Hertzian contact was calculated from the measured wavelength at which maximum constructive interference occurred (λ_{Max}), by solving an equation analogous to equation (IV) for h_{sp}. N was known from the approximate thickness of the silica layer and ϕ was assumed to be 0.28 from the value measured previously (in air). The refractive index of the separating medium is known to affect ϕ by less than 2% [199]. The refractive index of the spacer layer (n_{sp}) was measured as 1.476 ± 0.001 as described in § 8.2.2.2.

Figure 8.6 shows that the two calibration methods did not agree when a thin silica spacer layer was used. This was tentatively ascribed to the effect of penetration of the the reflected beam into the substrate. This has been termed the "effervescent wave" phenomenon [225]. When a wave is reflected at the surface of a thin film it penetrates slightly into the substrate and the extent of penetration (and the phase change upon reflection) depends on the film thickness. Any additional oil film will therefore alter the phase change on reflection.

The solution to this problem was to use a spacer layer with a thickness of the order of the wavelength of visible light, which represents the limit of penetration of a reflected light beam. Any variation above this value, due to spacer layer or oil, will have no further effect on phase change. Figure 8.7 shows the good agreement between the two calibration methods with the thick spacer layer. This disc was employed in all subsequent work.

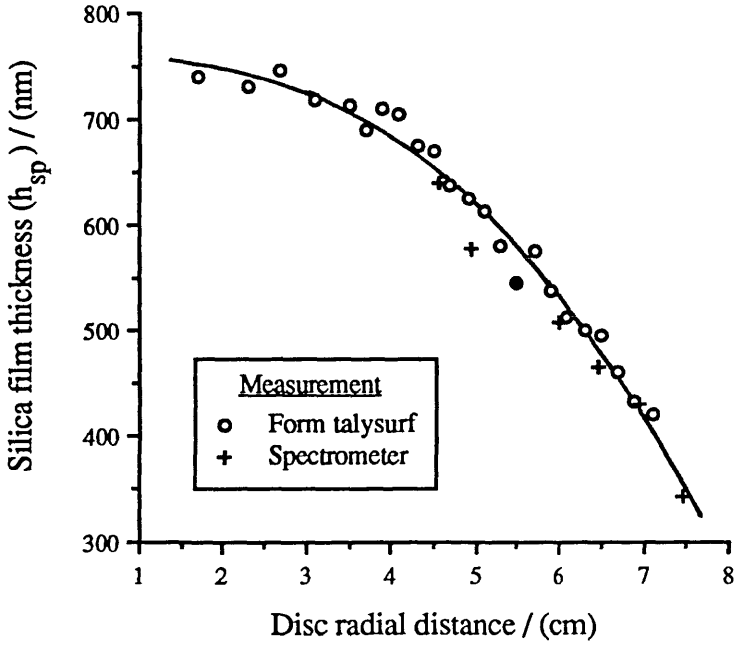


Figure 8.7 Measured film thickness - thick spacer layer

8.2.2.2 Evaluation of refractive index of silica film

The refractive index of the silica films (n_{sp}) was measured using the method of Kauffman [226]. The 'thick' silica coated disc displayed clear interference fringes when observed with the naked eye due to a division of amplitude undergone by the light incident upon the silica surface. The reflected wavefront undergoes interference with the light that penetrates the silica and reflects off the chromium layer. Reflection at the air / silica interface occurred due to a sharp change in refractive index. The interference patterns were particularly clear around the the silica free region. A dark step was similarly evident, in this region, with the thinly coated disc.

If a liquid with a refractive index equal to n_{sp} is placed on the disc the interference patterns will disappear. This provided a means of measuring n_{sp} by gradually mixing two miscible liquids - toluene ($n = 1.4961 > n_{sp}$) and acetone ($n = 1.3588 < n_{sp}$) - and covering the disc with a range of the resulting solutions. Samples of the toluene / acetone mixtures at which the fringes first disappeared and then reappeared were retained. The refractive indices of the two solutions were measured conventionally (as described in § 5.2.1.6). It was found that fringes were visible in the range $1.4860 > n > 1.4670$. Therefore $n_{sp} = 1.476 \pm 0.001$.

8.2.2.3 Spectral measurement of film thickness (sputtered disc)

With the spacer layer present the oil film thickness (h_{oil}) is calculated according to equation (VII), from the spacer layer thickness (h_{sp}) measured with the disc stationary (equation V) and the combined spacer layer plus oil film thickness ($h_{sp}+ h_{oil}$) at a given rolling speed (equation VI). An advantage of this system of film thickness measurement is that the phase change need not be measured directly, since it is measured twice and subtracted.

$$N\lambda_{sp} = 2\, n_{sp}\, h_{sp} + \phi \qquad (V)$$

$$N\lambda_{sp+oil} = 2\, n_{sp}\, h_{sp} + \phi + 2\, n_{oil}\, h_{oil} \qquad (VI)$$

$$\therefore \quad h_{oil} = \left[\frac{\left(N\lambda_{sp+oil} - N\lambda_{sp} \right)}{2\, n_{oil}} \right] \qquad (VII)$$

The spacer layer varied in thickness in the radial direction, but was approximately constant circumferentially around the disc, so that as the disc rotates the contact sees a near-constant thickness. The image captured for analysis was triggered by the disc rotation so that all spectra in a series could be taken from the same position on the disc circumference. This minimised any effects due to slight changes in spacer layer thickness. The delay between physical triggering and frame capture was in the range 0 - 2.4 ms, which represents negligible movement of the disc at the slow surface speeds employed (see § 8.2.3). It can be seen from figure 8.7 that the silica film thickness falls from approximately 620 to 440 nm as the track radius changes from 50 to 70 mm. Most film thickness measurements were obtained in this region of the disc. The film material therefore has a gradient of 170 / 20 = 9 nm / mm. Since the Hertzian diameter is typically 0.5 mm and the region monitored is less than 1/4 of the Hertz width, the silica film thickness changes by less than 1 nm over the observed region. The measuring system provides an average thickness over this region. An example of the application of the technique is given in § 8.3.1.

8.2.3 Experimental conditions and lubricants tested

Table 8.1 summarises the test conditions employed.

Load	23 N
Max. Hertz pressure	0.445 GPa
Speed range	0.0034 - 0.13 ms^{-1}
Temperature	24.5 ± 0.5 ° C

Table 8.1 Experimental conditions

Table 8.2 lists the lubricants used.

LUBRICANT	VISCOSITY / (Pa.s) (24.5 ± 0.5 °C)	REFRACTIVE INDEX
Mineral oil	0.364	1.4868
Synthetic hydrocarbon (PAO)	0.0497	1.4570
Type II (polyol) ester	0.0349	1.4516
Methyl phenyl siloxane - A	0.1536	1.4974
Methyl phenyl siloxane - B	0.0546	1.4225
Liquid crystal (E 44)*	0.0448	1.5270
tri-tolyl phosphate (TCP)	0.0758	1.5535
Squalane	0.0302	1.4498
Hexadecane	0.0030	1.4323

* Eutectic cyano alkyl biphenyl

Table 8.2 Measured viscosities and refractive indices for experimental lubricants

8.3 Results

8.3.1 Validation of experimental technique

Two experiments were conducted to validate the spectral technique (§ 8.3.1.1) and the spacer layer method (§ 8.3.1.2). In both cases the oil used was a well characterised mineral oil having a viscosity of 0.364 Pa.s and an effective pressure-viscosity coefficient (α value) of 21.75 GPa^{-1} at the test temperature of 24.5 ± 0.5 °C. In both cases the film thicknesses measured for the mineral oil, by the various techniques, were indistinguishable from those calculated using EHD theory.

8.3.1.1 Spectral measurement of the film thickness - conventional disc

The spectrometer was tested by carrying out film thickness measurements with the mineral oil at a range of rolling speeds using (i) conventional colour-recognition chromatic optical interferometry and (ii) the spectrometer method of wavelength measurement. A conventional disc coated with a semi-reflective chromium coating only was used. The oil film thickness was calculated from λ_{Max} as described in § 8.2.1.2 i.e. by solution of equation (IV) above. Figure 8.8 shows the good agreement between the two methods and illustrates how many more data points the spectrometer can provide compared to the colour-recognition method.

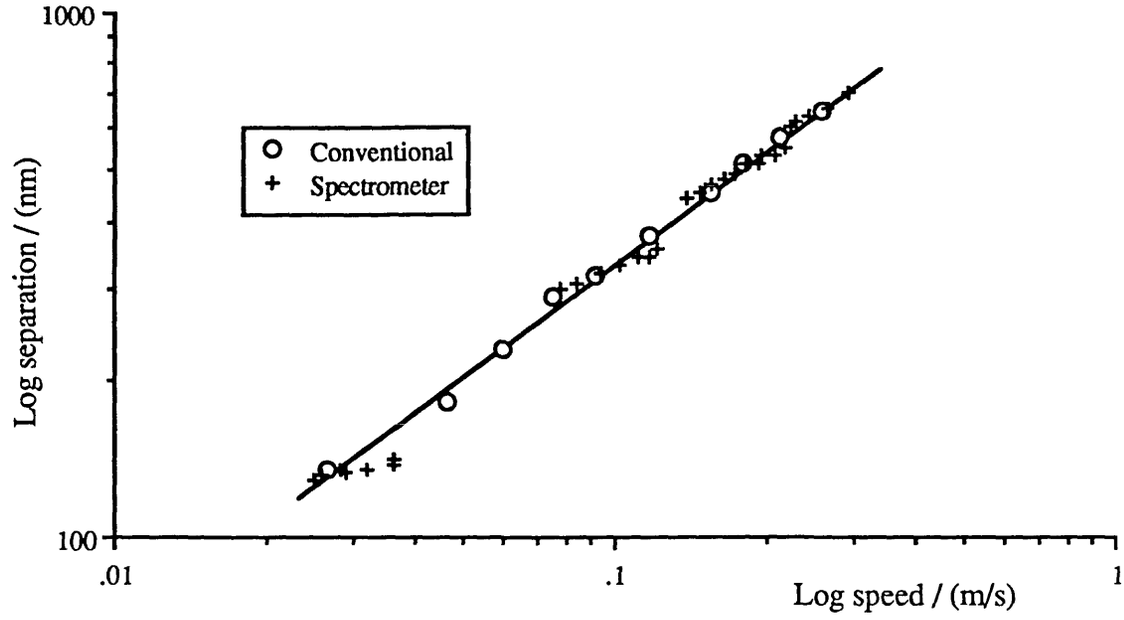


Figure 8.8 log (separation vs. speed) measured conventionally and using spectrometer (uncoated disc)

8.3.1.2 Spacer layer method

A similar comparison was carried out on the same oil using (i) the spectrometer without a spacer layer and (ii) the spectrometer with a spacer layer on the disc. Figure 8.9 shows, again, good agreement between the measurements made with the two different discs. The figure shows that much lower film thicknesses are measurable with a much improved resolution, using the spacer layer. With this, quite viscous oil, the minimum film thickness measured (approximately 30 nm) was constrained by the lowest speed attainable on the test-rig.

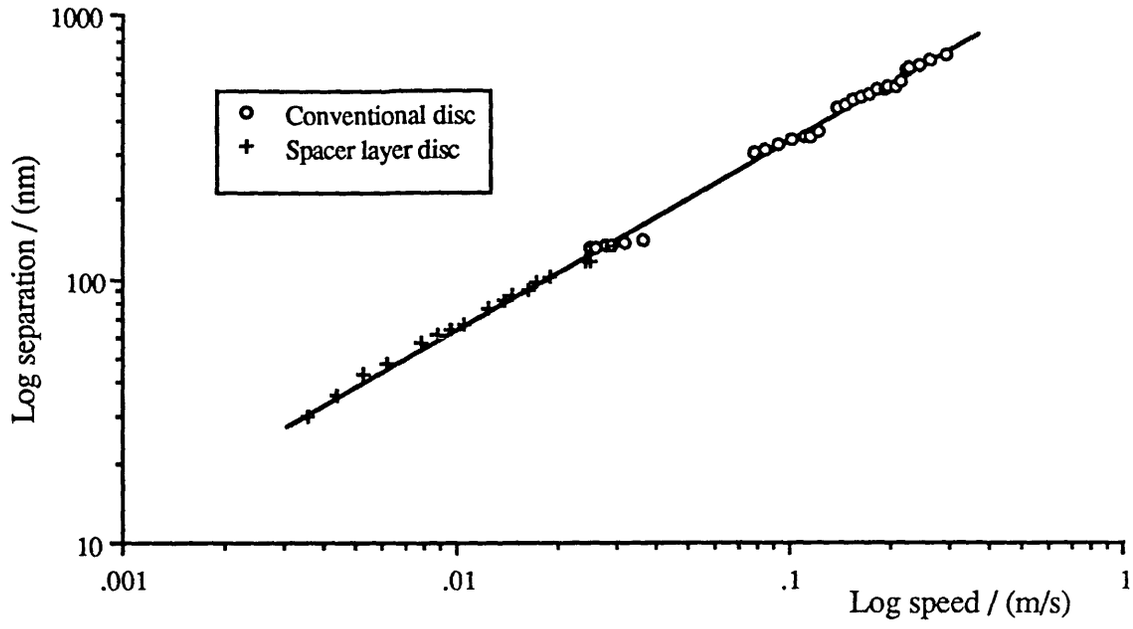


Figure 8.9 log (separation vs. speed) measured using spectrometer on an uncoated disc and a disc coated with a spacer layer

8.3.2 Results with different base stocks

Figures 8.10 to 8.12 show logarithmic plots of film thickness versus rolling speed for seven fluids tested using the combined spacer layer / spectrometer system. Each point in the figures represents an average of at least three measurements. The results indicate that the method can currently measure film thicknesses reliably down to approximately 5 nm. With more viscous fluids these film thicknesses could not be reached because the test rig was unable to run at sufficiently low speed. It is considered that the results are $\pm$ 2 nm but, for figure 8.13, where more measurements were taken at each speed, results are $\pm$ 1 nm.

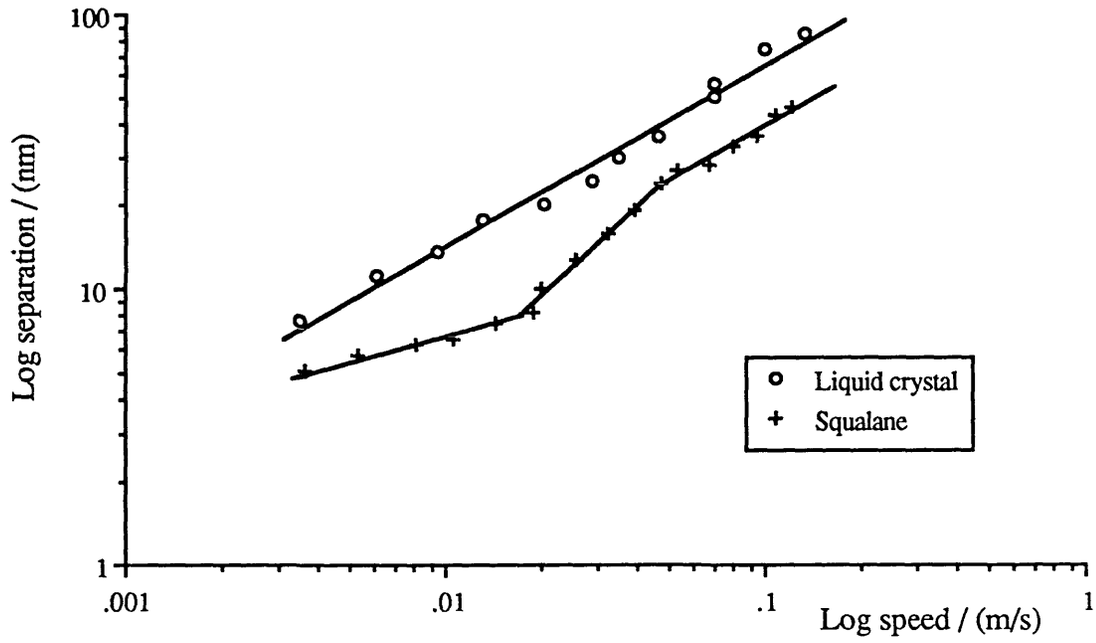


Figure 8.10 Log separation vs. speed - liquid crystal and squalane

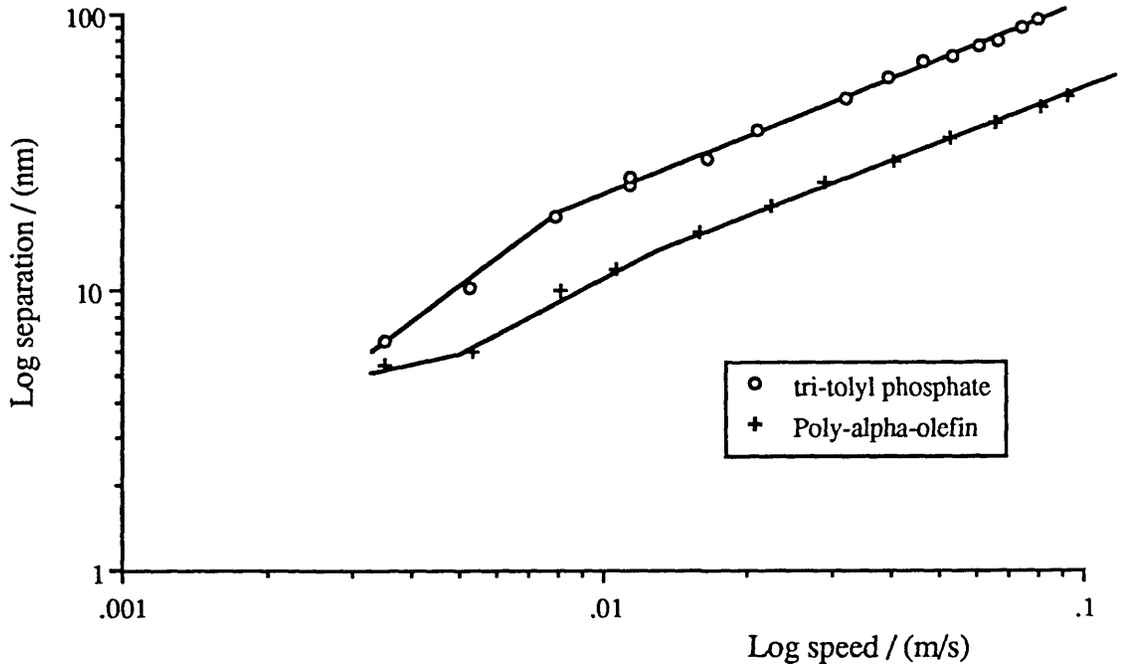


Figure 8.11 Log separation vs. speed - tri-tolyl phosphate and poly-alpha-olefin

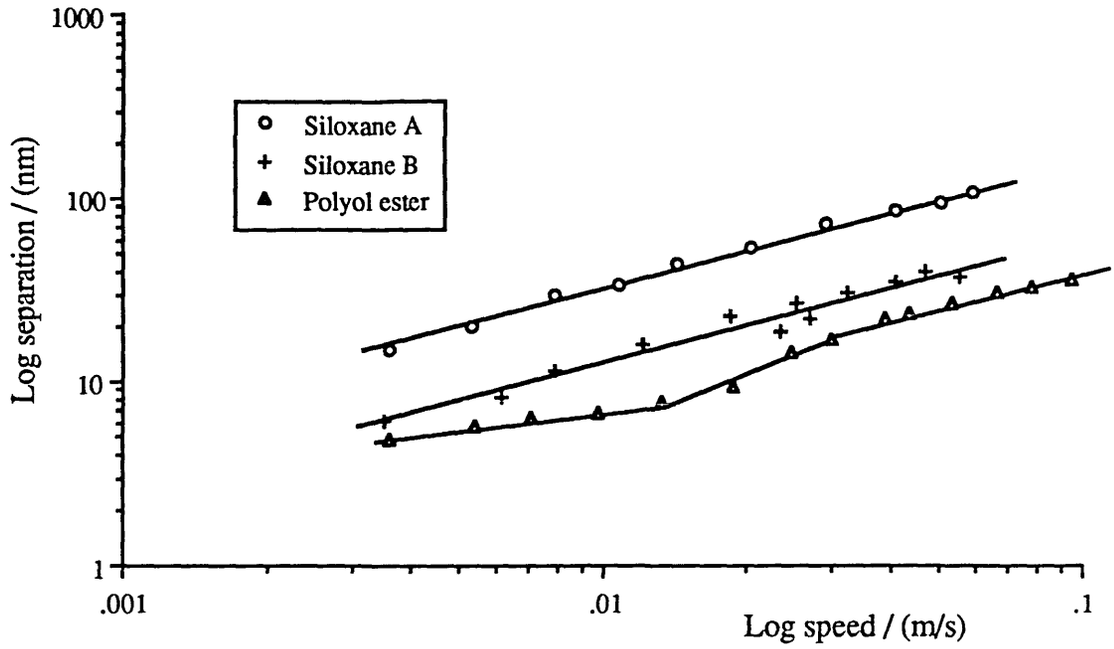


Figure 8.12 Log separation vs. speed - siloxanes A and B, and polyol ester

8.3.2.1 Discussion - calculation of α values

The results in figures 8.10 - 8.12 and the gradients in table 8.3 show that all the fluids obey quite closely the well-known elastohydrodynamic relationship between central film thickness and entrainment velocity (§ 1.4) down to a film thickness of approximately 15 nm. By comparing the film thicknesses obtained for the fluids tested with those of the reference mineral oil - of known viscosity and pressure viscosity coefficient - it was possible to determine the effective pressure-viscosity coefficients of the test fluids. Table 8.3 summarises the pressure viscosity coefficients obtained. The values were calculated at the fixed value of log $(U.\eta) = -2.5$ N/m as described in § 5.2.4. The table includes the gradients of the best fit lines drawn through the log h vs. log U plots and a list of α values obtained from the literature for similar fluids. As can be seen these compare well with values from either conventional optical interferometry or from high pressure viscometry. The widely different pressure-viscosity coefficients observed with the two siloxanes are due to differences in the ratio of Methyl Methyl siloxane to Methyl Phenyl siloxane in the base stocks. Full details of the respective compositions of the base fluids and some comparative α-values from the literature are given in reference (VI) in the list of Authors publications.

LUBRICANT	CALCULATED α VALUE / (GPa^{-1})	PREVIOUS α VALUE / (GPa^{-1})*	GRADIENT
Mineral oil	21.75	21 [227]	0.71
Synthetic hydrocarbon (PAO)	10.8	-	0.70
Type II (polyol) ester	8.5	7.5 [227]	0.68
Methyl phenyl siloxane - A	18.3	-	0.69
Methyl phenyl siloxane - B	12.0	-	0.68
Liquid crystal (E 44)	17.1	-	0.66
tri-Tolyl phosphate (TCP)	22.5	19 [227]	0.69
Squalane	9.5	14 [204]	0.69
Hexadecane ± stearic acid	10.6	8 [228]	0.69

* Similar basestocks [references in brackets]

Table 8.3 Measured and literature α values. Gradients for calculated values

Below 15 nm there appear to be some anomalous film thickness effects. With squalane, tri-tolylphosphate and the polyol ester there was evidence of an increased dependence of film thickness on rolling speed, in the range 5-15 nm. This was not seen with the liquid crystal. With the synthetic hydrocarbon and the low viscosity silicone the same effect was observed but it was within error estimates.

The reason for this effect is not clear. It may originate from a breakdown in the continuum assumption used in hydrodynamic theory although, in this context, it must be remembered that an EHD film is generated at the inlet where the film thickness is slightly greater than the central film thickness.

One possibility is that with very thin films, fluid ordering near the surfaces produces molecular alignment which results in the fluid having an effective viscosity less than its bulk value. Thus, in the range 5 to 15 nm we might be seeing the loss of this non-Newtonian effect as we move towards the bulk fluid properties. Viscosity reductions near surfaces have been observed by Derjaguin using the oil film blow off technique and, for a diacid ester, occur at between 10 and 15 nm [229]. Further study is needed to confirm and further investigate this effect.

With the low viscosity fluids squalane and polyol ester, there was evidence of a residual separating film of approximately 5 nm thickness, which was almost speed-independent. This film disappeared however, when rolling was completely halted.

The current rig could not be run at sufficiently low speed to see whether a similar effect occurred with the other fluids. Very much clearer evidence of the phenomenon is presented in the next section.

8.3.2.2 Hexadecane ± stearic acid

Figure 8.13 shows the result of two tests, with purified hexadecane and with a saturated solution of stearic acid in hexadecane. These results are at the limit of resolution of the method, but show that purified hexadecane gave no apparent residual film. The very low film thickness measurement for hexadecane was an average of six readings and is believed to be 1 nm ± 1 nm. However the stearic acid solution appeared to give a separation of about 2 nm, which persisted down to very low speeds, although it disappeared when rolling was halted.

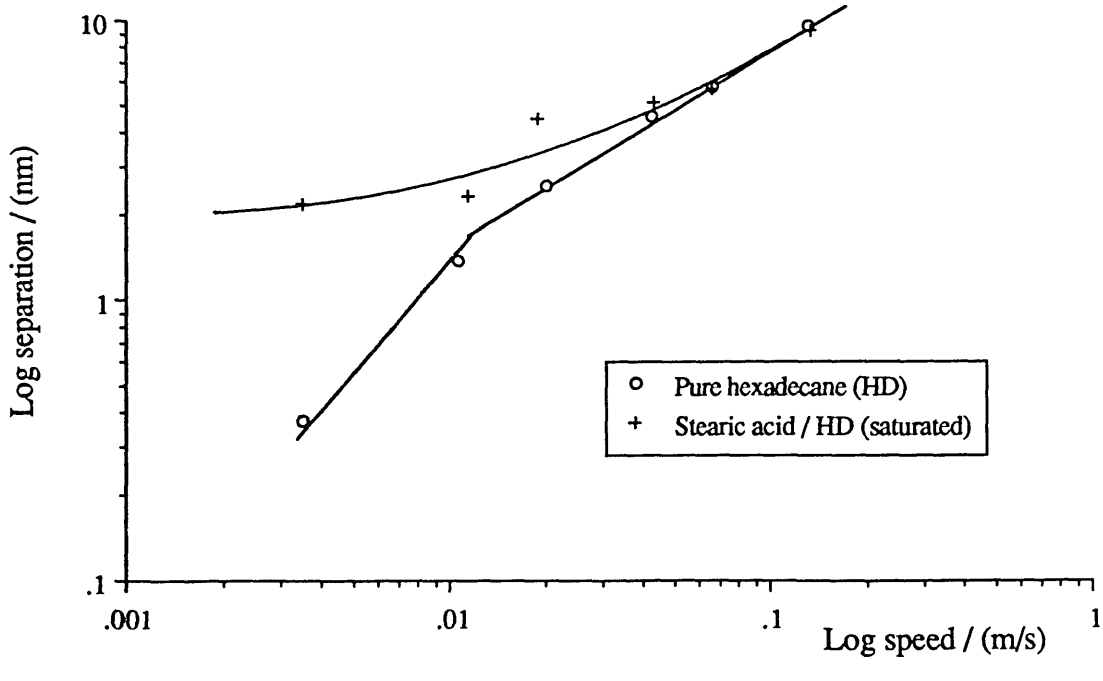


Figure 8.13 Log separation vs. speed - purified hexadecane ± stearic acid

The author tentatively ascribes this effect to an absorbed film of stearic acid on one or both surfaces. The height of an upright, aligned stearic acid molecule is approximately 2.5 nm, [8] but little is known about its likely orientation under a Hertzian contact pressure. If this interpretation is correct, then it must be inferred that the adsorbed film cannot persist on surfaces under static contact pressures but is squeezed off. This interpretation is by no means the only one. The effect may be due to a viscous surface film of polar material. Further study, after refinement of the experimental technique, should help elucidate the matter. It is interesting to note that, as speed increases and a hydrodynamic film is generated, the residual 2 nm film thickness due to the stearic acid does not appear to continue to augment the film thickness of the fluid. The reason for this is not understood but may result from a boundary shear effect at high speeds or from localised heating and desorption in the inlet.

In the above discussion, the possible effects of surface roughness have not been considered. The composite surface roughness of the contact was 11 nm but it must be noted that this is an out-of-contact value. Elastic flattering will greatly reduce this. It is difficult to predict the effect on film thickness of load being carried by asperities. The fluid pressure in the inlet will drop, and this will reduce the inlet viscosity and thence the film-generating capabilities of the lubricant. However this will be counter-balanced by the fact that the contacting asperities will, themselves, help hold the surfaces apart. A further possible explanation for the change in gradient of log h against log U for some fluids tested is that it represents a transition from EHD to isoviscous lubrication as load is borne by contacting asperities, thus reducing the oil pressure in the inlet.

In view of the fact that the anomalous film thickness effects below 15 nm were fluid dependent it seems unlikely that they originate directly from surface roughness effects.

CHAPTER 9 - CONCLUSIONS AND SUGGESTIONS FOR FURTHER WORK

9.1 Conclusions

The aims and the experimental approach employed in the current work were described in sections 1.10 and 1.11. The following section details conclusions drawn from the experimental studies. Section 9.2 contains proposals for further work in light of the conclusions presented in section 9.1.

A comprehensive review of the literature uncovered conflicting evidence for the mechanism by which phosphorus-based anti-wear additives act. A hydrolytic mechanism was proposed for phosphonates by a number of workers [35], [47] and [48]. An oxidation mechanism was preferred in [76], [44] and [49], although both water and oxygen were shown to increase the reaction rate [76]. These two schools of thought imply respectively phosphonate and acid phosphate as the active film-forming species. Considerable evidence was found to support the presence of thick, viscous or solid films that result in bodily separation of the surfaces (§ 2.4.2). No mechanistic conclusions could be drawn from the conflicting evidence found in the literature. The following conclusions were drawn from the experimental work described in chapters four to eight.

Chapter 4 - Some novel synthetic methods were used to prepare a range of organo-phosphorus esters. A number of di-alkyl phosphonates were synthesised. Their primary oxidation products (di-alkyl acid phosphates) and their hydrolysis products (mono-alkyl phosphonates) were also synthesised. Both syntheses are complicated and mixtures invariably result. The method used to prepare the mono-phosphonates gave improved, but still limited, purity. Brief attempts at further purification proved unsuccessful. The classical synthetic route to di-alkyl acid phosphates - through esterification and partial hydrolysis of $P(O)Cl_3$ - is known to produce mixtures that are difficult to separate. The synthetic route adopted in the current study - oxidation of the respective di-alkyl phosphonate - produced a range of di-alkyl phosphates of high purity. Neutral amine salts were prepared, for both classes of compound, to improve the oil solubility and to decrease the excessively corrosive behaviour observed with the free acids. High purity products resulted in both cases. The

synthetic products were characterised in terms of purity and contaminants by elemental analyses, infra-red spectra and $^{31}P_{NMR}$.

Chapter 5 - (i) A number of test rigs were used to model the various lubrication regimes encountered by additives in practical systems. An elevated temperature rolling / sliding, optical interferometric rig was designed and commissioned. This permitted direct observation of the build-up of reacted layers in an operating contact. Oil inlet temperature control up to 200 ± 1° C was achieved. Extremely accurate speed control was incorporated for proposed traction studies. Some commissioning tests were undertaken to (i) measure α-values as a function of temperature and (ii) to confirm the prediction of EHD theory that film thickness is independent of the degree of sliding and depends only on the average rolling speed. A mini-disc machine and a high frequency reciprocating device were used to follow film build-up in boundary lubricated contacts having a more realistic contact metallurgy than glass on steel. Calibration of the respective test-rigs was described.

Chapter 6 - (i) The observation of Lacey et al [76] that longer chain length di-alkyl / aryl phosphonates form thick films in rolling / sliding contacts at elevated temperatures was confirmed. The maximum thickness was shown to be controlled by depletion of the hydrolysis product (which was identified as the active thick film forming species). Maximum thicknesses of ~ 550 nm were found, but the material was shown to be unevenly distributed within the operating contact. A general increase in film build-up rate observed in successive tests was concluded to be due to increased levels of the active component. Other additives commonly included in formulated oils had little affect on film formation. Comparison of the observed growth rate with a model showed that the material enhanced the EHD film in a solid, speed-independent manner (rather than as a viscous liquid). The film material continued to separate the stationary surfaces, after testing, in the absence of an EHD film.

(ii) Longer chain length mono-alkyl phosphonates also demonstrated thick film formation in the EHD rig. No film formation was observed with short chain mono / di-alkyl phosphonates, neutral amine salts of mono-alkyl phosphonates or tri-*iso*-propyl phosphite. Although these materials formed polymeric material with iron their physical properties did not encourage their retention within the contact.

(iii) Longer chain length mono and di-phosphonates also formed protective layers in contacts operating under initial conditions of low specific film thickness and high sliding i.e. in the boundary lubrication regime. Mono-dodecyl phosphonate approximately doubled the film thickness present in a mini-disc machine. The presence of reacted layers, of the order of 100 nm thick, was confirmed by reflection infra-red studies.

(iv) The behaviour of a range of phosphoric acid esters was investigated in different lubrication regimes. Little or no film formation was observed with di-alkyl acid phosphate or TCP at the maximum temperature attainable in the EHD rig (~ 200^{o} C). TCP was shown to form a reacted layer at 250^{o} C in a boundary lubricated contact. Specimens pretreated with TCP, in this temperature range, were shown to give enhanced film thicknesses of approximately 75 nm in the EHD rig.

Chapter 7 - (i) The physical properties of the film material generated with di-alkyl / aryl phosphonates was shown to be dictated by the environment in which it was formed and, more specifically, by the availability of iron in the correct oxidation state ($Fe^{(III)}$). Static, solution studies produced a viscous, liquid polymer with iron powder. The extent of polymer formation was limited by oxidation of iron. The material was found to undergo slight shear thinning and not to be rheopectic (as reported in [76]). The polymer viscosity increased with time / iron availability. As the polymer chain length grew its oil solubility fell, encouraging its retention at the surface. Surface pretreatment with a rust inhibitor prevented polymer formation. This surface pre-treatment has obvious and potentially damaging practical consequences.

(ii) Polymer material was shown to contribute towards separation in a high sliding, boundary lubricated contact by build-up of a thick, protective layer rather than by chemical polishing. The material formed under these severe conditions was insoluble in common solvents and it could only be removed by using a very rigorous solvent (di-methyl sulphoxide).

(iii) The film material could be 'grown' in a rolling / sliding EHD contact. Under pure sliding conditions a thick reacted layer was formed which produced a transition from boundary, through mixed, to almost full separation of the surfaces. Under rolling

conditions a thick, elastic solid was formed, which was concentrated in the rolling track. The material was not of uniform distribution around the rolling track and it was shown to have a hardness approximately equal to that of annealed glass (at room temperature).

(iv) Model polymeric compounds were prepared in static, solutions tests by reacting additives with oil soluble $Fe^{(III)}$ salts. These materials formed faster and at lower temperatures than materials generated with iron powder and soluble $Fe^{(II)}$ salts. Infra-red spectra confirmed the material to be the same as that formed with iron powder and in operating contacts. A shift in the phosphoryl bond vibration indicated co-ordination to a central iron species, probably by bridging, as described below and in chapter seven. No reaction was observed with Fe_2O_3. All of the model compounds formed were sufficiently temperature stable to prevent their 'melting out' of the contact. However, only the materials formed with long chain mono / di-alkyl phosphonates behaved plastically when stressed. This accounts for their retention in the operating contact.

(v) Solution studies confirmed the proposed hydrolytic break-down of di-alkyl / aryl phosphonates suggested earlier. Some further hydrolysis / cross-linking may occur in the phosphonate anion-bridged oligomers under the severe conditions of temperature and shear present in a rubbing contact. However, the presence of the P—H bond rules out oxidation. Polymeric material was generated with mono and di-phenyl phosphinic acids - in which cross-linking cannot occur - which showed that similar products form in the absence of cross-linking. TCP was shown to form polymeric material by partial hydrolysis.

(vi) The mechanism of polymer formation for di-alkyl / aryl phosphonates is believed to occur as follows. Hydrolysis results in loss of an alkyl group which generates two P—O ligands for co-ordination. The phosphate anion formed has reduced oil solubility which leads to its accumulation in the boundary layer of oil covering the metal surface. The phosphonate anion reacts with $Fe^{(III)}$ created by oxidation in the rubbing / rolling contact. Evidence of the availability of sufficient oxygen is given in reference [129]. The reaction with iron occurs through bridging. Evidence of bridging, rather than chelation, appears in the literature for phosphonates [96], phosphinates [97] and, at high iron concentrations, di-alkyl acid phosphates [95]. The increasing insolubility and viscosity observed, with time, implies formation of a polymeric compound. The physical nature of the material formed is dictated by the availability of $Fe^{(III)}$ and it is presumed to graduate from a glass

like solid at the surface to a soft, viscous liquid (as the polymer chain length falls). Modern EHD theory shows that any material with a viscosity appreciably higher than the base oil will contribute towards surface separation. The formation of a thick, adherent layer has a number of beneficial effects in practical systems. It mitigates the decline in EHD film thickness observed at high temperature, due to viscosity loss, thus permitting operation at higher temperatures than currently attainable. Systems running in the presence of thick EHD films, at relatively high Lambda values, have minimal asperity interaction and surface initiated failure is rare. However, problems are encountered during start-up and stopping when the EHD separation falls to zero. The presence of a thick, reacted layer provides a permanent, speed-independent, alternative separating medium. Large improvements in fatigue life have been reported in the literature [26].

Chapter 8 - (i) Conventional interferometry is subject to the dual restrictions of (i) a minimum measurable film thickness of approximately 100 nm and (ii) measurement of discrete film thicknesses separated by intervals of approximately 50 nm. An improved system was developed incorporating (i) spectroscopic analysis of fringes (to permit continuous measurement of oil film thickness) and (ii) a spacer layer (to reduce the minimum film thickness measurable). The minimum film thickness measurable has been reduced by two orders of magnitude. Films of 1 ± 1 nm were measured at the limits of the technique. Routine measurements down to 5 nm were made.

(ii) The improved technique was used to measure the film forming abilities of a range of conventional lubricants at very low speeds and a range of very low viscosity lubricants at moderate speeds. Effective pressure-viscosity coefficients were measured for lubricants with viscosities as low as 0.003 Pa.s. Many fluids displayed deviation from EHD theory at separations of less than 15 nm. A residual film was observed at very low speeds in some cases. A solution of hexadecane and a boundary / oiliness additive (stearic acid) gave a residual film of approximately 2 nm thickness (which approximates to the length of an aligned stearic acid molecule).

9.2 Suggestions for further work

The experimental work described above has made a contribution towards understanding the mechanisms by which phosphorus-based anti-wear additives form reacted layers. In addition, the physical properties of the polymeric materials have been investigated, where possible, under the unusual conditions of temperature, pressure and shear present in a range of contacts, operating at different specific film thicknesses. 'Activation temperatures' have been identified at which polymer formation is initiated with different groups. This may help in the formulation of lubricants for extreme environments. However, much further work is required to completely understand the situation.

In particular the role of additive impurities requires further work. For example, the rapid film build-up observed with the impure mono-alkyl phosphonate, compared to the di-substituted ester, could have resulted from higher levels of an active thick film forming species present in the mono-phosphonate. Di-substituted phosphonates were shown to operate through the mono-substituted phosphonate hydrolysis-product. This could be further tested by adding a small quantity of amine to a di-phosphonate and comparing the rate of film build-up ± amine. Modern chromatographic techniques should permit separation of the respective components. A comprehensive test procedure comparing individual components, component pairs etc should clarify the mechanism and any synergistic effects etc. Complete elucidation of the mechanism will require very careful control of humidity and oxygen levels in the lubricant and the test environment. A controlled atmosphere chamber would be valuable in this regard. A chamber of this sort would permit the relative oxidative, thermal and hydrolytic stabilities of pure components to be measured with confidence. The use of such well-characterised additives and controlled atmospheres should permit a genuine link to be made between additive structure and functionality.

The thin film technique developed in the course of the current work has numerous potential applications, both to the studies of anti-wear additives and in other cases.

The growth of a reacted layer from initial conditions of very low film thickness may now be possible (albeit for a rather unusual contact metallurgy).

Investigation of the behaviour of lubricants and additives at film thickness where Lambda tends towards 1 is probably of most interest to tribologists. The newly developed technique permits the direct observation of the lubricant / additive behaviour in this region that could previously only be modelled or measured by indirect means.

The high-temperature optical EHD rig was designed to be capable of making traction measurements and development of this area may be expected to produce valuable information.

Combination of thin film and traction measurements should provide information about the limiting shear stress of anti-wear additive films. An additive film grown within a thick EHD film may be subjected to various slide-roll ratios and increased traction forces, as the EHD film thickness is reduced until, presumably, a limiting shear stress is achieved and breakdown of the film is observed. In addition, the film forming abilities of additives will be able to be measured at much higher temperature where viscosity loss prevents the base fluid from forming EHD films thick enough to be measured by conventional interferometry. Thus the role of additives with much higher activation temperatures e.g. TCP may be measured directly.

APPENDIX A1

α REF.		SHC 234		OEP 215		OIL A	
T / ° C	η / Pa.s	T / ° C	η / Pa.s	T / ° C	η / Pa.s	T / ° C	η / Pa.s
23.8	0.381	26.4	0.785	26.5	0.423	26.5	0.275
26.3	0.341	40.0	0.359	40.0	0.172	40.0	0.132
30.0	0.266	60.0	0.135	60.0	0.058	59.5	0.055
39.3	0.150	79.5	0.062	79.5	0.026	79.5	0.028
59.0	0.052	100.0	0.033	99.2	0.014	99.2	0.016
77.0	0.026	115.0	0.023	-	-	-	-

Figure A1 - Temperature-viscosity characteristics of lubricants used in current study

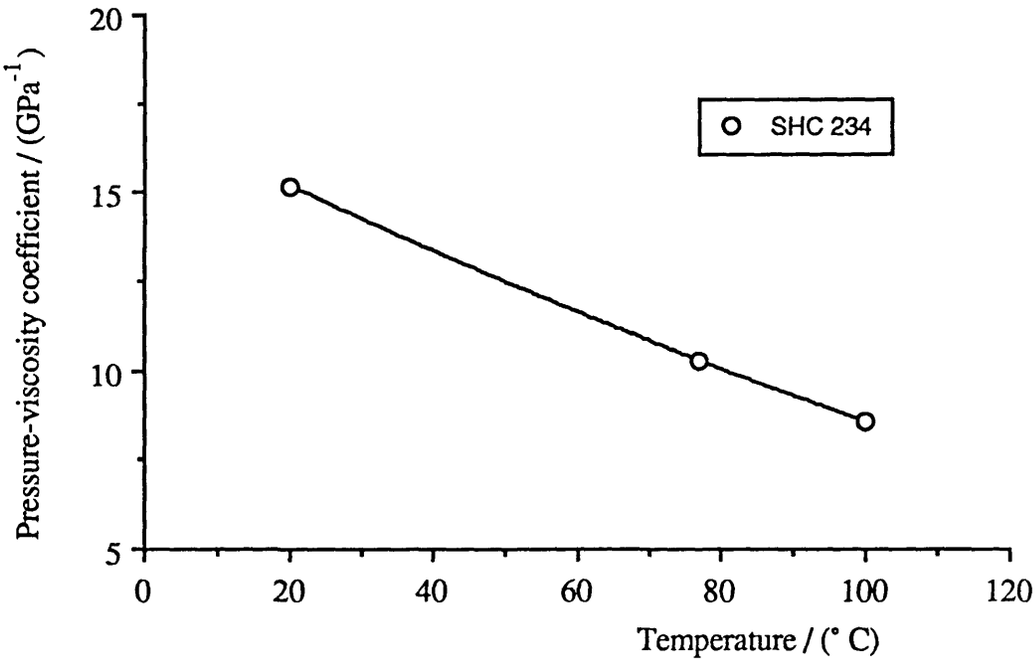


Figure A2 - Effective pressure-viscosity coefficient as a function of temperature

REFERENCES

[1] Buckley, D.H., "*Friction, Wear and Lubrication in Vacuum*," NASA SP-277, National Aeronautics and Space Administration, Washington D.C., pp. 56 - 60, (1971).

[2] Dorinson, A. and Ludema, K.C., "*Mechanics and Chemistry in Lubrication*," Tribology Series, **9**, Elsevier Science Publishing Company Inc., New York, (1985).

[3] Bowden, F.P. and Tabor, D., "*The Friction and Lubrication of Solids*," Oxford Science Publications, Clarendon Press, Oxford, pp. 98 - 99, (1986).

[4] Thomas, T.R., "*Rough Surfaces*," Longman, England, (1981).

[5] Sastry, V.R.F., Sethuramiah, A. and Singh, D.Y., "*A Study of Wear Under Partial EHL Conditions*," Proc. Leeds / Lyon Symp., (1984).

[6] "*Life Adjustment Factor for Ball and Roller Bearings*," ASME Eng. Design Guide, (1971).

[7] Tallian, T.E., Chiu, Y.P., Huttenlocher, F., Kamenshine, J.A., Sibley, L.B. and Sindlinger, N.E., "*Lubricant Films in Rolling Contact of Rough Surfaces*," ASLE Trans, **7**, pp. 109 - 126, (1964).

[8] Cameron, A., "*Basic Lubrication Theory*," 3rd Edition, Ellis Horwood Limited, Chichester, (1981).

[9] Hamrock, B.T. and Dowson, D., "*Isothermal Elastohydrodynamic Lubrication of Point Contact. Part III. Fully Flooded Results*," ASME J. Lub. Tech., pp. 264 - 276, (1977).

[10] Koye, K.A. and Winer, W.O., "*An Experimental Evaluation of the Hamrock and*

Dowson Minimum Film Thickness Equation for Fully Flooded EHD Point Contacts," ASME J. Lub. Tech. **103**, pp. 284 - 294, (1981).

[11] Murch, L.E. and Wilson, W.R.D., "*A Thermal Elastohydrodynamic Inlet Zone Analysis*," ASME J. Lub. Tech., **97**, pp. 264, (1975).

[12] Hamrock, B.J. and Dowson, D., "*Ball Bearing Lubrication*," Wiley, (1981).

[13] Partington, J.R., "*An Advanced Treatise on Physical Chemistry*," Vol. 2, Longmans, Green and Co., London, (1951).

[14] Barus, C., "*Isothermal, Isopiestics and Isometrics Relative to Viscosity*," Am. J. Sci., **45**, pp. 87 - 96, (1893).

[15] A Report of the ASME Research Committee on Lubrication, "*Pressure-Viscosity Report*," The Am. Soc. Mech. Engnrs., Vol **I** and **II**, New York, N.Y, (1953).

[16] So, B.C.Y. and Klaus, E.E., "*Pressure-Viscosity Correlation of Liquids*," ASLE Trans., **23**, 4, pp. 409 - 421, (1980).

[17] Hirst, W. and Hollander, A.E., "*Surface Finish and Damage in Sliding Contacts*," Proc. Roy. Soc. Lond., **A337**, pp. 379 - 394, (1974).

[18] Bigelow, W.C., Pickett, D.L. and Zisman, W.A., "*Oleophobic Monolayers (I) Films Adsorped from Solution in Nonpolar Liquids*," J. Colloid Sci., **1**, pp. 513 - 538, (1946).

[19] Reference [2], Chapter 10.

[20] Smith, H.A. and Allen, K.A., "*The Adsorption of Nonadecanoic Acid on Metal Surfaces*," J. Phys. Chem., **58**, pp. 449 - 452, (1954).

[21] Smith, H.A. and Fort, T., "*The Properties of Surface Films formed by the Adsorption of Nonadecanoic Acid on Mechanically Activated Surfaces*," J. Phys.

Chem., **62**, pp. 519 - 527, (1958).

[22] Furey, M.J., "*The Formation of Polymeric Films Directly on Rubbing Surfaces to Reduce Wear*," Wear, **26**, pp. 369 - 392, (1973).

[23] Dorinson, A., "*A Theory of Cutting-tool Wear and Cutting-oil Action*," ASLE Trans., **1**, pp. 131 - 138, (1958).

[24] Beeck, O., Givens, J.W. and Williams, E.C., "*On the Mechanism of Boundary Lubrication. II. Wear Prevention by Addition Agents*," Proc. Roy. Soc. Lond., **177A**, pp. 103 - 118, (1940).

[25] Parker, R.J. and Kannel, J.W., "*Elastohydrodynamic Film Thickness Between Rolling Discs with a Synthetic Paraffinic Oil to 589 K (600 ^{o} F)*," NASA Technical Note, TN D-6411, (1971).

[26] Fowles, P.E., Jackson, A. and Murphy, W.R., "*Lubricant Chemistry in Rolling Contact Fatigue - The Performance and Mechanism of one Antifatigue Additive*," ASLE Trans., **24**, pp. 107 - 118, (1981).

[27] Rounds, F.G.,"*Effect of Additives on the Friction of Steel on Steel. (I) Surface Topography and Film Composition Studies*," ASLE Trans., **7**, pp. 11 - 23, (1981).

[28] Lacey, I.N., Kelsall, G.H., Spikes, H.A. and MacPherson, P.B., "*Thick Anti-Wear Films in Elastohydrodynamic Contacts (1). Film Growth in Rolling/Sliding EHD Contacts*," ASLE Trans., **29**, 3, pp. 299 - 305, (1986).

[29] Lacey, I.N., Kelsall, G.H., Spikes, H.A. and MacPherson, P.B., "*Thick Anti-Wear Films in Elastohydrodynamic Contacts (2). Chemical Nature of the Deposited Films*," ASLE Trans., **29**, 3, pp. 306 - 311, (1986).

[30] Trachman, E.G. and Cheng, H.S., "*Traction in Elastohydrodynamic Line Contacts for Two Synthesised Hydrocarbon Fluids*," ASLE Trans., **17**, 4, pp. 271 - 279, (1974).

[31] Barcroft, F.T. and Daniel, S.G., "*The action of Neutral Organic Phosphates as EP Additives*," J. of Basic Engineering, Trans. A.S.M.E., **87**, pp. 761 - 770, (1965).

[32] Goldblatt, I.L. and Appeldoorn, J.K., "*The Antiwear Behaviour of TCP in Different Atmospheres and Different Base Stocks*," ASLE Trans., **13**, 4, pp. 203 - 214, (1970).

[33] Zisman, W.A., "*Influence of Constitution on Adhesion*," Industrial and Engineering Chemistry, **55**, 10, pp. 19 - 38, (1963).

[34] Nylen, P., "*Kinetics of Hydrolysis of Dialkyl Phosphites I. Hydrolysis with Hydrogen and Hydroxyl Ions*," Svensk. Kem. Tid. , **49**, pp. 29 - 52, (1937).

[35] Forbes, E.S. and Battersby, J., "*The Effect of Chemical Structure on the Load-Carrying and Adsorption Properties of Dialkyl Phosphites*," ASLE Trans., **17**, 4, pp. 263 - 270, (1974).

[36] Forbes, E.S. and Silver, H.B., "*The Effect of Chemical Structure on the Load-Carrying Properties of Organo Phosphorus Compounds*," J. Inst. Pet., **56**, 548, pp. 90 - 98, (1970).

[37] Barcroft, F.T., "*A Technique for Investigating Reactions between E.P. Additives and Metal Surfaces at High Temperatures*," Wear, **3**, pp. 440 - 453, (1960).

[38] Wiegand, H. and Broszeit, E., "*Zum Mechanismus der Additiv Wirkung Modelluntersuchungen mit Trikresyl Phosphate*," Wear, **21**, pp. 289 - 302, (1972).

[39] Sakurai, T. and Sato, K., "*Chemical Reactivity and Load Carrying Capacity of Lubricating Oils Containing Organic Phosphorus Compounds*," ASLE Trans., **13**, pp. 252 - 261, (1970).

[40] Davey, W.,"*Extreme Pressure Lubricants. Phosphorus Compounds as Additives*," Industrial and Engineering Chemistry, **42**, 9, pp. 1841 - 1847, (1950).

[41] Thorpe, R.E. and Larsen, R.G., "*Antiseizure Properties of Boundary Lubricants*," Industrial and Engineering Chemistry, **41**, 5, pp. 938 - 943, (1949).

[42] Tingle, E.D., "*Fundamental Work on Friction, Lubrication and Wear in Germany during the War Years*," J. Inst. Petroleum, **34**, pp. 743 - 773, (1948).

[43] Forbes, E.S., Neustadter, E.L., Silver, H.B. and Upsdell, N.T., "*The Effect of Chemical Structure on the Load-Carrying Properties of Amine Phosphates*," Wear, **18**, pp. 269 - 278, (1971).

[44] Hall, J.M., "*Antiwear Additives in Neopentyl Ester Oils*," ASLE Trans., **14**, 4, pp. 292 - 300, (1971).

[45] Yamamoto, Y. and Hirano, F., "*Effect of Different Phosphate Esters on Frictional Characteristics*," Trib. Int., **13**, pp. 165 - 169, (1980).

[46] Yamamoto, Y. and Hirano, F., "*Effect of Addition of Phosphate Esters to Paraffinic Base Oils on their Lubricating Performance under Sliding Conditions*," Wear, **78**, pp. 285 - 296, (1982).

[47] Barber, R.I., "*The Preparation of Some Phosphorus Compounds and Their Comparison as Load-Carrying Additives by the Four-Ball Machine*," ASLE Trans., **19**, 4, pp. 319 - 328, (1976).

[48] Jayne, G.J.J., Barber, R. and Elliot, J.S., "*Amine Salts of Phosphorus-Containing Esters*," U.K. Patent 1,302,894, (1973).

[49] Rounds, F.G., "*Effects of Additives on Friction of Steel on Steel I. Surface Topography and Film Composition Studies*," ASLE Trans., **7**, pp. 11 - 23, (1964).

[50] Rounds, F.G., "*Effects of Additives on Friction of Steel on Steel II. Additive-Base Oil Interactions*," ASLE Trans., **8**, pp. 21 - 28, (1965).

[51] Cann, P.M. and Spikes, H.A., "*The Influence of Lubricant on Temperature Generated in Elastohydrodynamic Contact*," To be published, ASLE Trans, (1989).

[52] Rounds, F.G., "*Some Effects on Nonhydrocarbon Base Oil Constituents on the Friction and Surface Coating Formation Obtained with Three Additives*," ASLE Trans., **11**, pp. 19 - 30, (1968).

[53] Rounds, F.G., "*Effect of Aromatic Hydrocarbons on Friction and Surface Coating Formation with Three Additives*," ASLE Trans., **16**, 2, pp. 141 - 149, (1968).

[54] Forbes, E.S., Upsdell, N.T. and Battersby, J.,"*Current Thoughts on the Mechanism of Action of Tricresyl Phosphate as a Load Carrying Additive*," Proc. Trib. Conv., C **64/72**, pp. 7 - 13, (1972).

[55] Rounds, F.G., "*Influence of Steel Composition on Additive Composition*," ASLE Trans., **15**, 1, pp. 54 - 66, (1972).

[56] Mortimer, D. and Sharp, W.B.A., "*Oxidation of Fe-Cr Binary Alloys*," Br. Corros. J., **3**, pp. 61 - 67, (1968).

[57] Hall, J.M., "*Wear and Friction Studies of Neopentyl Ester Oils*," ASLE Trans., **12**, pp. 242 - 253, (1969).

[58] Furey, M.J., "*Surface Roughness Effects on Metallic Contact*," ASLE Trans., **6**, pp. 49 - 59, (1963).

[59] Larsen, R.G. and Perry, G.L., "*Chemical Aspects of Wear and Friction*," in "*Mechanical Wear*," American Society for Metals, Novelty, Ohio, pp. 73 - 94, (1950).

[60] Bita, O. and Dinca, I., "*Behaviour of Phosphorus Additives under Heavy Loads*," Rev. Mecan. Appl., **8**, pp. 441 - 452, (1963).

[61] Godfrey, D., "*The Lubrication Mechanism of Tricresyl Phosphate on Steel,*" ASLE Trans., **8**, pp. 1 - 11, (1965).

[62] Klaus, E.E. and Bieber, H.E., "*Effects of P^{32} Impurities on the Behaviour of Tricresyl Phosphate-32 as an Antiwear Additive,*" ASLE Trans., **8**, pp. 12 - 20, (1965).

[63] Bieber, H.E., Klaus, E.E. and Tewkesbury, E.J., "*A Study of Tricresyl Phosphate as an Additive for Boundary Lubrication,*" ASLE Trans., **11**, pp. 155 - 161, (1968).

[64] Cottington, R.L. and Ravner, H., "*Interactions in Neopentyl Polyol Ester - Tricresyl Phosphate - Iron Systems at 500 F,*" ASLE Trans., **12**, pp. 280 - 286, (1969).

[65] Murphy, C.M., Ravner, H. and Timmons, C.O., "*Factors Influencing the Lead Corrosivity of Ester Oils During Long-Term Storage,*" J. Chem. Eng. Data, **6**, pp. 135, (1961).

[66] Morecroft, D.W., "*Reactions of Octadecane and Decoic Acid with Clean Iron Surfaces,*" Wear, **18**, pp. 333 - 339, (1971).

[67] Weber, K., Eberhardt, E. and Keil, G., Schmierungs Technik, **1**, pp. 10, (1970).

[68] Eberhardt, E., Keil, G. and Weber, K., Schmierungs Technik, **1**, pp. 101, (1970).

[69] Shafrin, E.G. and Murday, J.S., "*Analytical Approach to Ball-bearing Surface Chemistry,*" J. Vac. Sci. Technol., **14**, 1, pp. 246 - 253, (1976).

[70] Shafrin, E.G and Murday, J.S., "*Auger Compositional Analysis of Ball Bearing Steels Reacted with Tricresyl Phosphate,*" ASLE Trans., **21**, 4, pp. 329 - 336, (1977).

[71] Llopis, J., Arizmendi, L., Gamboa, J.M., Martinez-Vilche, V. and Perez-

Fernandez, P., "*Surface Reaction of Iron with Solutions of Phosphorus Organic Compounds*," Corros. Sci., **5**, pp. 319 - 325, (1965).

[72] Faut, O.D. and Wheeler, D.R., "*On the Mechanism of Lubrication by Tricresylphosphate (TCP) - The Coefficient of Friction as a Function of Temperature for TCP on M-50 Steel*," ASLE Trans., **26**, 3, pp. 344 - 350, (1983).

[73] Wheeler, D.R. and Faut, O.D., "*The Adsorption and Thermal Decomposition of Tricresylphosphate (TCP) on Iron and Gold*," Appl. Surf. Sci., **18**, 1 - 2, pp. 106 - 122, (1984).

[74] Gauthier, A., Montes, H. and Georges, J.M., "*Boundary Lubrication with Tricresylphosphate (TCP). Importance of Corrosive Wear*," ASLE Trans., **25**, 4, pp. 445 - 455, (1982).

[75] Donovan, M., Scott, J.W. and Scheir, L.L., "*Phosphoric Acid Treatments for Steel I. The nature of Coatings Produced by the Action of Phosphoric Acid and Steel*," J. Appl. Chem., **8**, pp. 87 - 96, (1958).

[76] Lacey , I.N., "*The Anti-Wear Performance of Some Phosphorus (III) Esters*," Ph.D Thesis , University of London , (1985).

[77] Rounds, F.G., "*Some Environmental Factors Affecting Surface Coating Formation With Lubricating Oil Additives*," ASLE Trans., **9**, pp. 88 - 100, (1966).

[78] Knapp, G.G. and Orloff, H.D., "*Improved Lube Oil Antioxidants*," Industrial and Engineering Chemistry, **53**, 1, pp. 63 - 66, (1961).

[79] Lindinger, H., "*Studies on the Formation of Reaction Layers on Metal Surfaces by Lubricant Blending*," Dtsch Luft-Raumfahrt Forshungsber, DLR-FB 77 - 31, (1977), ex. CA, **89**, 112625, (1978).

[80] Gentle, C.R. and Day, R.S., "*Effect of some Antiwear Additives on the Elastohydrodynamic Lubrication of a Point Contact*," Proc. Trib. Conv. C 81 / 72,

(1972).

[81] Chiu, Y.P., Hahn, D. and Rosenberg, N., "*Exploratory Analysis of EHD Properties of Lubricants*," SKF Report SKF-AL 72 POO1, (1972).

[82] Myers, H., "*Lubricating Oils Containing Phosphorus Products*," U.S. Patent 3,329,742, (1967).

[83] Raich, H., "*Method for Applying Fatigue-resistant Surface Coating*," U.S. Patent 4,054,694, (1977).

[84] Schmitt, K.D., "*Process for Preparing Tertiary Alkylphosphorodichlorodites*," U.S. Patent 4,120,917, (1978).

[85] Parker, R.J., Zaretsky, E.V. and Bamberger, E.N.,"*Bearing Torque and Fatigue Life Studies with Several Lubricants for use in the Range 500 ^{o} to 700 ^{o} F*," NASA Technical Note, TN D-3948, (1967).

[86] Zaretsky, E.V. and Anderson, W.J., "*Preliminery Determinations of Temperature Limitations of Ester, Ether, and Hydrocarbon Base Lubricants in 25 mm Bore Ball Bearings*," NASA Technical Note, TN D-4146, (1967).

[87] Parker, R.J., Bamberger, E.N. and Zaretsky, E.V.,"*Evaluation of Lubricants for High-temperature Ball Bearing Applications*," Trans. ASME, J. Lub. Tech., **90**, pp. 106 - 112, (1968).

[88] Bamberger, E.N., Zaretsky, E.V. and Anderson, W.J., "*Fatigue Life of 120 mm Bore Ball Bearings at 600 ^{o} F with Fluorocarbon, Polyphenyl Ether, and Synthetic Paraffinic Base Lubricants*," NASA Technical Note, TN D-4850, (1968).

[89] Zaretsky, E.V., Anderson, W.J. and Bamberger, E.N., "*Rolling-element Bearing Life from 400 ^{o} to 600 ^{o} F* ," NASA Technical Note, TN D-5002, (1969).

[90] Bamberger, E.N., Zaretsky, E.V. and Anderson, W.J., "*Effect of Three Advanced*

Lubricants on High-temperature Bearing Life," Trans. ASME, J. Lub. Tech., **92**, pp. 23 - 33, (1970).

[91] Parker, R.J. and Zaretsky, E.V.,"*Effect of Oxygen Concentration on the Performance of Synthetic Paraffinic Oils in Short Term Bearing Tests from 400 ^{o} to 500 ^{o} F* ," NASA Technical Note, TN D-5152, (1969).

[92] Zaretsky, E.V. and Bamberger, E.N., "*Advanced Airbreathing Engine Lubricants Study with a Tetraester Fluid and a Synthetic Paraffinic Oil at 492 K (425 ^{o} F)*," NASA Technical Note, TN D-6771, (1972).

[93] Jones, W.R., Johnson, R.L., Winer, W.O. and Sanborn, D.M., "*Pressure-viscosity Measurements for Several Lubricants to 5.5 x 10 ^{8} Newtons per Square Meter (8 x 10 ^{4} psi) and 149 ^{o} C (300 ^{o} F)*," NASA Technical Note, TN D-7736, (1974).

[94] Jones, W.R., Johnson, R.L., Winer, W.O. and Sanborn, D.M., "*Pressure-viscosity Measurements for Several Lubricants to 5.5 x 10 ^{8} Newtons Per Square Meter (8 x 10 ^{4} psi) and 149 ^{o} C (300 ^{o} F)*," ASLE Trans., **18**, 4, pp. 249 - 262, (1975).

[95] Hardy, C.J. and Fletcher, P.R., "*Polymers of Heavy Metals with Dialkyl Phosphonic Acids*," AERE Report R-4281, (1963).

[96] Mikulski, C.M., Karayannis, N.M. and Pylewski, L.L., "*Phosphato and Diorgano Phosphonato Metal Complexes - Characteristic Studies and Physico Chemical Correlation*," J. Inorg. Nucl. Chem., **36**, 5, pp. 971 - 981, (1974).

[97] Block, B.P., "*Polymeric Metal Phosphinates*," Inorg. Macromolecular Rev., **1**, pp. 115 - 125, (1970).

[98] Corbridge, D.E.C., "*Phosphorus*," Elsevier, Amsterdam, pp. 151, (1978).

[99] Chadwick, D.H and Watt, R.S., "*Manufacture of Phosphate Esters and Organic*

Phosphorus Compounds," in *Phosphorus and its Compounds*, Vol. **II**, Van Wazer, J. R., Editor, Interscience, New York, pp. 1272, (1961).

[100] Walker, B.J., "*Organophosphorus Chemistry*," Penguin, England, pp. 96, (1972).

[101] Kirby, A.J. and Warren, S.G., "*The Organic Chemistry of Phosphorus*" in *Reaction Mechanisms in Organic Chemistry*, Eaborn, C. and Chapman, N.B., **5**, Elsevier, Amsterdam, pp. 24, (1967).

[102] Pauling, L.S., "*The Nature of the Chemical Bond*," Cornell University Press, Ithaca, New York, pp. 324, (1960).

[103] Sykes, P., "*A Guidebook to Mechanism in Organic Chemistry*," 4th Ed., Chapter 3 "*The Strength of Acids and Bases*," Longman Group Ltd., London, pp. 52 - 76, (1975).

[104] Anon., "*Nomenclature for Compounds Based on one P Atom*," J. Chem. Soc., pp. 5122, (1952) and Chem. Eng. News., **30**, pp. 2336, pp. 4515, (1952).

[105] Emsley, J. and Hall, D.,"*The Chemistry of Phosphorus*," Harper and Row, London, pp. 307, (1976).

[106] Reference [100], Chapter 1 "*Structure and bonding*," pp. 15 - 47.

[107] Doak, G.O. and Freedman, L.D., Chem. Rev., **61**, pp. 31 - 44, (1961).

[108] Reference [98], pp. 207 - 208.

[109] Reference [105], Chapter 2 "*Bonding at Phosphorus*," pp. 29 - 76.

[110] Hudson, R. F., "*Structure and Mechanism in Organo-phosphorus Chemistry*," Chapter 3 "*d-Orbital Bonding*," Academic Press, London, pp. 46 - 89, (1965).

[111] Kosolapoff, G.M. and Maier, L., (Editors), "*Organic Phosphorus Compounds*,"

Wiley, New York, (1973).

[112] Sasse, K., "*Phosphorus Compounds*," in *Methoden der Organishen Chemie* (Houben-Weyl), Vol. **12**, Muller, E., (Editor), Theime, (1963).

[113] Chadwick, David H. and Watt, Richard S., "*Manufacture of Phosphate Esters and Organic Phosphorus Compounds*," Chapter 19 of *Phosphorus and its Compounds*, Vol. **II**, Van Wazer, J.R., (Editor), Interscience, New York, pp. 1221 - 1279, (1961).

[114] Gerrard, W., "*The Interaction of n-Butyl Alcohol and the Chlorides and Oxychlorides of Phosphorus in the Absence and Presence of Pyridine*," J. Chem. Soc., (ii), pp. 1464 - 1469, (1940).

[115] Gunderloy, Frank C., "*Synthesis of Partial Esters of Phosphorus Acids and Salts Thereof*," U.S Patent 3,019,249, (1962).

[116] Reference [111], Vol. 5, pp. 24 - 26.

[117] M^{c} Combe, H., Saunders, B.C. and Stacy, G.J., "*Esters containing Phosphorus. Part I*," J. Chem. Soc., (i), pp. 380 - 382, (1945).

[118] Bloch, H.S., "*Preparation of Dialkyl Phosphites*," U.S Patent 2,570,512, (1951).

[119] Gamrath, H.R. and Hatton, R.E., "*Dialkyl Phosphoryl Monochlorides*," U.S Patent 2,739,977, (1956).

[120] Gerrard, W., "*Interaction of Hydroxy Compounds and Phosphorus and Thionyl Halides in the Absence and in the Presence of Tertiary Bases (II)*," J. Chem. Soc., 106, (1945).

[121] Freeman, H.F. and Colver, C.W., "*Synthesis of Di-sodium Phenyl Phosphate*," J. Am. Chem. Soc., **60**, pp. 750, (1938).

[122] Koebner, A. and Williamson, A.G., "*Neutral Esters of H_3PO_4*," Brit. Patent 734,768, (1955).

[123] Zenftman, H. and McGillivary, R., "*Aryl Oxyphosphoryl Chlorides*," Brit. Patent 651,656, (1955).

[124] Orloff, H.D., Worrel, C.J. and Markely, F.X., "*Synthesis of Alkyl Aryl Phosphates from Aryl Phosphorochloridates (I) Na Alkoxide Route, (II) Solvolysis Route*," J. Am. Chem. Soc., **80**, pp. 727, (1958).

[125] Faith, W.L., Keyes, D.B. and Clark, R.L., "*Industrial Chemicals*," 2nd Ed., John Wiley & Sons Inc., New York, pp. 777, (1957).

[126] Shuman, R.L., "*Phosphonate Esters*," U.S Patent 2,078,421, (1937).

[127] Anon, Chem. Week., No. 15, **79**, pp. 67, (1956).

[128] Vanderbilt, B.M. and Gottlieb, H.B., "*Neutral Phosphonic Esters of Aliphatic Alcohols*," U.S Patent 2,008,478, (1935).

[129] Tabershaw, I.R., Kleinfield, M. and Feiner, B., "*Tritolyl Phosphate and Alkyl Phenyl Phosphates (I) Environmental Factors*," Arch. Ind. Health, **15**, 537, (1957).

[130] Reference [98], pp. 267.

[131] Shuman, R.L., "*Organic Phosphates and Thiophosphates*," U.S Patent 2,133,310, (1938).

[132] "*Aktien-Gesellschaft fur Anilin-Fabrikation*," Ger. Patent 246,871, (1912).

[133] ter Horst, W.P., U.S Patent 1,837,176, (1931).

[134] Adler, H. and Gottlieb, H.B., "*Triaryl Phosphates*," U.S Patent 1,983,588,

(1934).

[135] Buchheim, K., "*Neutral Esters of Phosphoric Acid with Aliphatic Mono Hydric Acids*," U.S Patent 2,059,084, (1934).

[136] Bannister, W.J., U.S Patent 1,799,349, (1931).

[137] Woodstock, W.H. and Pelltier, P.E., "*Trialkyl Phosphate Esters*," U.S Patent 2,410,118, (1946).

[138] Farbenfabriken Bayer A.-G., Fr. Patent 1,081,003 (1954).

[139] Hochwalt, C.A., Lum, J.H., Malowan, J.E. and Dyer, C.P., "*Alkyl Esters of H_3PO_4*," Ind. Eng. Chem., **34**, pp. 20, (1942).

[140] de Jonge, J.B., "*Separating Mono and Dialkyl Phosphites*," Dutch Patent 77,925, (1955).

[141] Max, N., "*Separating Mono and Dialkyl Phosphites*," Dutch Patent 77,924, (1955).

[142] Zenftman, H. and Whitworth, E., "*Acid Esters of Phosphoric Acid and their Salts*," U.S Patent 2,725,394, (1955).

[143] Adler, H and Woodstock, W.H., "*Alkyl Esters of H_3PO_4*," Chem. Industries, **51**, pp. 516, (1942).

[144] Woodstock, W.H., "*Neutral Esters of Molecularly Dehydrated Phosphoric Acids*," U.S Patent 2,402,703, (1946).

[145] Kosolapoff, G.M. and Maier, L., (Editors), "*Organic Phosphorus Compounds*," John Wiley & Sons, Inc., New York, pp. 232, (1950).

[146] Zwierzak, A., "*Oxidation of Dialkyl Phosphites with Potassium Permanganate. A*

Convenient Preparative Route to Dialkyl Hydrogen Phosphates," Roczniki Chemii, Ann. Soc. Chim. Polonorum, **39**, pp 1411 - 1416, (1965).

[147] Anschutz, R. and Emery, W.O., "*Uber die Einwirkung von Phosphortirichlorid auf Salicylsaure und auf Phenol*," Ann. Chem., **239**, pp. 301 - 313, (1887).

[148] Ford-Moore, A.H. and Williams, J.H., "*The Reaction between Trialkyl Phosphites and Alkyl Halides*," J. Chem. Soc., pp. 1465 - 1467, (1947).

[149] Gerard, W. and Sheperd, B.D., "*Formation of Sulphites, Phosphites and Phosphates of Alcohols containing an Aryl Group*," J. Chem. Soc., pp. 2069 - 2074, (1953).

[150] Mark, V. and Van Wazer, J.R., "*Tri-t-butyl Phosphite and some of its Reactions*," J. Org. Chem., **29**, pp. 1006 - 1008, (1964).

[151] Chadwick, D.H. and Reetz, T., "*Phosphorus Acid Esters and Method of Making Same*," U.S. Patent 2,865,942, (1958).

[152] Virginia-Carolina Chemical Corp., "*Alkyl and Aryl Esters of Phosphorous Acid*," U.K. Patent 853,982, (1960).

[153] Hoffman, F.W., Ess, R.J. and Usinger, R.P., "*Tranesterification of Trialkyl Phosphites with Aliphatic Alcohols*," J.A.C.S, **78**, pp. 5817 - 5822, (1956).

[154] Yamazaki, N. and Higashi, F., "*Triphenyl Phosphite*," Japan Kokai, **77**, 42,858 (1977), ex. C.A., **87**, pp. 134,558, (1977).

[155] Bliznyuk, N.K., Protasova, L.D., Sakharchuck, T.A., Klopkova, R.S. and Klimova, T.A., "*Dialkyl Phosphites*," U.S.S.R. Patent 488,280, (1975), ex. C.A., **84**, pp. 4473, (1976).

[156] Walsh, E.N., "*Conversion of Tertiary Phosphites to Secondary Phosphonates. Diphenyl Phosphonate*," J.A.C.S., **81**, pp. 3023, (1959).

[157] Schimmelschmidt, K. and Kleiner, H.J., "*Dialkyl Phosphites*," U.K. Patent 1,298,156, (1972).

[158] Cook, H.G., M^{c}Combie, H. and Saunders, B.C., "*Esters containing Phosphorus. Part II*," J. Chem. Soc., pp. 873 - 874, (1945).

[159] Jenker, H., "*Alkyl Phosphites*," U.K. Patent 1,122,450, (1968).

[160] Nifant'er, E.E., Blagoveshchenskii, V.S., Sokurenko, A.M. and Sklyarskii, L.S., "*Monoalkyl Phosphonates*," U.S.S.R. Patent 363,708, (1972), ex. C.A. **78**, pp. 159865, (1973).

[161] Bridger, R.F. and Schmitt, K.D., "*Process for Preparing Monoaryl Phosphonates and Lubricant Compositions Containing Same*," U.S. Patent 4,092,254, (1978).

[162] Michalski, J., Modro, T. and Zwierzak, A., "*Anhydrides of Organophosphorus Acids. Part II ; The Synthesis of Tri and Tetra Alkyl Esters of Phosphorus and Phosphoric Anhydrides*," J. Chem. Soc., pp. 4904 - 4906, (1961).

[163] Smith, T.D. and Parker, J., "*Reaction of Thiourea with Dialkyl Phosphites and Trialkyl Phosphates*," J.C.S., 442, (1961).

[164] Smith, T.D., "*The Preparation of Ammonium Alkyl Hydrogen Phosphites*," J.C.S., 997, pp. 5050 - 5051 (1961) and "*The Preparation of Ammonium Alkyl Hydrogen Phosphites*," Wear, **18**, pp. 269, (1971).

[165] Finegold, H., "*Complimentary Use of N.M.R. and Infrared Absorbtion Studies in Organic Phosphorus Chemistry*," Ann. N.Y. Acad. Sci., **70**, pp. 875 - 889, (1958).

[166] Thomas, L.C., "*Identification of Functional Groups in Organophosphorus Chemistry*," Academic Press, London, pp. 23 - 48, (1974).

[167] Reference [105], Chapter 3, "*$^{31}P_{n.m.r}$ and vibrational spectra of phosphorus compounds.*"

[168] Cruthfield, M.M., Dungan, C.H., Letcher, J.H., Mark, V. and Van Wazer, J.R., "*P^{31} Nuclear Magnetic Resonance,*" Vol. 5, *Topics in Phosphorus Chemistry,* Interscience, New York, (1967).

[169] Thomas, L.C., "*Interpretation of the Infrared Spectra of Organophosphorus Compounds,*" Heyden and Son Ltd., London, (1974).

[170] Corbridge, D.E.C., "*Infrared Analysis of Phosphorus Compounds,*" J. Appl. Chem., **6**, pp. 456 - 465, (1956).

[171] Smith, A. Lee., "*Applied Infrared Spectroscopy. Fundamentals, Techniques and Analytical Problem-solving,*" Vol. 54, *Chemical Analysis,* (Editors) Elving, P.J. and Winefordner, J.D., Wiley-Interscience, New York.

[172] Bance, S., "*Handbook of Practical Organic Microanalysis,*" Ellis-Horwood, Chichester, (1980).

[173] Harless, H.R., "*Organophosphites - The Effect of Ionizing Electrons on the Relative Abundance of their Ion Species,*" Anal. Chem., **33**, 10, pp. 1387 - 1389, (1961).

[174] Occolowitz, J.L. and White, G.L., "*The Mass Spectroscopy of Esters of Phosphorus and Phosphonic Acids,*" Anal. Chem., **35**, 9, pp. 1179 - 1182, (1963).

[175] Ferrante, J., Buckley, D.H., Pepper, S.V. and Brainard, W.A., "*Use of LEED, Auger Emission Spectroscopy and Field Ion Microscopy in Microstructural Studies,*" in *Microstructural Analysis: Tools and Techniques,* (Editors) McCall, J.L. and Mueller, W.M., Plenum Press, New York, pp. 241 - 279, (1973).

[176] Buckley, D.H., "*The Use of Analytical Surface Tools in the Fundamental Study of*

Wear," Wear, **46**, pp. 19 - 53, (1978).

[177] Godfrey, D., "*Review of the Usefulness of New Surface Analysis Instruments in Understanding Boundary Lubrication*," in *Fundamentals of Tribology*, (Editors) Suh, N.P. and Saka, N.A., MIT Press, Cambridge, pp. 945 - 967, (1980).

[178] Ferrante, J., "*Practical Applications of Surface Analytical Tools in Tribology*," Lubrication Eng., **38**, 4, pp. 223 - 236, (1982).

[179] "*Characterization of Solid Surfaces*," (Editors) Kane, P.F. and Larrabee, G.B., Plenum Press, New York, (1974).

[180] Singer, I.L. and Murday, J.S., "*Investigation of Lubricated Bearing Surfaces by X-Ray Photoelectron and Auger Electron Spectroscopies*," in *Fundamentals of Tribology*, (Editors) Suh, N.P. and Saka, N.A., MIT Press, Cambridge, pp. 239 - 252, (1980).

[181] Oppelt, J., Mueller, K. and Bartz, W.J., "*Wear Scar Analysis by Ion Beam Technology*," ASLE Preprint N^{o}. 79-LC-2B-4, (1979).

[182] Gefter, E.L.,"*Organophosphorus Monomers and Polymers*," pp. 110, Associated Technical Services Ltd., New Jersey, (1961).

[183] Weast, Robert C., "*CRC Handbook of Chemistry and Physics*," 55th Edition, CRC Press Inc., Cleveland, Ohio, (1974-5).

[184] Thomas, L.C., Chittenden, R.A. and Hartley, H.E.R., "*Hydrogen Bonding in Alkyl Phosphonic and Alkyl Phosphonothionic Acids*," Nature, **192**, pp. 1283 - 1284, (1961).

[185] Thomas, L.C. and Chittenden, R.A., "*Characteristic Infrared Absorption Frequencies of Organophosphorus Compounds - II P — O — (X)*," Spec. Acta., **20**, pp. 489 - 502, (1964).

[186] Bellamy, L.J., "*The Infrared Spectra of Complex Molecules*," Vol. 1, 3rd Edn., Chapman and Hall, London, pp. 348 - 353, (1975).

[187] Pouchert, C.J., "*The Aldrich Library of Infrared Spectra*," Aldrich Chemical Company Inc, pp. 407 - 415 and 865 - 872, (1975).

[188] Thomas, L.C. and Chittenden, R.A., "*Characteristic Infrared Absorption Frequencies of Organophosphorus Compounds - I The Phosphoryl (P=O) Group*," Spec. Acta., **20**, pp. 467 - 487, (1964).

[189] Meyer, D.R. and Wilson, C.C., "*Measurement of Elastohydrodynamic Oil Film Thickness and Wear in Ball Bearing by the Strain Gauge Method*," ASME J. Lub. Tech., **93**, pp. 224 - 230, (1971).

[190] Johnson, K.L. and Roberts, A.D., "*Film Thickness Variation with Load in EHL Contacts*," Wear, **27**, pp. 391 - 393, (1974).

[191] Sibley, L.B. and Orcutt, F.K., "*Elastohydrodynamic Lubrication of Rolling Contact Surfaces*," ASLE Trans., **4**, pp. 234 - 249, (1961).

[192] Crook, A.W., "*The Lubrication of Rollers*," Phil. Trans. Roy. Soc., **250**, pp. 387 - 409, (1958).

[193] Furey, M.J., "*Metallic Contact and Friction between Sliding Surface*," ASLE Trans., **4**, pp. 1 - 11, (1961).

[194] Willis, T., Seth, B. and Dave, M., "*Evaluation of a Diffraction Method for Width Measurements of Oil Filled Gaps*," ASME J. Lub. Tech., **97**, 4, pp. 649 - 650, (1975).

[195] Gohar, R. and Cameron, A., "*The Mapping of Elastohydrodynamic Contacts*," ASLE Trans., **10**, pp. 215 - 225, (1966).

[196] Tolansky, S., "*An Introduction to Interferometry*," Longmans, London, (1966).

[197] Francon, M., "*Optical Interferometry*," Academic Press, New York, (1966).

[198] Steel, W.H., "*Interferometry*," Cambridge University Press, London, (1967).

[199] Wedeven, L.D., Ph.D Thesis, University of London, (1970).

[200] Gentle, C.R., Ph.D Thesis, University of London, (1971).

[201] Jackson, A., Ph.D Thesis, University of London, pp. 61 - 65, (1972).

[202] Michelson, A.A., "*Light Waves and their Uses*," The Decennial Publications, University of Chicago Press, Chicago, Second Series, Vol. **III**, (1907).

[203] Westlake, F.J., "*A Study of Ultra Thin Films*," Ph.D Thesis, University of London, (1971).

[204] Foord, C.A., Hamman, W.C. and Cameron, A., "*Evaluation of Lubricants using Optical Elastohydrodynamics*," ASLE Trans., **11**, pp. 31 - 43, (1968).

[205] Paul, G.R. and Cameron, A., "*An Absolute High-Pressure Microviscometer Based on Refractive Index*," Proc. Roy. Soc., London, **A 331**, pp. 171 - 184, (1972).

[206] Hartung, H.A., "*Density-Temperature-Pressure Relations for Liquid Lubricants*," Trans. Am. Soc. Mech. Engrs., **78**, pp. 941 - 947, (1956).

[207] Hares, J.A., "*The Commissioning of an Elastohydrodynamic Lubrication Rig*," Internal Report, Imperial College, (1978-9).

[208] Mills, T.N., "*Boundary Lubrication at High Repetition Rates*," Ph.D Thesis, University of London, (1979).

[209] Tonk, A., Martin, J.M., Kapsa, P.H. and Georges, J.M., "*Boundary Lubrication with Anti-wear Additives : Study of Interference Film Formation by Electrical*

Contact Resistance," Tribology Int., pp. 209 - 213, (1979).

[210] Cann, P.M., Spikes, H.A. and Cameron, A., "*Thick Film Formation by Zinc Dialkyl Dithiophosphate*," ASLE Trans., **26**, pp. 48 - 52, (1983).

[211] Georges, J.M., "*Colloidal Behaviour of Films in Boundary Lubrication*," Tribol. Ser., **7**, pp. 729 - 761, (1982).

[212] Cann, P.M.E., Johnston, G.J. and Spikes, H.A., "*The Formation of Thick Films by Phosphorus-Based Anti-Wear Additives*," Proc. I.Mech. E., I.Mech. E. Conf. (1987 -88), Vol.1, **C208/87**, pp. 543 - 554, (1987).

[213] Crook, A.W., "*Simulated Gear Tooth Contacts*," Proc. I. Mech. E., **171**, pp. 187 - 214, (1957).

[214] Dr. P.M.E. Cann, Private Communication.

[215] Dyson, A., Naylor, H. and Wilson, A.R., "*Measurement of Oil Film Thickness in EHD Contacts*," Proc. I. Mech. E., **180**, (3B), pp. 119 - 134, (1965).

[216] Perkin, R.T., "*The Measurement of Oil Film Thickness in Elastohydrodynamic Contacts*," Internal Report, Final Year Project, Imperial College, (1986).

[218] Burfield, D. and Smithers, R., "*Desiccant Efficiency in Solvent Drying 3. Dipolar Aprotic Solvents*," J. Org. Chem., **43**, pp. 3967, (1978).

[219] Goldstein, J.I. and Yakowitz, H. (Eds.), "*Practical Scanning Electron Microscopy*," Chapters **9** and **11**, Plenum Press, New York, (1975).

[220] Scott, V.D. and Love, G., "*Quantitative Electron Probe Microanalysis*," Chapters **2**, **4** and **5**, Ellis Horwood, Chichester, (1983).

[221] Rounds, F.G., General Motors Research Laboratories. Warren, Michigan,

48090 - 9055, USA. Private Communication.

[222] Liang, X. and Linqing, Z. *"A New Method for the Experimental Investigation of Contacts in Mixed Lubrication,"* Wear **132**, pp. 221 - 233, (1989).

[223] Westlake, F. J., *"An Interferometric Study of Ultra-Thin Films,"* PhD Thesis, Univ. of London, (1970).

[224] Guangteng, G. and Spikes, H.A. *"Properties of Ultra-Thin Lubricating Films Using Wedged Spacer Layer Optical Interferometry,"* Proc. 14th Leeds-Lyon Symp. on Tribology, "Interface Dynamics," Ed D. Dowson, Elsevier 1988.

[225] Born, M., *"Principles of Optics. Electromagnetic Theory of Propagation, Interference and Diffraction of Light,"* Longmans, (1950).

[226] Kauffman, A.M., *"A Simple Immersion Method to Determine the Refractive Index of Thin Silica Films,"* Thin Solid Films, **1**, pp. 131 - 136, (1967).

[227] Spikes, H.A., Cann, P. and Caporiccio, G., *"Elastohydrodynamic Film Thickness Measurements of Perfluoropolyethers,"* J. Synth. Lubrication, **1**, 1, pp. 73 - 86, (1984).

[228] Duocoulombier, D., Zhou, H., Boned, C., Peyrelase, J., Saint-Guirons, H. and Xans, P., *"Pressure (1-1000 bars) and Temperature (20-100 ℃) Dependence of the Viscosity of Liquid Hydrocarbons,"* J. Phys. Chem., **90**, pp. 1692 - 1700, (1986).

[229] Akhmatov, A.S., *"Molecular Physics of Boundary Friction, (Chap. 8),"* Israel Prog. for Sci. Transl., (1966).

AUTHORS PUBLICATIONS

(I) Johnston, G. J., Cann, P.M. and Spikes, H.A., "*Phosphorus Anti-Wear Additives: Thick Film Formation and its Influence on Surface Distress*," Proc. 12th Leeds-Lyon Symposium, **VI(ii)**, pp. 128 - 134, (1985).

(II) Johnston, G.J., Cann, P.M.E. and Spikes, H.A., "*A New Mechanism for Gear and Bearing Anti-Wear Additive Behaviour*," Proc. 5th International Colloquium, Technische Akademie Esslingen, Vol.1, **3.12-1**, pp. 1 - 16, (1986).

(III) Waterhouse, C., Johnston, G.J., Ewing, P. and Spikes, H.A., "*The Elastohydrodynamic Behaviour of Simple Liquids at Low Temperatures*," Proc. 13th Leeds-Lyon Symposium, **VIII**, pp. 267 - 275, (1986).

(IV) Cann, P.M.E., Johnston, G.J. and Spikes, H.A., "*The Formation of Thick Films by Phosphorus-Based Anti-Wear Additives*," Proc. I.Mech. E., I.Mech. E. Conf. (1987 -88), Vol.1, **C208/87**, pp. 543 - 554, (1987).

(V) Johnston, G. J., Cann, P.M.E. and Spikes, H.A., "*In-situ studies of Phosphorus Anti-Wear Films*," Presented ACS Meeting, Dallas, Texas, April, (1989).

(VI) Johnston, G.J., Wayte, R. and Spikes, H.A., "*The Measurement and Study of Very Thin Lubricant Films in Concentrated Contacts*," Accepted for Publication, ASLE Trans, (1990).